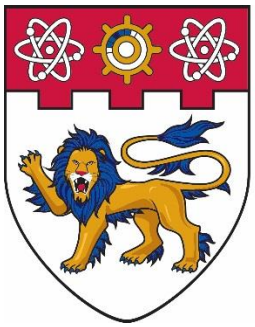

NANYANG TECHNOLOGICAL UNIVERSITY
SINGAPORE

INVESTIGATION OF MEMBRANE FOULING USING MOLECULAR DYNAMICS SIMULATION

MA YUNQIAO

INTERDISCIPLINARY GRADUATE PROGRAMME

Singapore Membrane Technology Centre

Nanyang Environment and Water Research Institute

2022

INVESTIGATION OF MEMBRANE FOULING USING MOLECULAR DYNAMICS SIMULATION

MA YUNQIAO

INTERDISCIPLINARY GRADUATE PROGRAMME
Singapore Membrane Technology Centre
Nanyang Environment and Water Research Institute

A thesis submitted to the Nanyang Technological University in partial fulfillment of the requirement for the degree of
Doctor of Philosophy

2022

Statement of Originality

I hereby certify that the work embodied in this thesis is the result of original research, is free of plagiarised materials, and has not been submitted for a higher degree to any other University or Institution.

1/6/2022

. . . . . .

Date

. . . . . .

Ma Yunqiao

Supervisor Declaration Statement

I have reviewed the content and presentation style of this thesis and declare it is free of plagiarism and of sufficient grammatical clarity to be examined. To the best of my knowledge, the research and writing are those of the candidate except as acknowledged in the Author Attribution Statement. I confirm that the investigations were conducted in accord with the ethics policies and integrity standards of Nanyang Technological University and that the research data are presented honestly and without prejudice.

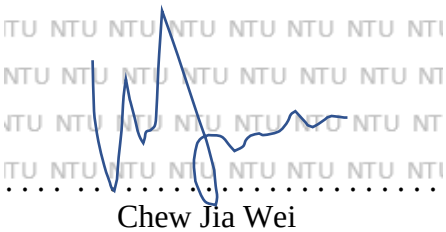

1/6/2022

. . . . . .

Date

. . . . . .

Chew Jia Wei

Authorship Attribution Statement

This thesis contains material from 7 papers published in the following peer-reviewed journals in which I am listed as an author.

Chapters 1, 2 and 9 is published as Y. Ma, J. W. Chew, Investigation of Membrane Fouling Phenomenon Using Molecular Dynamics Simulations: A Review, *Journal of Membrane Science*, 661 (2022) 120874. DOI: https://doi.org/10.1016/j.memsci.2022.120874

The contributions of the co-authors are as follows:

- Prof Chew Jia Wei provided the initial direction of compiling papers for review and edited the manuscript drafts.
- I prepared the manuscript drafts with all figure plotting, literature summary and paper compilation/interpretation conducted by me.

Chapter 3 is published as Y. Ma, S. Velioğlu, M.B. Tanis-Kanbur, R. Wang, J.W. Chew, Mechanistic understanding of the adsorption of natural organic matter by heated aluminum oxide particles (HAOPs) via molecular dynamics simulation, *Journal of Membrane Science*, 598 (2020) 117651. DOI: https://doi.org/10.1016/j.memsci.2019.117651

The contributions of the co-authors are as follows:

- Prof Chew Jia Wei and Prof Wang Rong provided the initial project direction and edited the manuscript drafts.
- I prepared the manuscript drafts with all the data analysis and interpretation conducted by me.
- I co-designed the study with Dr. Sadiye Velioğlu and Dr. Melike Begum Tanis-Kanbur, and they taught me how to prepare input files and run simulation on the resource of High Performance Computing Centre of NTU.

Chapter 4 is published as Y. Ma, T. Hua, T.A. Trinh, R. Wang, J.W. Chew, Molecular dynamics simulation of the competitive adsorption behavior of effluent organic matters by heated aluminum oxide particles (HAOPs), *Separation and Purification Technology*, 292 (2022) 120961. DOI: https://doi.org/10.1016/j.seppur.2022.120961.

The contributions of the co-authors are as follows:

- Prof Chew Jia Wei and Prof Wang Rong provided the initial project direction and edited the manuscript drafts.
- I prepared the manuscript drafts with all the data analysis and interpretation conducted by me.
- Dr. Hua Tao and Dr. Thein An Trinh provided laboratory experimental data for the validation, and I have discussed the interpretation of simulation results with them.

Chapter 5 is published as Y. Ma, A.L. Zydney, J.W. Chew, Membrane fouling by lysozyme: Effect of local interaction, *AIChE Journal*, 67 (2021) e17212. DOI: https://doi.org/10.1002/aic.17212.

The contributions of the co-authors are as follows:

- Prof Chew Jia Wei and Prof Andrew Zydney provided the initial project direction and edited the manuscript drafts.
- I prepared the manuscript drafts with all the simulation, data analysis and interpretation conducted by me.

Chapter 6 is published as Y. Ma, A.L. Zydney, R. Wang, J.W. Chew, Molecular dynamics study on membrane fouling by oppositely charged proteins, *AIChE Journal*, 67 (2021) e17335. DOI: https://doi.org/10.1002/aic.17335.

The contributions of the co-authors are as follows:

- Prof Chew Jia Wei and Prof Andrew Zydney provided the initial project direction and edited the manuscript drafts.
- Prof Wang Rong provided guidance regarding paper writing and the interpretation and presentation of simulation results.
- I prepared the manuscript drafts with all the simulation, data analysis and interpretation conducted by me.

Chapter 7 is published as Y. Ma, S. Velioğlu, T.A. Trinh, R. Wang, J.W. Chew, Investigation of Surfactant–Membrane Interaction Using Molecular Dynamics Simulation with Umbrella Sampling, *ACS ES&T Engineering*, 1 (2021) 1470-1480. DOI: https://doi.org/10.1021/acsestengg.1c00262.

The contributions of the co-authors are as follows:

- Prof Chew Jia Wei and Prof Wang Rong provided the initial project direction and edited the manuscript drafts.
- I prepared the manuscript drafts with all the simulation-related data analysis and interpretation conducted by me.
- I co-designed the study with Dr. Sadiye Velioğlu and Dr. Thien An Trinh.
- Dr. Sadiye Velioğlu helped me prepare the original membrane structure file and adviced me how to perform further modification.
- Dr. Thien An Trinh performed all the experiments and compiled experimental data, and guided me regarding how to interpret them.

Chapter 8 is published as Y. Ma, S. Velioğlu, Z. Yin, R. Wang, J.W. Chew, Molecular dynamics investigation of membrane fouling in organic solvents, *Journal of Membrane Science*, 632 (2021) 119329. DOI: https://doi.org/10.1016/j.memsci.2021.119329.

The contributions of the co-authors are as follows:

- Prof Chew Jia Wei and Prof Wang Rong provided the initial project direction and edited the manuscript drafts.
- I prepared the manuscript drafts with all the simulation-related data analysis and interpretation conducted by me.
- Dr. Sadiye Velioğlu helped me prepare the original membrane structure file and adviced me how to perform further modification.
- Dr. Yin Ziqiang performed all the experiments and compiled experimental data, and guided me regarding how to interpret them.

1/6/2022

. . . . . .
Date

. . . . . .
Ma Yunqiao

Acknowledgements

Shall there be no torch henceforth

Let me be the only light

Well, this is really the grand finale. After these splendid 9 years of youth at NTU, I'm about to own a Dr title accompanying me till the end. It just feels unbelievable thinking of how much thick and thin I have been through. As a grown-up I don't really have a dream; all I do is just continuously putting effort into my domain. Now I can proudly say that dream has found me. Hey, it's just a degree; you still got a life to live.

I must thank my supervisor Prof. Chew Jia Wei first. I took her courses during my undergraduate time, and her passion was one key reason I decided to stay at NTU. She had quite high expectations for me, but did provide valuable guidance and ample room of freedom for me to achieve a work-life balance. All I want to say is that if given another chance, I'll still choose to do a PhD under her. The same goes for my co-supervisor Prof. Wang Rong, who happens to share the identical hometown with me. I feel so honoured to work under one of the leading researchers in the membrane technology field. Not only did she help me to get this PUB scholarship in the first place, but she also dedicates great effort to creating and maintaining a lively and thriving environment of SMTC. Along with my supervisors, I also want to thank my high school physics teacher Mr. Zhou Hai who oversaw our class. His personality, enthusiasm, trust, and guidance always inspire me when pursuing knowledge and higher degrees in these 9 years.

Next, I give my appreciation to fellow researchers from SMTC and our group. Many seniors have given me patient guidance about simulation, modeling, and experiment; and in the meantime offered me suggestions regarding the planning of my PhD and future career. In particular, I want to thank the following seniors: Han Qi, Hua Tao, Sadiye Velioğlu, Tanis Kanbur Melike Begum, Thien An Trinh, and Wang Jingwei. I shall also thank Lay Huang Teik who joined the group on the same batch as me. We help each other survive these 4 years by constantly exchanging ideas, sharing opinions, and giving technical and emotional support. Finally, my travelling partner, Lim Yu Jie. It's such a blessing to hold the same scholarship with him, so that we can do all the conference travel planning together. Despite Covid, with great determination from both of us, we still managed to attend quite a handful of conferences and see the beautiful world with our own eyes. I'll forever cherish all the collaboration and communication we had, no matter it's about administration, research, or personal life.

I am not a very social person, but I do have quite some personal friends to thank. When I feel down, I can always find inspiration and encouragement from them. These include my fellow CBE friends who have already gone to various parts of the world (Huang Xing, Jin Xiaojia, Li Fanxiang, Ng Chong Yong, Ren Junjie, Wang Zhe), sporting friends who are willing to "all in" on the field (Shao Yiyang, Zhou Yunqi, Zhu Yimin), close friends since bridging course (Huang Shuai, Liu Xiaoyu, Ren Daxuan, Yang Fan, Zhang Jinyan, Zhong Yixuan, Zhou Yi), and a few others (Ning Xiaoyu, Xu Hanyi, You Chengyun, Zhang Ming). Thank you all for accepting me as who I am, and bringing bright colours to my life. Especially, I want to thank my Disney cartoon, data science, music and Domino mate, the "giraffe" Liu Yuming who has been by my side since childhood. I always cherish the seasons in the sun we had before I left for university. Our friendship still stays fresh after that, with the most frequent conversation and regular reunion shining along our separate journeys. I couldn't do all these without you, and I'll tell you all about it when I see you again.

Lastly, I never feel like I'm walking alone. Despite the geographical distance, my family is always giving me strong support at the back. Our regular reunion has always been a critical knot for me to recharge and hit the road again. Now that I have finished this important chapter of my life, you can all proudly say that you have completed the mission impossible: raise a kid and lead the way for him to become a spark. Here is my ultimate gratitude to my mom, dad, uncle, aunt, and chipmunk-like cousin.

And, I save the best for the very end. The entire thesis is dedicated to my beloved maternal grandparents, Mr. LIU HAIJI and Mrs. WANG YUNXIU. For me, you two are the brightest star in the night sky; I'm everything I am because you love me.

Table of Content

List of Publications

First-author publications:

1. Y. Ma, J.W. Chew, Investigation of Membrane Fouling Phenomenon Using Molecular Dynamics Simulations: A Review, *Journal of Membrane Science*, 661 (2022) 120874.
2. Y. Ma, T. Hua, T. A. Trinh, R. Wang, J.W. Chew, Molecular dynamics simulation of the competitive adsorption behavior of effluent organic matters by heated aluminum oxide particles (HAOPs), *Separation and Purification Technology*, 292 (2022) 120961.
3. Y. Ma, S. Velioğlu, T.A. Trinh, R. Wang, J.W. Chew, Investigation of Surfactant–Membrane Interaction Using Molecular Dynamics Simulation with Umbrella Sampling, *ACS ES&T Engineering*, 1 (2021) 1470-1480.
4. Y. Ma, A.L. Zydney, R. Wang, J.W. Chew, Molecular dynamics study on membrane fouling by oppositely charged proteins, *AIChE Journal*, 67 (2021) e17335.
5. Y. Ma, S. Velioğlu, Z. Yin, R. Wang, J.W. Chew, Molecular dynamics investigation of membrane fouling in organic solvents, *Journal of Membrane Science*, 632 (2021) 119329.
6. Y. Ma, A.L. Zydney, J.W. Chew, Membrane fouling by lysozyme: Effect of local interaction, *AIChE Journal*, 67 (2021) e17212.
7. Y. Ma, S. Velioğlu, M.B. Tanis-Kanbur, R. Wang, J.W. Chew, Mechanistic understanding of the adsorption of natural organic matter by heated aluminum oxide particles (HAOPs) via molecular dynamics simulation, *Journal of Membrane Science*, 598 (2020) 117651.

Co-author publications:

1. H.J. Tanudjaja, A. Anantharaman, A.Q.Q. Ng, Y. Ma, M.B. Tanis-Kanbur, A.L. Zydney, J.W. Chew, A review of membrane fouling by proteins in ultrafiltration and microfiltration, *Journal of Water Process Engineering*, 50 (2022) 103294.
2. Y.J. Lim, G.S. Lai, Y. Zhao, Y. Ma, J. Torres, R. Wang, A scalable method to fabricate high-performance biomimetic membranes for seawater desalination: Incorporating pillar[5]arene water nanochannels into the polyamide selective layer, *Journal of Membrane Science*, 661 (2022) 120957.
3. M.S.R.S. Kapavarapu, Y. Ma, S. Vasudevan, J.W. Chew, Economic Analysis of Membrane-Based Separation of Biocatalyst: Mode of Operation and Stage Configuration, *Industrial & Engineering Chemistry Research*, (2022).
4. Y.J. Lim, Y. Ma, J.W. Chew, R. Wang, Assessing the potential of highly permeable reverse osmosis membranes for desalination: Specific energy and footprint analysis, *Desalination*, 533 (2022) 115771.
5. H.T. Lay, R.J.E. Yeow, Y. Ma, A.L. Zydney, R. Wang, J.W. Chew, Internal membrane fouling by proteins during microfiltration, *Journal of Membrane Science*, 637 (2021) 119589.
6. Z. Yin, R.J.E. Yeow, Y. Ma, J.W. Chew, Link between interfacial interaction and membrane fouling during organic solvent ultrafiltration of colloidal foulants, *Journal of Membrane Science*, 611 (2020) 118369.
7. Z. Yin, Y. Ma, B. Tanis-Kanbur, J.W. Chew, Fouling behavior of colloidal particles in organic solvent ultrafiltration, *Journal of Membrane Science*, 599 (2020) 117836.
8. J. Tian, M. Pan, Y. Ma, J.W. Chew, Effect of membrane fouling on chiral separation, *Journal of Membrane Science*, 593 (2020) 117352.
9. T.A. Trinh, Q. Han, Y. Ma, J.W. Chew, Microfiltration of oil emulsions stabilized by different surfactants, *Journal of Membrane Science*, 579 (2019) 199-209.

Conference presentations:

1. Organic Matter Removal for Reverse Osmosis Fouling Mitigation: From Lab Prototype and Numerical Simulation to Pilot Plant, at 2022 Meeting of the North American Membrane Society (NAMS) (Oral).
2. Investigation of Interaction Between Membrane and Surfactant-stabilized Oil Emulsion: From Experiments to Molecular Dynamics Simulation, at 5th International Conference on Applied Surface Science (Oral).
3. Investigation of surfactant-membrane interaction using molecular dynamics simulation with umbrella sampling, at Singapore International Water Week 2022 (Poster).
4. Molecular Dynamics Investigation of Membrane Fouling in Organic Solvents, at Euromembrane 2021 (Poster).
5. Molecular dynamics study on membrane fouling by oppositely charged proteins, at 5th International Conference on Desalination using Membrane Technology (MEMDES) 2021 (Poster).
6. Investigating adsorption of natural organic matter by HAOPs via molecular dynamics simulation, at Singapore International Water Week 2021 (Poster).
7. Mechanistic understanding of the adsorption of natural organic matter (NOM) by heated aluminum oxide particles (HAOPs) via molecular dynamics simulation, at 12th International Congress on Membranes & Membrane Processes (ICOM) 2020 (Poster).
8. Mechanistic understanding of the adsorption of natural organic matter (NOM) by heated aluminum oxide particles (HAOPs) via molecular dynamics simulation, at The Annual Meeting of the Membrane Society of Australasia (MSA) 2020 (Best Poster Award).
9. Microfiltration of oil emulsions stabilized by different surfactants, at TechConnect World Innovation Conference & Expo 2019 (Oral).

Nomenclature

AFM	Atomic force microscopy
BSA	Bovine serum albumin
CFD	Computational fluid dynamics
CNT	Carbon nanotube
COM	Center of mass
CTAB	Cetyltrimethylammonium bromide
CV	Collective variable
DEM	Discrete element method
DM	Dynamic Membrane
DMAPS	[2-(methacryloyloxy)ethyl]dimethyl-(3-sulfopropyl)ammonium hydroxide
DOTM	Direct observation through the membrane
DTAB	Dodecyltrimethylammonium bromide
EEM	Excitation emission matrix
EfOM	Effluent Organic Matter
FEL	Free energy landscape
FITC	Fluorescein isothiocyanate
FO	Forward osmosis
FTIR	Fourier-transform infrared spectroscopy
GFlop/s	Giga-floating operation per second
GO	Graphene oxide
HA	Humic acid
HAOPs	Heated Aluminum Oxide Particles
HPC	High performance computing
I-TASSER	Iterative Threading ASSEmbly Refinement
LC-OCD	Liquid chromatography with organic carbon detection
LMW	Low molecular weight
MBR	Membrane bioreactor
MC	Monte Carlo
MD	Molecular dynamics
MF	Microfiltration
MS	Materials Studio
NF	Nanofiltration
NOM	Natural organic matter
PA	Polyamide
PAC	Powdered Activated Carbon
PAN	Polyacrylonitrile
PDB	Protein Data Bank
PE	Polyethylene
PEG	Polyethylene glycol
PEO	Poly(ethylene oxide)
PES	Polyethersulfone
PE5	Polyoxyethylene octyl ether
PFAS	Per- and polyfluoroalkyl substance
PFOS	Perfluorooctane sulfonate
PMF	Potential of mean force
PTFE	Polytetrafluoroethylene
PVDF	Polyvinylidene difluoride
QCM-D	Quartz crystal microbalance with dissipation
RDF	Radial distribution function
RMSD	Root-mean-squared deviation

RMSF	Root-mean-squared fluctuation
RO	Reverse osmosis
SAM	Self-assembled monolayer
SASA	Solvent accessible surface area
SDBS	Sodium dodecyl benzene sulfate
SDS	Sodium dodecyl sulfate
SEM	Scanning electron microscope
SMD	Steered molecular dynamics
SPC	Simple point charge
TIP	Transferable intermolecular potential
TNB	Temple-Northeastern-Birmingham
TrOC	Trace organic compound
UF	Ultrafiltration
VDW	van der Waals
VMD	Visual Molecular Dynamics
VSOMM2	Vienna soil organic matter modeler 2
WHAM	Weighted histogram analysis method
WTM	Well-tempered metadynamics
XPS	X-ray photoelectron spectroscopy
XRD	X-ray diffraction
μGAF	Microgranular Adsorptive Filtration

Summary

For the past few decades, tremendous progress has been made in the field of membrane technology, for the usage in water purification, pharmaceutical separation, and many other processes. The revolutionary technology of membrane filtration has out-performed conventional ones thanks to its advantages like lower energy and maintenance cost, easiness of scale-up, etc. Nevertheless, until today, membrane fouling still remains a tremendous obstacle in the implementation of membrane technology, which has motivated the use of a wide range of experimental techniques to study fouling behavior in the past decades. However, molecular-level insights, which underlie the macroscopic observable phenomena, remain incomplete.

With the rapid advancement of computational power, molecular dynamics (MD) simulation has become increasingly popular to explore the interaction occurring at the ternary interface (i.e., foulant, membrane and solvent) by using explicit atom representations. MD studies have quantified interfacial physical properties and generated MD trajectories for direct visualization of the adsorption process. Therefore, it serves as an important supplement to experiments since it can easily overcome the scale limitation that limits the application range and resolution of conventional laboratory techniques. However, the usage of MD in membrane fouling field is relatively sparse compared to other domains. Thus, our group has dedicated great effort to apply MD in various fouling systems, and obtained fruitful molecular-level insights that form this thesis.

This thesis is built with a structure of following: A comprehensive literature review focusing on past MD studies for membrane fouling and related foulant adsorption processes is conducted first. Next, a few studies related to using MD simulation for fouling investigation are presented. Specifically, we have investigated the following topics: (i) removal of key natural organic matters by dynamic membrane made from heated aluminium oxide particles which mitigates the downstream reverse osmosis fouling; (ii) the importance of local interaction in protein fouling under different feed conditions; (iii) relative flux trend of surfactants carrying different charges, and mechanisms underlying the surprising flux enhancement phenomenon of positively charged surfactant solution; and (iv) fouling in organic solvent environment as compared to that in aquatic system. Finally, considering the rapid progression of computational power and algorithm, future perspectives are proposed to enhance the value of MD as a tool for understanding and predicting membrane fouling.

Chapter 1 – Introduction

This Chapter will briefly discuss the membrane fouling phenomenon that the industry is trying to mitigate, and the advantages of running molecular dynamics (MD) simulation to obtain molecular-level insights.

1.1 Overview of membrane technology and fouling

The development of membrane technology has flourished in the past few decades. Based on beneficial advantages like excellent selectivity, ease of scale-up and low operating cost [1, 2], membrane technology has revolutionized wastewater purification and desalination, which contributes towards alleviating the pressing water scarcity problem [3-5]. Membranes have also been used widely in other industries for separations, including bioprocessing [6, 7], dairy production [8], petroleum refining [9], etc.

One important reason for membrane technology to be so versatile is the possibility of tailoring the material or process based on specific needs. Based on nominal pore size, the membrane process can be classified as microfiltration (MF), ultrafiltration (UF), nanofiltration (NF), and reverse osmosis (RO), depending on the targeted species to be rejected. To obtain sufficient permeation rate, the trans-membrane pressures can be varied over a wide range from around 0.1 bar for MF to around 80 bar for RO. Moreover, the membrane configuration can be designed based on specific process requirements, with the common ones being flat-sheet, spiral-wound, tubular and hollow fiber that have their respective pros and cons. Furthermore, membrane systems are readily hybridized with other processes to tackle a wider range of problems, for example, membrane bioreactor and membrane distillation [10-12].

Unfortunately, membrane fouling remains a major hindrance in the broader adoption of membrane technology. Various foulants present in the feed can either deposit into the membrane pores or onto the membrane surface, which increases permeation resistance and consequently increases the operating cost as well as shortens the membrane lifespan. Correspondingly, the topic of membrane fouling has been thoroughly reviewed with respect to mechanism, modeling, characterization, mitigation, etc [13-17]. These papers have pointed out that membrane fouling can be caused by a wide range of foulants, like colloids, organics, inorganics (scaling) and biofilm, with some similar features but many unique behaviors for each, too. Different fouling mechanisms have also been proposed to better describe the dynamic process of fouling, including pore blockage, pore constriction, cake layer formation, etc. However, past

reviews have mainly focused on the insights obtained from experiments, which excludes a molecular-scale understanding of membrane-foulant interaction due to the spatial limitation.

Our research group has dedicated great effort to understand the mechanism of membrane fouling for the past few years via the conjugated method of experiments of simulation. In this thesis, six studies under the field of molecular dynamics simulation are going to be presented for various membrane fouling systems that mimic industrial operating ones. Fouling insights regarding diverse foulants under different solution environment have been extracted, and are expected to be valuable to supplement experimental findings and guide the actual operation of membrane systems in laboratory, pilot plant, and industry.

1.2 Molecular dynamics (MD) investigation of membrane fouling

Unlike laboratory experiments that essentially undertake quantitative measurements of phenomena detectable by available instruments, computational simulations perform such "experiments" by solving models numerically at different time and length scales depending on the targeted resolution. There has been an extremely rapid growth of computational performance and capacity in the past three decades, as reflected in Figs. 1A and B. Fig. 1A shows the fastest computing speed for high-performance computing (HPC) is almost 10^3 GFlop/s (Giga-floating operation per second), and Fig. 1B shows that the corresponding number of cores used is on the order of 10^7. The approximately linear trendlines on the log plots indicate that both the computational speed and data transmission have been growing exponentially since 1993. Leveraging this fast development of computational power, simulation has become an increasingly popular tool in various research fields to explain, probe, or even replace experiments.

Based on the length scale of the target problem, different simulation methods can be applied. Common methods range from continuum methods like computational fluid dynamics (CFD) to particle-level discrete element methods (DEM) to atom-level molecular dynamics (MD), and to quantum mechanics methods like density functional theory which deals with electrons within the atoms. This review focuses on MD, which serves as a "computational microscope" [18] to visualize the interactions between foulant, solvent and membrane at an atomistic level and thereby extracts useful insights on the membrane fouling process.

The essence of MD is to solve Newton's equations of motion with respect to time to describe the dynamics of each atom or molecule, so that the thermodynamics and transport properties of the system can be extracted based on how different species

interact with each other. This type of information is difficult, if not impossible, to obtain via macroscopic analytical tools. Hence, it is not surprising to see an increasing trend of membrane fouling research conducted using MD since membrane fouling originates from the dynamics of foulant and solvent near the membrane surface or pores. Fig. 1C summarizes the increase in the number of publications discussing MD simulations with reference to membrane fouling over the past three decades. Lagging a little behind the fast increase in computational power, the annual number of publications in MD studies of membrane fouling started to become double-digit in early 2000s. Since around 2005, more and more researchers became aware of MD as a valuable complementary tool to laboratory experiments for understanding fouling, which ignited an approximately exponential growth of membrane fouling studies involving MD. However, to date, there is no comprehensive review focusing on this topic. In 2013, Ebro et al. [19] published a short review on the use of MD simulation in water treatment processes using membranes, covering membrane materials development, behavior of ion and water molecules, and fouling. In 2021, Mollahosseini and Abdelrasoul [20] reviewed the current state-of-the-art of MD simulations, focusing on the separation of species using membranes and more generally porous materials, covering water transport through the membrane matrix, gas separation, characterization of membrane materials, swelling and strength of membrane, etc, but without much discussion on fouling.

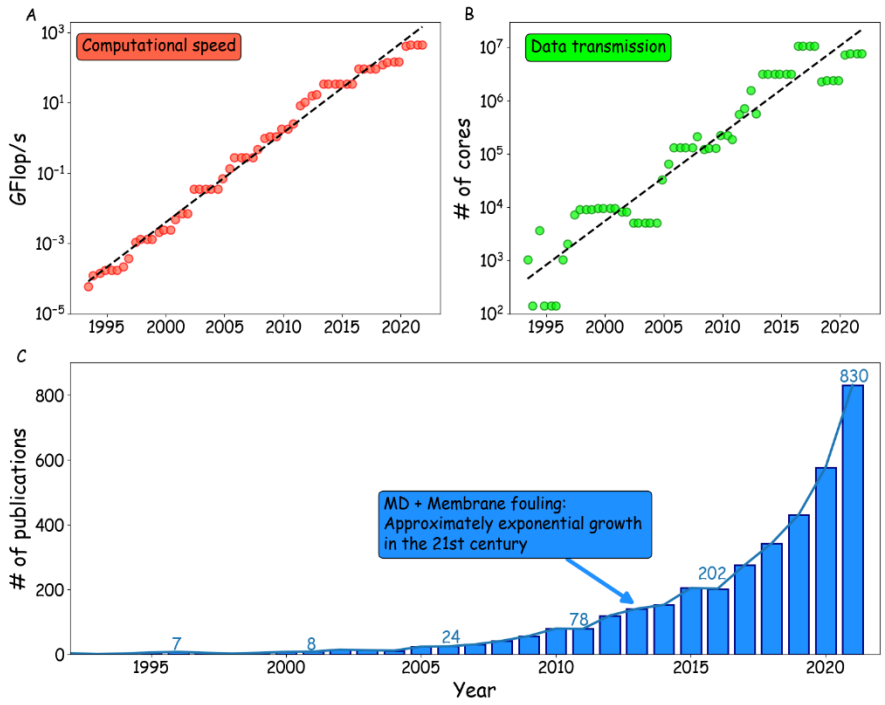

Fig. 1. (A, B) Rapid growth of HPC simulation capability reflected by computational speed (in the unit of GFlop/s) and data transmission efficiency (indicated by the number of cores). Data correspond to the Number 1 ranked HPC system worldwide (retrieved from TOP500.org [21]). Dash lines are fitting line which indicate the approximate exponential growth trend. (C) Dash lines are fits which indicate the approximate

exponential growth trend. (C) Number of publications involve usage of MD in the field of membrane fouling. Source: Scopus; Keyword: "molecular dynamics simulation" AND "membrane fouling" in "All fields". Data retrieved on 16th Dec, 2021.

1.3 Structure of this thesis

Based on the identified research gap, we have attempted to conduct several studies using MD simulation to obtain various insights regarding membrane fouling phenomenon. Chapter 2 is a literature review about the principles, methods and past usage of MD simulation in fouling/adsorption related studies. Chapter 3 and 4 investigate the pretreatment of wastewater using heated aluminum oxide particles (HAOPs), and quantified the adsorption strength of various components of natural organic matters (NOMs) by HAOPs using MD. Chapter 5 and 6 discuss protein fouling simulation studies and highlight the importance of local interaction. Chapter 7 describes the study of membrane fouling in organic solvent environment, and points out that fouling insights obtained from aqueous systems may not be directly translatable into organic solvent systems. Chapter 8 is about a biased simulation study of surfactant systems which aims at gaining explanations of the surprising flux enhancement phenomenon observed in earlier laboratory dead-end filtration study. Finally, Chapter 9 summarizes the future perspective of using MD for membrane fouling investigation.

Chapter 2 – Literature Review

This Chapter compiles existing literature regarding the usage of MD simulation for the investigation of membrane fouling or foulant adsorption process, as well as basic MD theories that is good to know when designing a MD study and performing corresponding post-processing of trajectories generated. It should be noted that as mentioned in Chapter 1, due to material, spatial and temporal limitations of MD, the current status-of-the-art simulation setup is still a quite simplified model as compared to the well-established experimental investigation. In other words, the differentiation of the wide range of fouling type and mechanisms is still only available in laboratory, while MD simulation serves as a simple but useful supplement.

2.1 Principles of MD & general workflow for fouling investigation

2.1.1 MD scale and limitations for fouling characterization

The typical length scale of MD is on the order of nanometers, and the time scale is on the order of nanoseconds to microseconds. Table 2-1 summarizes the system size and total simulation time for some representative MD studies in the area of membrane fouling. Compared to continuum simulation methods like CFD, the spatial and time scales of MD are much smaller, since the computational cost for discretely calculating the movement of individual atoms / molecules is substantial, especially in the liquid environment wherein the system density is relatively high. On the other hand, compared to another atomistic simulation method like Monte Carlo (MC) simulation, MD has a larger spatial scale. The reason is that MC requires a very large number of mutations of system configuration until convergence, which are generated via a Markov chain process based on the appropriate equilibrium ensemble probability [22], so the final system configuration represents the equilibrium at infinite time. For MD, the trajectory generated is an evolution of the system configuration with time, from which physical quantities can be extracted and time-averaged. Thus, MD can simulate a larger number of atoms (on the order of 10^4 to 10^5) compared to MC (maximum of a few thousands). Nevertheless, the total time duration simulated by MD is still orders of magnitude smaller compared to experiments, since the time step of MD is in the order of femtoseconds (10^{-15} second) as constrained by the time scale of the atomistic oscillation period of the simulated molecules [23]. In addition, in a liquid system, the number of atoms (denoted by N) increases roughly cubically with respect to the length of the simulation box, and within each time step, the number of pair-wise interactions that need to be calculated are of the order $\mathcal{O}(N^2)$. Hence, as shown in Table 2-1, most MD

studies on membrane fouling reflect physical time spans of hundreds of nanoseconds, with a few attaining several microseconds. The exact duration simulated depends on the specific system, software used, number of replicates and calculation speed of the specific HPC used, but has increased significantly compared to the routine "tens of nanoseconds" mentioned in an MD review paper a decade and half ago in 2006 [24].

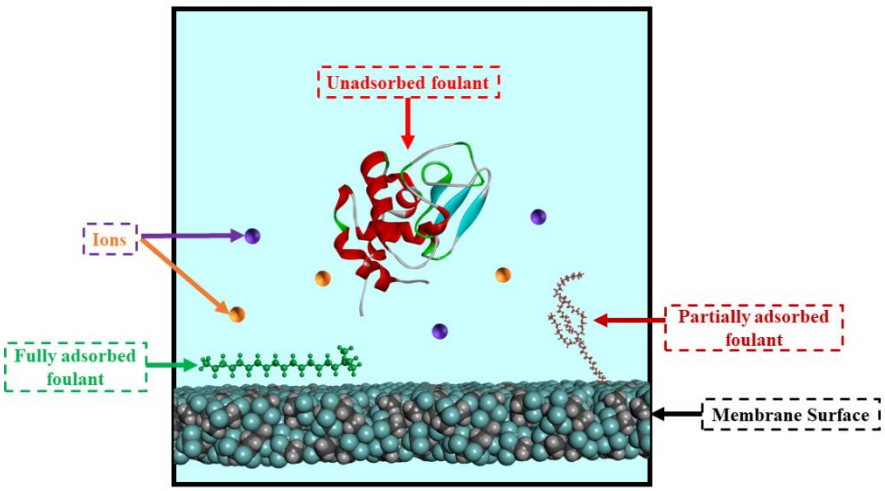

Fig. 2-1. Schematic illustration of a typical MD system configuration for investigation of membrane fouling, with annotations for various constituents. α-Lactalbumin is used as an illustration for unadsorbed foulant, and surfactant CTAB and Tween 20 are used as illustrations for fully and partially adsorbed foulants, respectively. PVDF slab is used as an illustration for the membrane surface. Light blue background indicates that water molecules fill the entire system.

Fig. 2-1 displays a schematic view of a typical ternary solvent-membrane-foulant interfacial system simulated by MD, which is a simplified representation of what happens during the actual experimental filtration. Depending on the relative strengths of interaction between the foulant and membrane, the foulant may fully adsorb, partially adsorb, or not adsorb to the membrane surface by the end of the MD simulation runs. It should be noted that the orientation of the foulant is important, particularly for large molecules that have different local affinities. A couple of pitfalls are worth noting. Within the limited time scale of one MD run, the foulant may or may not have sufficient time to orientate itself with respect to the membrane surface into a favorable orientation to adsorb. Moreover, a fundamental problem of MD is that the system tends to be trapped in a local minimum of adsorption without tending towards the global minimum spontaneously [24, 38]. To circumvent such issues, some studies chose to perform a few replicate runs starting from different initial foulant positions/orientations to improve the statistical validity [22], as shown in Table 2-1.

Table 2-1. Summary of the length and time scale of representative MD fouling studies.

Membrane	Foulant	Total simulation time	Replicates	System longest dimension (nm)	Approximate number of atoms simulated	Ref., year
Oligo (ethylene glycol) SAM [A]	Lysozyme	10.8 μs	6	12	Not mentioned	[25], 2016
PA [B] (Pristine and PEG[C]-coated)	1-Ethyl-2-methyl benzene, n-decane	200 ns	1	39	Not mentioned	[26], 2019
PA and PA-graphene composite	BSA [D]	12 ns	1	15	110,000 and 170,000	[27], 2017
PA and GO [E]	BSA	844 ns	1	27	Not mentioned	[28], 2021
PA (PEG-grafted)	Calcium alginate	110 ns	6	15	Not mentioned	[29], 2016
PAN [F]	Dextran	360 ns	2	8.5	50,000	[30], 2021
PE [G]	Lysozyme	2.7 μs	27	11.3	26,000	[31], 2012
PES [H]	Vanillin	850 ns	1	7.5	14,000	[32], 2018
PVDF [I]	α-Lactalbumin, lysozyme	480 ns	6	10	100,000	[33], 2021
PVDF	BSA	2.13 μs	1	17.1	200,000 and 180,000	[34], 2018
PVDF	CTAB [J], SDS [K], Tween 20	660 ns	1	10	100,000	[35], 2021
PVDF	SDS stabilized oil emulsion	64 ns	1	11	150,000	[36], 2018
PVDF (Zwitterionic grafted)	Hydrolyzed poly(acrylamide)	135 ns	1	15	70,000	[37], 2021

[A] = Self-assembled monolayer; [B] = Polyamide; [C] = Polyethylene glycol; [D] = Bovine serum albumin; [E] = Graphene oxide; [F] = Polyacrylonitrile; [G] = Polyethylene; [H] = Polyethersulfone; [I] = Polyvinylidene difluoride; [J] = Cetyltrimethylammonium bromide; [K] = Sodium dodecyl sulfate.

In addition to the limitations mentioned above, other factors that usually are not accounted for in MD simulation are described as follows. Firstly, permeation and hydrodynamic effects are seldom taken into account in MD fouling studies. While the porous matrix has been simulated in solvent permeation through NF/RO membranes [39, 40], UF/MF membrane pores are of a larger spatial scale than that simulated. For the investigation of macromolecular fouling, usually only a non-porous solid slab is used to represent the membrane surface, as shown in Fig. 2-1. Secondly, membrane roughness, which usually is on the order of tens to hundreds of nanometers [3, 41-43], is too large to be accountable by MD. A recent study by Wang et al. [44] attempted to tackle this problem by using idealized graphene and alumina membrane surface with sinusoidal wave shape with a maximum amplitude of 0.5 nm. While the amplitude is insufficient to represent the roughness elements in practical membranes, this setup may lay the groundwork for future MD studies on surface roughness effects. Thirdly, the entire process of membrane-induced conformational change of foulant (e.g., like protein unfolding and rearrangement [45]), which may have a physical time span of a few hours, is not observable within the limited time scale of MD. Fourthly, cake layer structure and many-body foulant-foulant interaction are not captured by MD due to the time and spatial scales limitations. The dimension of an MD simulation domain only allows a maximum of a few foulant molecules to be incorporated, which is far less than the number needed to form an aggregation and subsequently a cake layer on the membrane surface. Moreover, the time needed for the growth of foulant layer, and the transition from the dominance of membrane-foulant interaction to foulant-foulant interaction also goes beyond the typical MD time scale [46]. Thus, foulant-foulant interaction is often only studied between a very small number of foulants, or simply ignored. These limitations should be kept in mind when assessing MD simulation results and attempting to compare with experimental ones.

2.1.2 Construction of MD systems

Fig. 2-2 shows a typical roadmap for performing a MD simulation from scratch. The blue segments represent the initialization steps of a MD system, which will be discussed in detail in this section. The red segments represent the simulation run, which will be discussed in Section 2.1.3. The yellow segments are post-processing and data analysis of the generated MD trajectories, which will be discussed in section 2.2 and 2.3. Typical methods to validate MD results against experimental ones are summarized in Section 2.1.4, which are also discussed in section 2.2 and 2.3.

This section briefly summarizes the protocol of preparing a MD domain to be used as the initial condition for running the simulation. After determining the constitution of the solvent-membrane-foulant ternary system to be investigated, there are three main steps: (1) prepare individual molecule structures; (2) pack the system; and (3) assign force field parameters. For this step, commercial software like Materials Studio (MS) provides a convenient and user-friendly platform to run MD from scratch, and many open-source codes and related supporting utilities have been developed (as summarized by Cummings et al. [22]) to ease implementation of MD simulations.

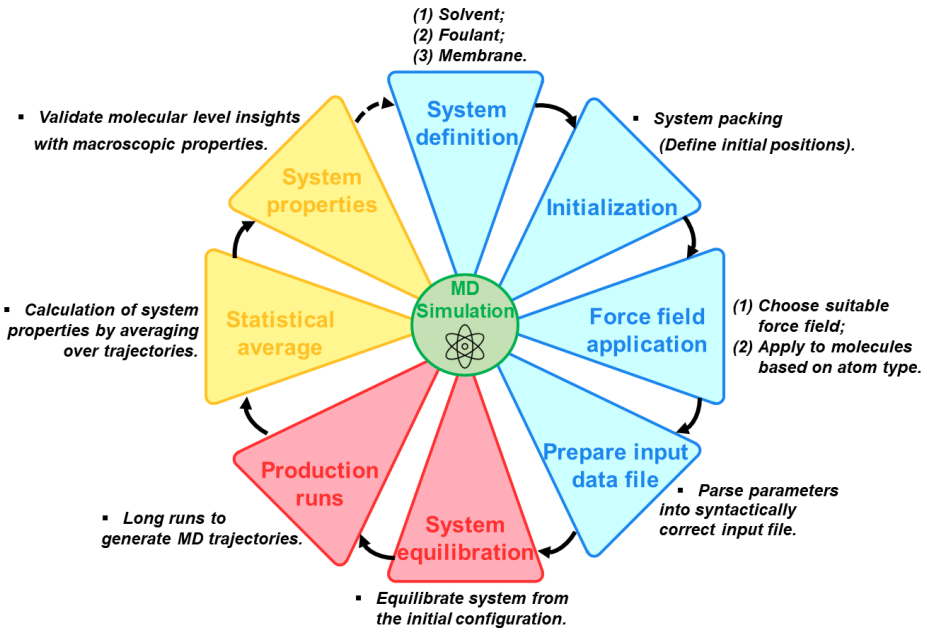

Fig. 2-2. A typical roadmap showing the general steps needed to perform a MD simulation for membrane fouling system. Colors of the triangle boxes indicate whether the step belongs to the initialization phase (blue), simulation phase (red), or post-processing and data analysis phase (yellow). Redrawn and modified based on the conceptual figure from [22].

2.1.2.1 Structures of solvent/foulant/membrane

This section describes the very first step of a MD study (i.e., "System definition" as shown in Fig. 2-2). It is essential to clearly define all the different molecules in the system at the beginning. For membrane fouling investigation, typically there are main types of molecules, namely, solvent, foulant and membrane.

Regarding solvent, water is the most commonly studied one for membrane filtration and fouling. A number of computational chemistry models for water are readily available, which differ by the number of interaction points, partial charge, bond length/angle, etc. The most commonly used water models in the literature include TIP3P (transferable intermolecular potential 3P) [47], TIP4P [47], and SPC/E (extended simple point charge) [48]. For other types of solvents (e.g., ethanol and formamide) and

small foulant molecules with relatively simple structures (e.g., n-decane and alginate), it is straightforward to draw them directly using software like Discovery Studio or Material Studio (MS) so that the connectivity of atoms is well-defined. For large foulant molecules whose structures are more complex and difficult to draw from scratch, it may be possible to directly download the structure from an online database. An example is protein, which is a common foulant but is structurally complex with secondary and tertiary structure elements. Fortunately, the structure file of many kinds of model protein foulants can be obtained from sources like PDB (Protein Data Bank) [49] and I-TASSER (Iterative Threading ASSEmbly Refinement) [50]. The former is an archive for protein 3D structures developed by researchers worldwide, and the latter is a hierarchical approach to predict protein structures based on amino acid sequence. Another example is HA, which is a collective name of a wide range of compounds with different chemical formula. The Vienna soil organic matter modeler 2 (VSOMM2) [51] has thus been developed based on the data collected worldwide, in order to model the structure of humic acid (HA) by connecting a variety of small building blocks based on parameters like molecular weight and elemental compositions.

The membrane structure usually takes the most effort to prepare. The membranes used in fouling studies can be largely classified as two types, namely, crystal and amorphous. The former represents membranes with well-defined crystal-like structures with long-range periodicity. Once the unit cell information is known, such membranes are usually generated from commercial software like MS, Avogadro [52], and Visual Molecular Dynamics (VMD) [53], or open-source Python toolbox like mBuild [54]. Examples of such membranes include aluminum oxide (Al_2O_3) [55], graphene oxide (GO) [28, 56], silicon dioxide (SiO_2) [57], etc. The other category (i.e., amorphous membrane) includes the more common polymeric membranes and thus are more widely simulated, as evidenced in Table 2-1. Due to the amorphous nature, some studies simply pack short polymer chains into a box, then perform equilibration runs so that chains relax to favorable orientations [30, 43, 58, 59]. An example of such a membrane-construction process is the 7-step compression and relaxation scheme developed by Shi et al. [60], which involves a large number of compression-relaxation cycles to reach the finalized structure under ambient condition. Once the resultant plane-like structure converges to a density value close to the experimentally measured value, it can be deemed to be a good representation of the actual polymeric membrane. For the membrane model construction, other studies have developed more sophisticated protocols to mimic the interfacial polymerization process [28] or vapor induced phase separation [61, 62], which are methods widely used in the laboratory to fabricate

membranes. Harder et al. [63] developed a method to simulate the interfacial polymerization of a RO membrane by progressively cross-linking monomers based on a heuristic distance criterion, with various stages during the building process illustrated in Fig. 2-3A. Based off that, Li et al. [64] developed an in-house toolkit MembrFactory to construct polyamide (PA) RO membranes based on the modelling workflow shown in Fig. 2-3B, so as to investigate the structural and antifouling performance of such a membrane using MD simulations [26].

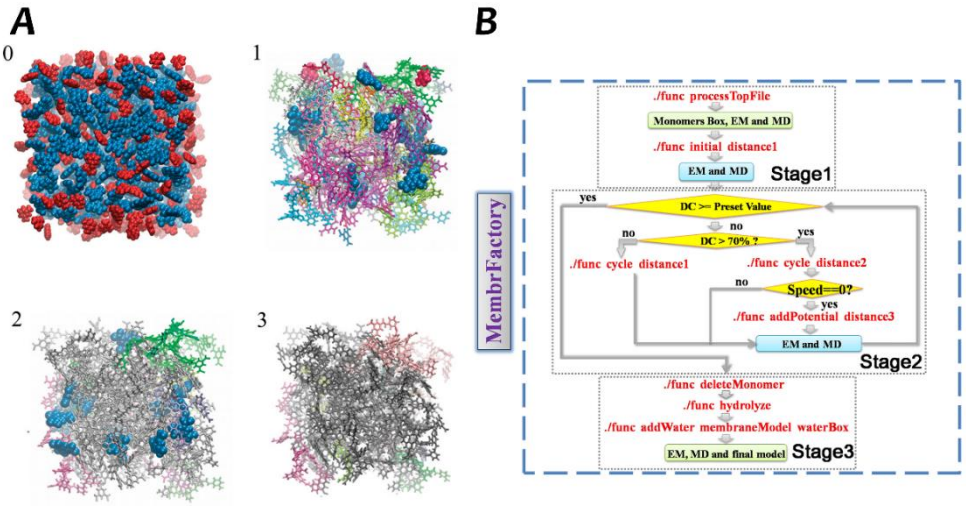

Fig. 2-3. (A) Snapshots of the four stages involved in the heuristic membrane build process as a simulation of interfacial polymerization. Different colors are used to distinguish polymerized clusters, and the largest cluster is indicated by gray. Free monomers are represented in the style of van der Waals surface. Adapted from [63]. (B) Modeling workflow of MembrFactory toolkit used to construct PA RO membrane. Adapted from [64].

2.1.2.2 System packing

After obtaining structures of individual molecules, the next step is to assemble them into a system that looks like what is shown in Fig. 2-1. In other words, this is the step whereby the positions of individual atoms are initialized, and a packed box is formed. For membrane fouling studies, the usual rule-of-thumb is to fix the membrane at the bottom of the box, and foulant molecules above it with some initial separation distance, with the remaining space of the box filled with solvent molecules based on experimental density value. A periodic boundary condition is typically specified, such that the top of the box is a mirror image of the membrane. This is also the step whereby the system size should be determined. It should not be too large to make the simulation cost too high, but it also cannot be too small to unrealistically cause excessive interactions between the foulant and the membrane (or its mirror image). Particularly in view of the limited time span simulated, it is prudent to pack a few systems with different initial

foulant orientations, as shown in Table 2-1, to facilitate the interaction of different regions of the foulant with the membrane and thus provide a more complete reflection of the adsorption process.

Some above-mentioned software like MS and VMD can perform such a packing process. Many open-source toolboxes are available as well. PACKMOL [65] is one of the most popular choices due to its seamless compatibility with different file formats and the ease to specify spatial constraints of molecules by packing optimization. In addition, the "Multicomponent Assembler" module in CHARMM-GUI [66] is another convenient option if the structure files prepared has specific recognizable formats (e.g., PSF and CRD).

2.1.2.3 Assigning force field parameters

The system can readily be visualized as that in Fig. 2-1 after packing. However, atoms do not possess instructions yet on how to interact with one another up to this step. Therefore, the force fields have to be specified by assigning different force field parameters based on atom type. Generally, force field terms can be divided into bonded terms and non-bonded terms. Bonded describes the interaction of atoms connected by covalent bonds, while non-bonded refers to the van der Waals (VDW) and electrostatic interactions occurring between atoms from different molecules, or within the same molecules but separated by more than 3 covalent bonds. Force field parameters are usually determined by fitting experimental data or conducting quantum chemistry calculations. This will be further discussed in the next section. Both bonded and non-bonded interactions can be calculated within each time step, so that the net force acting on each atom can be determined to update atom momentum and position in the next step. Table 2-2 summarizes common force fields and corresponding expressions used in membrane fouling studies. As a result of collective maintenance and update efforts from many research groups, force field parameters for common molecules are readily available online so that researchers can choose the appropriate one for running MD simulations easily.

It is critical to combine force field and geometrical information of the packed system into a syntactically correct format, so that the simulation software can read it as the input and carry out subsequent runs. Depending on the specific force field and software chosen, many tools can be used to perform this final step of initialization phase, including Automated Topology Builder [67], CHARMM-GUI [66], Antechamber [68], Python package foyer [69], etc.

Table 2-2. Expressions of various terms in common force fields used in membrane fouling MD studies.

Force field	Bonded interactions				Nonbonded interactions		Ref.
	Bond stretching	Angle bending	Dihedral torsion	Special term	Electrostatics	van der Waals (VDW)	
AMBER	Harmonic $K_r(r-r_{eq})^2$	Harmonic $K_\theta(\theta-\theta_{eq})^2$	Periodic/Trigonometric $\sum_n \frac{V_n}{2}[1+\cos(n\varphi-\gamma)]$		Coulombic $\frac{kq_iq_j}{r_{ij}}$	12-6 Lennard-Jones [C] $4\varepsilon_{ij}\left[\left(\frac{\sigma_{ij}}{r_{ij}}\right)^{12}-\left(\frac{\sigma_{ij}}{r_{ij}}\right)^{6}\right]$	[70]
CHARMM		Harmonic $K_\theta(\theta-\theta_{eq})^2$ Urey-Bradley 1,3-term [A] $K_{UB}(r_{13}-r_{13,eq})^2$	Periodic/Trigonometric $\sum_n \frac{V_n}{2}[1+\cos(n\varphi-\gamma)]$ Harmonic improper $\frac{1}{2}K_\chi(\chi-\chi_{eq})^2$	2D dihedral correction map (CMAP) [B].			[71]
CVFF	Morse potential $K_r\left[1-e^{-\alpha(r-r_{eq})}\right]^2-K_r$	Harmonic $K_\theta(\theta-\theta_{eq})^2$		Coupling terms between different types of interactions.			[72]
GROMOS	Fourth power $\frac{1}{4}K_r(r^2-r_{eq}^2)^2$	Cosine based $\frac{1}{2}K_\theta(\cos\theta-\cos\theta_{eq})^2$					[73]
OPLS-AA	Harmonic $K_r(r-r_{eq})^2$	Harmonic $K_\theta(\theta-\theta_{eq})^2$	Fourier series $\frac{1}{2}[V_1(1+\cos\varphi)+V_2(1-\cos 2\varphi)+V_3(1+\cos 3\varphi)]$				[74]

Symbols: K = force constant; r = distance between two atoms; θ = bond angle; V = force constant for dihedral torsion; n = multiplicity; φ = dihedral torsion angle formed by two covalent bonds; γ = phase angle; k = Coulomb's constant; q = charge; ε = depth of the potential well; σ = distance at each the intermolecular potential becomes zero; χ = improper dihedral angle; α = width of the potential well.

Subscripts: eq = equilibrium value; UB = Urey-Bradley; 13 = between the first and third atoms which is separated by the second atom; ij = between two arbitrary atoms i and j.

[A] = Additional harmonic term used for correction of the angle bending interaction.

[B] = Developed for protein backbone to improve accuracy [75].

[C] = Values of ε and σ are assigned to each atom type. To obtain inter-atom values of ε_{ij} and σ_{ij}, mixing rules are applied, with the most common ones being geometry mixing (e.g.: $\varepsilon_{ij} = \sqrt{\varepsilon_i \varepsilon_j}$) and arithmetic mixing (e.g.: $\sigma_{ij} = (\sigma_i + \sigma_j)/2$).

2.1.3 Performing the simulation

All steps discussed in the previous section are to prepare a MD system with reasonable geometry and sufficient information to represent how atoms interact with one another. This initial system is static, and the MD simulation runs are triggered only when no divergence is observed due to bad initial condition or missing inputs. The commonly used MD platforms for running the simulations in the membrane fouling field are LAMMPS [76], GROMACS [77], NAMD [78], and MS. The first three are free, whereas MS is a commercial software with a graphic user interface and its own built-in force field (COMPASS).

Regardless of what simulation platform is used, the role is to use Newton's equations of motion to solve for the motions of atoms, and update their momentum and position iteratively. One important breakthrough for MD simulation is the development of the Verlet integration algorithm [79], which is prevalent in MD studies nowadays:

$$\mathbf{r_i}(t+h) = -\mathbf{r_i}(t-h) + 2\mathbf{r_i}(t) + \frac{\mathbf{F_i}(t)}{m}h^2 + \mathcal{O}(h^4) \quad \text{Eq. (1)}$$

where $\mathbf{r_i}(t)$ is the position of the ith atom at time t, h is the timestep of the simulation, m_i is the atom mass and $\mathbf{F_i}(t)$ is the net force acting on the atom at time t that is calculated based on force field parameters. Due to the error term $\mathcal{O}(h^4)$ being scaled to the fourth power of h, the Verlet algorithm is outstanding in terms of conserving the system energy after performing a large number of time steps with insignificant influence of round-off errors [80]. Some MD papers use the term "leap-frog algorithm" to describe the method, which is simply the Lagrange-Hamilton formulation of the Verlet algorithm and introducing momentum $\mathbf{p_i}$ to avoid the subtraction operation [80]:

$$\mathbf{r_i}(t+h) = \mathbf{r_i}(t) + \frac{h}{m_i}\mathbf{p_i}\left(t+\frac{h}{2}\right) \quad \text{Eq. (2)}$$

$$\mathbf{p_i}\left(t+\frac{h}{2}\right) = \mathbf{p_i}\left(t-\frac{h}{2}\right) + h\mathbf{F_i}(t) \quad \text{Eq. (3)}$$

The most computationally expensive term in Eq. (1) or (3) is $\mathbf{F_i}(t)$, which in principle requires the computation of pair-wise interaction between one atom and all other atoms in the system at each time step. Thus, as mentioned in section 2.1, for an N-atom system, the number of computed pair-wise interactions has the order of $\mathcal{O}(N^2)$. Since there are far less bonded interactions occurring relative to non-bonded interaction, researchers have developed methods to simplify the calculation of non-bonded VDW and electrostatic interactions (Table 2-2). so as to make MD computationally cheaper. A typical cut-off distance range is approximately 8 Å to 18 Å, so that the computational cost is reduced to $\mathcal{O}(N)$ [81]. In other words, for a given atom, atoms and thus the associated intermolecular interactions outside the cutoff distance are excluded in its

"neighboring list". It is also possible to define two cutoff distances, so that the interaction is switched off gradually from the inner cutoff to the outer cutoff, instead of being switched off abruptly when a single cut-off distance is used.

On the other hand, for electrostatic interactions that are on the order of with r^{-1} instead of r^{-6} (Table 2-2), such a cutoff distance compromises the accuracy [81]. Therefore, a few scalable and fast methods have been developed to compute such long-ranged interactions under periodic boundary condition, which can reduce complexity to $\mathcal{O}(N \log N)$ or even $\mathcal{O}(N)$ [82]. Common ones include fast multiple method, fast Fourier transform-based method, multigrid-based method, etc. They exhibit different performance and stability depending on the specific system size and desired accuracy, as compared by Arnold et al. [82].

Another approach to speed up MD simulation is to introduce constraints, typically freezing bond length and angle. This is to decouple fast internal vibrations from rotational and translational motion of polyatomic molecules, obviating such irrelevant fast degrees of freedom [83] and therefore allowing larger MD timesteps as mentioned in Section 2.1.1. Common algorithms used include LINCS [84], SHAKE [83] and SETTLE [85], which are often applied to water molecules and hydrogen-containing bonds in foulant molecules.

Lastly, the default sampling in MD is carried out in a constant-energy manner (i.e., microcanonical ensemble). However, it is usually desired to conduct sampling under constant temperature condition (i.e., canonical ensemble), so it is necessary to introduce the thermostat algorithm to control the system average temperature [86]. The common types of thermostats for MD simulation with different physical basis are Andersen [87], Berendsen [88], Nosé-Hoover [89], etc. Some studies also choose to let the system be both isothermal and isobaric (Gibbs ensemble), so additional pressure-controlling variables need to be set by a barostat [90], such as Berendsen [88] and Nosé-Hoover barostat [91].

2.1.4 Model validation

Simulation models have to be validated against experiments to ensure reliability and accuracy. Table 2-3 summarizes typical membrane fouling experiments and characterization methods used for validation in MD literature. In general, both model structures, as well as simulation results, should be compared with available experimental data.

Table 2-3. A summary of methods used to validate MD models with regards to both the structure determination of molecules involved and simulation results.

Experimental metrics used to validate **model structures** which serve as the input of MD simulation	Refs.	Typical experimental results or characterization methods used to compare **MD simulation results** against	Refs.
Composition of feed/membrane	[92, 93]	Conductivity	[36, 94]
Cross-linking degree	[95, 96]	Contact angle	[97, 98]
Density of grafting sites on the membrane surface	[26, 29]	DOTM [A]	[55]
Density of membrane	[30, 40, 99, 100]	Flux decline profile	[30, 33, 37, 101]
Spectroscopy (e.g., XPS [B], FTIR [C])	[35, 102, 103]	Isotherm of static adsorption (e.g., by QCM-D [D])	[104-106]
Zeta potential	[107]	Rejection of foulant	[35, 102]
		SEM [E]	[108]
		Spectroscopy (e.g., Raman, EEM [F], FTIR)	[32, 109, 110]
		XRD [G]	[27, 106]

[A] = Direct observation through the membrane; [B] = X-ray photoelectron spectroscopy; [C] = Fourier-transform infrared spectroscopy; [D] = Quartz crystal microbalance with dissipation; [E] = Scanning electron microscope; [F] = Excitation emission matrix; [G] = X-ray diffraction.

In summary, by following the steps described in this chapter, a ternary MD system consisting of solvent, membrane and foulant become ready for simulating. With reasonable simulation times and replicates, as well appropriate parameter settings, MD trajectory files are generated to reflect how species interact with one another. After validating it against experiments, insights from simulation trajectories are deemed reliable. Using post-processing software like VMD, trajectories can be visualized to facilitate interpretation of the tendency of the foulant to adsorb onto the membrane or not. Moreover, MD simulations allow quantitative estimation of thermodynamic parameters like Gibbs free energy that is commonly used as a fouling indicator [13]. In the following chapter, we review some common parameters generated from unbiased MD simulations and discuss how they are tied to membrane fouling.

2.2 Fouling insights obtained from MD parameters

In this section, we analyze parameters generated from unbiased MD simulations. In such simulations, molecules move purely under the effect of mutual interactions without the addition of any external forces, and kinetic and thermodynamic parameters are averaged across the resulting states [111]. The unbiased method is accurate when

ergodicity of the system is assumed [112], which means that the results may be unreliable in cases whereby states of interest are rarely sampled due to energy barrier, limitations in the physical model, or the short time scale [113]. To address this shortcoming, enhanced sampling methods have been introduced based on the characteristics of investigated system, such as choosing a meaningful collective variable (CV) to guide the system from an initial state to a final state using a biasing potential [112, 113]. Such biases are used to increase the sampling of relevant states and transitions, and calculation results need to be appropriately reverted to obtain system properties under unbiased conditions [111]. Details of the biased MD simulation and corresponding enhanced sampling algorithms will be discussed in the next chapter.

Parameters from unbiased MD trajectories are more straightforward to obtain. These can describe the thermodynamic, kinetic, or structural properties of membrane fouling systems. To improve statistical validity, these parameters are extracted by either running longer simulations, running more replicates, or introducing more foulant molecules for averaging purposes. Fig. 2-4 provides a Venn diagram for the general overview and classification of unbiased MD parameters discussed in this chapter. For example, separation distance can be regarded as a reflection of both thermodynamic property (i.e., the affinity between two species) and kinetic property (i.e., motion of species of interest).

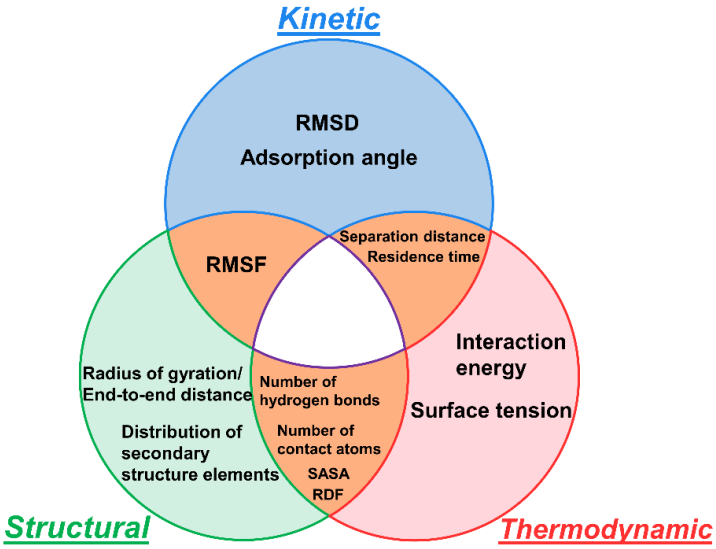

Fig. 2-4. Venn diagram for common parameters calculated from unbiased MD simulation. Parameters are classified into thermodynamic, kinetic, or structural characteristics of the system. Abbreviations: RMSD = Root-mean-squared deviation; RMSF = Root-mean-squared fluctuation; SASA = Solvent accessible surface area; RDF = Radial distribution function.

2.2.1 Separation distance

The membrane-foulant separation distance is the most direct indicator of the extent of fouling. The evolution of separation distance with respect to time is usually used to identify whether adsorption has occurred, and thereby allows for comparing the fouling potential of different foulants or membranes. Since both foulant and membrane are made of many atoms, the distance between these two entities can be defined either by (i) the minimum distance in between [28, 31, 34, 114]; (ii) distance between selected atoms [95]; (iii) distance between the centers of mass (COM) [93, 98]. As shown in Fig. 2-5A, Kubiak-Ossowska et al. [98] traced the distance between the silica surface and COM of BSA throughout the 500 ns simulation, and identified seven stages of adsorption. Kawabata et al. [95] adopted a different method by choosing terminal carbon/oxygen atoms in foulant molecules as reference, and computing their average distance from the water-PA membrane interface throughout the simulation. Based on results shown in Fig. 2-5B, they concluded that maltose was stable on the PA surface, whereas the behavior of amphipathic nonionic surfactant polyoxyethylene octyl ether (PE5) was highly dependent on the dissociation degree of the carboxyl group of the PA membrane.

It should be noted that there is no universal threshold value for separation distance that can be used to distinguish whether a foulant is adsorbed or unabsorbed, so variour studies have sought different means to determine adsorption or lack thereof. We have used the average separation distance ($\bar{d}$) and fraction of time whereby the separation distance is less than 4 Å (f_4) to classify MD trajectories into categories of stable adsorption, transient adsorption, and no adsorption [33, 107]. Another quantity commonly used to compare adsorption is the number of contact atoms that are within a specified distance from the membrane surface. Common choices of this threshold values are 3 Å [115], 5 Å [116], and 6 Å [32, 117].

For a macromolecule like protein, it may have various adsorption or anchoring points onto the membrane, which results in different interaction behaviors. To identify dominant amino acid residues responsible for the anchoring of foulants onto the membrane surface, some studies assessed the separation distance of each individual residue and the membrane surface [33, 116, 118, 119]. As a representative example, Fig. 2-5C shows the identification of two adsorption sites of lysozyme onto the PVDF membrane by plotting the instantaneous separation distance for each residue at five time points in the simulation.

In addition to membrane-foulant separation distance, foulant-foulant separation distance has also been computed to identify fouling patterns. As shown by the simulation snapshots and evolution of separation distance (i.e., foulant-surface and

foulant-foulant) in Fig. 2-5D, Tournois et al. [114] proved that α-chymotrypsin is able to adsorb on top of the adsorbed lysozyme to form a multilayer structure, with the interaction between α-chymotrypsin and the ligand surface hindered by the electrostatic field of lysozyme. Similarly, Tiwari et al. [118] conducted MD studies for lysozyme in forward osmosis (FO) and RO mode by applying different salt concentrations and boundary pressure values to the simulation systems. The distance between two protein molecules were compared, suggesting a thicker fouling layer in FO relative to RO in view of the closeness of protein molecules.

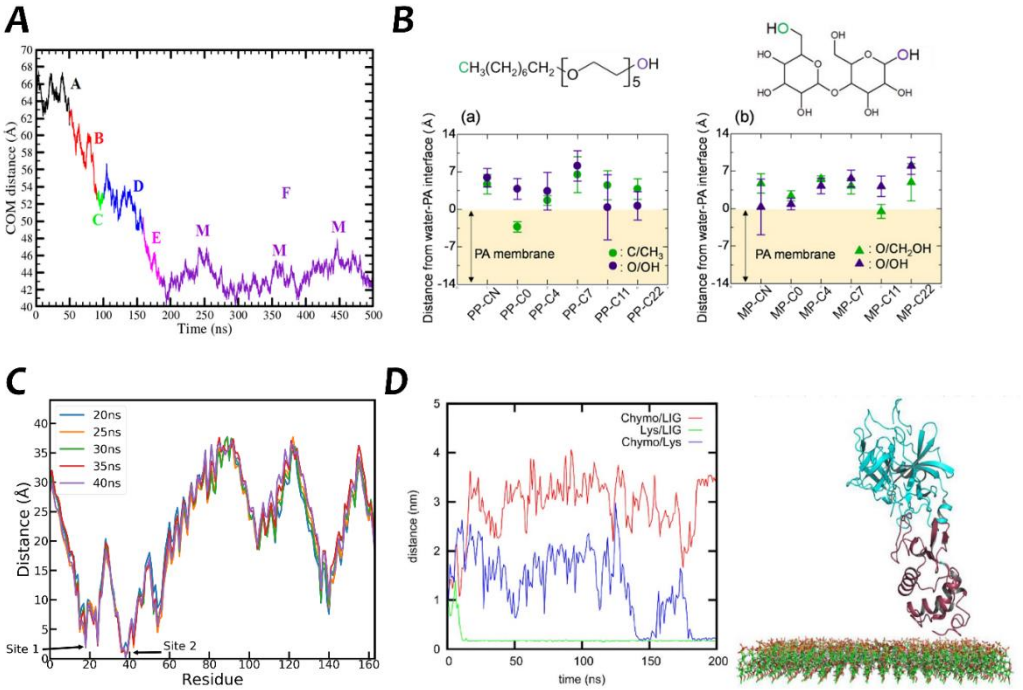

Fig. 2-5. Investigation of separation distance in various MD studies. (A) Plot of the distance to the surface from COM of BSA versus simulation time. Colors are used to differentiate adsorption stages A-F and M. Adapted from [98]. (B) Average distance of (a) PE5; and (b) maltose from the water-PA interface averaged over 3 ns of simulation. Marker colors are used to represent reference carbon/oxygen atoms selected from two terminals of PE5 and maltose, as indicated by the schematic drawn on the top panel. Labels on the horizontal axis represent the surface modification of PA membrane. CN: surface terminated by -NH_2 group; C0, C4, C7, C11, C22: surface terminated by carboxylic group, and 0%/4%/7%/11%/22% of the carboxylic groups are dissociated. Adapted from [95]. (C) Instantaneous distances between PVDF membrane and all amino acid residues of lysozyme between 20 ns and 40 ns of simulation runs at neutral pH and low ionic strength, with an initial orientation of $a_x = 90°$. Labels indicate adsorption site identified. Replotted based on simulation data of [107]. (D) Evolution of protein-protein (blue) and protein-ligands minimum distance (red and green) over simulation time, and the last frame of MD simulation. Lysozyme (Lys) is depicted in red while α-chymotrypsin (Chymo) is depicted in cyan. Ligand surface (LIG) is depicted in green and brown. Adapted from [114].

2.2.2 Interaction energy

MD simulation enables direct calculation of the interaction energy between two entities to illustrate whether the interaction is attractive or repulsive. The most commonly investigated interaction energy is the one between membrane and foulant. As indicated by Table 2-2, the intermolecular interaction is composed of electrostatics and VDW components. The most common way to express interaction energy is with respect to simulation time. For example, Fig. 2-6A displays the evolution with time of electrostatic and VDW interactions between HA and three types of carbon nanotube (CNT) membranes [102], which indicates that HA sieving and adsorption was controlled by VDW interaction for pristine CNT and hydroxylated CNT, whereas electrostatic interaction only played a significant role when the CNT is carboxylated. Shaikh et al. [34] adopted a similar approach to analyze the interaction between BSA and PVDF membrane with or without extra ions, and concluded that excess ions delays adsorption due to increasing negative charge of PVDF ascribed to adsorbed Cl^- ions.

In addition to understanding the trend of interaction energy with respect to time, some studies also compute the trend with respect to other parameters to obtain new insights. Wei et al. [31] defined an additional adsorption angle (θ), based on the principal axis of inertia of proteins to capture the relative foulant-surface orientation, and created a contour plot of the relationship with membrane-foulant separation distance, as shown in Fig. 2-6B. Results indicate that $\theta \approx 0°$ is the most favorable orientation when lysozyme is near the PE surface. Other studies have presented similar relationships [107, 120, 121].

As mentioned above, interaction energy also depends on the exact anchoring point of the foulant onto the membrane surface, which means the adsorption orientation is worth investigating. A few studies [33, 56, 115] have analyzed the interaction energy between specific regions of the foulant and the membrane, and indicated distinctly different energies particularly for macromolecules with multiple domains of different properties (e.g., a protein is made up of amino acid residues with diverse properties). O'Mahony et al. [122] took snapshots during MD near the alkylamine self-assembled monolayer (SAM) films when a hydrophobin (i.e., a kind of small globular protein with high surface activity) was adsorbed, and subsequently computed the adsorption energy of each residue that exhibit significant binding (Fig. 2-6C). Selective adsorption of specific regions was observed, whereby the protein prefers to anchor onto the methyl-terminated film via its hydrophobic regions while onto the amine-terminated film via the more hydrophilic regions. Another macromolecular foulant commonly used as a model foulant is HA. Qin et al. [56] broke down the foulant-membrane interaction energy term into the contribution from each functional group in HA, and found that

strong π-π interaction and CH-π interaction are responsible for the adsorption of HA onto the graphene nanosheets, whereas polar interactions are dominant for the carboxylated membrane.

Lastly, membrane-foulant interaction is not the sole factor contributing to fouling. Other types of interactions also need to be accounted for to fully understand the fouling mechanisms. Foulant-solvent interaction [109, 123], solvent-membrane interaction [56, 94], and also foulant-foulant interaction [118, 124] are often investigated and correlated with experimental data. Fig. 2-6D compares the interaction energy terms of the same foulant and membrane in three different polar and protic solvents [30], indicating the strong solvation film formed around membrane and dextran by formamide and ethanol, respectively, as the key contributor to less extensive fouling experimentally observed in organic solvent environments.

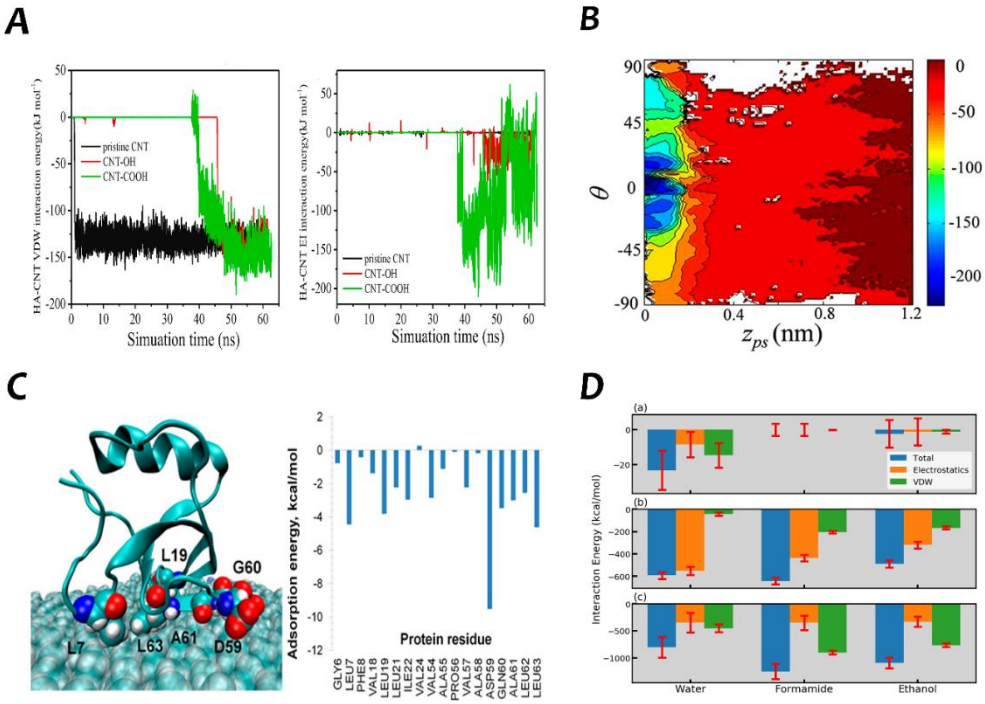

Fig. 2-6. Representative interaction energy plots for membrane fouling studies using MD. (A) The evolution with time of VDW interaction (left) and electrostatic interaction (right) between HA and CNT surfaces in aqueous solution with Ca^{2+}. CNT-OH and CNT-COOH stand for hydroxylated and carboxylated CNT membrane, respectively. Adapted from [102]. (B) Contour map of protein-surface interaction energy (represented by color bar) as a function of θ and protein-surface separation distance z_{ps}. The unit of color bar is k_BT, and white areas represent lack of data. Adapted from [31]. (C) Left: snapshot of protein-SAM graphene complexes formed, with protein residues strongly anchored to the surface highlighted by space-filling representations and labels, and water molecules omitted for clarity; Right: contributions of individual residues to protein-surface interaction. Adopted from [122]. (D) Average interaction energy between different pairs of entities in three solvent environments: (a) dextran-PAN membrane; (b) solvent-dextran; (c) solvent-PAN membrane. Error bars represent standard deviations. Adapted from [30].

Some interaction energy results have been found to be poorly correlated to membrane fouling. Our earlier study found that none of the interaction energy term is sufficient to explain the relative flux trend of feeds containing anionic, cationic and non-ionic surfactants [35]. Tiwari et al. [118] observed the affinity of two proteins despite the repulsive protein-protein interaction energy, and found that protein-solvent and protein-ion interactions play critical roles. This implies that more parameters (e.g., radial distribution function (RDF), number of hydrogen bonds) from unbiased simulation should be incorporated to more accurately reflect fouling, which will be discussed in the next few sections (e.g., Section 2.2.4 and 2.4). Another explanation is that enhanced sampling algorithm and biased simulations are needed for some systems, which will be the focus of next section.

2.2.3 RMSD

RMSD is a measurement of how far a molecule drifts away from its initial position as a function of time:

$$\mathrm{RMSD}(t) = \sqrt{\frac{1}{N}\sum_{i=1}^{N}|\mathbf{r_i}(t) - \mathbf{r_i}(0)|^2} \qquad \text{Eq. (4)}$$

where N stands for number of atoms of the molecule of interest, and $\mathbf{r_i}(t)$ stands for the positional vector of the ith atom at time t. Einstein's equation further relates MSD (the square of RMSD) with the self-diffusion coefficient D:

$$D = \frac{1}{6}\lim_{t\to\infty}\frac{d}{dt}\langle \mathrm{MSD}(t)\rangle \qquad \text{Eq. (5)}$$

where operator $\langle\ \rangle$ means an ensemble average over all molecules of interest. Eq. (5) is usually used for water molecules near the membrane surface to identify the effect of various factors on the water layer structure [36, 43, 95]. If Eq. (5) is applied for the foulant, it must be assured that within the time frame studied, the foulant still exhibits a normal diffusion behavior (i.e., an approximate linear relation between MSD and t) [61, 104, 109]. Generally, RMSD, especially the *z*-component that is perpendicular to the membrane surface [44, 109], is used to characterize foulant mobility, with a lower value indicating a higher tendency to remain deposited on the membrane surface and thus cause more severe fouling [33, 58].

The RMSD trend may also be interpreted from other angles to reveal other mechanistic insights. A high RMSD value has been related to a better solvent [57], and large fluctuations in measured conductivity and flux decline [94], whereas a low RMSD

value has been tied to the coalescence of droplets induced by the surfactant [55]. Furthermore, RMSD also sheds light on the dynamics of the foulant structure at the interfacial region. Fig. 2-7 displays the RMSD profile of a peptide molecule made of 18 amino acid residues in bulk water and near a SiO_2 surface at two temperatures [125]. While the peptide diffuses freely in water with smooth transition between conformations, adsorption onto the SiO_2 surface induces significant restrictions to the molecule that limits the number of conformations. Also, a higher temperature accentuates the difference between the free and adsorbed molecule. Zare et al. [117] investigated the conformational change of a protein induced by a membrane surface, and found that the RMSD of β-lactoglobulin increases drastically upon adsorption, which is indicative of large-scale rearrangement of secondary structure elements. Similar conclusions were drawn in another study [34], which quantified the mobility of different domains in BSA. The domain I-A that is in direct contact with the PVDF membrane has the highest RMSD, while the RMSD of the whole molecule starts to decrease upon adsorption, indicating that the protein structure remains stable without any abrupt change.

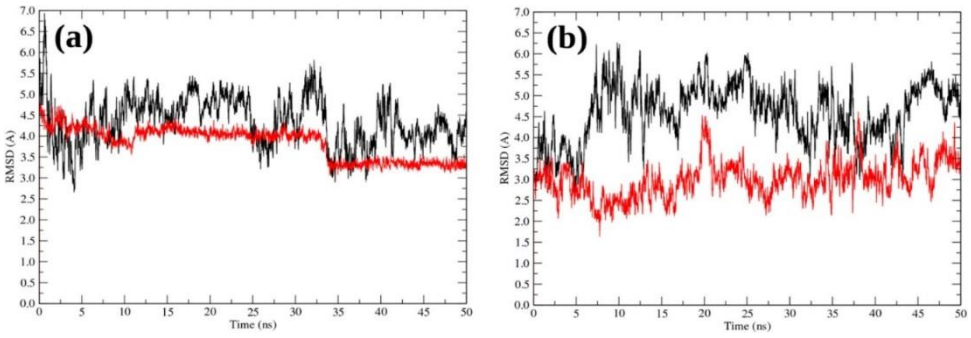

Fig. 2-7. RMSD profile of a peptide molecule in water (red) and in water-SiO_2 surface system (black) under (a) 293 K; and (b) 333 K. Only production runs were included, omitting preparation period of energy minimization, heating and equilibration. Adapted from [125].

2.2.4 RDF

RDF, which is usually denoted by $g(r)$, represents the radial distribution of a certain type of atoms around another atom type of interest. It may be interpreted as the ratio of local density over the bulk density. Given a selected pair of atoms, RDF is computed as:

$$g(r) = \frac{Vp(r)}{4N\pi r^2 \Delta r} \qquad \text{Eq. (6)}$$

where V stands for the volume of system, $p(r)$ stands for the number of atom pair within the spherical shell with inner radius r and outer radius $r + \Delta r$, and N stands for the total number of selected pairs in the system. RDF is used to assess the structure

formed in MD by calculating the concentration distribution of one species around another, and judicious selection of atom pairs enable direct description of species affinity.

While the interactions between the foulant and membrane are usually investigated via separation distance or interaction energy, RDF is also applied in some studies to compare fouling extent, and understand which specific domain contribute more to fouling. Xia et al. [126] computed the RDF between the cationic head of the surfactant dodecyltrimethylammonium bromide (DTAB) with respect to the coal surface. Due to strong polar dipole interaction, DTAB molecules preferentially adsorb onto the oxygen-containing sites. Since surfactants are usually present in oily wastewater as a stabilizing medium, MD studies have also been conducted for oil emulsion stabilized by surfactants. Tanis-Kanbur et al. [55] performed RDF analysis and revealed that positively charged DTAB had higher affinity with Al_2O_3 membrane compared to negatively charged SDS. This caused DTAB-stabilized oil emulsions to be more likely found near the membrane surface, which is consistent with the lower critical flux observed in experiment. Moreover, RDF also reveals the orientation of foulants at the interface. For example, the majority of polyaromatic molecules were found to be in tiled state (i.e., polyaromatic rings parallel to the surface) near the silica surface with fewer in a slant state (i.e., polyaromatic rings perpendicular to the surface) [57].

Due to the large number of solvent molecules present in the MD system, RDF is particularly powerful to reveal the structure of the solvent network. Since Eq. (6) may also be applied to the same type of atoms, a common practice to characterize the water network is selecting oxygen atoms as reference to plot the water-water RDF. For such an RDF, the coordination number of water n is defined as:

$$n = \int_{r_1}^{r_2} 4\pi r^2 g(r) dr \qquad \text{Eq. (7)}$$

where r_1 is the r value at which $g(r)$ starts to be non-zero, and r_2 is the first local minimum of $g(r)$. Velioğlu et al. [36] computed the water coordination number for a variety of oil-surfactant systems, and concluded that the presence of NaCl consistently loosens the water network by decreasing n, as shown by Fig. 2-8A. The looser water network means SDS could move freely to the pore mouth, decrease the surface tension and cause severe pore-wetting during membrane distillation. In other studies, a tighter water network was correlated to a stable hydration layer [26] and thus antifouling capability [127].

Plotting the RDF between solvent and foulant or membrane is also common. Solvent-foulant RDF has been used to depict the solvation film formed near the foulant

molecule so as to quantify its hydration/dehydration characteristics or hydrogen-bond forming ability in different systems [30, 104, 119]. Fig. 2-8B displays the RDF between water and polar atoms (oxygen and nitrogen) in the R-groups (i.e., side chain) of lysozyme in both FO and RO systems [118]. It was found that the peaks for RO are higher, which contributes to stronger hydration repulsion force between protein molecules. The RDF intensity is lower for nitrogen compared to oxygen, but there is a secondary hydration shell at around 5 Å. Similar analysis can be performed to investigate the hydration extent and the atom distribution profile on the membrane surface too [101, 128]. For example, owning to strong electrostatics interaction, the penetration depth of the first water layer is deeper for a TiO_2 surface compared to a SiO_2 one, with the latter forming more random water layers [129]. For non-water systems, such RDF analysis has also been applied to compare the strength of solvation film of different solvents [30].

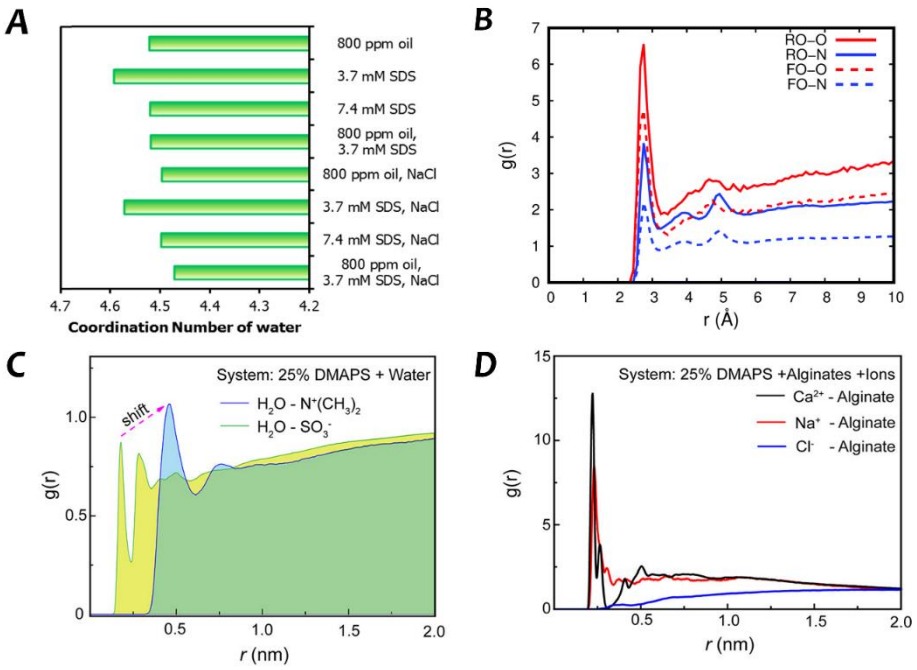

Fig. 2-8. Sample plots based on RDF between different entities to reveal local structure near the interface. (A) Coordination number of oxygen atoms in water molecules for a variety of surfactant-stabilized oil emulsion calculated from Eq. (7), with composition specified by tick labels on the vertical axis. Adapted from [36]; (B) RDF between oxygen atoms in water and non-backbone nitrogen/oxygen atoms in lysozyme, with the operating mode being FO and RO as indicated by legends. Adapted from [118]; (C, D) RDF between water and membrane, and between different types of ions and alginate foulant. PVDF membrane used in this study was grafted with zwitterionic [2-(methacryloyloxy)ethyl]dimethyl-(3-sulfopropyl) (DMAPS). System with 25% DMAPS grafting ratio is used to plot these two RDF diagrams. Adapted from [108].

Moreover, the effect of ions may be evaluated as well. The most commonly used ions in MD are Na^+ and Cl^- [28, 99, 105], either to make the system charge-neutral or

to simulate the high salt concentration encountered in water treatment. Some other ions may also be added, depending on the targeted feed chemistry. RDF provides a straightforward quantification of the extent of ion enrichment near the membrane surface or foulant. Liu et al. [108] investigated the behavior of sodium alginate near a zwitterionic monomer-grafted PVDF membrane. It was found that water molecules cluster much nearer the negatively charged sulfonate group on the surface, as shown in Fig. 2-8C. With enrichment of cations (i.e., Na^+ and Ca^{2+}) near the foulant (Fig. 2-8D) and membrane, a thick ion layer forms, which contributes to the antifouling property of the modified membrane via electrostatic repulsion. Ahn et al. [101] analyzed the RDF between three types of ions, PES membrane and natural organic matter (NOM) foulant, and concluded that Ca^{2+} associate the most strongly with the carbonyl group of NOM due to its looser second hydration shell, which caused significant aggregation of NOM and more severe fouling. Such an ionic bridging effect was also observed in another study focusing on perfluoroocatane sulfonate (PFOS) with K^+ and Ca^{2+} ions [130].

2.2.5 Other parameters

In addition to the four parameters commonly reported in MD simulations discussed above (namely, separation distance, interaction energy, RMSD, and RDF, a few others are also often quantified from unbiased simulations, as shown in Fig. 2-4. Table 2-4 offers a brief summary of these parameters and their links to membrane fouling. The choice of which parameters to analyze from unbiased MD simulation largely depends on the exact type of foulant, experimental results available for validation, and the targeted gap MD simulation is expected to address.

Partly because it is relatively easier to run and do post-processing for unbiased simulation, it is more commonly utilized. However, as mentioned in the beginning of this chapter, inherent limitations cause the results (e.g., adsorption interaction energy) obtained from one or a few short unbiased runs to be inaccurate, because of the limited time scale and the possible presence of significant energy barriers. Thus, in the next chapter, the determination of these parameters by running biased MD simulation with enhanced sampling algorithms is discussed in more detail.

Table 2-4. Summary of other parameters that are often analyzed from unbiased MD simulations of membrane fouling systems.

Parameter	Definition / description	Interpretation	Refs.
Adsorption angle	Orientation angle of foulant when adsorbed onto the membrane surface, typically defined with reference to the principal axis of the foulant.	Used to identify preferential orientation of foulant during adsorption, and whether adsorption is stable or there is still intensive rotational motion after adsorption.	[34, 119, 131, 132]
Distribution of secondary structure elements	Identify how many residues can be classified as certain secondary structure element (e.g., random coil, α-helix, β-sheet, etc.) for a protein foulant.	Track the dynamic surface-induced rearrangement of protein to quantify the extent of deformation/unfolding based on the percentage change of each element.	[116, 117, 123, 133]
Number of hydrogen bonds	A hydrogen bond between two entities is recognized based on a distance threshold and an angle threshold of a donor-acceptor pair.	Explore if foulant-membrane hydrogen bonding is a major reason for fouling; compare the ability of foulant/membrane to form hydrogen bonds with solvent molecules as an indication of binding strength.	[27, 58, 105, 110, 134]
Radius of gyration/ end-to-end distance	These two parameters give a simple measurement of foulant shape. Radius of gyration is computed based on the COM of the foulant, and is more suitable for a sphere-like molecule, while the end-to-end distance is more suitable for a rod-like molecule.	Both parameters are related with the degree of folding and extent of structural rearrangement of a foulant. Radius of gyration indicates the compaction level of the whole molecule. End-to-end distance is more like the extension of the backbone.	[38, 103, 121, 135]
Residence time	Expected time spent by selected species within the specified region. Calculated by time correlation function $C_r(t)$:	Reflect the rate of exchange of certain species within regions of interest, and thus the affinity of solvent/ions with the foulant or membrane surface.	[25, 99, 136]

	$C_r(t) = \frac{1}{N}\sum_{i=1}^{N}\frac{\langle P_{Vi}(0)P_{Vi}(t)\rangle}{\langle P_{Vi}(0)\rangle^2} \approx A\exp\left(-\frac{t}{\tau}\right)$ Eq. (8) [A]		
RMSF	Deviation of the position of each residue from the mean position, calculated by: $\mathrm{RMSF}(k) = \sqrt{\frac{1}{M}\sum_{j=1}^{M}\left\|\mathbf{r_k}(t_j) - \mathbf{r_k^{avg}}\right\|^2}$ Eq. (9) [B]	RMSF is related to the flexibility of different domains of a macromolecule. A low RMSF implies the residue is inflexible.	[33, 122]
SASA	Surface area of foulant molecule that is accessible for solvent molecules, calculated by rolling a probe of certain size around the VDW surface of the foulant.	Quantify the degree of folding and affinity to surrounding solvent molecules of a foulant when subjected to different feed conditions.	[103, 137]
Surface tension (γ)	Attractive force preventing the spreading of the solvent onto the membrane surface: $\gamma = \frac{1}{2}\int_{-\infty}^{\infty}(P_N - P_T)\,dz = \frac{L_z}{2}\left(P_{zz} - \frac{P_{xx}+P_{yy}}{2}\right)$ Eq. (10) [C]	Check whether the adsorption of foulant would significantly affect the original interfacial tension exerted by the membrane surface.	[109, 117]

[A]: N_w is the total number of investigated molecules in region V at time 0. $P_{Vi}(t)$ is a binary function with value 1 when molecule i is present in region V at time t, otherwise 0. A and τ are the exponential fitting constant of $C_r(t)$ curve, with τ being the residence time.
[B]: RMSF is a function of residue number k. $\mathbf{r_k}(t_j)$ stands for the positional vector of the k^{th} residue at time point t_j, and $\mathbf{r_k^{avg}}$ stands for its average positional vector throughout all M time points investigated.
[C]: **P** is the pressure tensor and P_{xx}, P_{yy}, P_{zz} are its diagonal components; P_N and P_T are respectively the normal and tangential components of the pressure tensor at z; L_z is the height where the deformation of the system occurs.

2.3 Quantify & interpret free energy landscape of foulants

As mentioned in the previous chapter, a single interaction energy term may not be a good representation of foulant-membrane affinity under filtration due to the interplay of multiple interactions occurring near the interface. For example, when foulant-membrane interaction energy is very attractive, fouling may still be relatively mild if the solvent-foulant or solvent-membrane is strong, since the solvation film formed makes the foulant preferentially stay in the bulk liquid. In other words, the fouling extent may be more dependent on the relative strength of multiple types of interactions simultaneously occurring in the system. Therefore, the free energy landscape (FEL) has been employed to capture the combined effect of all interactions of interest, making it important for investigation for membrane fouling.

The potential of mean force (PMF) method is popular for quantifying the adsorption free energy as a function of the reaction coordinate (denoted by ξ). In MD, the terms "reaction coordinate" and "collective variable (CV)" are often used interchangeably, which refer to the one-dimensional coordinate through which the system progresses. For example, the energy change of adsorption/fouling (and many other thermodynamic process) may be interpreted by following the evolution of generalized coordinates defined as CV, such as the separation distance between the foulant (i.e., adsorbate) and membrane surface (i.e., adsorbent). The key step is to integrate the mean force along the pathway (i.e., evolution of CV) [138], allowing the calculation of the variation of free energy as the foulant is transported from the bulk solution to the surface, or vice versa. Therefore, FEL gives a more comprehensive quantification of the adsorbate-adsorbent binding affinity and thus of the adsorption mechanism [139, 140].

Despite the rapid improvement of computational power, the computational cost of MD is considerable. Unbiased MD simulations is not able to sufficiently sample the system configurations (e.g., orientations of foulant near the surface) within the limited time scale to generate sufficient data for an accurate determination of PMF [141-143], due to either strong surface binding or the existence of energy barrier [139, 144]. Therefore, enhanced sampling algorithms via biased MD simulations are developed to generate accurate FEL [145]. The core idea is to bias CV by adding an appropriate external force (e.g., harmonic potential) in order to accelerate the sampling of all degrees of freedom without sacrificing computational efficiency and accuracy [144, 146]. Hence, the system is forced to visit all states of interest, especially those that are otherwise hindered by high energy barriers that system may not be able to visit spontaneously. This is discussed in detail in this section. Biased simulations should be run in a manner that the bias introduced by the additional force can be addressed

appropriately in analysis, so that free energy profile can be calculated accurately despite the bias addition [135]. Regardless of what biased simulation method is used, the starting configuration should be the equilibrated system after running the unbiased simulation [115, 141]. Under the scope of PMF techniques, three well-established computational algorithms are summarized in this chapter, with representative results in literature presented to highlight the usefulness of biased MD simulations in obtaining membrane fouling insights.

2.3.1 Umbrella sampling

The essence of umbrella sampling is to overcome insufficient sampling at energetically unfavorable configurations using an extra harmonic spring potential to restrain the system [147]. A schematic of umbrella sampling is shown in Fig. 2-9A for a surfactant-membrane system [35]. The sequence of implementing the umbrella sampling procedure is detailed as follows.

The first step is to define a convenient reaction coordinate ξ, which in the case of membrane fouling studies is typically the foulant-membrane separation distance, so that the PMF is expressed as a function of ξ (denoted by $\mathcal{W}(\xi)$). Note that, similar to that mentioned in section 2.2.1, the reference point in umbrella sampling for foulant position can either be its COM or position of a representative atom, like the nitrogen atom in the headgroup of surfactant CTAB in Fig. 2-9A. The second step is to determine the range of ξ. The minimum ξ value is the closest distance between the foulant and membrane based on the physical constraint of atoms on the membrane surface, which is usually non-porous due to scale limitation. As for the maximum value of ξ, it is when the foulant is fully detached and remains in bulk liquid, reflected by the plateau of the PMF. Since free energy is a relative parameter, the rule-of-thumb is to set shift $\mathcal{W}(\xi)$ such that $\mathcal{W}(\xi_{max}) = 0$ [105, 148].

After determining the overall range of ξ, a series of simulation is conducted by forcing ξ to take on a series of consecutive values (called "windows", shown by yellow dashed lines in Fig. 2-9A) in an alternating pulling-equilibrating manner. Four parameters that need to be set for this process are described as follows. The first is the pulling (or pushing) rate to force the adsorbate to visit all investigated ξ values consecutively. The commonly chosen velocity values are 1 m/s [149, 150] and 10 m/s [57, 108, 151], with Yan and Yuan [132] showing that the PMF curves remain consistent across a reasonable range of pulling rates. The second is the interval s of adjacent umbrella sampling windows, which depends on the resolution required for the investigated system and the available computational power. The typical values of s are

within the range of 0.4 Å - 2 Å [26, 131, 135]. The third is the force constant K of harmonic potential applied to the adsorbate. Unlike the pulling of foulant, which is a "dynamic" process, the biased simulation is run in each window by applying an additional spring harmonic w on ξ in each window:

$$w_i(\xi) = \frac{K}{2}(\xi - \xi_i)^2 \qquad \text{Eq. (11)}$$

where ξ is the real-time reaction coordinate value at each time point, and ξ_i is the reaction coordinate value set for the i^{th} window. Applying this harmonic potential restrains the lateral motion of foulant around ξ_i in each window. However, the rotation and horizontal translation of the foulant remain unconstrained. This is demonstrated by representative snapshots of CTAB in three windows (Fig. 2-9A): while the nitrogen atom in the headgroup of CTAB lies within one window, the remaining parts of the molecule can adopt any orientation under the influence of membrane and water. Li et al. [150] presented a method to select suitable values of K based on window spacing s:

$$1.5 \leq s\sqrt{\frac{K}{k_B T}} \leq 4 \qquad \text{Eq. (12)}$$

where k_B is Boltzmann constant and T is system temperature. Generally, the value of K is on the order of 10 $\frac{kJ}{mol \cdot Å^2}$. The fourth is the length of production run spent in each window for sampling, with common values ranging from a few nanoseconds [96, 108] to tens of nanoseconds [140, 150].

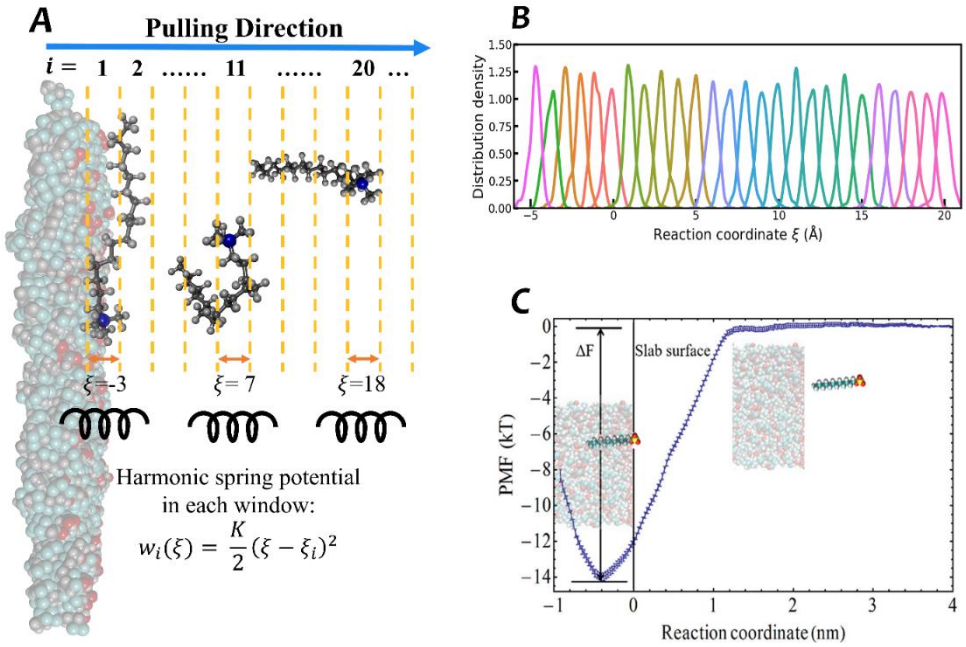

Fig. 2-9. Schematics of the steps of running MD with umbrella sampling. (A) Schematic illustration of umbrella sampling simulation, with hydrophilic PVDF membrane as representative surface, and CTAB as adsorbate. Configurations of CTAB are taken by snapshots from data files of previous study [35]. Reaction coordinate ξ is defined with

respect to nitrogen atom in the polar headgroup of CTAB (atom in blue). The space between yellow dashed lines stands for one window, and CTAB was pulled so that the nitrogen atom spanned through each window consecutively. Biased simulations were run within each window by applying a harmonic potential $w_i(\xi)$. (B) Histogram distribution $h_i(\xi)$ of CTAB along the reaction coordinate axis, with different colors used to distinguish windows. Reasonable overlap between adjacent windows is needed for proper sampling. Replotted based on data of [35]. (C) PMF of pulling SDS away from a polymer slab obtained from WHAM. The zero-point of reaction coordinate is taken as the slab surface, with cartoons depicting configuration of SDS at the minimum point and plateau. Error bars of PMF were computed by the bootstrap method. Adapted from [150].

The key information extracted from each umbrella sampling window is the histogram distribution $h_i(\xi)$, with reasonable overlap between adjacent windows for proper sampling [135, 139], as shown in Fig. 2-9B. Such histograms represent the probability distribution $P(\xi)$ of foulant position biased by umbrella potential $w_i(\xi)$ [147]. To reverse the bias of the obtained probability distribution and compute $\mathcal{W}(\xi)$, the most widely used approach is the weighted histogram analysis method (WHAM) [152]. Two key equations for WHAM are:

$$P(\xi) = \frac{\sum_{i=1}^{n_w} g_i^{-1} h_i(\xi)}{\sum_{j=1}^{n_w} N_j g_j^{-1} \exp\left[-\beta\left(w_j(\xi) - F_j\right)\right]} \qquad \text{Eq. (13)}$$

$$\exp\left(-\beta F_j\right) = \int d\xi \exp[-\beta w_j(\xi)]\, P(\xi) \qquad \text{Eq. (14)}$$

where n_w is the total number of umbrella sampling windows, g is the statistical inefficiency related to the integrated autocorrelation time, N is the total number of configurations in each window, β is the inverse temperature $(1/k_B T)$, F is the free energy constant. Eqs. (13) and (14) have two unknowns, namely, F_j and $P(\xi)$. Hence, in WHAM, they are solved iteratively till self-consistency of free energy constants is achieved. Finally, the PMF profile is obtained by:

$$\mathcal{W}(\xi) = -\frac{\ln\left[\frac{P(\xi)}{P(\xi^*)}\right]}{\beta} \qquad \text{Eq. (15)}$$

where ξ^* is an arbitrary reference point ($\mathcal{W}(\xi^*) = 0$).

A few studies [35, 103, 149] have performed error analyses of WHAM by conducting Bayesian bootstrapping. The detailed methodology can be found in the introduction of the software g_wham [147]. Briefly, a large set of bootstrapped trajectories are sampled from umbrella histograms to compute the so-called bootstrapped PMF $\mathcal{W}_b(\xi)$, and the uncertainty of the original PMF is quantified by the standard deviation $\sigma(\xi)$ of these N_b bootstrapped PMFs:

$$\sigma(\xi) = \sqrt{(N_b - 1)^{-1} \sum_{l=1}^{N_b} \left(\mathcal{W}_{b,l}(\xi) - \frac{1}{N_b} \sum_{k=1}^{N_b} \mathcal{W}_{b,k}(\xi) \right)^2} \quad \text{Eq. (16)}$$

After applying WHAM and error analysis, the PMF curves can be generated in the pre-determined range of ξ. One sample plot is shown in Fig. 2-9C, which reflects the PMF of SDS with respect to a model acrylate latex surface [150]. The shape of this PMF curve is very commonly encountered, with the minimum point often referred to as the equilibrium distance, and the binding free energy of SDS (denoted by ΔF in the figure) defined as the difference between the minimum and plateau values. The relatively larger error at small ξ values has been attributed to more vigorous fluctuations of the polymer-SDS force that result in slower relaxation of the system. Hughes and Gale [99] computed the PMF profile of model foulants with respect to a PA RO membrane using umbrella sampling, and found that glucose and phenol has stronger binding compared to oxygen. More recently, Xiang et al. [96] calculated the FEL between mannuronic acid (M)/guluronic acid (G) alginate monomers and five different types of benzene rings present on the PA membrane surface. The hydrophilic G monomer exhibits consistent free energy curves with shallow valleys (i.e., insignificant dissociation energies), whereas the M monomer displays amphiphilic characteristics that resulted in deeper global minimum in the free energy curves with respect to three out of five types of benzene rings. Although such a hydrophobic attraction identified from umbrella sampling may not be as strong as the ionic bridge binding, it still drastically reduced the docking time of the M-containing oligomers and thus led to more severe membrane fouling.

2.3.2 Steered molecular dynamics (SMD)

SMD stands for the process whereby a harmonic potential with moving center is applied to the adsorbate so as to pull it away from the surface. The SMD process highly resembles the experimental atomic force microscopy (AFM) technique, and allows for quantification of energy profile, rupture force, unbinding pathway, etc [153, 154]. For example, Lecot et al. [115] used SMD to investigate the adsorption of streptavidin-biotin complex on SiO_2 surface functionalized with different silane SAMs. During SMD, the COM of pre-adsorbed streptavidin was fixed and a moving spring force was only added onto the biotin. An example of the obtained force profile versus simulation time is shown in Fig. 2-10A. This representative profile indicates the amount of rupture force needed (i.e., the peak value of force just before the sudden drop) and the corresponding unbinding time. It was concluded that adsorption-induced conformational changes led

to a much lower rupture force of the streptavidin-biotin complex compared to the non-adsorbed case in water. Zhao et al. [153] used a similar approach to quantify the binding strength of xyloglucan to a cellulose surface, and pointed out that the failure stress of the hydrophobic link established between these two entities is on the same order of typical wall stress values.

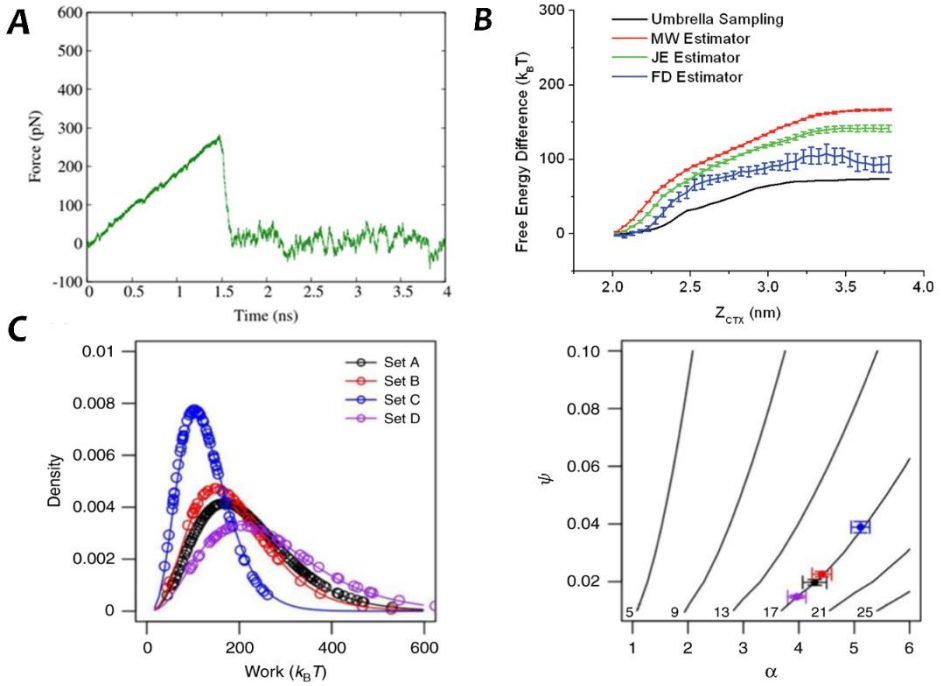

Fig. 2-10. Sample plots of SMD trajectory analysis. (A) Force curve for SMD pulling of biotin away from preadsorbed streptavidin domain on amorphous SiO_2 surface functionalized by silane monolayer n-butyltrimethoxysilane ($C_7H_{18}O_3Si$). Adapted from [115]; (B) PMF profiles of a cobra cardiotoxin A3 protein with respect to a methyl-terminated SAM surface calculated by using umbrella sampling and SMD. The pulling speed was fixed at 0.25 m/s. The performance of three types of estimators were compared: MW for mean work (simple arithmetic mean), JE for Jarzynski's equality (Eq. (18)), and FD for fluctuation-dissipation (Eq. (24)). Adapted from [155]; (C) Performance of gamma estimator for SMD simulation of peptide A3 and gold surface, whereby conventional estimators failed due to non-Gaussian work distribution. Left: total work distribution diagram fitted by Gamma distribution with four random data sets, which did not show overfitting; right: adsorption free energy values (in the unit of k_BT, represented by solid contour lines) as a function of fitting parameter α and ψ. Estimated free energy values from four datasets all converged to a value of roughly $17k_BT$, indicating the excellent robustness of gamma estimator for SMD. Adapted from [154].

The rupture force calculation summarized above is relatively easier when compared to the computation of PMF. The umbrella sampling discussed in the previous section is known to be an equilibrium approach, since fully sampled equilibrium runs are conducted in all windows. SMD, instead, is a nonequilibrium approach that requires less computational resources [29, 156, 157], but may give relatively poor performance than umbrella sampling for charged hydrophilic surfaces [139]. SMD involves dynamic pulling of the adsorbate to compute the PMF, although the process does need to be

repeated many times for averaging purposes. The computational complexity of SMD is lower, since the necessity to solve coupled nonlinear equations as that in WHAM is eliminated. The external work done during SMD is usually denoted by W; to avoid confusion with the previous notation of PMF, $\mathcal{W}(\xi)$, the notation of PMF will be changed to Φ in this section.

Based on the second law of thermodynamics, for any process changing any system parameter λ from its initial value λ_0 to the final value λ_t at time t, the change in free energy is expressed as:

$$\Delta F = F(\lambda_t) - F(\lambda_0) \leq \langle W \rangle \quad \text{Eq. (17)}$$

where F is the free energy, and the equality sign is only valid when the process is quasi-static. For a finite number of SMD experiments conducted with recorded work values as $\{W_i\}_{i=1}^{M}$, if the arithmetic mean of this ensemble formed by M observations is simply taken as the estimator for free energy change ΔF, it is called the mean work estimator, whose accuracy tends to be low since Eq. (17) only gives an upper limit of ΔF. The basis of SMD calculation is the Jarzynski's equality [158], which brilliantly correlates equilibrium free energy difference with work done through nonequilibrium processes:

$$e^{-\beta \Delta F} = \langle e^{-\beta W} \rangle \quad \text{Eq. (18)}$$

Eq. (18) holds for processes occurring at any speed, allowing quantification of ΔF from nonequilibrium SMD simulations. ΔF estimated with this equation is called the Jarzynski's equality estimator. A major difficulty for applying Eq. (18) is that, mathematically, the average of exponential work is dominated by rare trajectories with particularly low work values [142]. To ensure suitable sampling is done for such rare trajectories, in practice, the process in SMD should be slow enough such that the fluctuation of W is comparable to temperature [158]. In membrane fouling studies, the adsorbed foulant (i.e., adsorbate) is often pulled away from the membrane surface to calculate PMF. Here, parameter λ is termed as evolution coordinate which is moving with a speed v:

$$\lambda_t = \lambda_0 + vt \quad \text{Eq. (19)}$$

$$w(\mathbf{r};\, \lambda) = \frac{K}{2}[\xi(\mathbf{r}) - \lambda]^2 \quad \text{Eq. (20)}$$

where v is the pulling speed of the adsorbate, w is the harmonic potential with force constant K, and $\mathbf{r}$ is the 3N-dimension position vector of the system. Similar to umbrella sampling, such a harmonic potential $w(\mathbf{r};\, \lambda)$ constrains ξ near λ_t [139]. Therefore, the amount of external work done during a pulling process is given as:

$$W = \int_{\lambda_0}^{\lambda} \partial_\lambda w(\mathbf{r};\, \lambda)\, d\lambda \; = -Kv \int_0^t [\xi(\mathbf{r}|_{t'}) - \lambda_0 - vt']dt' \qquad \text{Eq. (21)}$$

Note that up to now, only free energy is discussed, not PMF. To link these two similar but not identical concepts, under the stiff-spring approximation (i.e., when K is sufficiently large), it has been derived that [142]:

$$\Phi(\lambda) = F(\lambda) + \frac{1}{2K}F'(\lambda)^2 - \frac{1}{2\beta K}F''(\lambda) + \mathcal{O}\left(\frac{1}{K^2}\right) \qquad \text{Eq. (22)}$$

Eq. (22) shows that PMF $\Phi(\lambda)$ can indeed be treated similarly as free energy $F(\lambda)$ after dropping out higher-order terms, which are much smaller than the overall scale of PMF. Hence, the values of v and K should be carefully chosen to fulfill the requirement of slow pulling and stiff spring, specifically in that K should make the reaction coordinate ξ closely follow the constraint center λ during the nonequilibrium pulling [142]. The commonly chosen values range from 1 - 100 $\frac{kcal}{mol\cdot Å^2}$, depending on the exact system constituents. Meißner et al. [159] investigated the adsorption free energy of a polypeptide molecule on an amorphous SiO_2 surface, and showed that v should be smaller than 1 m/s so that the frictional contribution of the pulling force does not become appreciable, which is consistent with the speed chosen by most SMD studies [98, 153, 157]. They also pointed out that it is possible to obtain a large number of independent configurations for SMD by mimicking AFM experiments, by repeatedly pushing and pulling probe molecules toward and away from the surface.

Due to finite sampling, estimation using Eq. (18) can be further improved by taking the logarithm and using cumulant Maclaurin expansion subsequently [158]:

$$\ln\langle\exp[-\beta W]\rangle = -\beta\langle W\rangle + \frac{\beta^2}{2!}(\langle W^2\rangle - \langle W\rangle^2) - \frac{\beta^3}{3!}(\langle W^3\rangle - 3\langle W^2\rangle\langle W\rangle + 2\langle W\rangle^3) + \cdots \qquad \text{Eq. (23)}$$

Note that Eq. (23) degenerates into the mean estimator $\langle W\rangle$ if the expansion is truncated after the first term. If the distribution of W is Gaussian, third and higher order terms are identically zero [155]. Thus, the second order cumulant expansion formula is often the most suitable choice [134]. However, for a finite set $\{W_i\}_{i=1}^M$, the exponential average is biased due to the convexity of the logarithmic function [142]. A more accurate approach is to correct it by using the unbiased estimator for the variance, which would result in the fluctuation-dissipation estimator of free energy:

$$\Delta F = \frac{1}{M}\sum_{i=1}^{M} W_i - \frac{\beta}{2}\frac{1}{M-1}\left[\sum_{i=1}^{M} W_i^2 - \frac{1}{M}\left(\sum_{i=1}^{M} W_i\right)^2\right] \qquad \text{Eq. (24)}$$

As expected, the fluctuation-dissipation (FD) estimator gives the best results among the three estimators, but with the potential trade-off of larger variance, as shown in Fig. 2-10B for the PMF profile of cardiotoxin protein desorption from a methyl-terminated SAM [155]. The PMF obtained by all three estimators deviate from umbrella sampling results due to the dissipated work induced by pulling, indicating that moderate velocity and a sufficient number of independent pulling trajectories are needed to estimate PMF using SMD.

As mentioned earlier, the reliability of truncation of Eq. (23) and the validity of Eq. (24) require the steering work to have a Gaussian distribution, which can be tested by conducting the Kolmogorov-Smirnov test on the frequency histogram. De Angelis et al. [120] conducted SMD to quantify the FEL of SDS at the interface of water and a curvy α-alumina nanoparticle surface. It was pointed out that the system dynamics deviate significantly from Markovian when SDS is very close to the particle surface, resulting in non-Gaussian-like distribution of external work. Although the model particle surface is not flat, unlike typical membrane surface in MD studies, similar observations were also reported by Kuang et al. [154]. By running SMD simulation with a peptide A3 and an Au (111) surface, it was found that the fluctuation-dissipation estimator (Eq. (24)) fails due to the presence of unphysical negative work values occurring in the left tail of the Gaussian distribution. This was also evidenced by the poor fitting and failure of significance testing shown in Fig. 2-10C. To address this, it was proposed that the work distribution $\rho(W)$ should follow a Gamma distribution instead (Eq. (25)), with the corresponding gamma estimator of Jarzynski's equality defined by Eq. (26):

$$\rho(W) = \frac{\psi^{\alpha} W^{\alpha-1} e^{-\psi W}}{\Gamma(\alpha)} \qquad \text{Eq. (25)}$$

$$\Delta F = \alpha \ln\left(\frac{\psi + 1}{\psi}\right) \qquad \text{Eq. (26)}$$

where Γ is the Gamma function, α and ψ are respectively the shape and rate parameters, estimated by maximizing the logarithm likelihood function L:

$$L = \sum_{i=1}^{M} \log\left[\frac{\psi^{\alpha} W_i^{\alpha-1} e^{-\psi W_i}}{\Gamma(\alpha)}\right] \qquad \text{Eq. (27)}$$

Despite different shapes of the distribution of the work dataset, applying the gamma estimator resulted in excellent curve-fitting and robustness, as evidenced by consistent values of free energy of adsorption calculated from different datasets (Fig. 2-10C), which agrees with experimentally measured values (~$17k_BT$).

2.3.3 Metadynamics

Metadynamics is a simulation technique that attempts to bias the normal system evolution by adding an additional history-dependent potential term, which is usually expressed as a sum of Gaussians along selected CVs. By doing so, it discourages the system from visiting regions that have been visited before, so that the sampling of the whole configurational space is enhanced [139]. This bias can describe system characteristics in a reduced dimension while letting the system explore more states within a single run [144], since the appropriate biased potential is able to help the system escape from the local minimum, unlike umbrella sampling or SMD whereby a number of runs are necessary to generate the PMF.

However, Barducci et al. [160] pointed out that the conventional metadynamics has a significant problem in the difficult determination of the terminal point of simulation, which may result in the system being irreversibly pushed into an unrealistic configurational space. Thus, they proposed a modified version named well-tempered metadynamics (WTM) to control regions of FEL, which has become the most adopted version nowadays. In WTM, for a set of CVs denoted by s, the system dynamics is biased by potential V:

$$V(s,t) = \Delta T \ln\left[1 + \frac{\omega N(s,t)}{\Delta T}\right] \quad \text{Eq. (28)}$$

where ΔT is temperature boost factor, ω is initial Gaussian height, and $N(s,t)$ is histogram of s from the biased simulation. A smaller value of $\frac{\omega}{\Delta T}$ leads to more accurate results at the expense of higher computational cost. By approximating the time derivative of $N(s,t)$ with finite width Gaussian, the rate with which V changes is:

$$\dot{V}(s,t) = \omega e^{-V(s(t),t)/\Delta T} \exp\left[-\frac{\left(s - s(t)\right)^2}{2\sigma^2}\right] \quad \text{Eq. (29)}$$

where σ is the initial Gaussian width. To calculate FEL denoted by $F(s)$, $\dot{V}(s,t)$ can be assumed to reach equilibrium [160] at large t, implying that:

$$\lim_{t\to\infty} V(s,t) = -\frac{\Delta T}{T + \Delta T} F(s) \quad \text{Eq. (30)}$$

In practice, combining Eqs. (28) and (30), FEL is estimated as:

$$\tilde{F}(s,t) = -(T + \Delta T) \ln\left[1 + \frac{\omega N(s,t)}{\Delta T}\right] \quad \text{Eq. (31)}$$

Tuning of ΔT facilitates the exploration of configurational space and automatically limits the exploration range of FEL to the order of $T + \Delta T$, making the determination of termination point simpler [160]. Therefore, WTM has been widely used in adsorption-related studies. Mao et al. [129] investigated the adsorption of peptide on rutile TiO_2 and quartz surface with WTM. Based on FEL, phosphorylation was found

to consistently increase the binding energy of peptide. YazdanYar et al. [38] found that the adsorption of amino acids on rutile surface was hard to interpret using a single CV. Thus, a reweighting approach was performed to generate FEL with respect to two CVs, namely, distances from the surface of the COMs of the backbone and side group, as shown in Fig. 2-11A. Based on the two-dimensional FEL, it was concluded that adsorption via the backbone occurs for all amino acids studied, whereas adsorption via the side group only occurs for amino acids with polar and charged side groups.

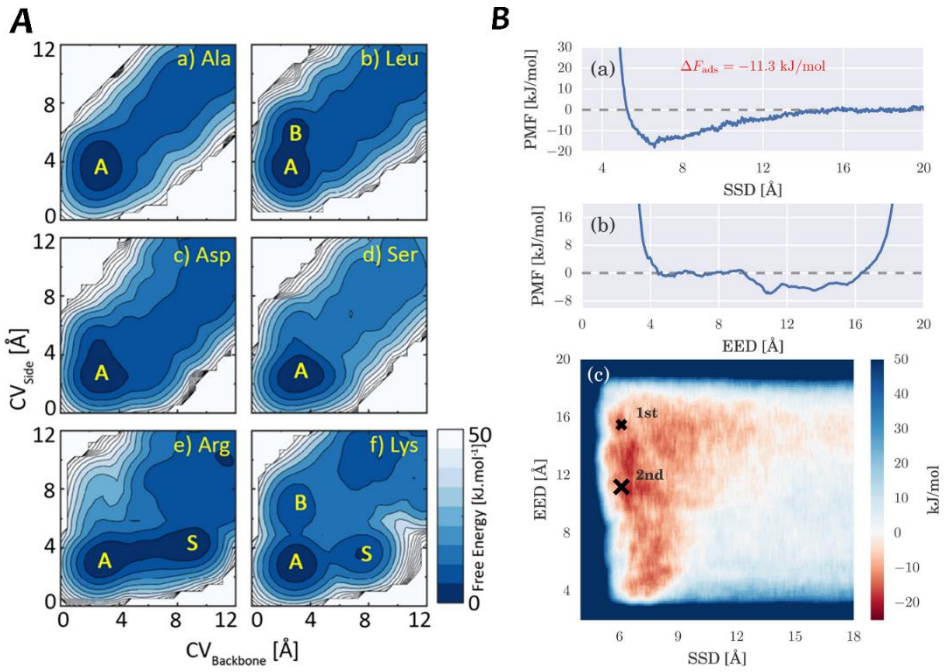

Fig. 2-11. Example of FELs generated from biased simulation with metadynamics. (A) FEL of six amino acids (Ala, Leu, Asp, Ser, Arg, Lys) computed from metadynamics biased simulation. Free energy is expressed as a function of two CVs: $CV_{Backbone}$ and CV_{Side}, which represent the distances to the surface for the COMs of the backbone and side group of each amino acid, respectively. Annotation A, B, and S denote free energy well representing adsorption onto the rutile surface via both backbone and side group, backbone only, side group only, respectively. Adapted from [38]; (B) Adaptive WTM simulation results of the adsorption of a titanium binding peptide onto the TiO_2 surface. PMF was plotted in both 1D (subplot a and b) and 2D (subplot c). CVs selected were surface separation distance (SSD), calculated as the *z*-component distance between COMs of surface atoms and the adsorbate and peptide's end-to-end distance (EED). Two crosses in (c) indicate two binding modes identified from unbiased simulation. Adapted from [135].

It is also possible to combine metadynamics with other techniques to obtain more physical insights near the interface. Replica Exchange with Solute Tempering has been augmented with metadynamics to investigate the adsorption of tetrapeptide on an amorphous SiO_2 surface [159]. Compared with SMD, which requires stiffer spring and low pulling velocity, the adequate convergence of this novel hybrid method was ensured by long simulation time alone. In another study focusing on peptide [144], parallel

tempering method was conjugated with WTM under a well-tempered ensemble methodology in order to quantify FEL with respect to multiple CVs. Rapid convergence was achieved. Compared with umbrella sampling, this method has higher efficiency with respect to exploring many conformational states under different temperatures. Brandt and Lyubartsev [135] made use of the adaptive WTM method to simulate adsorption, the motivation of which is to make σ in Eq. (29) time-dependent so as to optimize filling time and improve convergence by dynamically adapting the Gaussian width to the local FEL. The PMF of a titanium binding peptide with respect to a TiO_2 surface is shown in Fig. 2-11B in both 1D and 2D. The free energy was found to be weakly dependent on the peptide end-to-end distance (denoted by EED in Fig. 2-11B), and the total binding energy of this peptide is higher than the summation of the individual side chain analogue.

2.3.4 Decomposition of free energy

The term "free energy" is used generally in biased MD studies, but strictly speaking, it is necessary to differentiate Gibbs free energy G and Helmholtz free energy A from a thermodynamics point of view:

$$\Delta G = \Delta H - T\Delta S \quad \text{Eq. (32)}$$

$$\Delta A = \Delta U - T\Delta S \quad \text{Eq. (33)}$$

Eq. (32) indicates that ΔG consists of an enthalpic term and an entropic term, which is applicable in an NPT ensemble (i.e., constant number of particles, pressure and temperature). On the other hand, ΔA consists of an internal energy term ΔU and is applicable in an NVT ensemble (i.e., constant number of particles, volume and temperature) instead [161]. However, the difference between these two terms does not have significant impact on the exact algorithm, and the pressure-volume term relating G and A is also negligible after system equilibration [143], so they are sometimes used interchangeably in literature. After determining the corresponding FEL using methods discussed in previous sections, some studies also attempted to decompose it into the corresponding two sub-terms so as to gain additional insights of the foulant adsorption process.

Table 2-5 summarizes common methods used for decomposition. Generally, such a decomposition is able to identify the changes occurring during the adsorption process, and whether the adsorption is governed by enthalpy or entropy. Wang et al. [149] computed the entropy term of both free and adsorbed xyloglucan using the quasiharmonic method. Results indicate that the adsorption of xyloglucan at the interface come with significant entropy penalty, but the majority of it is cancelled out

by the entropy gain in liberating water molecules and ions that originally occupy the clay surface, making the free energy change roughly equal to the potential energy change. This enthalpy-driven adsorption was also observed to be more likely for rigid molecules, whereas the entropy term for flexible molecule may match that of enthalpy instead, as illustrated by Gaberle et al [162]. More recently, Wang et al. [140] pointed out that the free energy decomposition is highly dependent on surface type as well. Using finite temperature different method, they found that peptide adsorption onto a hydrophilic gold surface is enthalpy-driven, with entropy loss of peptide resulting from surface-restraining effect outweighing entropy gain of the release of surface-bound water. In contrast, adsorption onto a hydrophobic graphene surface is entropy-driven, with enthalpy variation hindering molecular transport to the surface from bulk solution.

Table 2-5. Summary of methods used to decompose free energy obtained from biased simulation to the enthalpic and entropic term.

Method	Definition	Interpretation	Refs.
Direct computation of system potential energy difference	ΔU is readily accessible from some simulations by taking the difference between the free and adsorbed adsorbate, especially when foulant-foulant interaction is negligible.	This method may lead to some uncertainty, due to subtraction of two numbers of the same magnitude, as well as possible large fluctuations of system potential energy.	[143, 149, 156]
Entropic formula proposed by Smith et al. [163]	$-T\Delta S(\xi) = \frac{1}{k_B T}\int_{\xi_{max}}^{\xi}\left[\langle E\frac{\partial E}{\partial r}\rangle_r - \langle E\rangle_r\langle\frac{\partial E}{\partial r}\rangle_r\right]dr$ Eq. (34) [A]	Direct calculation by taking the reference state at ξ_{max} whereby the adsorbate is fully dissolved in the bulk liquid. Requires quantification of ensemble average when reaction coordinate is fixed.	[35, 162]
Finite temperature difference	Run biased simulations at different temperature values, and estimate entropic term with linear fitting or finite differencing: $-T\Delta S(\xi) = T\left[\frac{\Delta G(\xi,T+\Delta T)-\Delta G(\xi,T-\Delta T)}{2\Delta T}\right]$ Eq. (35)	ΔT often is on the order of 10 K. May lead to an underestimation since system dynamics related to accessible vibrational/rotational modes are ignored, and enthalpic and entropic term are assumed to be constant with respect to temperature.	[140, 148, 151]
Quasiharmonic approximation	Calculate entropy term by approximating the system as a collection of quantum mechanical harmonic oscillators.	Quantify the conformational entropy of foulant by neglecting any contribution from the translational and rotational motion of COM.	[149, 164]

[A]: E stands for the total configurational energy.

2.4 Foulant-based insights

The two preceding sections have systematically discussed parameters quantified from MD simulation that can be used to reflect molecular-level insights happening at the interface during membrane fouling. In this chapter, key insights on the fouling behavior by different types of foulants obtained from MD are summarized. These insights are obtained based on parameters discussed earlier, but here the focus is on the characteristics of the foulants. By reviewing literature results based on foulant type, a better understanding of how the fouling behavior of individual foulants differentiates from one another can be established, so that foulant-specific fouling mitigation methods may be proposed. This highlights the important contribution of MD simulations in such analysis, as experimental methods cannot easily provide such spatial resolution.

2.4.1 Protein/Peptide/Amino acid

Protein is one of the most common foulants studied in membrane fouling literature. Here, the molecular-level insights of protein fouling are discussed in more details with respect to four aspects, namely, local interaction, hydration, ion, and conformational change. It should be noted that, due to the scale limitation of MD, some studies chose to use smaller structural units (i.e., peptide or amino acid residues) as simplified models, which are also included in this section. Key highlights are described as follows.

Firstly, protein is a macromolecule that consists of multiple domains of different properties. Thus, the measured overall characteristic of the protein may not be well correlated with its fouling behavior, because the local interaction between specific regions on the protein and membrane surface has been found to be more important [33, 107, 129]. Kubiak-Ossowska et al. [165] pointed out that, in order for a negatively charged BSA to adsorb onto a negatively charged silica surface, BSA has to rotate itself so that the IIIB domain faces the membrane such that constituent positive lysine residues could extend their long side chains to establish interaction with the surface (Fig. 2-12A). Similar observations have been made by other studies, wherein a positively arginine residue was found to play important roles in the anchoring of the overall negative protein to the negative surface [125, 159, 166]. Expectedly, hydrophobic residues are preferentially adhere to hydrophobic surfaces [117, 119], while hydrophilic ones exhibit affinity to hydrophilic surfaces [122], implying that the local regions of proteins need to be scrutinized to determine anchoring onto the membrane or not [114].

Secondly, the distribution of water molecules at the interface has been examined, because the associated extent of hydration of both protein and membrane surface can be tied to fouling. Wei et al. [31] pointed out that the dehydration of lysozyme is an

important part of the adsorption process, and the asymmetric distribution of lysozyme orientations when adsorbed to the PE surface is a direct result of different hydration extents of various protein sites. In other words, the partial de-solvation of the foulant is unfavorable in terms of the enthalpic component of free energy [156]. Thus, accumulation of water molecules and ions around the protein and membrane surface could lead to substantial hydration repulsion, which has been related to a thinner fouling layer [118]. Takizawa et al. [27] conducted quantitative analysis of interfacial water layer of a graphene-PA composite membrane, and concluded that the localization of hydrogen bonds at the surface played an important role in mitigating fouling by BSA.

Thirdly, the effect of ions in solution on fouling has received much attention in MD. The well-known charge screening effect has also been observed in MD, with ions delaying the adsorption of BSA and lysozyme onto the PVDF membrane surface [34, 107] and peptide onto the silica surface [125], or restricting the motion of bone morphogenetic protein-2 onto a gold surface [116]. In a more recent study, Tiwari et al. [28] found that the effect of ionic strength on BSA fouling is also dependent on the membrane type. As expected, with increasing salt concentration, repulsion was observed between BSA and GO membrane due to the accumulation of Cl^- ions near each, but no difference was spotted for PA membrane. This was attributed to the lack of functional groups on PA and its higher attraction to Na^+ ions.

Lastly, the secondary and tertiary structure of proteins may go through significant change after being adsorbed, which in turn results in changes in the protein-membrane interaction [115, 166]. Sajib et al. [133] plotted the evolution with time of adsorbed lysozyme on a PA surface, as shown in Fig. 2-12B. The local areas of large secondary structure change were found to be near the adsorption site, which led to even stronger surface-protein interaction in the later stage of adsorption. Another study [117] observed that β-lactoglobulin may flatten itself on the hydrophobic surface to expose more hydrophobic residues, or go through large-scale conformational rearrangement while preserving the secondary structure. In contrast, when the surface is hydrophilic, the protein may simply form a small number of contacts without significant change in secondary or tertiary structure. It was pointed out that the unfolding of the protein was not observed due to the time scale of MD. Indeed, accelerated MD needs to be applied to bias the system dynamic in order to observe protein unfolding. Mücksch and Urbassek [123] used this method to analyze the spreading mechanism of streptavidin on a hydrophobic graphite surface and a hydrophilic rutile surface. Entropic reasons were linked with the adsorption on graphite surface, while protein can either adsorb via

the interfacial water layer, or penetrate through it to establish direct electrostatic interaction with the rutile surface.

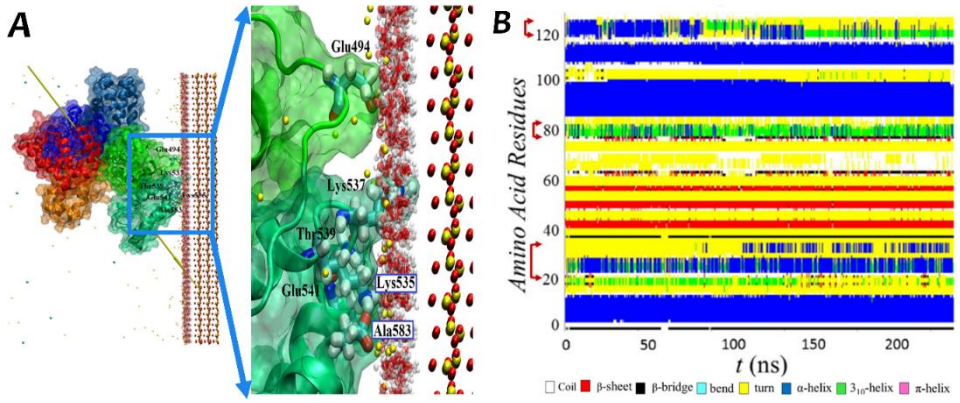

Fig. 2-12. Schematics related to MD simulation of protein fouling. (A) Snapshots showing the adsorption of BSA onto a silica surface (left), with a zoom-in view for the adsorption sites (right), at 186 ns. The silica surface is shown as individual atoms representing by red sphere (oxygen) or yellow sphere (silicon). BSA is depicted with a "ghost" surface, with secondary structure elements shown in "cartoon" style. Different domains are colored according to: IA – red, IB – orange, IIA – blue, IIB – light blue, IIIA – green, IIIB – lime. The yellow arrow denotates the dipole moment of BSA. Key residues responsible for adsorption have been annotated with "licorice" style. Adopted from [165]; (B) Time evolution of secondary structure elements present in an adsorbed lysozyme with respect to a PA membrane surface, with a pressure difference 5 MPa applied. Red arrows denote regions going through large structural changes. Adopted from [133].

2.4.2 Surfactant-stabilized oil emulsion

Membranes are widely used to treat oily wastewater generated from various industrial processes. In addition to oil molecules, surfactants are naturally present in oily wastewater and serve to stabilize the oil droplets. The surfactant-stabilized oil emulsion is another typical foulant that has received much attention in membrane fouling studies. Due to the complex interaction between the hydrophobic oil molecules, amphiphilic surfactant molecules and the membrane, MD studies are designed provide more understanding on the myriad of interactions.

Relatively fewer MD studies have focused on oil alone. Since crude oil is a mixture of different components, the effect of polarity on adsorption was investigated. MD results has shown that polar components has less difficulty in penetrating through water films and being adsorbed by silica, which in turn improves the adsorption capability of apolar ones by serving as the anchor and weakening surface polarity as well as the binding strength of water [167]. Regarding oil-water separation, Darvishi and Foroutan [128] found that an oleophilic PVDF membrane can be used as a separation media, with the presence of positively and negatively charged nanodomains affecting the positioning and orientation of water molecules. More recently, Bui et al. [58] focused

on the ability of a mixed matrix PVDF membrane to mitigate fouling by oil, and concluded that both zwitterion type and preparation method of membrane influences its stability and hydrophilicity, resulting in different fouling potential. Another study [97] concluded that ultra-thin titanium carbide membrane is very efficient for oil-water separation since it displays excellent anti-oil adhesion property due to the high PMF value near the surface.

MD systems consisting of surfactants have been given more attention, since surfactants may play crucial roles in the fouling behavior by surfactant-stabilized oil emulsion. The flux enhancement experimentally observed for feeds containing CTAB has been tied to the resulting water network near the membrane surface [35]. Moreover, the head and tail groups of surfactants have distinctly different properties that affect surfactant adsorption differently [95, 120]. Indeed, they have been considered as two independent parts when it comes to PMF [150]. Meconi et al. [105] conducted MD simulation for the adsorption of ionic and non-ionic surfactants on a polystyrene surface, with SDS representing the former and copolymers of poly(ethylene oxide) (PEO) and PE representing the latter. Fig. 2-13A displays the snapshots of surfactant layer structures at the interface, indicating that SDS tends to assemble perpendicular to the surface with a slight tilt, and the two non-ionic surfactants form disordered structures due to the interwoven configuration of the head and tail groups. It was explained that the head groups of the PEO-PE surfactants are too large and only weakly hydrophilic, and thus, with an increase in concentration, the attractive force between the surfactant and surface increases for SDS but decreases for PEO-PE. Hence, the comparison of surfactants of different types can also be performed. For example, the anionic surfactant SDS has better dispersion behavior on graphene sheets due to the shorter chain and smaller head group [137]. When comparing surfactants of similar charges, the more hydrophobic ones exhibit stronger surfactant-membrane interaction, which resulted in worse membrane distillation performance [94].

Regarding simulation systems with both oil and surfactant present, a more complete picture is expected. It was found that surfactants could disturb the layering of oil droplets on the surface by penetrating the hydrophobic chains into the oil phase, while leaving the hydrophilic heads outside oil droplets to form water channels [132]. Similarly, Xia et al. [126] attempted to simulate the distribution of dodecane molecules near the coal surface in the presence and absence of the surfactant DTAB. As shown in Fig. 2-13B, the adsorption of dodecane improves significantly when DTAB is present. This is because DTAB is able to alter the surface lipophilicity by exposing the hydrophobic domains of the coal-DTAB complex, and consequently make dodecane

collapse onto the surface to form a more compact structure. MD simulations of surfactant-stabilized oil emulsion has been compared to experimental observations [36, 55]. The critical flux and conductivity measured under different feed conditions has been found to agree with MD parameters like interaction energy, surface tension, RMSD, etc.

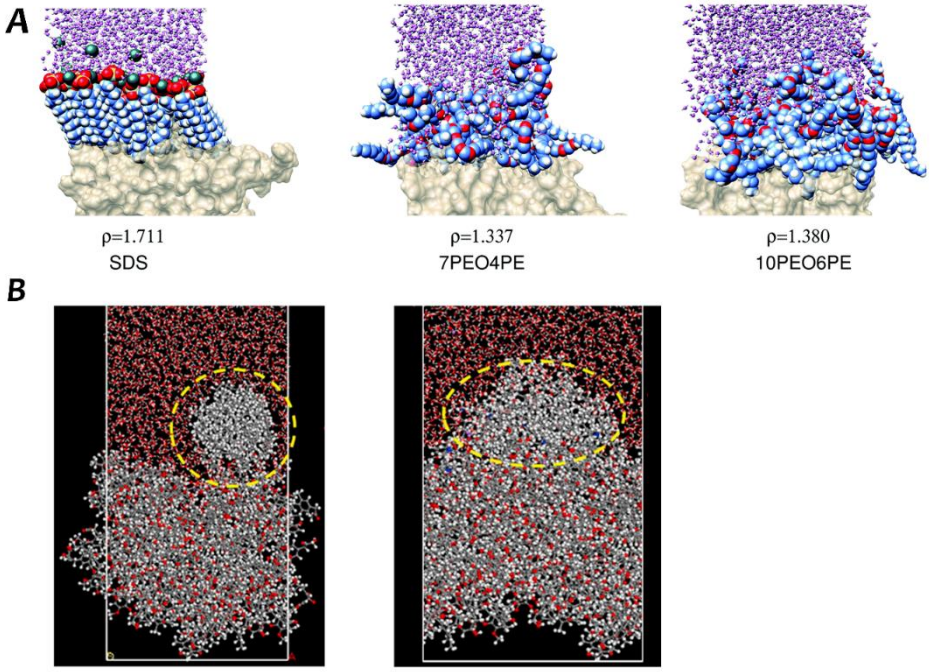

Fig. 2-13. Schematics related to MD simulation of surfactant-stabilized oil emulsion. (A) MD simulation snapshots of assembly of three kinds of surfactants near a polystyrene surface. 7PEO4PE and 10PEO6PE stands for copolymer of PEO and PE with a shorter length (7 PEO monomer units and 4 PE monomer units) and a longer length (10 PEO monomer units and 6 PE monomer units), respectively. Values of ρ stand for 2D density of surfactant in the system with a unit of mg/m^2. Surfactant molecules are drawn with a space-filling model. Water molecules and sodium ions are drawn with ball-and-stick model and green spheres, respectively. Polystyrene molecules are drawn with a surface representation in beige. Adapted from [105]; (B) Equilibrium configuration of dodecane adsorption on the surface of coal with (left) or without (right) the addition of DTAB. The cluster of dodecane molecules are highlighted by the yellow circle. Adapted from [126].

2.4.3 NOMs

NOM is a collective name for a wide range of organic compounds present in surface water from natural sources, which may cause severe fouling in both low-pressure and high-pressure membrane filtration processes. To model its fouling using MD, representative model molecules have to be selected. Liquid chromatography with organic carbon detection (LC-OCD) is a commonly used analytical tool to experimentally measure the concentration of different NOM constituents in water [168]. A few classes of compounds have been identified as main constituents based on

retention time, including biopolymer, humic substances and low molecular weight (LMW) acids/neutrals. Therefore, MD studies targeted at each class are reviewed in this section. It should be noted that polysaccharide and protein are two key representatives for biopolymer, and since a separate section has already been dedicated to protein fouling due to its significance in MD area, only polysaccharide MD studies are reviewed in this part.

2.4.3.1 Polysaccharide

Due to spatial scale limitation, the polysaccharide molecule is typically modelled as a chain of 5 to 12 sugar monomer units in membrane fouling MD studies [153, 169, 170]. Similar to protein, it is sometimes indeterminable whether the polysaccharide is hydrophobic or hydrophilic. One study [170] showed that short alginate chains display amphiphilic characteristics which resulted in the formation of hydrophobic patches along the chain that facilitate its interaction with a polypropylene membrane surface. Similar observations were made by a recent study, which indicated the structure of an M alginate monomer can be divided into a hydrophobic and a hydrophilic part [96]. Moreover, features of the side chains of polysaccharides have received much research attention as well. Zhang et al. [134] found that, although the variation in one side chain unit does not affect the magnitude of interaction energy between a cellulose surface and xyloglucan significantly, it does affect the equilibrium structure properties, which in turn contributes to the favorable interaction between the molecule and surface. Similar observations have been made in a separate study of xyloglucan [149], showing that the inclusion of a galactose side group makes the backbone conformation flatter and thus enhances interfacial interaction. Polysaccharide has also been a popular choice as a general foulant in simulation studies elucidating the role of surface modification on membrane antifouling properties. Xiang et al. [29] modelled the effect of PEG coating on a PA membrane ,with calcium alginate gel serving as the foulant. The tightly bound hydration water layer, as shown by Fig. 2-14A, led to very strong repulsive hydration force that effectively mitigated fouling. Therefore, despite attractive VDW and electrostatics interactions, alginate still found it difficult to form ionic bridging or hydrogen bonds with the modified PA surface. More recently, another study [108] used sodium alginate as the model foulant, and proved that $CaCl_2$ as well as a high grafting ratio of DMAPS on PVDF membrane surface enhances the energy barrier of foulant deposition. They also proposed a ternary synergistic antifouling mechanism among foulant, electrolyte and modified zwitterionic membrane, which could be useful for the design and preparation of membranes.

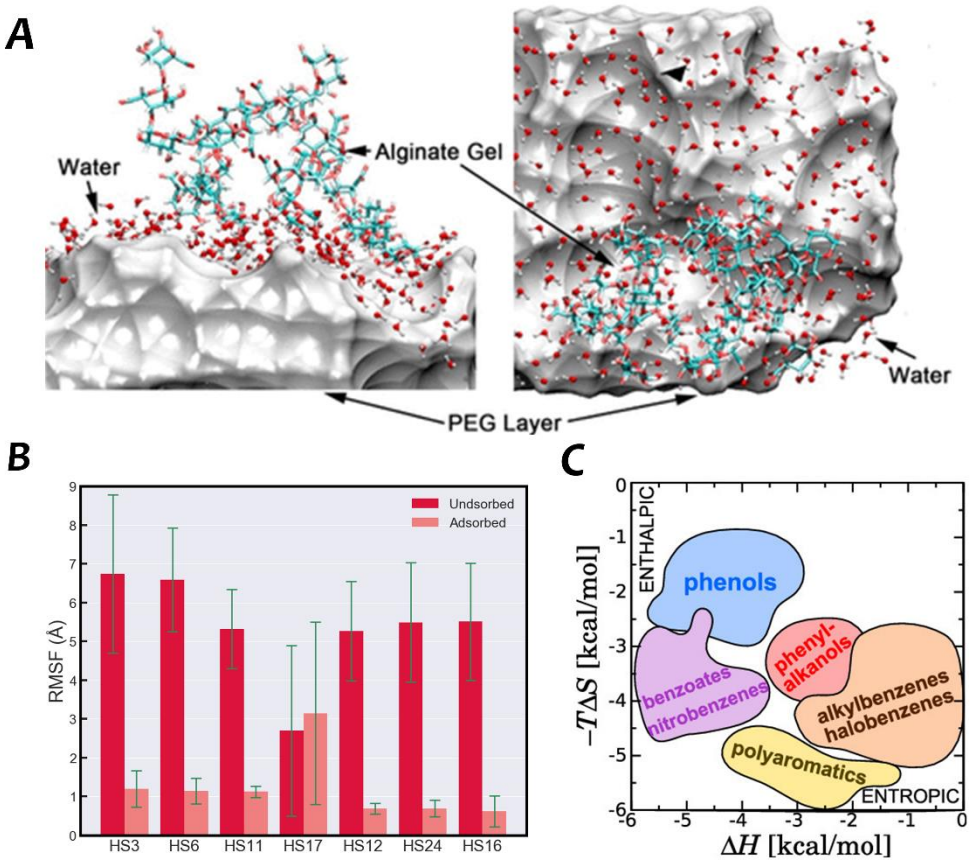

Fig. 2-14. Schematics related to MD simulation of different constituents of NOM. (A) MD snapshots of hydration water layer on top of the PEG coating of PA membrane, in the vicinity of model foulant alginate gel. PEG coating is shown by the grey and white VDW surface. Adopted from [29]; (B) Average RMSF of different residues ("HSx", consistent with the notation in the modeler VSOMM2) in model HA foulant built when HA was adsorbed/unadsorbed. Error bars stand for standard deviations across different molecules. Replotted based on data of [93]; (C) Entropic and enthalpic contribution to the minimum of adsorption free energy of 31 selected aromatic LMW foulants with respect to the graphene surface. Enthalpy-dominated compounds lie on the top left of the plot, while entropy-dominated compounds lie on the bottom right. Adopted from [148].

2.4.3.2 Humic substances

Humic substances are also a complex mixture of a wide range of compounds, in which HA is the most common representative simulated. Regarding HA models used, the Temple-Northeastern-Birmingham (TNB) model, Stevenson model, and model structure generated from VSOMM2 are the most common choices [93, 103, 110]. In an earlier study [101], the effect of ion on HA fouling has been discussed. Divalent ions such as Ca^{2+} were found to exacerbate fouling by forming ion-foulant complexation and promoting aggregation, instead of forming ionic bridges. Similar observations were made in a recent study by He et al. [102], whereby Ca^{2+} weakened electrostatic repulsion between HA and CNT membranes and caused HA aggregation and fouling. Moreover,

due to the presence of aromatic groups in HA, it may unfold via π-π interaction when specific types of membranes are used (e.g., CNT or graphene), exposing polar groups which were originally buried inside the folded structure of HA to the surrounding solvent molecules [136]. It has been reported that π-π interaction causes HA to orientate such that aromatic rings are parallel to the membrane surface, which result in less reversible fouling compared to the case whereby HA anchors via functional groups [56]. In the same study, HA molecules were also observed to have interesting fouling behaviors, such as pore constriction inside the interlayer or slit of graphene, or pore blocking at the slit entrance, which leads to different permeate flux declines. Regarding the flexibility of adsorbed HA, Ma et al. [93] computed the RMSF of different residues and concluded that, except for the simple hinge structure of four alkyl groups that connects different HA domains, adsorption consistently decreases the flexibility of different residues in HA, as shown in Fig. 2-14B.

2.4.3.3 LMW molecules

The LMW portions of NOM refer to molecules with molecular weight less than 350 g/mol [168]. Due to the simple structure, they are also widely used in MD studies as model foulants [44, 99]. Virtanen et al. [32] simulated the fouling of vanillin on a PES membrane surface. MD results indicated that fouling is highly pH dependent and occurs via two mechanisms with different time scales, specifically that hydrophobic interaction-induced binding occurs first on a rapid timescale, followed by dissociation of vanillin molecules from each other on a slower timescale as hydrogen bonds form between the foulant and membrane. Adsorption based on these two types of interaction was also observed in an earlier study [131] with catechol, in which cooperative hydrogen bonding of two neighboring hydroxyl groups results in the strongest adsorption onto the alumina surface. Singam et al. [148] computed the enthalpic and entropic components of the PMF of a diverse set of LMW molecules during interaction with a graphene surface, and observed that different classes of compounds can be readily distinguished based on the relative magnitudes of enthalpy and entropy (Fig. 2-14C). Moreover, they found that hydroxylation of the surface leads to preferential adsorption of aromatics to the remaining regions of bare graphene. Hence, surface modification was deemed to be an efficient method for fouling mitigation. This has also been shown by another study [26] using 1-ethyl-2-methyl benzene and n-decane as model organic foulants, whereby the antifouling capability of a PEG-modified PA membrane was found to be positively correlated with foulant size and hydrophobicity. More recently, Monroe et al. [171] simulated the adsorption of eight different LMW

molecules with SAM layers. Surprisingly, surface affinity shows poor correlation with conventional measures of solute hydrophobicity, specifically in that all solutes display attraction to the hydrophobic methyl interface, and some solutes are attractive to the hydrophilic hydroxyl interface. More importantly, free energy calculation using umbrella sampling illustrated a trade-off between solute affinity and water transport, which contributes towards membrane material design studies.

2.4.4 Other foulants

In addition to common types of foulants summarized in above sections, there are a few studies which chose other molecules for fouling/adsorption investigations. A large number of trace organic compounds (TrOCs) have been identified as emerging problems in the purification of drinking water. Hence, Liu et al. [92] attempted to simulate the interaction between PA NF membrane and seven model TrOCs. The PA layer is capable of being either an electron donator or acceptor when forming hydrogen bonds with solutes, and depending on its protonation state, different modes of interaction was observed with varying strength. In particular, per- and polyfluoroalkyl substances (PFASs), a special group of TrOCs, have received increasing attention in water treatment due to their bioaccumulation and carcinogenicity potential. There have been a few studies investigating the adsorption of this group of contaminants on surfaces like rutile, modified silica and clay [104, 106, 130]. Yan et al. [106] conducted a combined experimental and MD study on the adsorption of PFASs onto the sodium bentonite surface. A two-step adsorption scheme was proposed, with anionic PFASs first occupying the interlayer edge sites which corresponds to a linear isotherm, and subsequently occupying interlayer surface sites which corresponds to a Langmuir isotherm. Moreover, adsorption was mainly controlled by ionic interactions between cationic intercalant and terminal oxygen atoms in PFASs, as well as lateral interactions (e.g., fluorophilic attraction) among PFASs. Jiang et al. [37] studied hydrolyzed poly(acrylamide) as the model foulant, and found that a positive ion layer was formed between this foulant and a zwitterionic-grafted PVDF membrane. Therefore, strong electrostatic repulsion contributes to the excellent antifouling property of the membrane, which corresponds to an approximately 100% flux recovery ratio observed in experiments. In another study, to simulate the adsorption of typical compounds with fused polyaromatic rings in asphaltenes in organic solvent environments, the model molecule C5Pe was studied [57]. C5Pe was found to adsorb onto the silica surface rapidly in heptane but not in toluene, with polar terminal groups anchoring first followed by perylene cores, and forms aggregates shaped as long stripes.

Chapter 3 – Mechanistic Understanding of the Adsorption of Natural Organic Matter on a Dynamic Membrane formed by Heated Aluminum Oxide Particles (HAOPs) via Molecular Dynamics Simulation

This Chapter presents the very first work of my PhD conducted during Year 1. Inspired by the impressive experimental results of our HAOPs project in SMTC, we have investigated the adsorption behavior of individual NOM foulant onto the HAOPs and powdered activated carbon (PAC) surface, and related simulation results with experimental data like removal rate and flux decline.

3.1 Introduction

As one of the major foulants that dictate the rate and extent of membrane fouling, NOM has received much attention in research and practical operation [172, 173]. NOM is a complex mixture of carbohydrates, amino acids, humic substances and many other groups of organic compounds [174, 175]. Sources of NOM in water include terrestrial and vegetative debris, and autochthonous algae species [176]. In addition to worsening membrane fouling, NOM also causes unappealing color and taste of water, reduces dissolved oxygen concentration and serves as a precursor for disinfection byproducts (DBP) [177, 178]. Thus, the removal of NOM early in the water treatment train is necessary so as to not interfere with downstream operations [174].

Methods for NOM removal include coagulation, adsorption, biofiltration, ion exchange and ozonation, with the first two being most common [174, 179]. Conventional coagulation makes use of coagulants like alum, and polyelectrolytes species like iron chloride ($FeCl_3$), polyaluminum chloride [178, 180], etc. However, even though coagulation can remove a large portion of NOM from the feed, it leads to the production of compressible chemical sludge and related secondary problems [181]. As for adsorption, rigid compounds with low solubility are usually selected as adsorbents, such as PAC, silica (SiO_2) and polysulfone colloids [179, 182]. Unfortunately, both coagulation and adsorption suffer from the same problem of inconsistent performance, in that while fouling can be usually mitigated significantly, they sometimes exhibit no effect or even exacerbate fouling [183, 184]. The poor performance is underlain by the tendency of the colloidal metal hydroxides or NOM-metal complex formed to deposit on the membrane surface and thereby worsening fouling [185-187].

To tackle these problems, the Benjamin group has proven the superior performance of a novel adsorbent for NOM removal, namely, the HAOPs [174, 177, 179, 184, 188-193]. Permeation drag makes HAOPs deposit on the surface of primary membrane, forming a dynamic membrane (DM) layer which enables higher permeate flux by minimizing fouling. In other words, this DM layer, which is not chemically bound nor permanently adhered to the conventional primary membrane, forms before the actual filtration process and acts as a critical protective layer against foulants in the feed. With the size of HAOPs being around 5 to 10 µm, this DM layer also serves as a thin granular media filter, suggesting that the organics removal occurs by both filtration and adsorption. Although HAOPs get progressively saturated with NOM foulants during the filtration, this DM layer can be easily removed with the primary membrane remain pristine [184]. The schematic for DM layer formed by HAOPs on top of the primary membrane is shown in Fig. 3-1, and foulants in the feed had been proven to be effectively captured by HAOPs during the normal dead-end filtration process.

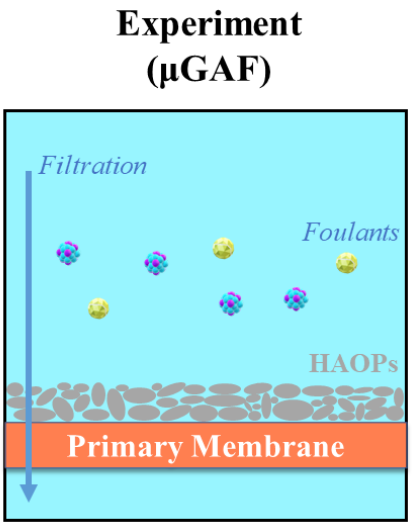

Fig. 3-1. Schematic diagram for the HAOPs DM configuration used for pre-treatment of MBR effluent.

Earlier experimental studies indicate that for such a hybrid adsorption-filtration system based on HAOPs, it did not show better performance compared to adsorbents like PAC with respect to the removal of overall dissolved organic carbon (DOC) or UV absorbance value at 254 nm (UV_{254}). Nevertheless, fouling potential of feed water is significantly reduced as indicated by lower transmembrane pressure (TMP) values. It was concluded that HAOPs are particularly efficient in removing portions of NOM that are tied to severe fouling [184, 189, 191], and thus reducing membrane backwashing frequency remarkably [193]. Based on EEM spectrometry and FTIR, it was identified

that HAOPs achieved significant removal of humic acids, fulvic acids and polysaccharide-like materials from raw water [177]. For practical operations, as opposed to directly dosing HAOPs into the bulk fluid (pre-adsorption), pre-depositing a thin layer of HAOPs on the membrane surface was found to be more effective, especially since the NOM-HAOPs layer can be detached during cleaning, therefore readily removing both the foulant and adsorbent [174]. Moreover, other studies found the performance of HAOPs to be only minimally dependent on membrane composition [184, 191], indicating the suitability for HAOPs to be used for various applications.

Despite the impressive results obtained experimentally, an in-depth understanding of the mechanisms underlying the superior performance by HAOPs remains amiss. To contribute towards a molecular-scale understanding not possible through experiments, this study aimed at using MD simulations to bridge this gap. Although the time scale and length scale of MD simulations are limited (on the scale of nanoseconds and Angstrom, respectively), it is well-acknowledged as a useful tool for providing mechanistic insights [194]. In particular, for membrane-filtration systems, past studies have attested to the capability of MD for elucidating membrane fouling behaviors. In this study, MD simulation was employed to understand why HAOPs mitigate NOM-fouling more effectively than a conventional adsorbent, namely, PAC. Since NOM is a complex mixture of different compounds, representative molecules have to be selected. Experimental results from literature indicated that HAOPs is more effective in removing high molecular weight (HMW) NOM [177, 179, 189], while PAC adsorbs strongly LMW NOM. Hence, in the current study, three HMW NOM (namely, polysaccharide, humic acid and fulvic acid) and three LMW NOM (namely, oxalic acid, pyruvic acid and 3-oxopentanedioic acid) were studied. The interactions between the six NOM molecules and two adsorbents, which reflect incipient adsorption, are evaluated. The results are expected to offer mechanistic insights underlying the better fouling mitigation capability of HAOPs, thereby guiding the translation of this technology to the practical operation of membrane units for wastewater treatment.

3.2 MD Simulation Setup

3.2.1 Chemical structures of molecules

Fig. 3-2 shows the two adsorbents studied, namely, HAOPs and PAC, represented as thin planes reflective of DM layers. Roughness effects are neglected here since the area simulated of 100 Å × 100 Å is orders of magnitude smaller than the areas characterized for roughness elements (e.g., by AFM [195]). For HAOPs, it is structured in the corundum crystal form ($\alpha - Al_2O_3$), which is the most common and heat-stable

form [196], and the top and bottom alumina surfaces are hydroxylated, which are stable termination facets under humid atmospheres [197]. It should be noted that sulfate groups (SO_4^{2-}) and crystalline water have been reported to be present in HAOPs [198], but are not accounted for here. Regarding SO_4^{2-}, our experiments indicated leaching of the SO_4^{2-} from HAOPs. Specifically, HAOPs were made in-house based on the reported protocol [198] and deposited as a DM layer on the primary ceramic membrane. At the end of 6 hours of filtration, the SO_4^{2-} concentration in the permeate of 123 ppm was more than twice that in the feed of 49 ppm, providing evidence of the leaching of SO_4^{2-} from HAOPs and the negligible change in TMP further proving SO_4^{2-} did not play a significant role in adsorption. Moreover, crystalline water is omitted in the HAOPs structure because HAOPs is hydrated by the water molecules in the simulation box. As for PAC, the slit-pore model is used by stacking three graphene layers together [199], with 72 carbon atoms at the interface saturated by oxygen atoms to form carbonyl groups. The surface carbonyl group density and orientation format are determined through earlier simulation [200] and experimental [201] studies. For water molecules, the SPC/E model is used [48].

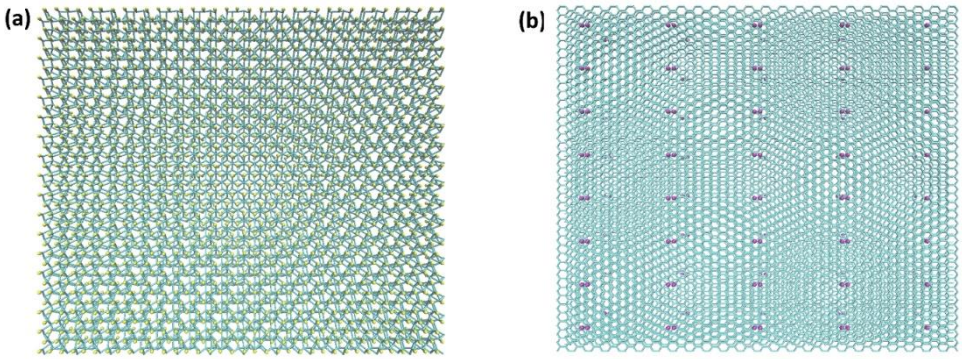

Fig. 3-2. Top view of adsorption layers used in the simulation: (a) HAOPs ($\alpha - Al_2O_3$ form) with hydroxylated surface, with aluminum-oxygen backbone in cyan and surface hydrogen atoms in yellow; and (b) PAC via the slit-pore model, with carbon in cyan and surface oxygen atoms in purple.

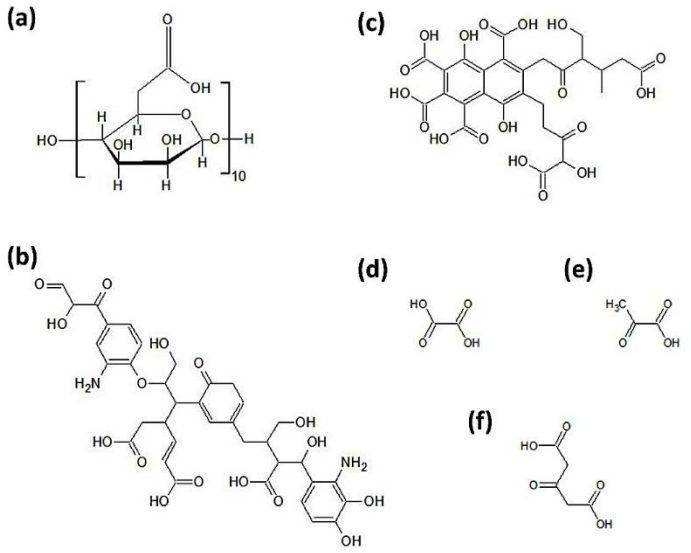

Fig. 3-3. Chemical structures of three HMW and three LMW foulant molecules used in the simulation: (a) polysaccharide represented by 10 monomers of alginic acid for (MW = 1778.95 g/mol); (b) humic acid via the TNB model (MW = 756.63 g/mol); (c) fulvic acid via the Buffle's model (MW = 477.24 g/mol); (d) oxalic acid (MW = 90.014 g/mol); (e) pyruvic acid (MW = 88.047 g/mol); and (f) DBP precursor represented by 3-oxopentanedioic acid (MW = 130.079 g/mol).

Fig. 3-3 displays the structures of the three HMW and three LMW NOM molecules studied in the simulation. It should be noted that: (i) while the LMW molecules have deterministic structures, the HMW ones are less well-defined and require models to represent the structures; and (ii) NOM like humic acid and fulvic acid are actually collective names for a wide range of compounds, so there is no universal molecular formula for these. Accordingly, the six NOM molecules simulated are (a) polysaccharide represented by 10 monomers of alginic acid [202], with a molecular weight (MW) of 1778.95 g/mol; (b) humic acid via the TNB model [203], with a MW of 756.63 g/mol; (c) fulvic acid via the Buffle's model [204], with a MW of 477.24 g/mol; (d) oxalic acid [205], with a MW of 90.014 g/mol; (e) pyruvic acid [205], with a MW of 88.047 g/mol; and (f) DBP precursor represented by 3-oxopentanedioic acid [206], with a MW of 130.079 g/mol.

3.2.2 Simulation methodology

For all MD simulations carried out in this study, the initial system configurations were constructed by the Packmol software based on packing optimization [65]. The actual simulations were conducted via LAMMPS [76]. For visualization and analysis, the VMD software was used [53]. The foulant-adsorbent interface, which reflects incipient adsorption or fouling of the DM layer, is of particular interest here. Thus, the adsorbent layer was fixed at the bottom of a three-dimensional periodic box, with SPC/E type water molecules randomly distributed throughout, which correspond to a water

layer thickness of around 70 Å. Model foulants were solvated in an aqueous environment at an initial distance of approximately 15 Å from the adsorbent layer. Only one HMW foulant molecule (i.e., polysaccharide, humic acid, fulvic acid) was placed in the simulation box each time, which corresponds to an actual concentration of 6 – 7 ppm. For the LMW molecules (i.e., pyruvic acid, oxalic acid, 3-oxopentanedioic acid), due to the much smaller size relative to the whole box, three molecules were put into the simulation box and statistically averaged.

To calculate the force acting on each atom, force field parameters must be assigned to every molecule in the system. The Optimized Potentials for Liquid Simulations-All Atoms (OPLS-AA) force field [207] is applied to model foulants, with a few missing terms adopted from relevant literature [208]. Regarding HAOPs and PAC, force field parameters presented by Phan et al. [197] and Jorge et al. [200] are used, respectively. In the simulations, the time step was 1 fs, the cut-off distance of non-bonded interactions was set to be 18 Å, and the electrostatic interaction was described by the Particle-Particle Particle-Mesh (PPPM) Ewald method. The pressure of the system was maintained at 1 atm (Nosé-Hoover barostat), while the temperature was controlled by the Nosé-Hoover thermostat. The coupling time constants for the barostat and thermostat were 500 fs and 100 fs, respectively. For each system, energy minimization was carried out by performing a canonical ensemble (NVT) run at 30 K for 100 ps. Subsequently, the system temperature was increased from 30 K to room temperature (298 K) by an NVT run of 200 ps. Then the system was relaxed by a 500 ps NVT run at 298 K, followed by a 1 ns NPT run for equilibration. The configurations were saved every 10,000 time steps. Finally, the evolution of equilibrated systems was tracked by carrying out an NPT run at 298 K and 1 bar for 4 ns, in which the final 2 ns was used for the analysis of conformational characteristics based on detailed atomistic model matrices. The choice of physical duration simulated is based on earlier related MD studies [36, 55, 94, 167, 209].

The following characteristics are quantified for all simulation systems: (1) inter-molecular interaction energy, which is the summation of electrostatic interaction and Lennard-Jones interaction (as shown in Table 2-2); (2) diffusion coefficient of water molecules determined from MSD (mean-square deviation) [210]; (3) RDF (radial distribution function); denoted by g, which is the probability of finding a pair of atom at distance r with respect to the average probability value [211]; (4) coordination number of water [212]; (5) hydrogen bond formed per water molecule [213, 214]; and (6) surface tension of the adsorbent-water interface [215, 216].

3.3 Results and Discussion

3.3.1 Intrinsic characteristics of adsorbent systems

Table 3-1 lists the properties of the HAOPs and PAC layers calculated based on a 10 Å thick water layer near the adsorbent surface, since the interfacial phenomenon is of particular interest in this study. The same cut-off has been applied in previous MD studies [36, 55, 94]. Due to the presence of a highly hydroxylated surface, the HAOPs layer is much more hydrophilic compared to PAC, as evident in the twentyfold higher interaction energy with water. It should be noted that, although activated carbon is hydrophobic, the presence of surface oxygen atoms on the PAC layer increases its affinity to water [217]. Furthermore, a much higher surface tension γ is observed for the more hydrophobic PAC compared to the highly hydrophilic HAOPs. The other three parameters reflect the relative looseness of the water network near the adsorbent surface. The HAOPs system consistently shows a more compact hydration layer, as indicated by the higher water coordination number, lower self-diffusion coefficient of water and more hydrogen bond formed per water molecule on average, which is tied to the greater hydrophilicity of HAOPs. The self-diffusion coefficients of water agree with literature results [218], and the coordination number is reasonably lower than the maximum coordination number reported in bulk water of between 4.8 and 5.0 [36, 219]. This provides validation of the simulation parameters used.

Table 3-1. Properties of HAOPs and PAC calculated based on a 10 Å thick water layer near the adsorbent surface. The values represent averages across the six foulant systems.

	HAOPs	PAC
Adsorbent-water interaction energy (kcal/mol)	-13618 $\pm$ 1803.6	-646.8 $\pm$ 16.58
Surface tension γ (mN/m)	27.33 $\pm$ 1.07	108.2 $\pm$ 9.03
Water coordination number	4.49	4.38
Self-diffusion coefficient of water (10^{-9} m^2/s)	1.58 $\pm$ 0.05	1.89 $\pm$ 0.05
Hydrogen bond formed per water molecule	1.34	1.31

3.3.2 Interaction profile for different foulants

Side-view snapshots of all 12 simulated systems (i.e., six foulants and two adsorbents) at the end of the 4 ns production runs are shown in Fig. 3-4 (three HMW foulants) and Fig. 3-5 (three LMW foulants). Fig. 3-4 shows that, regarding the three HMW foulants, the polysaccharide molecule is adsorbed to HAOPs but not PAC, the humic acid molecule is adsorbed to both HAOPs and PAC, while the fulvic acid

molecule is adsorbed to the PAC but not HAOPs. On the one hand, the affinity of polysaccharide and humic acid to HAOPs agrees with experimental results that indicated superior removal of polysaccharide and humic substances from raw water, as evident in the FTIR spectra [177]. On the other hand, some inconsistencies with experimental results, which indicated that the HMW foulants had stronger affinity to HAOPs than PAC [177, 179, 189], were observed. The disagreement may be because past models [220] and pilot-scale results [221] do not account for individual NOM constituents, as per the simulations here. As for the LMW foulants in Fig. 3-5, oxalic acid exhibits strong affinity to both HAOPs and PAC, pyruvic acid has no affinity to HAOPs but strong affinity to PAC, and DBP precursor has some affinity to both HAOPs and PAC. Due to the much smaller sizes, the behaviors of the LMW foulants are more stochastic, particularly in that the foulant may not stay adhered to the adsorbent layer for weaker affinities due to influence by the bulk liquid. The general stronger affinity of the LMW foulants to PAC relative to HAOPs is in line with experiment results [221].

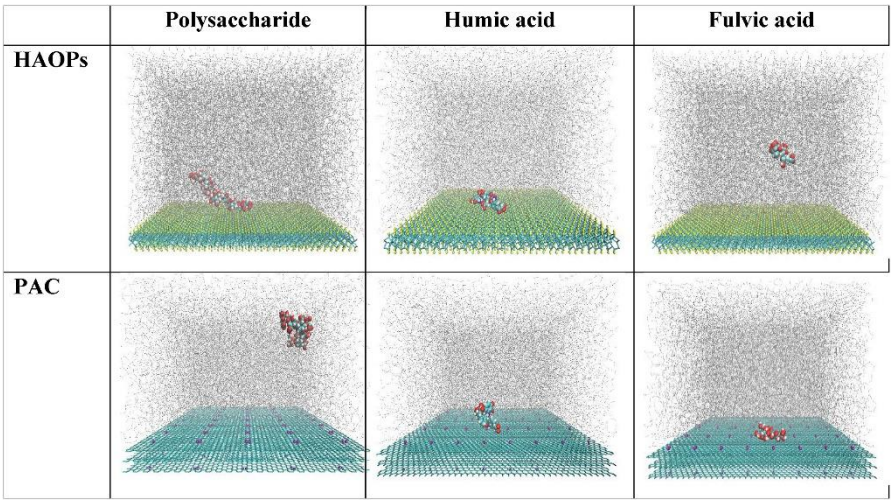

Fig. 3-4. Side-view snapshots of the MD periodic box at the end of the production runs, presenting the behavior and distribution of HMW foulants in the bulk liquid phase and near the adsorbent surface. HAOPs backbone is colored in cyan and surface hydrogen atoms colored in yellow. PAC slit-pore sheets are colored in cyan and surface oxygen atoms colored in purple. Carbon, oxygen, hydrogen and nitrogen atoms in the foulants are colored in light green, red, white and blue, respectively. The simulation boxes are filled with water molecules, represented by the grey background.

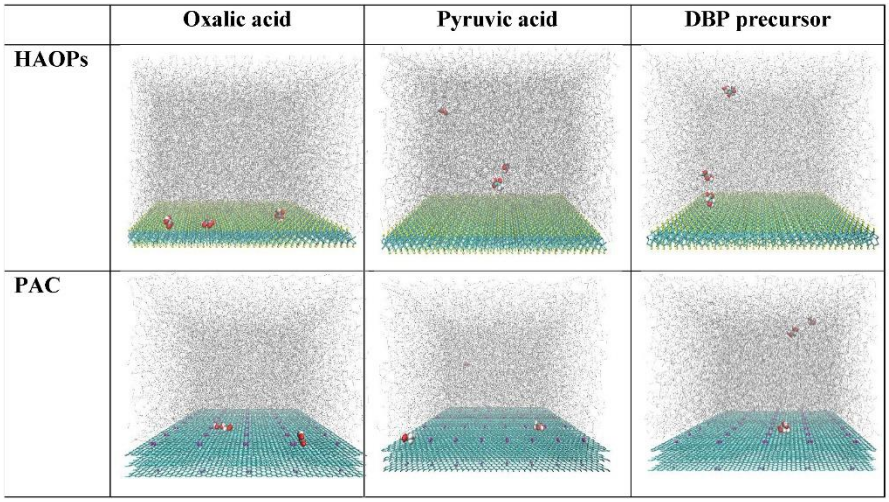

Fig. 3-5. Side-view snapshots of the MD periodic box at the end of the production runs, presenting the behavior and distribution of LMW foulants in the bulk liquid phase and near the adsorbent surface.

The interaction energy between different species has been shown to be a good predictive indicator of the membrane fouling phenomena [222-224]. To quantify the interactions, the foulant-adsorbent interaction values are displayed in Fig. 3-6 for all 12 systems studied. Only four out of the six foulants have interaction energies consistent with the experiments [177, 179, 189, 221], namely, (i) two of the HMW foulants, namely, polysaccharide and humic acid, whereby the interaction energy is more negative for HAOPs than PAC; and (ii) two of the LMW foulants, namely, pyruvic acid and DBP precursor, whereby the interaction energy is more negative for PAC than HAOPs. Consistent results obtained for these four foulants highlight that strong foulant-adsorbent interaction is a significant factor underlying the superior performance of HAOPs observed experimentally. On the contrary, the results of fulvic acid (an HMW foulant) and oxalic acid (an LMW foulant) disagree with experimental ones. This suggests that, while superior removal of foulants by either PAC or HAOPs is tied to more attractive foulant-adsorbent interactions, other mechanisms are at play too.

To understand the hydration effects, Fig. 3-7 plots the foulant-water interaction energy, which appears negligibly affected by whether the adsorption layer is HAOPs or PAC. Fig. 3-7 indicates that the HMW foulants generally have more attractive interaction energy with water, which is tied to the multiple hydroxyl groups in the structures. Thus, greater hydration effects associated with the highly hydrophilic HAOPs appear tied to the better removal of the HMW foulants. Polysaccharide has the highest interaction energy with water because of the large number of hydroxyl and carboxylic groups along the main carbon backbone, which leads to significantly stronger attraction to the water molecules compared to the rest. The other two HMW

foulants (namely, fulvic acid and humic acid) have more similar interaction energies as the LMW foulants due to the hydrophobic aromatic rings.

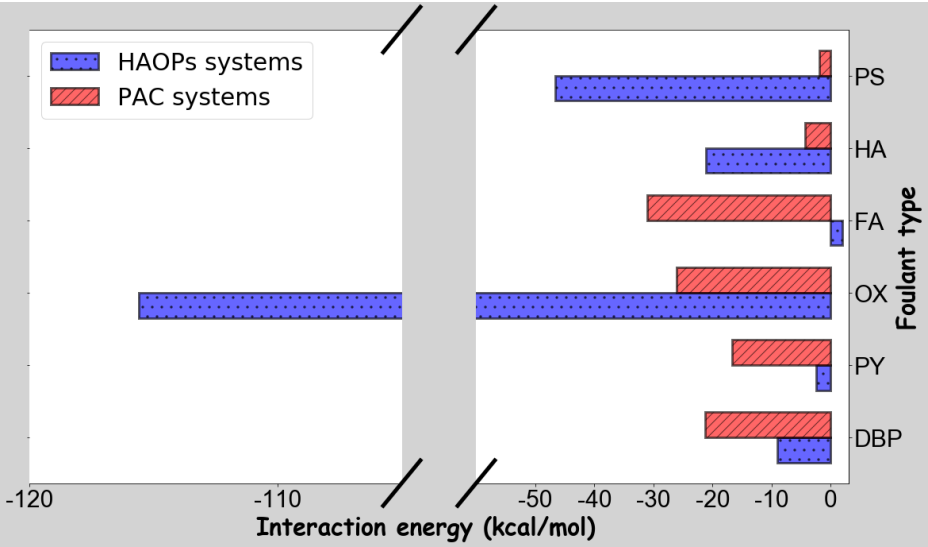

Fig. 3-6. Average interaction energy values between foulants and adsorbents over the last 2 ns of the production run. On the vertical axis, PS stands for polysaccharide, HA for humic acid, FA for fulvic acid, OX for oxalic acid, PY for pyruvic acid, and DBP for 3-oxopentanedioic acid (DBP precursor).

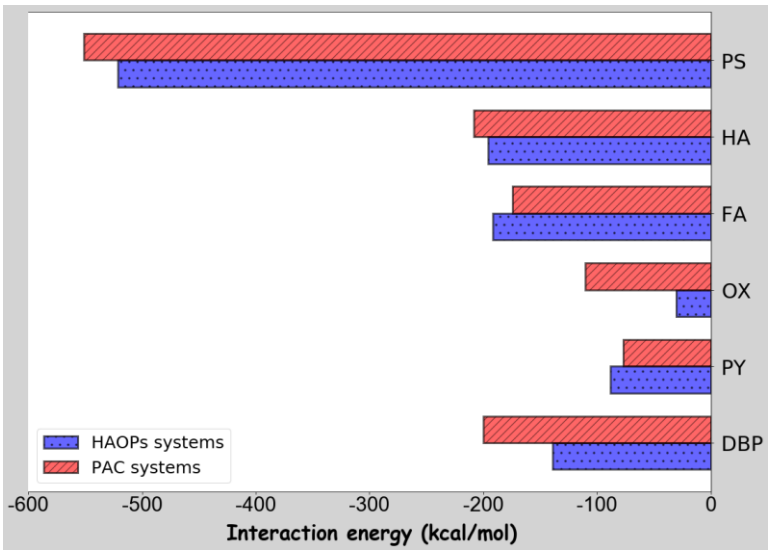

Fig. 3-7. Interaction energy values between foulant and water are averaged over the last 2 ns of the production run in HAOPs/PAC systems to reflect the hydration effect of foulants.

3.3.3 Mobility of foulants

Fig. 3-8 shows the differences in the mobility characteristics of the different foulants in the different adsorbent systems. Specifically, Figs. 3-8a and b present the evolution of the MSD of foulants throughout the entire 4 ns of production runs for the HAOPs and PAC systems, respectively. It should be noted that, unlike for water molecules,

diffusion coefficients are not computed for the foulants, since the foulant molecules do not exhibit a normal diffusion behavior due to interaction with the adsorbent.

Clearly, mobility characteristics depend on both foulant type and adsorbent type. Two key highlights are noted as follows. Firstly, Fig. 3-8 shows that two of the LMW foulants, namely, pyruvic acid and DBP precursor, exhibit the highest MSD values due to the smaller sizes. The other LMW foulant, oxalic acid, has negligible MSD values in the HAOPs system due to the significant affinity to HAOPs, and relatively lower MSD values in the PAC system due to the strongest affinity to PAC among the LMW foulants (Fig. 3-6). As earlier MD simulation studies have shown, foulant mobility has a significant influence on fouling propensity. Regarding membrane fouling in systems containing surfactants, when the surfactant molecule is less mobile, it tends to deposit onto the membrane and cause severe fouling [36, 55, 94]. However, in this study, it is desirable for the foulant to have lower mobility, such that it can stay adsorbed on the HAOPs or PAC surface. Although the interaction energy between oxalic acid and PAC is relatively lower (Fig. 3-6), the lower mobility may contribute to augment removal of oxalic acid by PAC. Secondly, the adsorbent type does affect the mobility of the foulants. While Fig. 3-8 shows that three foulants (namely, polysaccharide, humic acid and oxalic acid) have negligible MSD values for the HAOPs system, all foulants have some mobility for the PAC system, which agrees well with the relatively lesser removal of the foulants by PAC compared to HAOPs experimentally [177, 179, 189]. As for the LMW foulants, for which experimental results indicate PAC is better at removing, oxalic acid and pyruvic acid exhibit greater mobility with PAC, which reflects movement along the PAC surface. However, DBP precursor has the greatest MSD values for HAOPs, which substantiates the poorer removal by HAOPs. Therefore, both mobility and interaction energy appear to impact foulant removal by adsorbents. These observations imply that the superior adsorbent performance of HAOPs involves the decreasing of the mobility of NOM in water upon adsorption. Fig. 3-8a also shows that the MSD values of polysaccharide, humic acid and oxalic acid, which are strongly adsorbed by HAOPs, are approximately constant with time. In contrast, even if a molecule has been adsorbed by PAC, it still has relatively larger mobility to move along the surface of PAC. As can be seen from Fig. 3-8b, all MSD trends are noisy, which imply that all foulant molecules exhibit vigorous motion in PAC systems.

To further investigate the role of adsorbents in decreasing foulant mobility, MSD are decomposed into horizontal (average of *x*- and *y*-direction, parallel to adsorbent surface, same as crossflow direction) and vertical (*z*-direction, perpendicular to adsorbent surface, same as water flux direction) components as shown in Fig. 3-9.

Specifically, Fig. 3-9a compares mobility of HMW foulants in four systems that adsorption has occurred. In view of poor interactions between fulvic acid and HAOPs, as well as between polysaccharide and PAC (Fig. 3-6), these two systems are omitted here. Similarly, Fig. 3-9b compares mobility of LMW foulants omitting pyruvic acid and DBP precursor in HAOPs systems.

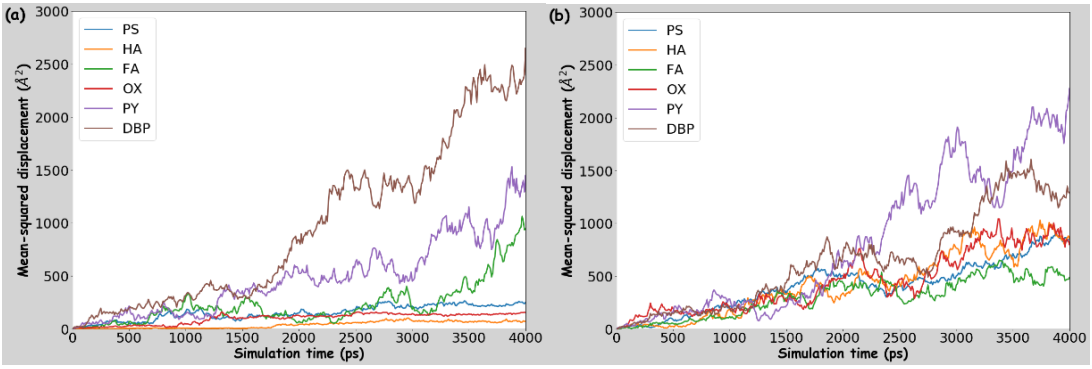

Fig. 3-8. Mobility characteristics of foulants: (a) MSD in HAOPs system; and (b) MSD in PAC system.

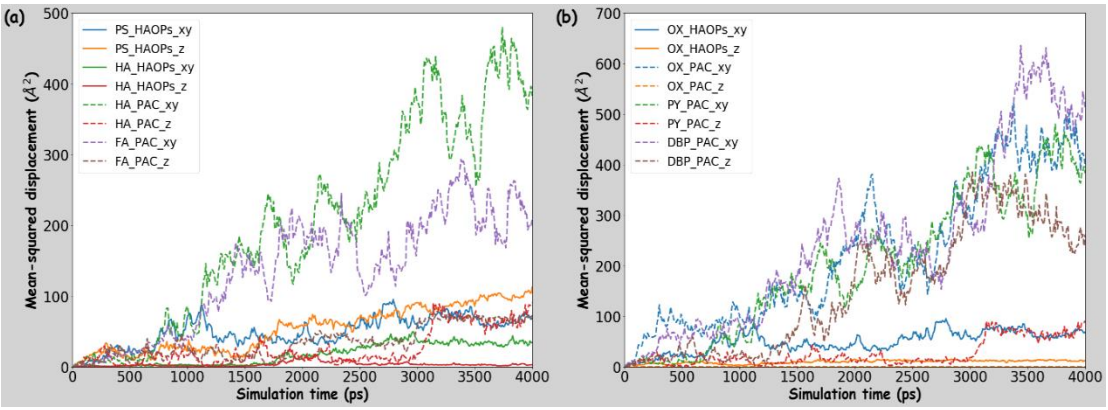

Fig. 3-9. Decomposition of MSD into horizontal (average of *x*- and *y*- direction, denoted by "xy" in legends) and vertical (*z*-direction, denoted by "z" in legends) for (a) HMW foulants; and (b) LMW foulants. All solid lines correspond to adsorption with HAOPs, and all dash lines correspond to adsorption with PAC. PS stands for polysaccharide, HA for humic acid, FA for fulvic acid, OX for oxalic acid, PY for pyruvic acid, and DBP for 3-oxopentanedioic acid (DBP precursor).

Based on Fig. 3-9a, it is clear that adsorption makes foulant much less mobile in vertical direction, indicated by lower MSD values for lines with legends ending by "z". Moreover, polysaccharide and humic acid are also quite immobile in horizontal direction when adsorbed to HAOPs surface (blue and green solid lines). Nevertheless, regarding two PAC systems investigated (humic acid fulvic acid), there are still substantial motion in *x*- and *y*- direction based on large MSD value shown by green and purple dash lines. Similar trends can also be observed in Fig. 3-9b for LMW foulants: only oxalic acid in HAOPs system (blue and orange solid lines) shows low mobility in both horizontal and vertical direction. On the other hand, all dash lines indicate that foulants still show quite vigorous motion, especially in horizontal direction, in PAC

system. Low mobility is only observed in vertical direction when oxalic acid and pyruvic acid are adsorbed by PAC (orange and red dash lines).

Based on above analysis, it can be concluded that adsorption by PAC generally can only make the foulant immobile in vertical direction. Significant surface motion in horizontal directions are still observable. In contrast, the superior performance of HAOPs appears tied to the significantly decreased mobility of the adsorbed foulants at the molecular level in both horizontal and vertical directions.

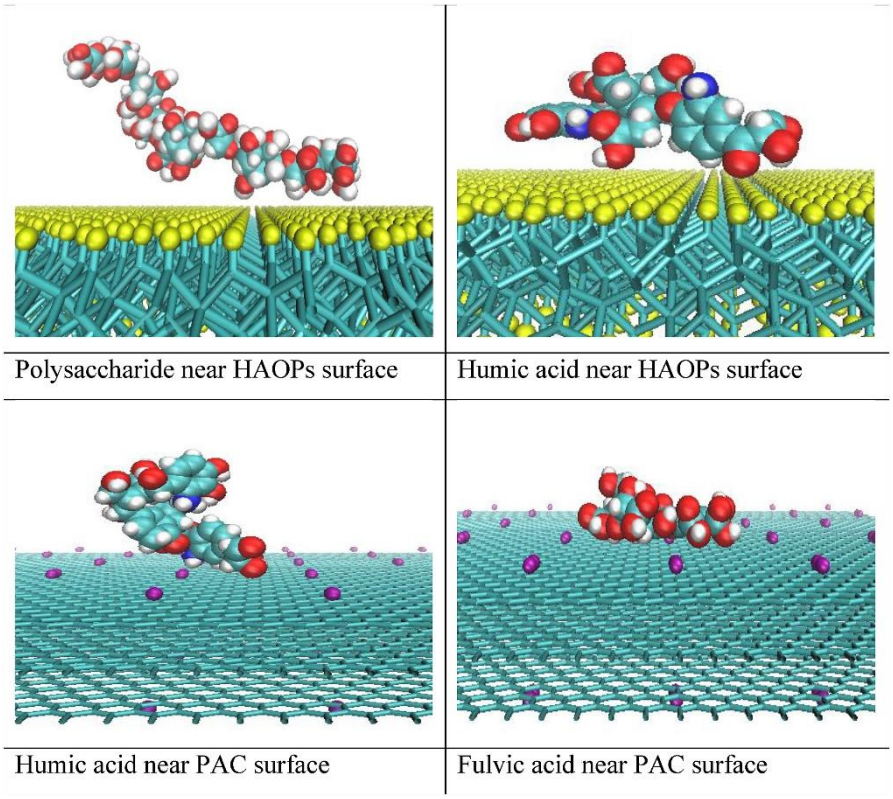

Fig. 3-10. Side views illustrating the orientations of HMW foulants adsorbed by HAOPs or PAC. Images are obtained at the end of 2 ns production run. Water molecules have been hidden for easier visualization.

3.3.4 Key functional groups contributing to adsorption based on RDF

To obtain a deeper understanding of the interaction between the foulant and adsorbent that leads to removal, the RDF plots are presented to further facilitate the understanding of these two adsorbents, and identify which functional groups in the molecule make a significant contribution to the adsorption process. Regarding the three HMW foulants, due to the more complex structures, it is critical to identify which part of the molecule interacts with the adsorbent most, and thus contributes to the adsorption. Fig. 3-10 depicts the magnified interface to understand how the foulant molecules are oriented near the adsorbent surface for four systems identical to Fig. 3-9a selected based on noticeable adsorption behavior. Three observations on molecular orientations are described as follows. Firstly, for polysaccharide, half of the total 10 monomers are

parallel position to the HAOPs surface, with hydroxyl and carboxyl groups appearing to be key interacting groups. Secondly, for humic acid, more functional groups interact with HAOPs compared with PAC. In the HAOPs system, two ends of humic acid, plus one carboxylic group in the middle, are all in close proximity with the HAOPs surface. On the other hand, in the PAC system, only the aromatic ring at one end of humic acid appears to be adsorbed. Therefore, HAOPs may be a better removal agent for humic acid, since it can interact with multiple parts of the humic acid molecule simultaneously to yield the strong attraction shown in Fig. 3-6. The capability to interact with multiple functional groups of HMW foulants is another critical mechanism for the superior fouling mitigation performance of HAOPs. Thirdly, fulvic acid seems to lay flat onto the PAC surface, which contradicts past experimental results [177, 179, 189]. In addition to interaction of the carboxylic groups at the terminal of two aliphatic chains, the naphthalene-like structure in Buffle's model also interacts.

Table 3-2. Notations and explanations of atoms in HMW foulant molecules used to generate RDF curves in Fig. 3-10.

Atom Notations	Explanation
HO	Hydroxyl hydrogen atom at 2' and 3' positions of polysaccharide.
HT	Terminal hydrogen atom in hydroxyl group at the 4' end of the polysaccharide.
HX	Hydrogen atom in the carboxylic group in all three HMW foulants.
HD	Hydrogen atom in the terminal aldehyde group of humic acid.
CB	Carbon atom in benzene rings of humic acid and fulvic acid.
HC	Ethyl hydrogen atom in fulvic acid.

To further investigate the effect of different functional groups, based on Fig. 3-10, RDF profiles are calculated for specific atoms in HMW foulants and the adsorbent surface, as displayed in Fig. 3-11. Specific representative atoms have been selected from each molecule, and their notations and corresponding descriptions are summarized in Table 3-2. Fig. 3-11 shows the RDF trends for the three HMW molecules. For polysaccharide (Fig. 3-11a), the $g(r)$ values of HO and HX are much lower than that of HT. The highest peak intensity in Fig. 3-11 for HT is due to the strong adsorption of one end of the polysaccharide chain to the HAOPs surface (Fig. 3-10). For humic acid (Fig. 3-11b), it is obvious that HAOPs is a better adsorbent than PAC, since the former gives high peak intensities in RDF plots for all three atoms whereas the latter only shows close contact with the HD atom. Moreover, since the peak position of RDF for the pair of HAOPs and HX is smaller (around 2 Å) than the other two pairs, it can be inferred

that the carboxylic group aids the adsorption of humic acid onto the HAOPs surface. Finally, for fulvic acid (Fig. 3-11c), the RDF trends are different to the other two HMWs (Figs. 3-11a and b), specifically in the much lesser noise in the $g(r)$ values, which tend to be noisy at higher values. This is tied to the more extensive and stable contact between fulvic acid and PAC (Fig. 3-10). In particular, the simulation results here for fulvic acid deviate from the experimental observations, because the Buffle's model adopted may not be a good representation for the actual fulvic acid molecule of interest. Comparing the structure of fulvic acid and humic acid shown in Fig. 3-4, the inconsistent results are likely due to the fused naphthalene ring leading to strong π-π interactions in the simulation of fulvic acid in the PAC system. Furthermore, the electron-rich naphthalene ring may result repulsion between fulvic acid and HAOPs too. The results for fulvic acid highlight the possible pitfall in such simulations, and underscore the need for experimental validation of the model structures employed.

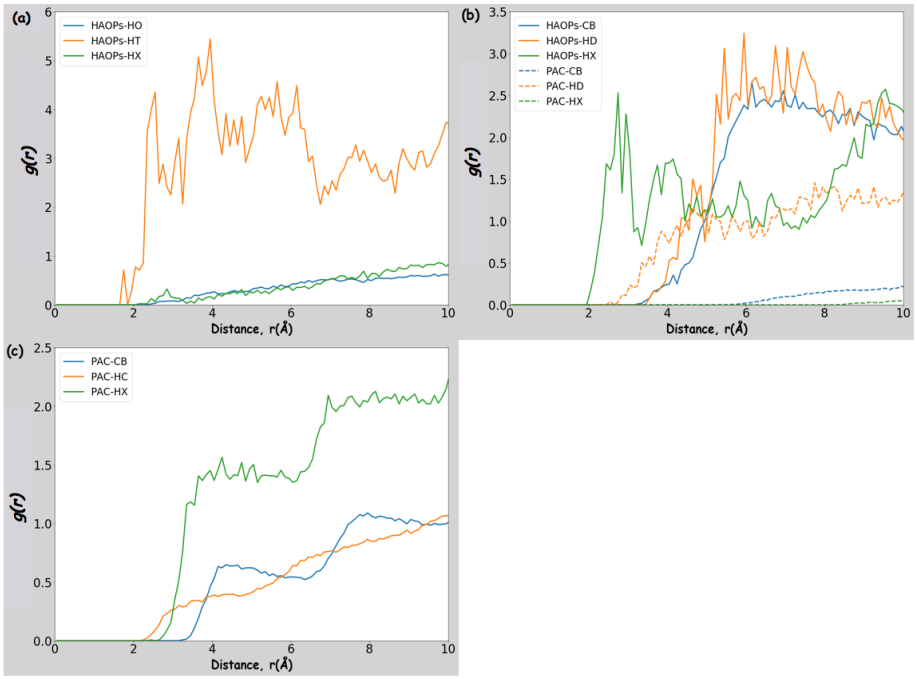

Fig. 3-11. RDF between specific atoms on HMW foulants and adsorbents: (a) atoms HX, HO and HT in polysaccharide, and HAOPs; (b) atoms HX, HD and CB in humic acid, and HAOPs (solid lines) and PAC (dash lines); (c) atoms HX, HC and CB in fulvic acid and PAC.

With respect to LMW foulants, the analogous RDF plot is presented in Fig. 3-12. In particular, there are only two kinds of hydrogen in pyruvic acid and DBP precursor, namely, hydrogen in the carboxylic acid group (denoted by HX) and hydrogen in the methyl or ethyl group (denoted by HC). As for oxalic acid, only the HX type is present. For easier readability, in Fig. 3-12, all RDF curves generated from the HAOPs and PAC systems are plotted as solid and dash lines, respectively. It is clear that the RDF values

are higher for the HAOPs system only for oxalic acid, but higher for pyruvic acid and DBP precursor for the PAC systems. This indicates that PAC tends to perform better when aliphatic groups like methyl or ethyl groups are present in the molecule, while HAOPs perform better when only carboxylic groups are present.

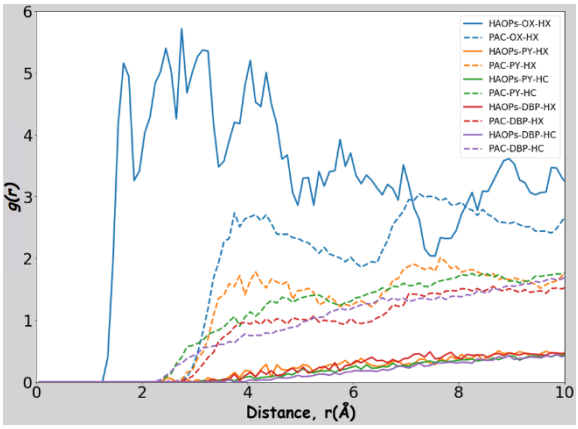

Fig. 3-12. RDF between two adsorbents and three LMW foulants. HAOPs and PAC are denoted by solid and dashed lines, respectively. Different hydrogen atom type is differentiated by different colors.

3.4 Conclusions

HAOPs have shown promising results for removing particularly the HMW NOM in water, and thereby mitigating membrane fouling in the hybrid adsorption-filtration system. To obtain a detailed mechanistic understanding underlying the superior performance of such HAOPs adsorbent at the molecular level, MD simulations were conducted to compare HAOPs with the conventional PAC adsorbent. Both HAOPs and PAC were modelled as thin planes representative of the DM layer. Six model foulants that are representative of both high HMW (namely, polysaccharide, humic acid and fulvic acid) and LMW (namely, oxalic acid, pyruvic acid and DBP precursor) constituents in NOM were studied. The superiority of HAOPs for HMW NOM removal, relative to PAC, is generally underlain by the following mechanisms: (1) higher foulant-HAOPs interaction energy; (2) increased hydration of the HMW NOM, as evident in the increased interaction energy with water, which thereby increases the affinity to the more hydrophilic HAOPs; (3) diminished mobility of the foulant once adsorbed in both horizontal and vertical direction, as evident in the lower MSD, which impedes desorption; and (4) higher peak intensity in the RDF between multiple functional groups on the HMW NOM foulants and HAOPs.

The results provide molecular-level insights on the better performance of HAOPs in the DM filtration applications. These are expected to be valuable for the better design of such materials and for the optimization of such systems in terms of operating cost reduction and extension of membrane lifespan.

Chapter 4 – Molecular Dynamics Simulation of the Competitive Adsorption Behavior of Effluent Organic Matters by Heated Aluminum Oxide Particles (HAOPs)

The previous simulation study of HAOPs focused on the adsorption behavior of individual foulants. During the project meeting, our collaborator pointed out that it might be interesting to investigate the competitive adsorption behavior of different foulants, since foulants will inevitably accumulate on the HAOPs surface with the progression of filtration. Therefore, MD simulation was expected to provide more insights regarding competitive adsorption under high foulant concentration condition, and further illustrate why HAOPs had shown superior performance in laboratory.

4.1 Introduction

Previously, MD has been used to understand the individual adsorption of three HMW and three LMW foulants onto HAOPs and PAC [109]. The effective removal of HMW foulants by HAOPS was attributed to the higher foulant-HAOPs interaction energy, greater hydration of HAOPs, diminished foulant mobility upon adsorption, and proximity of multiple functional groups in foulants with respect to HAOPs. It should be noted that effluent organic matter (EfOM), or equivalently referred to as NOM by previous studies depending on the source of feed water, is a complex mixture of a large variety of compounds. Even though chromatogram data obtained by LC-OCD can be processed by customized software to obtain the concentrations of different portions (namely, biopolymers, aquatic humics, building blocks, LMW neutrals, and LMW acids) [168], there is still no universal formula for each constituent, which makes MD simulation challenging. In the absence of precise structures, representative model structures were used in MD for each constituent [109]. With respect to concentration, the total organic carbon (TOC) concentration of the membrane bioreactor (MBR) effluent is about 6 to 7 ppm [225], so one HMW foulant, or three LMW foulants, were used in each simulation box to match the concentration value [109].

In the past studies, the adsorption behavior of different foulants has been investigated individually [99, 131, 199]. However, as more and more foulants accumulate onto the surface as filtration progresses, the concentration of the foulants at the boundary layer becomes elevated, and competition among the foulants for adsorption sites is inevitable. However, the knowledge on such competitive adsorption is sparse. Liang et al. [124] attempted to simulate the competitive adsorption of serum albumin and hemoglobin onto the ion-exchange chromatographic media using a coarse-

grained force field. Results indicate multi-layer adsorption, but not the displacement of pre-adsorbed protein. Tournois et al. [114] simulated the adsorption of multiple lysozyme and α-chymotrypsin molecules onto a cation exchanger surface, and found that α-chymotrypsin competed for adsorption sites and deposited in a multi-layer manner under high protein concentrations.

To enhance the understanding of competitive adsorption on DM layers, this MD study is targeted at comparing the competitive adsorption of high concentrations of different constituents of EfOM. Preliminary MD runs were conducted to validate the model structures selected for EfOM. After determining a high enough concentration for competitive adsorption to occur, production runs were conducted only for HAOPs to observe the dynamics of foulant molecules under the influence of other foulants. Simulation results obtained were validated with experimental data such as RO flux decline curves and removal percentage of EfOM constituents measured by LC-OCD, as presented in the earlier experimental paper of the microgranular adsorptive filtration (μGAF) prototype [225]. Results on the adsorption dynamics of EfOM at the molecular level provide mechanistic insights on the less reported competitive phenomenon, and are expected to be valuable in the optimization of adsorptive pre-treatments.

4.2 Simulation Methodology

4.2.1 Structure of HAOPs and PAC

Both HAOPs and PAC structures have been modeled as thin planes to represent the DM layer deposited on the primary membrane, with detailed descriptions listed in our earlier study [109]. It should be noted that surface roughness or inhomogeneity are beyond the scale of MD. In the earlier study, these two adsorbents were approximately 100 Å by 90 Å, with a slit-pore model (three graphene layers stacked together) adopted for PAC and corundum periodic crystal form (α-Al_2O_3) adopted for HAOPs. Surfaces of HAOPs are hydroxylated as the stable termination facet; and 72 oxygen atoms are attached to the PAC surface to form carbonyl group as per earlier studies [200, 201]. However, after preliminary runs in this study, it was found that the surface area was too large to study competitive adsorption effectively (details will be discussed in the later section). Hence, a smaller HAOPs layer was reconstructed using the open-source tool mBuild [54], with the area decreased to roughly 50 Å by 50 Å. Force field parameters of HAOPs and PAC were taken from earlier studies [197, 200], with the net charge being zero for both adsorbents.

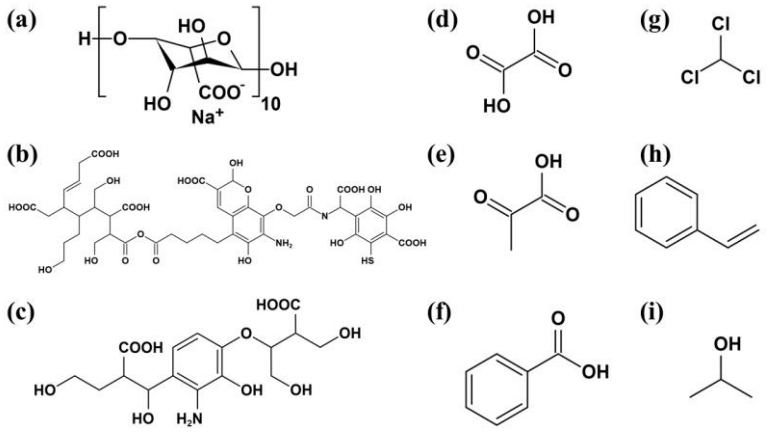

Fig. 4-1. Chemical structures of EfOM constituents simulated. The first three are HMW foulants: (a) polysaccharide (sodium alginate) representing biopolymer (MW = 2149.6 g/mol); (b) humic substances built from VSOMM2 (MW = 1054.0 g/mol); (c) building block built from VSOMM2 (MW = 389.4 g/mol). The remaining six are LMW acids and neutrals: (d) oxalic acid (MW = 90.0 g/mol); (e) pyruvic acid (MW = 88.0 g/mol); (f) benzoic acid (MW = 122.0 g/mol); (g) chloroform (MW = 119.4 g/mol); (h) vinylbenzene (MW = 104.2 g/mol); (i) tert-butyl alcohol (MW = 60.1 g/mol).

4.2.2 Structures of EfOM constituents

Due to the complex nature of EfOM, different model structures are needed to represent the different portions identified by LC-OCD. The schematics of all the compounds simulated are shown in Fig. 4-1, including the HMW portions of EfOM (namely, biopolymer, humic substance, and building block), as well as the LMW acids and neutrals.

For HMW ones, sodium alginate with 10 monomer units (Fig. 4-1a) was selected to represent a polysaccharide biopolymer, which is consistent with our earlier study [109] and other MD studies about fouling [108, 169, 226]. Regarding the other two HMW portions, since building blocks are the breakdown product of humic substances, these two were modeled together. Vienna soil organic matter modeler 2 (VSOMM2) [51] was used in this study, which was built based on data of the International Humic Substances Society (IHSS) that were collected from different source materials worldwide. VSOMM2 connected different small structures in a linear manner to match the given factors like molecular weight, percentage of elements, etc. Examination of the output structures (Fig. 4-1b and c) indicates that they had similar molecular weights as per that determined from LC-OCD [168], and carbon and nitrogen percentages (about 51% and 2%, respectively) close to the values measured from experimental samples [51]. These two output structures from VSOMM2 (Fig. 4-1b and c) contain most commonly encountered functional groups identified from humic substances experimentally [51, 227], like carbonyl group, carboxylic group, aromatic ether, etc. This provides further validation for our model structures.

LMW foulants have much simpler structures, but appropriate model structures should still be carefully selected since "LMW acids" and "LMW neutrals" are collective names for a large variety of compounds. Three common LMW organic acids found in water are used based on earlier studies [205, 228], namely, oxalic acid, pyruvic acid, and benzoic acid (Fig. 4-1d to f). As for the LMW neutrals, based on the rejection studies of 73 types of LMW neutral organics using polypropylene RO membrane indicating the important influence of specific structure elements (namely, aliphatic chain, aromatic ring, halogen, carbonyl, and hydroxyl group) [229], chloroform, vinylbenzene, and tert-Butyl alcohol (Fig. 4-1g to i) are chosen to represent the LMW neutrals. 3D structures of all EfOM constituents were drawn with Discovery Studio based on their respective chemical formula. After performing energy minimization at the beginning of the simulation, their structures remain relatively compact throughout the simulation. Nevertheless, there is no "stationary" 3D structure that can be provided for them, since they were not fixed as rigid entities; instead, constant internal rotational and folding motion persisted under the influence of surrounding water molecules and adsorbent surface throughout the simulation.

In order to be consistent with the development of VSOMM2, GROMOS force field 54A7 [73] was used for all EfOM compounds shown in Fig. 4-1, which include parameters for bonded interactions, Lennard-Jones parameter for atoms and partial charge values for electrostatic interaction.

4.2.3 System packing and simulation details

All system packing was done using Packmol [65]. The thin adsorbent layer (HAOPs or PAC) was fixed at the bottom of the simulation box and foulants were subsequently packed into the box, which was later filled with SPC/E type of water molecules [48] to reach a density of 1 g/cm^3. Since the MBR effluent collected from the plant was neutral (pH 7.12 – 7.2) [225], all carboxylic groups of EfOM were deprotonated in the simulation. Hence, cations need to be added to make the whole box charge-neutral. The following four types of cations have been detected from MBR effluent, namely, Na^+ (7.9 ppm), K^+ (21.3 ppm), Ca^{2+} (23.3 ppm) and Mg^{2+} (5.2 ppm) [225]. Therefore, these four ions were added based on their concentration ratios and the total negative charge of EfOMs. The details of the packed systems are summarized in Table 4-1.

Note that the first 10 preliminary runs (i.e., 5 for HAOPs and 5 for PAC) were conducted at the beginning to validate the model, and their results indicate that the box volume needs to be further decreased to observe competitive adsorption of different foulants. There are two main reasons for conducting five preliminary runs for each

adsorbent (Table 4-1). Firstly, as some foulants selected in this study (Fig. 4-1) are different from the previous study [109], it is necessary to make sure that the general behavior of foulants is still consistent, i.e., HMW EfOMs preferentially adsorb onto HAOPs, whereas LMW EfOMs to PAC. Secondly, although the equivalent TOC shown in Table 4-1 has already become much higher than MBR effluent, the higher concentrations are necessary to simulate competitive adsorption at the adsorbent surface. Note that this elevated foulant concentration scenario is still considered as reasonable, since favourable foulant would be captured in HAOPs gradually with the progress of filtration, resulting in a much higher local concentration compared to the bulk concentration in MBR effluent. MD simulation here serves as a simplified model while foulant inventory is fixed (batch-mode), rather than continuous supply as in real experiments.

Table 4-1. Summary of dimension and molecular composition of all 16 simulation systems.

	Preliminary Runs		**Production Runs**
Adsorbent	HAOPs	PAC	HAOPs
System dimension (Å)	104 × 90 × 70	103 × 88 × 70	55 × 52 × 90
Number of species			
Polysaccharide	1		2
Humic substance	1		2
Building block	1		2
Each LMW acid	1		2
Chloroform	1		2
Vinylbenzene	1		0*
tert-butyl alcohol	1		0*
Water	18,000		7,200
Na^+	2		4
K^+	6		12
Ca^{2+}	6		12
Mg^{2+}	1		2
Equivalent TOC (g/L)	4.7	4.9	22.3
Number of replicates	5	5	6

*: vinylbenzene and *tert*-butyl alcohol were excluded from production runs since it was observed that they were not adsorbed by HAOPs strongly.

After the validation step, 6 production runs were performed at even higher foulant concentration for a smaller surface area of HAOPs. To ensure statistical validity, replicate runs were carried out by initializing EfOMs and ions at different positions in the simulation box [25, 33, 56, 140]. Specifically, EfOMs and ions were placed in bulk liquid with at least 10 Å away from the HAOPs/PAC surface. The exact position and orientation of foulants were randomized in Packmol.

All simulations were conducted via the LAMMPS [76], with post-processing aided by VMD [53]. Periodic boundary condition was applied to all three dimensions. The cutoff distance of the non-bonded Lennard-Jones interaction was set to be 15 Å, in line with other simulation studies [155, 230]. Long-ranged electrostatic interaction was calculated in the reciprocal space by the PPPM method. Covalent bonds in water molecules were constrained to be rigid by the SHAKE algorithm for computational efficiency [83]. The simulation time step was set to be 2 fs [35, 199]. All five replicates of preliminary runs were run for 40 ns under NVT ensemble at 298 K with a Nosé-Hoover thermostat [89], which is a common practice for fouling/adsorption-related MD studies [25, 28, 169]. NPT ensemble was not chosen due to stability reason, and the fact that volume variation turned out to be very small (<0.2%) based on previous study [109]. After validating with experimental results, six independent production runs with smaller system volumes (Table 4-1) were subsequently conducted to evaluate the competitive adsorption behavior. Based on preliminary run results, production runs were all performed for 40 ns to stabilize the system (i.e., the overall energy and temperature exhibit small fluctuations, and to ensure foulants that preferentially adsorb have anchored onto the adsorbent surface). After that, all systems were run for another 10 ns for sampling of various parameters. Therefore, the total length of six production runs was 50 ns each.

4.3 Results and Discussion

4.3.1 Preliminary runs: model validation

Fig. 4-2 displays sample snapshots of simulation systems at the end of 40 ns, with different types of EfOMs in different colors. Clearly, the surface areas of both HAOPs and PAC were sufficient to allow simultaneous adsorption of different EfOM constituents. Moreover, due to the periodic boundary condition, foulants can adsorb either on the top or bottom surface of the adsorbent. The competition of adsorption sites was not observed, with foulants tending to find free spaces on the adsorbent surface to adsorb without any hindrance. Hence, for subsequent production runs, the system

volume was further decreased and more foulants were added to the simulation box, as indicated in Table 4-1, to simulate the competition between EfOMs.

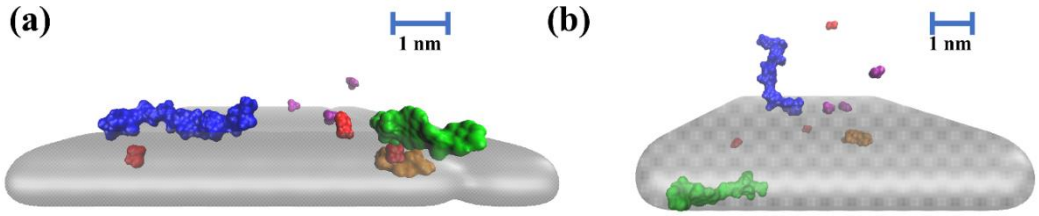

Fig. 4-2. Sample snapshots of preliminary runs at the end of simulation for (a) HAOPs; and (b) PAC. Both adsorbents are represented by the grey slab. Foulants are displayed in different colors: blue for polysaccharide, green for humic substance, orange for building block, red for LMW acids and purple for LMW neutrals. Foulants adsorbed at the bottom surface of HAOPs/PAC are more blurred compared to foulants adsorbed at the top surface. All water molecules and ions are hidden for visualization purpose.

Despite the fact that competitive adsorption was not observed, preliminary runs still provide validation for the simulation model. For quantitative analysis of adsorption, Fig. 4-3 shows the distribution of average interaction energy and separation distance between foulants and adsorbents. Interaction energy is computed as the sum of intermolecular electrostatic and VDW terms which are incorporated in the GROMOS force field. It is often used in simulation studies [28, 30, 56] related to membrane filtration to give a direct reflection of whether interaction between two species is attractive or repulsive, and provide relevant interpretation linked with macroscopic observations. In this study, a more negative foulant-adsorbent interaction energy value would indicate stronger affinity, and thus, more effective removal via electrostatics and VDW forces. Generally, consistency was found between systems starting from different initial orientations of foulants, indicating statistical validity. The separation distance (horizontal axis) is defined as the spatial difference between the *z*-coordinate of the center-of-mass of foulants and surface hydrogen atoms on HAOPs or surface oxygen atoms on PAC. The interaction energy (vertical axis) is plotted in logarithmic scale since the interaction energy of adsorbed foulants are orders-of-magnitude higher than those not adsorbed.

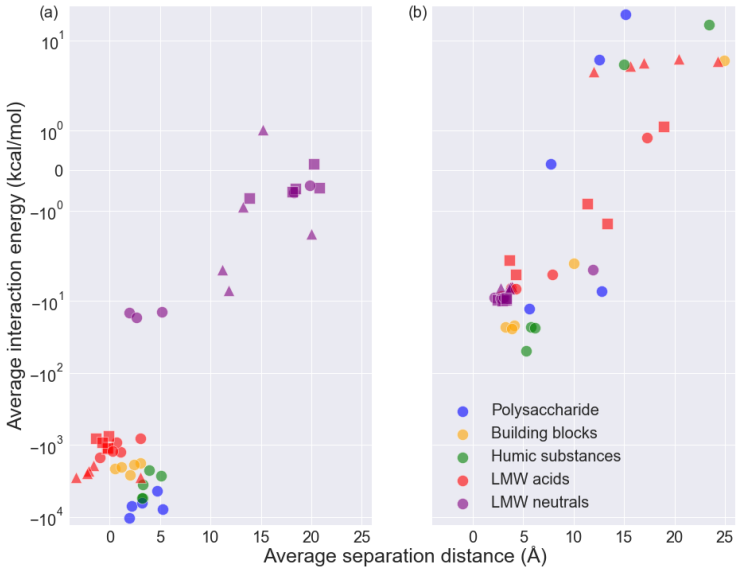

Fig. 4-3. Distribution of adsorbent-foulant interaction energy and separation distance averaged over the last 10 ns of preliminary runs for (a) HAOPs; and (b) PAC. The vertical axis is drawn in logarithm scale due to the large variation in interaction energy values between adsorbed foulants and unadsorbed ones. Scatter points with the same color and shape correspond to five independent repeats of simulation runs. Categories of EfOM are differentiated with marker colors as indicated by the legend, consistent with Fig. 4-2. Since there are three different types of compounds for both LMW acids and neutrals as shown by Fig. 4-1, they are further differentiated by their shapes: for LMW acids in red, circle stands for benzoic acid, triangle stands for oxalic acid, and square stands for pyruvic acid; for LMW neutrals in purple, circle stands for chloroform, triangle stands for *tert*-butyl alcohol, and square stands for vinylbenzene.

Based on Fig. 4-3, the following insights can be drawn: (i) HAOPs has consistently stronger adsorption tendency to all EfOM constituents except for LMW neutrals, and the trend is consistent across replicate runs; (ii) among LMW neutrals, chloroform is adsorbed occasionally by HAOPs while the other two (vinylbenzene and tert-butyl alcohol) are not adsorbed at all, indicating variation in adsorption tendency within the same category of EfOM; (iii) PAC has stronger adsorption tendency to LMW neutrals; and (iv) while sometimes HMW foulants and LMW acids are adsorbed by PAC, their interaction energy values are much weaker compared to that by HAOPs, and the variation across replicate runs are relatively larger, indicating the removal of these EfOM constituents by PAC is not as effective as HAOPs. The results shown in Fig. 4-3 are consistent with earlier studies demonstrating that HAOPs generally remove key foulants with high fouling potential, especially HMW foulants, better than PAC [109, 179, 193, 225]. This provides validation of the simulation model.

Systems for production runs were constructed with a focus on competitive adsorption of foulants on HAOPs. Note that, since vinylbenzene and tert-butyl alcohol are found to preferentially remain in the bulk liquid without adsorption by HAOPs, they

were excluded from production runs (Table 4-1). However, since chloroform did show some adsorption tendency, it was still included in production run systems.

4.3.2 Production runs: competitive adsorption

With a smaller system volume, which is equivalent to higher foulant concentrations, foulants must compete for limited adsorption sites on the HAOPs surface, so the adsorption is expected to be somewhat weaker than that in the larger systems (preliminary runs). Similar to Fig. 4-3, the average adsorbent-foulant interaction energy and separation distance are plotted in Fig. 4-4. In addition, to allow direct visualization of the adsorption at the high foulant concentration, snapshots at the end of simulation runs for all 6 production runs are shown in Fig. 4-5. Note that the top mirror image HAOPs surface shown in Fig. 4-5 is a direct result of applying periodic boundary condition in simulation. The sandwich-like structure can be regarded as a simplified model for the experimental scenario, since foulants were filtered through a packed bed of HAOPs in the μGAF process which resembles flowing through membrane pores. As expected, average separation distance values of each foulant generally became larger as compared to Fig. 4-3. This is a key observation to indicate the existence competitive adsorption: as the surface area of HAOPs becomes roughly 4 times lower in production runs, EfOM constituents had to fight for limited adsorption sites under high concentration environment, which inevitably led to relatively larger separation distance.

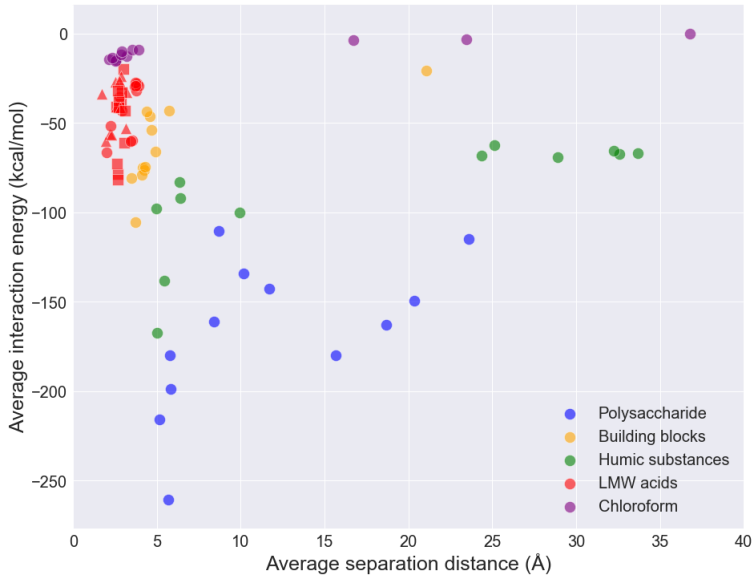

Fig. 4-4. Distribution of adsorbent-foulant interaction energy and separation distance averaged over the last 10 ns of production runs for HAOPs. Scatter points with the same color and shape correspond to six independent repeats of simulation runs. Categories of EfOM are differentiated with marker colors as indicated by the legend, consistent with Fig. 4-2. Since there are three different types of compounds for LMW acids, they are further differentiated by their shapes: for LMW acids in red, circle stands for benzoic acid, triangle stands for oxalic acid, and square stands for pyruvic acid. Note that

average values of each foulant are calculated individually; and since there are two molecules of each foulant in each of the six replicate production runs, there are 12 scatter points for each foulant included (Fig. 4-1a to g).

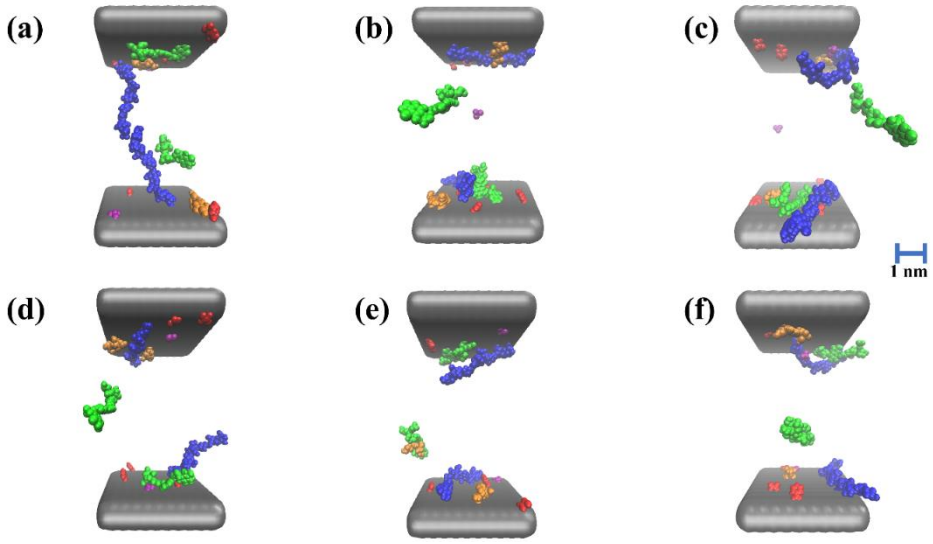

Fig. 4-5. Snapshots of six HAOPs production runs at the end of simulation. HAOPs is represented by the grey slab, with the one on top being the mirror image of the one at the bottom. Foulants are displayed in different colors: blue for polysaccharide, green for humic substance, orange for building block, red for LMW acids and purple for LMW neutrals (chloroform). All water molecules and ions are hidden for visualization purpose.

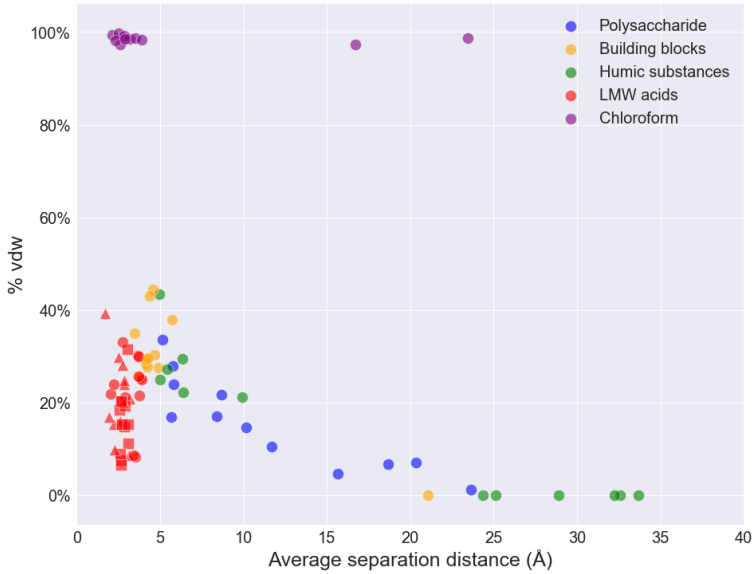

Fig. 4-6. Distribution of the percentage of VDW interaction in total interaction energy and separation distance averaged over the last 10 ns of production runs for HAOPs. %vdw on the vertical axis is calculated as the ratio of VDW interaction energy values between foulant and HAOPs, with respect to the total interaction energy values shown in Fig. 4-4.

Since the interaction energy is the summation of intermolecular electrostatics and VDW interaction, the relative contribution of these two components can be calculated. Results are shown in Fig. 4-6 as a function of separation distance. As expected,

electrostatic interaction is more long-ranged due to the application of PPPM method in MD simulations, so the percentage contribution of VDW interaction generally became non-zero only for small separation distance (i.e., when adsorption occurred). The adsorption of all HMW foulants and LMW acids appears to be driven by both type of interaction, with both components being negative in value (which means attraction) and electrostatic interaction plays a relatively more dominant role (higher than 60% in general). This is expected since all carboxylic groups carry negative charge under neutral pH. In contrast, VDW interaction is the main contributor for the interaction between HAOPs and chloroform since it is a LMW neutral compound. However, based on Fig. 4-4, all foulants still exhibit strong adsorption in some runs, except for chloroform, whose interaction energy with HAOPs is the lowest even when the separation distance is small. This observation is consistent with Fig. 4-3, which indicates that the adsorption of LMW neutrals is weaker for HAOPs compared to PAC. Although chloroform is adsorbed in some cases when there is sufficient space on the HAOPs surface (Figs. 4-2 and 4-3), its adsorption is not strong enough to compete with HMW EfOMs and LMW acids when the adsorption site becomes limited under high foulant concentration. Therefore, chloroform is not considered as adsorbed in production runs and thus excluded in the following discussion. Regarding the competitive adsorption between other foulant molecules, Fig. 4-4 and Fig. 4-5 should be analyzed together. Based on the segregation of EfOM constituents in Fig. 4-4 and the direct visualization of simulation systems in Fig. 4-5, the following observations are worth highlighting.

Firstly, with a larger separation distance, interaction energy values of adsorbed foulants are much lower than those in preliminary runs (Fig. 4-3). This is a reflection of competitive adsorption. Specifically, due to the limited surface area of HAOPs, foulants can no longer spread out on the surface, as such in Fig. 4-2 where there is still additional space for more parts of the foulants to establish stronger anchoring. In other words, the adsorbent-foulant attraction is diminished in the more crowded environment, due to the increased steric hindrance by other foulants on the HAOPs surface. This is evident in Fig. 4-5c, whereby the adsorbed foulants are more coiled up than spread out on the surface.

Secondly, despite the significant drop in absolute value, most adsorbent-foulant interactions are still highly attractive, except for chloroform. This indicates that, even at much higher foulant concentrations, HAOPs still have a relatively strong capability to adsorb HMW foulants and LMW acids, thereby preventing a significant portion of them from reaching the downstream RO unit. The strong adsorption affinity is clearly

observable in Fig. 4-5, where adsorption of various foulants can be visualized for all snapshots at both the bottom and top HAOPs surface.

Thirdly, the larger sizes of polysaccharide and humic substance cause a larger separation distance with respect to the HAOPs surface, compared to smaller building block and LMW acids. Nevertheless, strong attraction can still be established. For example, in Fig. 4-5a, only one terminal of the two polysaccharide molecules is anchored at the respective HAOPs surface, with the long chain floating in the bulk liquid. The structure unit responsible for such a partial adsorption was found out to be the carboxylic group of the first and second monomer unit at the adsorbed end, which agrees with previous observation that adsorption of HMW foulants were mainly driven by electrostatic interaction. More detailed analysis regarding functional group will be presented in the later section. Although such a single-point contact mode seems unsteady, the anchoring is stable throughout the simulation, with relatively high interaction energy determined (-114.8 kcal/mol and -149.6 kcal/mol, respectively). This provides molecular-level insights regarding the excellent biopolymer removal by HAOPs found in experiments [225]. Specifically, although sometimes polysaccharide fails to lay entirely flat on the HAOPs surface, most of the time it still manages to preferentially anchor onto the HAOPs surface even if challenged by steric hindrance from other adsorbed foulants. Such anchoring is often strong enough to prevent it from detaching and returning to the bulk.

Lastly, the intermediate behavior of humic substances is also a reflection of competitive adsorption. On the one hand, humic substances generally exhibit less attractive interaction energy compared to polysaccharide (Fig. 4-4), which agrees to a smaller removal percentage measured by LC-OCD [225]. On the other hand, as can be seen from Figs. 4-4 and 4-5, only around half of the humic substance molecules establish contact with the HAOPs surface, with the rest remaining freely in bulk water, which is different from smaller LMW acids and building blocks whereby almost all molecules are adsorbed. This is because humic substances are larger than building block and LMW acids, thus require a larger surface area for anchoring. However, the humic-HAOPs interaction energy is still quite attractive despite the large separation distance, which stems significantly from long-ranged electrostatic interaction, so that half of all simulated humic molecules are still adsorbed. It should be noted that the time scale of MD (nanoseconds) is much shorter than the actual μGAF process (hours to days), so the unadsorbed humic molecules may still squeeze through and find suitable anchoring place on the HAOPs surface throughout the filtration period, driven by the relatively

strong attraction. Thus, this provides a plausible underlying explanation for LC-OCD showing a similar removal efficiency of humic substances and building blocks [225].

In summary, both the enthalpic effect (attractive energy) and the entropic effect (steric hindrance of adsorption) should be considered when investigating foulant adsorption, which is consistent with the earlier study on surfactant fouling [35]. Note that we have conducted analysis based on snapshots, separation distance, and interaction energy only, without quantifying the adsorption free energy of each individual foulant [139], since it is desired to focus on the dynamic of each foulant under the influence of other foulants when the concentration is high, which inevitably makes our system inappropriate for enhanced sampling method like umbrella sampling to quantify free energy quantitatively. Nonetheless, it is possible to investigate the mobility and flexibility of adsorbed foulants, which have been found to be critical for fouling based on previous MD simulation studies [28, 33, 109], and serve to further supplement the mechanistic insights drawn above based on interaction energy and separation distance.

4.3.3 Mobility and flexibility characteristics

The mobility and flexibility of HMW foulants (namely, polysaccharide, humic substance and building block) are quantified and compared. The focus is on HMW foulants because (i) HAOPs is specialized in removing this portion of EfOM, which is a key contributor to the downstream RO fouling [109, 179, 189, 225]; and (ii) HMW foulants have long chains or more complex structures, so the flexibility warrants further discussion.

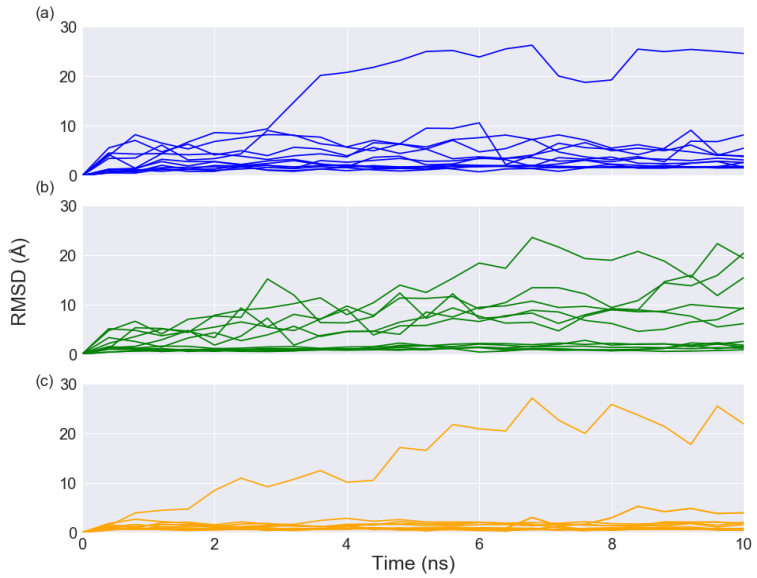

Fig. 4-7. Trends of RMSD in the last 10 ns of simulation for HMW foulants: (a) polysaccharide; (b) humic substance; (c) building block. Each line corresponds to one foulant in one specific run, so there are 12 curves in total in each subplot.

Table 4-2. Classification of behavior of all 36 HMW foulants in 6 independent production runs based on RMSD profile shown in Fig. 4-7.

Foulant	**Number of unadsorbed molecules**	**Characteristics**	**Number of adsorbed molecules**	**Characteristics**
Polysaccharide	**1**	RMSD > 12 Å mostly	**7**	Flat orientation at the surface, RMSD < 4 Å throughout
			4	Anchored on one end, RMSD < 12 Å throughout
Humic substances	**6**	RMSD > 6 Å mostly	**6**	RMSD < 6 Å throughout
Building block	**1**		**11**	

The mobility of the foulant is commonly quantified by RMSD, which is a function of simulation time t as shown by Eq. (4). RMSD represents how much foulant has drifted away from its initial position within a given time period; the larger the RMSD is, the more mobile the foulant is. Fig. 4-7 plots RMSD curves for three types of HMW foulants in the last 10 ns of the production runs. Similar to the previous study, once the foulant is adsorbed by HAOPs, the mobility diminishes as indicated by the consistently low RMSD values, which also proves that simulation systems can be considered as stable at the end of 50 ns of simulation. Such low mobility is a key mechanism for the effective removal of EfOM by HAOPs observed in experiments [109, 174, 225]. It can also be concluded that high foulant concentration and a competitive environment do not increase the mobility of the adsorbed foulant, indicating that the removal can stay effective throughout the filtration as long as HAOPs has not become saturated yet.

The RMSD trends of the three types of HMW foulants are quite different. In Fig. 4-7a, only 1 polysaccharide molecule is not adsorbed, while the other 11 are. However, as shown by subplots in Fig. 4-5, some polysaccharide molecules are only adsorbed at one terminal, leading to slightly higher mobility compared to the case where its orientation is flat, since the unadsorbed terminal still has some degree of freedom in the bulk liquid. It is possible to separate the polysaccharides that are adsorbed on one end (4 out of 11) versus those that adopt a flatter orientation and anchors more strongly (7 out of 11). From Fig. 4-7b, it is seen that half of the humic substance molecules are adsorbed while the remaining half are not. In comparison, while polysaccharide is a long-chain molecule and has more anchoring points, the structure of humic substance is more compact and thus either becomes fully adsorbed or unadsorbed. For the building block, which has the lowest molecular weight among these three (Fig. 4-7c), only 1 out

of 12 molecules is not adsorbed by HAOPs, as reflected by the significantly higher RMSD values. Compared to polysaccharide and humic substance, the RMSD curves of the unadsorbed building blocks are very distinct from that of the adsorbed building block (Fig. 4-7c), which is due to its smaller molecular size. Table 4-2 summarizes different categories of HMW foulants classified based on Fig. 4-7.

Therefore, based on the above mobility analysis, the following conclusions can be made: (i) HAOPs is still highly effective in reducing the mobility of adsorbed foulants even when the local concentration becomes very high; (ii) RMSD curves serve as a good indicator to differentiate adsorbed versus unadsorbed EfOM molecules; (iii) demarcation of adsorption versus non-adsorption is more distinct for molecules with relatively simple structure; extra caution should be placed when analyzing RMSD profiles of molecules like polysaccharide and humic substance due to their structural complexity.

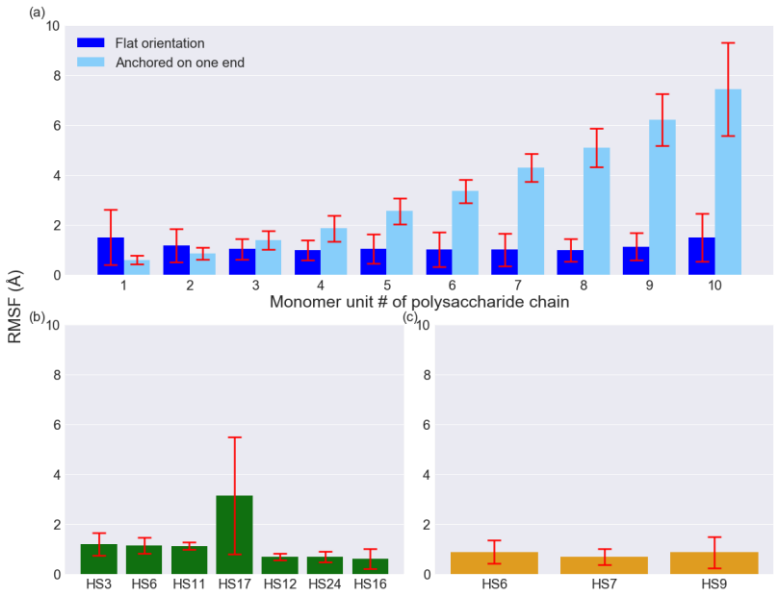

Fig. 4-8. RMSF of adsorbed HMW foulants, calculated during the last 10 ns of the production runs: (a) polysaccharide; (b) humic substance; (c) building block. Each sugar monomer in polysaccharide is treated as one residue, so there are 10 bars in (a). As shown in Table 4-2, polysaccharide may adopt a flat orientation on the surface, or only anchored on one terminal with the other floating in the bulk liquid, so these two scenarios are differentiated by bars of dark blue versus light blue. Small blocks of VSOMM2 with pattern "HSx" are used to represent residues in humic substance and building block, with their respective name shown as the horizontal axis ticks. Red error bars stand for standard deviations across different adsorbed molecules.

Another parameter worth investigation is the flexibility of different parts of adsorbed foulants, which is quantified by root-mean-squared fluctuation (RMSF) and is a function of residue number k as shown by Eq. (9). For previous MD simulation studies [33, 115], the foulant selected was protein with well-defined amino acid chains,

so each amino acid serves as a residue. Hence, in this study, similar "subunits" must be defined for three HMW foulants in a similar fashion as that of protein as "residues". For polysaccharide, it is intuitive to define each sugar monomer as a residue; for humic substance and building block which were built with VSOMM2, each small block labelled as "HSx" in the modeler is defined to be a residue [51]. Hence, polysaccharide, humic substance, and building block are divided into 10, 7, and 3 residues, respectively, for RMSF calculation.

Trends of RMSF values for different residues in adsorbed HMW foulants are shown in Fig. 4-8. In particular, two scenarios are differentiated for polysaccharide with different colors, namely, laying flat on the HAOPs surface, or anchored on one end. Due to the symmetry in structure, the anchored end was set to be monomer unit #1 for plotting of Fig. 4-8a. Previous MD studies deemed an RMSF value smaller than 3 Å to be low [33, 231], which is the case for most residues in adsorbed HMW foulants as shown by Fig. 4-8. There are two exceptions though: (i) for residues located in the unadsorbed half of polysaccharide, when only one terminal was anchored to the HAOPs surface, which are the light blue bars #6 to #10 in Fig. 4-8a; and (ii) for residue HS17 in humic substances. The former is expected since these sugar units are the free end of the partially adsorbed polysaccharide chain. The latter residue HS17 turns out to be four alkyl -CH2- groups without any other functional groups. The simple structure of HS17, which serves as a bridge between bulky (HS12) or rigid residue (HS11), may be the reason why it shows different behavior compared to other residues with larger sizes and more diverse structures. Based on the above RMSF analysis, considering the fact that foulants in bulk liquid tend to have much higher RMSF values, it can be concluded that adsorption by HAOPs significantly reduces the flexibility of EfOM constituents, which further contributes to the effective removal observed in experiments [174, 225], in addition to the energetic and mobility effects discussed in previous sections.

4.3.4 Ion and functional groups effect

Considering the fact that there are quite a number of ions in MD systems (Table 4-1), and all carboxylic groups in EfOM constituents are deprotonated, how these cations interact with negatively charged foulant and neutral HAOPs is worth of investigation. Ionic effect is often studied by computing RDF which is defined by Eq. (6). Here, it is chosen to calculate RDF between carboxylic oxygen atoms in foulants and monovalent ions (Na^+ and K^+)/divalent ions (Mg^{2+} and Ca^{2+}), as shown in Fig. 4-9. It is evident that divalent ions were strongly coordinated with EfOMs with a dominant first solvation shell located at around $r = 4.25$ Å, which was also observed in past studies [37, 102].

In contrast, monovalent ions had much weaker coordination with carboxylic group as indicated by the consistently lower RDF values. Furthermore, it was observed that Mg^{2+} and Ca^{2+} ions tended to "bridge" between negatively carboxylic groups in different compounds, which could serve a role of stabilizing the complex near the HAOPs surface. In other words, when HAOPs surface becomes crowded with increasing concentration of foulant, divalent ions in suitable positions serve as the "glue" to stabilize them. Hence, some foulants were still "left behind" in bulk liquid without being adsorbed since there may not be sufficient divalent ions to stabilize all foulants near the HAOPs surface, considering the fact that monovalent ions tend to float around in bulk liquid without interacting strongly with foulants.

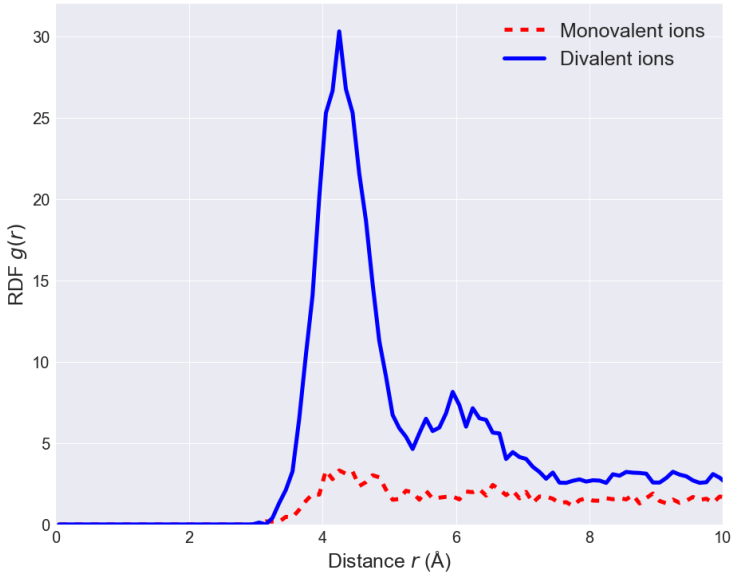

Fig. 9. RDF between carboxylic oxygen atoms in foulant molecules with monovalent ions (Na^+ and K^+) and divalent ions (Mg^{2+} and Ca^{2+}).

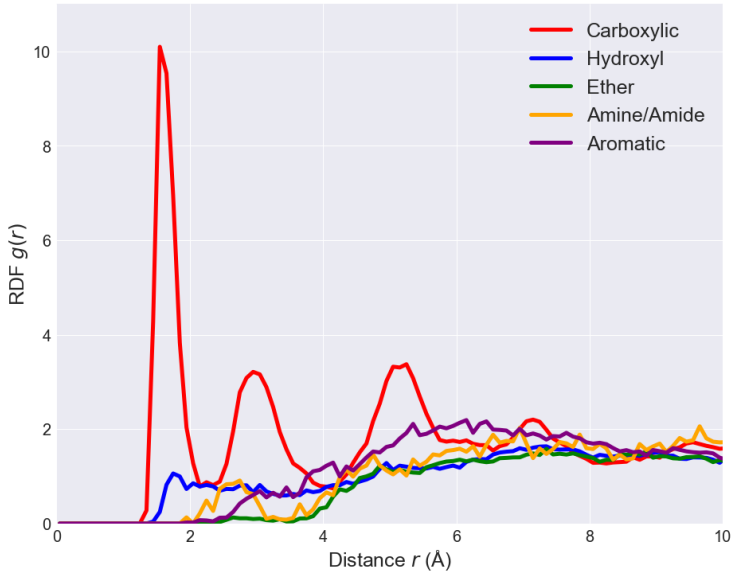

Fig. 4-10. RDF between HAOPs (represented by the surface hydrogen atoms) and different functional groups in foulants. Following atoms were selected to represent functional groups: oxygen atom for carboxylic, hydroxyl and ether groups; nitrogen for amine/amide groups; aromatic carbon for aromatic groups.

Moreover, since the structure of EfOM constituents are known, one question remains that which type of functional groups are primarily responsible for the anchoring of foulants. Fig. 4-10 plots the RDF between HAOPs and representative functional groups of foulants. It is evident that carboxylic group displayed the strongest anchoring, indicated by the significantly higher RDF peak value and closer distance, which is consistent with the visual observation discussed in section 4.3.2. Furthermore, the carboxylic group has shown three distinct peaks at $r = 1.55$ Å, 2.95 Å, 5.25 Å. In other words, the ample number of carboxylic groups present in EfOMs were able to form well-structured shell layers near the HAOPs surface. In comparison, other functional groups exhibited much lower RDF values without any distinctive peaks. Fig. 4-10 clearly shows that carboxylic group plays the dominant role in the adsorption of HMW EfOMs and LMW acids onto the HAOPs surface.

4.4 Conclusions

Although DM is promising in the pre-treatment of RO and HAOPS has been reported as a superior adsorbent compared to the more commonly used PAC, the understanding of the adsorption behavior remained incomplete. In particular, the competitive adsorption of EfOM constituents when the active sites become increasingly saturated is not well-studied. Therefore, this study used MD simulations to unveil the molecular interactions underlying the competitive adsorption behavior of the foulants on HAOPs.Three types of HMW foulants (namely, polysaccharide, humic substance, and building block) and two types of LMW foulants (namely, LMW acids and neutrals) were studied. Except for LMW neutrals, the adsorption is stronger to HAOPs compared to PAC, validating the simulation model. To mimic the competition of foulants, production runs were carried out with more foulants and less HAOPs surface area. The separation distance, interaction energy, mobility, and flexibility characteristics were quantified.

Agreeing with the excellent removal of biopolymer experimentally observed in μGAF, the interaction energy between polysaccharide and HAOPs is the highest. At the molecular level, due to its large size and limited HAOPs surface area, polysaccharide sometimes fails to adopt a flat orientation with all monomer units in close contact with HAOPs when adsorbed. Nevertheless, even if it is only anchored to the surface on one terminal, the polysaccharide still shows reduced mobility and flexibility, which reflects strong adsorption by HAOPs. On the other hand, due to their smaller sizes, building

blocks and LMW acids tend to squeeze through other surrounding foulants to establish stable adsorption on HAOPs. Humic molecules exhibit intermediate behavior, with the mobility and flexibility of adsorbed ones still comparatively low, indicating that HAOPs can still serve as a good adsorbent for humic substances. Moreover, RDF analysis was conducted to reveal ionic and functional group effect related to adsorption. Divalent ions were found to serve a crucial role by stabilizing the foulant complex formed near the HAOPs surface at high concentration. Carboxylic groups in EfOM constituents were identified to be crucial in the anchoring of foulant molecules onto the HAOPs surface.

As the adsorbent saturates, adsorption capacity is expected to lessen. In the case of HAOPs, the atomistic scale results here show that adsorption of the EfOM constituents remain superior even at high foulant concentration.

Chapter 5 – Membrane Fouling by Lysozyme: Effect of Local Interaction

We discussed the adsorption behavior of NOM foulants in the previous two chapters. One constituent of NOM is biopolymer, which we have modelled it as polysaccharide in Chapters 3 and 4. In fact, protein is another important category of biopolymer. It had been excluded in these two HAOPs studies due to its large size and complex nature. Thus, we have dedicated two separate studies that focused on protein fouling in particular. It should be noted that fouling behavior of protein is investigated with respect to polymeric PVDF membrane, rather than HAOPs, in this chapter and the subsequent one. In this Chapter, we presented the first one, which investigated the adsorption behavior of lysozyme in different feed conditions, and highlighted the significance of local interaction.

5.1 Introduction

Protein is one of the key foulants in membrane-filtration applications in industries like water, dairy and pharmaceuticals. Mitigation of protein fouling requires an understanding of the underlying fouling mechanisms. Electrostatic attraction/repulsion and charge shielding effects observed under elevated ionic concentration are generally used to explain the degree of fouling in protein filtration systems [232-235]. However, the interaction between protein and membrane is quite complex, with contributions stemming from charge distribution, molecular flexibility, chirality and geometrical unfolding of the protein macromolecule [166, 236-238]. Moreover, the physiochemical condition of the feed can significantly affect protein-membrane interactions [98, 232, 235, 239, 240], including electrostatic interactions [232, 241], hydrophobic interactions [98, 239, 240] and hydration forces [234, 242]. Breite et al. found that, unlike the model polystyrene foulant, fouling induced by BSA and lysozyme on zwitterionic PES membranes cannot be explained by either electrostatic or hydrophobic interactions [239]. Another study investigated the fouling of composite multiwall carbon nanotube (MWCNT) and PES membranes by BSA and lysozyme over a range of pH and ionic concentrations, and found that fouling was governed by either foulant-membrane interactions, foulant-foulant interactions, or sometimes both [232]. While it was identified that the MWCNT membrane performance was highly sensitive to the feed properties, especially in the cases of lysozyme or mixed proteins, the governing fouling mechanism was not clear [232]. In situ characterization confirmed the validity of a two-stage fouling model (i.e., internal then external fouling) [243], but the resolution was

not sufficient for capturing local behaviors to explain the underlying mechanisms for the different proteins. Collectively, experimental results indicate that fouling mechanisms for proteins are not easily interpreted or predicted based on overall characterization of the protein size and charge, primarily due to the overlap and competition of different mechanisms and the importance of local interactions [239]. This suggests that a more detailed evaluation of the phenomenon at the protein-membrane interface is necessary to better identify the fouling mechanisms.

To this end, MD simulations are useful and have been employed to provide mechanistic insights on membrane fouling at the molecular level [19, 24, 194], which is not possible experimentally. It should be noted that MD simulations are unable to account for effects known to affect protein fouling like membrane roughness, flux-induced mixing at the interface and deformation of proteins [244, 245], because the length and time scales are far beyond the current scale of MD simulations [194, 236]. Shaikh et al. [34] studied the adsorption behavior of BSA onto a PVDF membrane at pH 7, and found that increasing the chloride ion (Cl^-) concentration delays the adsorption. Mucksch and Urbassek [246] studied free and forced adsorption of BSA onto a graphite surface, illustrating the unfolding and spreading process of BSA via hydrophobic forces. Furthermore, the adsorption of protein/peptide onto a silica surface was found to be very dependent on local interactions [98, 125, 165, 247]. Specifically, it was revealed that the arginine group is important for the anchoring of a short peptide chain to the silica surface, with electrostatic interactions being the main driving force and hydrophobic interactions contributing moderately [125]. Moreover, higher salt concentration tends to slow down the adsorption process but does not alter the mechanism. The adsorption of a negatively charged BSA molecule onto a negatively charged silica surface was disclosed to be via a unique orientation while preserving the secondary structure of BSA [98, 165]. More specifically, during the adsorption of BSA, the lysine group was identified to be crucial for penetration into the water layer near the silica surface, allowing negatively charged subdomains of the protein to orientate above the ionic screening layer generated by Na^+ near the membrane surface. These MD simulation results highlight the importance of local structure and interactions. Due to the complex structure of the macromolecular protein, some subdomains inevitably carry charges different from that of the overall charge measured experimentally based on the electrophoretic mobility, and these local charges may exert a more significant influence on membrane fouling.

Experimental efforts fall short of revealing the angstrom-scale effects, and the importance of protein orientation and local interactions on the extent of adsorption. In

this study, unbiased (i.e., no external force) MD simulations were performed to understand the local interactions between positively charged lysozyme and a negatively charged PVDF membrane for different feed conditions. Our hypothesis was that local interactions are more important than the net charge in influencing lysozyme adsorption to the membrane. Lysozyme adsorption was studied under three pH and two ionic strength conditions, with six initial lysozyme orientations examined in each case. The evolution of the lysozyme-membrane separation distance was assessed, followed by evaluating the probability of adsorption in each feed. Then, the key anchoring sites on lysozyme were identified, along with the adsorption mechanisms. After that, the adsorption angles were calculated and correlated with adsorption probability. Finally, the interfacial interaction energies, namely, lysozyme-membrane, lysozyme-water, and interactions with ions, were derived. This study advances the understanding of membrane fouling by proteins at different feed conditions by providing molecular-level insights on the local interactions.

5.2 Methods

5.2.1 Experimental measurement of membrane zeta potential

PVDF membranes (Durapore, VVLP04700, pore size 0.1 μm) were purchased from Millipore. Zeta potential values were determined with a Surpass 3 (Anton Paar), with the PVDF membrane submerged in an electrolyte solution. Measurement was first conducted in 0.01 M sodium chloride (NaCl) solution at the neutral pH of 7. To account for the effect of pH, two subsequent measurements were carried out by adjusting the solution pH to 4 and 9.5 by adding hydrochloric acid (HCl) and sodium hydroxide (NaOH), respectively. As expected, the PVDF membrane was negatively charged due to the C-F moiety [248], with the zeta potential magnitudes increasing with increasing pH (-11.9 mV, -21.1 mV, -26.4 mV at pH = 4, 7, 9.5, respectively).

5.2.2 PVDF membrane structure

An amorphous PVDF membrane structure was constructed by packing 342 pentamer chains into a slab-like geometry with dimensions of approximately 100 Å length by 100 Å width by 10 Å depth. The resultant structure corresponds to a density of 1.75 g/cm^3, which agrees with the experimental value of 1.76 g/cm^3 [249]. This structure is the same as that in a previous study [36]. The force field parameters of PVDF were adopted from an earlier study [250].

For different pH values, the partial charges of atoms on the PVDF membrane were scaled to account for the different zeta potential values. Specifically, (i) the partial charge of all carbon atoms and fluoride/hydrogen atoms in the functional groups of -CF_2- and -CH_2- were kept unchanged as per an earlier report [242]; (ii) the charge of hydrogen in the methyl group was calculated based on Density Functional Theory (DFT); and (iii) the charge of fluoride in the -CF_3 group was adjusted based on the Grahame equation [251]:

$$\sigma = \sqrt{8c_0\varepsilon\varepsilon_0 k_B T}\sinh\left(\frac{e\psi_0}{2k_B T}\right) \quad \text{Eq. (36)}$$

where σ is surface charge density per unit area, c_0 is the overall number concentration of ions, ε is the relative permittivity of water, ε_0 is the permittivity of vacuum, k_B is the Boltzmann constant, T is temperature in Kelvin, e is the elementary charge of an electron, and ψ_0 is the measured surface potential.

5.2.3 Lysozyme structure and charge

The three-dimensional (3D) lysozyme structure was obtained from the Protein Data Bank (PDB ID 253L) [252] with ligands deleted. It should be noted that different lysozyme structures are available in the PDB as well as in the literature; the MD simulations may vary somewhat depending on the exact amino acid constituents and sequence [247]. This lysozyme structure was selected since it originates from Escherichia coli, which is commonly encountered in water treatment [253, 254]. The CHARMM36m force field [255, 256] was used in the simulation, with the protonation process for lysozyme carried out using CHARMM-GUI [66]. Specifically, the protonation states of acidic and basic amino acids were determined based on the pH and pK_a values of the side chains and terminal -NH_2/-COOH groups. CHARMM-GUI allows the manipulation of the protonation state of these five amino acid groups, namely, ASP and GLU, which are acidic with carboxylic acid groups in the side chain; and LYS, CYS, and HIS, which are basic with amine group, thiol group and imidazole ring in the side chain, respectively. ARG is consistently positively charged for all cases investigated here due to its high pK_a value of 12.48 [257]. The overall charge values of lysozyme under different pH conditions were calculated by summation over the amino acids plus terminal -NH_2/-COOH groups.

The pK_a values of the various groups in lysozyme used for calculation, along with the number of each amino acid residue. For all three pH values investigated in this study, lysozyme is positively charged. As a validation of the model, lysozyme has a slight

negative charge at pH values higher than 10.75, which agrees well with the experimental isoelectric point (IEP) of 10.4 [232] – 10.7 [258].

5.2.4 Simulation procedure

The PVDF membrane was fixed at the bottom of a three-dimensional periodic simulation box, and around 30,000 TIP3P model water molecules were added to correspond to a system density of 1 g/cm^3 [259]. The lysozyme molecule was placed approximately 10 Å above the PVDF membrane. Considering the large size and structural heterogeneity of lysozyme, different initial orientations of the lysozyme were considered. Six initial orientations were used, because too few may not be sufficiently representative since lysozyme may be trapped in metastable states [245], while too many would incur high computational costs. As illustrated in Fig. 5-1, other than the orientation shown (i.e., as downloaded from the PDB and designated $a_x = 0^o$, $a_y = 0^o$), three additional rotations about the *x*-axis (i.e., $a_x = 90^o$, $a_y = 0^o$; $a_x = 180^o$, $a_y = 0^o$; and $a_x = 270^o$, $a_y = 0^o$) and two additional rotations about the *y*-axis (i.e., $a_x = 0^o$, $a_y = 90^o$; and $a_x = 0^o$, $a_y = 270^o$) were investigated, similar to an earlier study [115]. These six orientations were selected to ensure a good coverage of lysozyme surface as shown in Fig. 5-1, so that membrane can be accessible to each part of the molecule. For the quantification of parameters such as interaction energy or rotational angle, the average value was taken from these six runs.

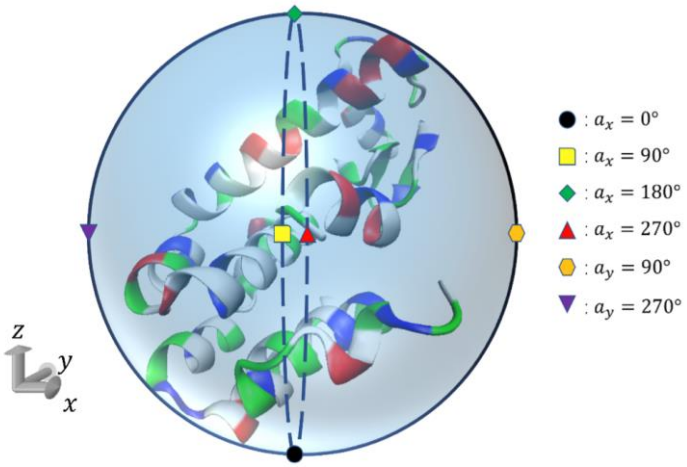

Fig. 5-1. Schematic diagram illustrating the lysozyme molecule in the pristine state as downloaded from the PDB. An imaginary sphere is drawn around the molecule for visualization purpose. Points on the sphere represent the initial close-contact points with the PVDF membrane at different orientations. The colors on lysozyme represent the nature of the amino acids: white for non-polar, blue for basic, red for acidic and green for polar.

Four initial feed conditions were investigated [247], namely, two ionic concentrations (i.e., 0.01 M and 0.1 M) at pH 7, and three pH values (i.e., 4, 7 and 9.5)

at the same salt concentration of approximately 0.01 M. To vary the ionic strength, different number of sodium and chloride ions were solvated at random initial positions, with the number of ions determined in the following way: (i) Na^+ ions were added to balance out the negative charges of the PVDF membrane; (ii) Cl^- ions were added to balance out the positive charges of lysozyme; and (iii) more Na^+ and Cl^- ions were added as necessary to achieve the targeted ionic strength. To reflect the variation of pH, the charge distributions on both membrane and lysozyme were adjusted. The total number of simulation runs was 24, consisting of four feed conditions and six initial orientations (Fig. 5-1). All MD simulations were run using LAMMPS [76], with visualization and post-processing facilitated by the VMD software [53]. Pair-wise non-bonded interactions in LAMMPS were set with "lj/charmm/coul/long" style with an outer cut-off distance of 10 Å, which is in line with other MD studies on proteins [34, 260]. The PPPM Ewald method was used for computing long-range electrostatics beyond this cut-off in reciprocal space. For consistency, CHARMM force field parameters were used for both water and ions. The SHAKE algorithm was applied to all bonds involving hydrogen [98, 260]. To stabilize the system, energy minimization was performed first with a canonical ensemble (NVT) run at 30 K for 100 ps, followed by another NVT run to bring the system up to room temperature (298 K), after which the system was relaxed at 298 K by another 500 ps NVT run. An equilibration run (i.e., 1 ns isothermal-isobaric NPT ensemble at 298 K and 1 bar) ensued with temperature and pressure controlled by Nosé-Hoover thermostat and barostat, respectively [36, 55, 109]. The coupling time constants for the barostat and thermostat were 500 fs and 100 fs, respectively [94]. Finally, production runs were performed for 40 ns to assess if the lysozyme preferentially adsorbed onto the PVDF membrane during that time frame [24] . The duration was selected based on the trade-off between computational cost and amount of dynamic information gained. The time steps for all runs were fixed at 1 fs, with a snapshot taken every 0.04 ns for analysis. The CPU time used for one single run was approximately 6.6 million hours, which corresponds to a real-world time of roughly 12 days.

5.3 Results and Discussion

5.3.1 Membrane-lysozyme distance

One way of identifying whether lysozyme has adsorbed onto the membrane is to check its position relative to the membrane surface. To achieve this, a separation distance *d* between the two entities was evaluated as a function of time, defined as:

$$d = \min(z_{upper} - z_{max}, z_{min} - z_{lower}) \quad \text{Eq. (37)}$$

where z_{min} and z_{max} represent the minimum and maximum z-coordinate of any atom in lysozyme, z_{lower} represents the maximum z-coordinate of any atom in the PVDF membrane placed at the bottom of the simulation box, and z_{upper} represents the minimum z-coordinate of any atom in the top mirror image of the PVDF plane. Fig. 5-2 displays the d versus time trends for all six initial lysozyme orientations in each of the four feed conditions. While the protein-membrane separation was set as 10 Å initially for all simulations, the initial d values in Fig. 5-2 are dissimilar due to the energy minimization, relaxation and equilibration steps that were applied prior to the 40 ns of production run displayed in Fig. 5-2. Also, the fluctuations are due to the analysis of snapshots every 0.04 ns.

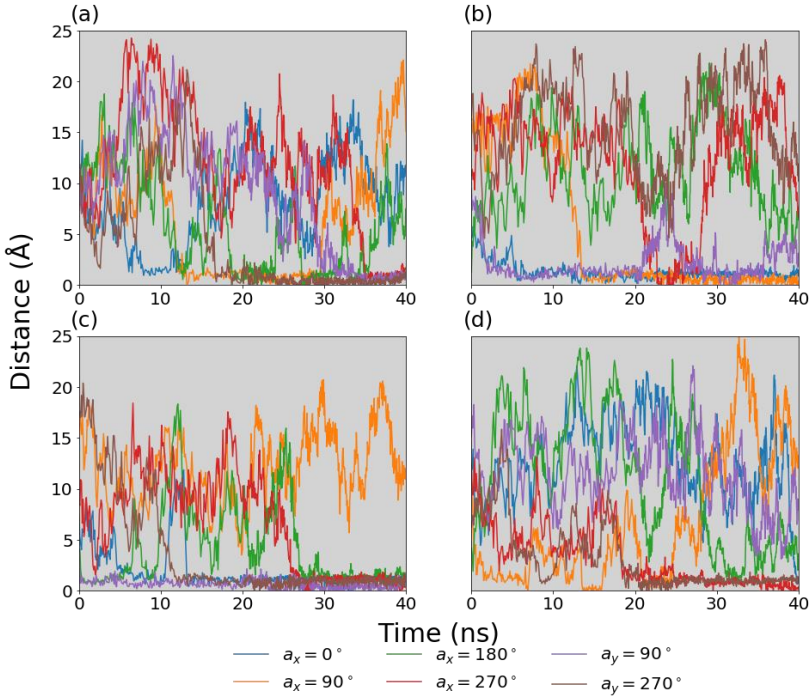

Fig. 5-2. Plots of the distance between the lysozyme and membrane (d) versus time for the four different feeds with six initial orientations each: (a) pH = 4 and low ionic strength ('Acidic'); (b) pH = 7 and low ionic strength ('Neutral'); (c) pH = 9.5 and low ionic strength ('Basic'); and (d) pH = 7 and high ionic strength ('Salt'). Distance are computed for each snapshot saved from LAMMPS within the 40 ns production run. Variation in the separation distance value at t = 0 of each subplot is the result of energy minimization, relaxation and equilibration run conducted before the production run. Initial protein-membrane separation distance is similar for all individual runs at the very beginning. The fluctuations are due to the analysis of snapshots every 0.04 ns.

Clearly, the evolution of d differs significantly between runs in spite of the same solution conditions, indicating that the initial orientation has a strong effect on the results. For each feed, instances of adsorption (i.e., d values close to 0) and no adsorption (i.e., large d values) are evident, with the adsorption or lack thereof being

relatively stable throughout most of the 40 ns in some cases while more transient in other cases. Taking the feed of pH 7 and low ionic strength ('Neutral'; Fig. 5-2b) for instance, (i) the *d* values remain relatively small for the initial orientations of $a_x = 0^o$ and $a_y = 90^o$, and low for the latter half of the duration for $a_x = 90^o$, indicating affinity between the lysozyme and membrane; (ii) the *d* values are the highest for the initial orientation of $a_y = 270^o$, followed by $a_x = 180^o$, indicating lack of lysozyme-membrane affinity; and (iii) the *d* values are low some times and high at other times for the initial orientation of $a_x = 270^o$, indicating weak affinity and transient adsorption. Therefore, Fig. 5-2 demonstrates that, even for the same feed condition, different orientations of such macromolecular foulants lead to different short-time adsorption tendencies arising from different local interactions. While the limited spatial and time scales in MD simulations impede direct linkage of these results to experimental observations, it should be noted that the molecular-scale insights obtained here are not possible through experiments and serve to provide some explanation on why experimental studies indicate that feed conditions alone do not predict membrane fouling [232, 239, 242].

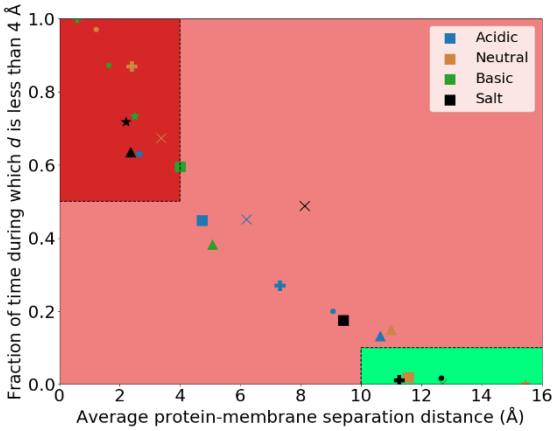

Fig. 5-3. Scatter plot depicting all 24 independent runs of lysozyme based on average membrane-protein separation distance and fraction of time adsorbed. The three colored regions represent different adsorption scenarios, namely, red, light red and green represent stable adsorption, transient adsorption and no adsorption, respectively.

To compare lysozyme adsorption under different feed conditions, the time-averaged *d* values of all 24 simulations are computed. The lower the mean *d* value is, the closer the lysozyme stays to the membrane, and thus the greater the underlying lysozyme-membrane affinity. Based on the calculated values, it appears that stable adsorption is tied to time-averaged *d* values of less than 4 Å. Correspondingly, adsorption fractions (i.e., duration whereby *d* is below the threshold of 4 Å compared to the total simulation time of 40 ns) for each of the 24 simulation runs were evaluated, with results presented in Fig. 5-3. Clearly, the adsorption behavior can be classified into three main categories,

namely, (A) stable adsorption, which corresponds to high adsorption fractions of greater than 0.5 and low average *d* values of below 4 Å; and (B) no adsorption, which corresponds to low adsorption fractions of below 0.1 and high average *d* values of above 10 Å; and (C) transient adsorption, which falls between the two categories. Despite the macroscopic charge affinity, the positively charged lysozyme adsorbs onto the negatively charged membrane as little as 34% of the time, highlighting the importance of local interactions. This underlies why reported results on the effect of ionic strength on fouling have been so inconsistent [234, 242, 261-263].

5.3.2 Anchoring amino acids

Macroscopic parameters such as zeta potential are often used in experiments to predict or explain protein fouling. However, Figs. 5-2 and 5-3 provide evidence that overall electrostatic considerations are insufficient for accurately predicting lysozyme-membrane affinity, implying that local interactions play significant roles in governing the adsorption or lack thereof. Because 164 amino acid residues make up the lysozyme molecule, with some being charged and some not [264], different parts of the molecule inevitably have different affinities with the membrane. In this study, an attempt was made to identify the amino acids that preferentially anchor onto the membrane, as defined by an amino acid group in which at least three atoms are within 4 Å from the membrane surface. Based on all trajectories where lysozyme has preferentially adsorbed to the membrane, either stably or transiently, seven key sites on the lysozyme molecule were identified, as depicted in Fig. 5-4a. It should be noted that the lysozyme in Fig. 5-4a is oriented differently than in Fig. 5-1 to more clearly show all seven adsorption sites. Three of the adsorption sites are not visible in Fig. 5-1 since they are on the back side of the protein. In order to examine the relative importance of these residues on adsorption, the total adsorption time for each site under the four feed conditions are plotted in a stacked bar chart in Fig. 5-4b. Fig. 5-5 depicts the representative zoomed-in snapshots of different anchoring sites and their corresponding adsorption mechanisms are discussed in the following.

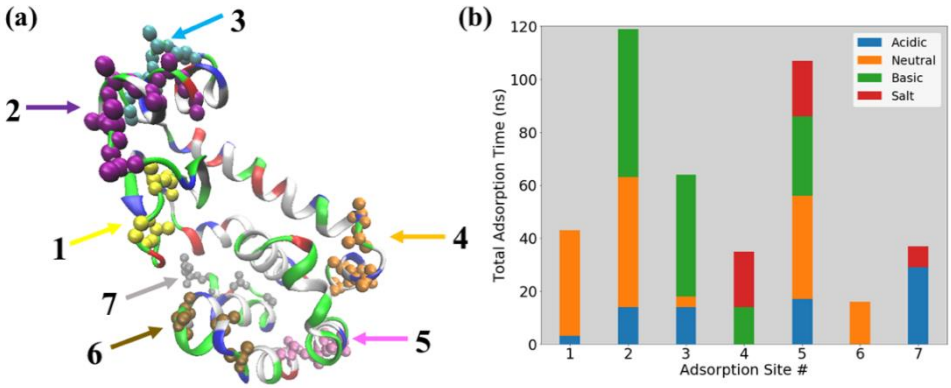

Fig. 5-4. (a) Spatial distribution of seven adsorption sites identified in the lysozyme molecule. Carbon and nitrogen atoms on the backbone of these identified residues are highlighted as spheres with various colors. The remaining lysozyme backbone structure is drawn with the ribbon-like "NewCartoon" style in VMD to display secondary structures. (b) Stacked bar chart showing the total adsorption duration for each adsorption site under different feed conditions. Different colors represent different feed conditions.

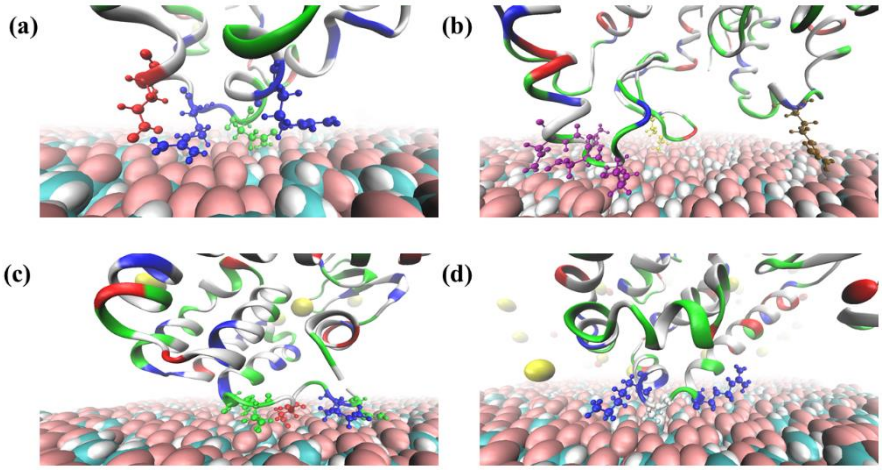

Fig. 5-5. Zoomed-in view of lysozyme adsorption sites when it is in close contact with the PVDF membrane at different conditions: (a) Site 5: 'Neutral', initial lysozyme orientation of $a_x = 0°$, $t = 16$ ns. (b) Site 2: 'Basic', initial lysozyme orientation of $a_y = 90°$, t =20 ns; (c) Site 7: 'Acidic', initial lysozyme orientation of $a_y = 270°$, $t =$ 30 ns; (d) Site 4: 'Salt', initial lysozyme orientation of $a_x = 270°$, $t = 25$ ns. The different colors on the membrane represent different elements: cyan for carbon, white for hydrogen, and pink for fluoride. Water molecules are all hidden for easier visualization. The backbone of lysozyme is shown with the ribbon-like structure ("NewCartoon" style in VMD), and the secondary structure is determined by the default algorithm. Sodium ions and chloride ions are depicted as red and yellow spheres, respectively. For (a), (c) and (d), the anchoring amino acids are displayed in ball-and-stick style and colored based on their type: white for non-polar, blue for basic (positively charged), red for acidic (negatively charged) and green for polar. For (b), since there are multiple adsorption sites involved, with Sites 1,2 and 6 colored in yellow, purple and brown, respectively.

It is clear from Fig. 5-4b that different adsorption sites are responsible for adsorption under different feed conditions. Notably, Site 2 and Site 5 appear to be the most dominant ones for adsorption, as evident by the highest adsorption durations. Distinct differences exist for these two Sites though. Site 5 is the only site that appears at all four

feed conditions. It contains positively charged residues LYS124 and ARG125, which drives electrostatic attraction to the membrane for adsorption. As shown in Fig. 5-5a, the neighboring negatively charged GLU128 can also be brought close to the negatively charged membrane. This highlights the dominant role of electrostatic attraction due to the LYS and ARG residues, as well as the interactions with neighboring residues. The local bridging of negatively charged resides with nearby anchored positively charged residues can be an important factor to further worsen fouling.

In comparison to Site 5, Site 2 exhibits different adsorption characteristics. Specifically, Site 2 consists of neutral amino acid residues, indicating electrostatic attraction is not a key influence for this site. As shown in Fig. 5-5b, Site 2 anchors by synergy with other Sites, namely, Sites 1 and 6 in this case. More specifically, Site 2 is the main anchoring point on the membrane, while the lysozyme structure orients such that part of the long side chain in Sites 1 and 6 interact with the membrane simultaneously. Therefore, Site 2 plays a critical role as the hinge between different sites when aligned properly, which significantly affects adsorption [264]. These results provide more insights into fouling being governed by local interactions of a few key sites rather than the overall protein characteristics.

Fig. 5-4b also indicates that each feed condition can lead to different preferential anchoring points on lysozyme. For example, Site 7 is prominent in governing adsorption for the ‘Acidic’ case, Site 6 is dominant for the ‘Neutral’ case, while Site 4 plays an important role in adsorption for both ‘Basic’ and ‘Salt’ cases. Fig. 5-5c shows the anchoring of Site 7 for the ‘Acidic’ case. Adsorption at this point is quite strong, with the total lysozyme-membrane interaction stabilizing at a significant -120 kcal/mol. Despite the large attraction energy, Site 7 is not a common anchoring point, mainly because it is located at one terminal of lysozyme, which is less accessible to the membrane compared to other portions of the lysozyme.

A closer look at the ‘Salt’ case is warranted, particularly in view of the well acknowledged charge screening effect in diminishing electrostatic interactions. In this case, Site 4 is a dominant adsorption site (Fig. 5-4b), which also manifests for the ‘Basic’ case. Fig. 5-5d displays the zoomed-in view of the anchoring of Site 4 onto the membrane. Notably, Site 4 also contains a few positively charged amino acids (namely, ARG80, LYS83, and LYS85) expected to form strong electrostatic interactions with the membrane, and the long side chain of LYS also extends out from the backbone to interact with the membrane. Also, Fig. 5-5d shows that quite a few Cl^- ions are in close proximity with the positively charged amino acid residues at this adsorption site. While ions exhibit quite high mobility in solution throughout the simulation runs, their

presence particularly near the anchoring of lysozyme serves to reduce the electrostatic interaction between the lysozyme and membrane, thereby reducing the interaction energy. This provides a molecular-level view of the "charge screening" effect observed in experiments.

In summary, this section underscores the importance of considering local interactions in understanding membrane fouling by such macromolecules especially in different feed conditions. Multiple adsorption sites are identified, with some of them responsible for anchoring in all feed conditions while others are dominant in specific feed conditions, indicating that pH and ionic strength have significant impact on the local interactions that govern adsorption.

5.3.3 Adsorption angle

Apart from identifying the anchoring amino acid groups, the rotational freedom of lysozyme can shed some light on the relative ease of adsorption. In earlier studies of lysozyme adsorption onto a surface, the concept of and calculation method for adsorption angles with respect to the principal axis were proposed [31, 119], and it was found that lysozyme tended to land onto the surface on its side, with adsorption angle θ fluctuating near 0°. In the current study, θ is similarly defined as the angle between the normal vector of the membrane surface and the vector pointing outward from the COM of lysozyme toward amino acid residue ASN163.

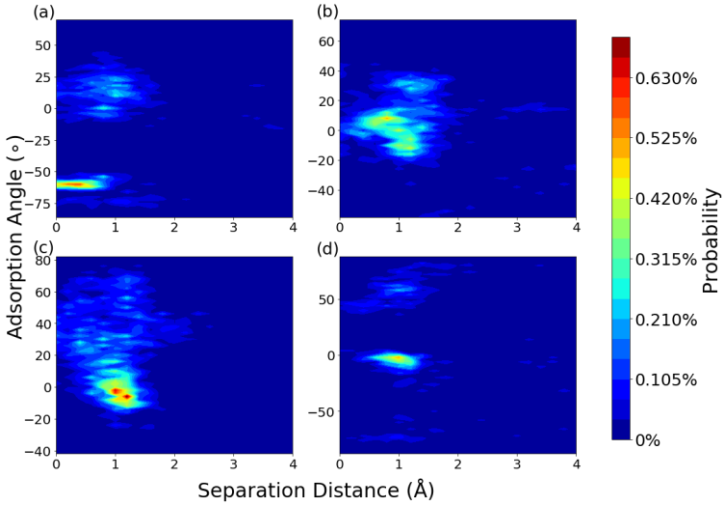

Fig. 5-6. Probability contour maps of adsorption angle versus separation distance *d* for different feed conditions: (a) 'Acidic'; (b) 'Neutral'; (c) 'Basic'; and (d) 'Salt'.

Fig. 5-6 displays the probability contour maps of adsorption angle versus separation distance for the four different feed conditions. The four maps are distinctly different, affirming the significant influence of pH and ionic strength on lysozyme adsorption. The smaller areas of high probabilities, which implies restrictive angles of adsorption,

are shown in Figs. 5-6a and d for the cases of 'Acidic' and 'Salt', respectively. In both cases, the probable orientations are approximately around $|\theta| = 0°$ and $60°$. Such limited adsorption angles are associated with lower adsorption fractions (Fig. 5-3), which agrees with an earlier study based on coarse-grained protein-surface calculations and with the well acknowledged effect of charge screening at high ionic strength conditions [264]. On the other hand, the more spread out clusters of high probabilities, which reflects greater flexibility in adsorption, are observed in Figs. 5-6b and c for the cases of 'Neutral' and 'Basic', respectively, whereby lysozyme is likely to adopt orientations of between $\theta = -20°$ to $50°$ upon adsorption. This relatively wide range of adsorption angles is tied to higher adsorption fractions, which indicates greater adsorption tendency and also a greater variety of adsorption sites (Fig. 5-4b). Therefore, Fig. 5-6 highlights that (i) a wider range of adsorption angles reflects more freedom in adsorption, giving greater adsorption tendency; while (ii) the more restrictive adsorption angles is tied to the greater probability of no adsorption. This agrees with earlier studies that entropic driving force plays an important role in adsorption [265], and increased rotational freedom favors adsorption due to the decreased conformational entropy loss during the adsorption process [264].

5.3.4 Interaction Energy

Interaction energy has become increasingly popular in explaining membrane fouling [13]. In this study, three types of interactions were analyzed, namely, membrane-lysozyme, water-lysozyme, and interaction with ions. They were all computed by LAMMPS based on CHARMM force field parameters.

5.3.4.1 Membrane-lysozyme

The interfacial interaction between the membrane and foulant has received tremendous attention in membrane fouling studies [13]. The distinction between adsorption and lack thereof is whether there is sustained negative VDW interaction energies that are more short-ranged than electrostatics. For the no adsorption case, although the periodically negative values of the total energy indicate periodic attraction, Fig. 5-2 shows that the lysozyme does not get close enough to the membrane for adsorption. This highlights that the heterogeneity and different preferential affinities by different amino acid residues causes transient attractive energies, which are not necessarily tied to adsorption. While fouling by more ideal, uniformly charged colloidal foulants tends to agree with simple interaction energy models [13, 222], a mis-match between interaction energy and extent of membrane fouling has earlier been reported

for an experimental study on surfactant stabilized oil emulsions [223, 224], which suggests that local interactions play a dominant role in dictating fouling for more complex foulants [264].

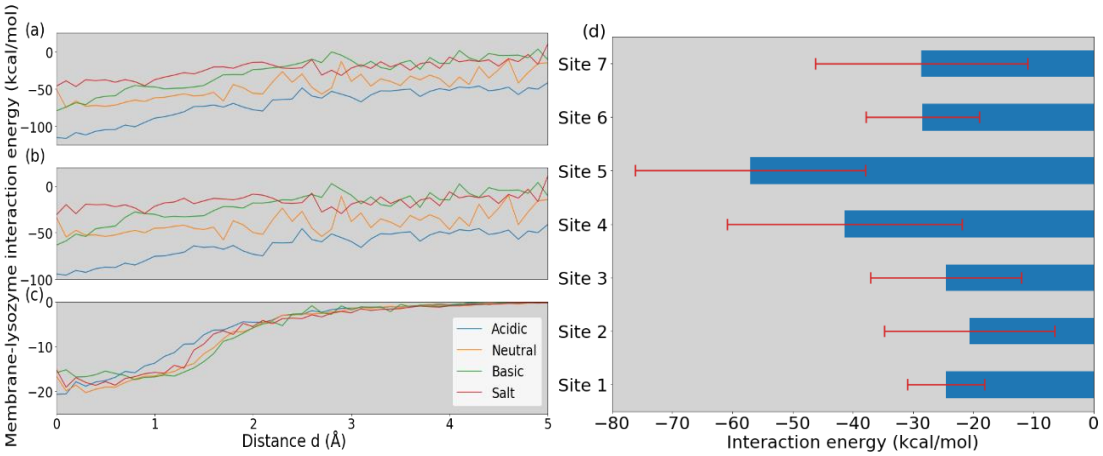

Fig. 5-7. Average membrane-lysozyme interaction energy versus separation distance d: (a) total; (b) electrostatic component; and (c) VDW component. The fluctuations are due to the high spatial resolution of 0.1 Å. (d) average lysozyme-membrane interaction energy during adsorption for each anchoring site. Red error bars stand for standard deviations.

Figs. 5-7a to c show plots of membrane-lysozyme interaction energies versus membrane-lysozyme separation distance for the region near the membrane surface ($d \leq 5$ Å). The data are the unbiased averages [129, 150] of the six initial lysozyme orientations at each feed condition, and the fluctuations are because of the high spatial resolution of 0.1 Å. Two noteworthy observations are described as follows. Firstly, whereas the long-range electrostatic component gives relatively flat profiles with respect to *d* (Fig. 5-7b), the short-range VDW component steeply plunges in magnitude as the lysozyme molecule approaches to within 3 Å of the membrane (Fig. 5-7c). The electrostatic component is distinctly the least attractive for the case of 'Salt' due to charge screening effects. Secondly, with respect to the total interaction energy (Fig. 5-7a), the magnitudes are somewhat surprisingly not straightforwardly tied to the adsorption fraction in Fig. 5-3. This implies that, other than the overall strength of membrane-lysozyme interaction energies, other local factors are at play that prevent or encourage adsorption. Some of the factors, like the exact anchoring site and the orientation freedom obtained from adsorption angle distribution, have already been analyzed in the earlier sections. To better understand the contribution of each adsorption site (Fig. 5-4), the interaction energy is further decomposed with respect to each adsorption site and shown in Fig. 5-7d. Sites 4 and 5 have higher interaction energies than the rest of the five sites that exhibit more comparable magnitudes, suggesting that

specific anchoring of the lysozyme onto the membrane plays an important role in determining the strength of adsorption.

5.3.4.2 Water-lysozyme

The interaction energy between water and lysozyme reflects the extent of hydration of the lysozyme molecule. The energies are attractive, which indicates the preferential hydration of the lysozyme molecule. Fig. 5-8 comprehensively illustrates all the runs and data points through a scatter plot of water-lysozyme interaction energy versus separation distance between the lysozyme and membrane (d). Two highlights are noted. Firstly, the water-lysozyme interaction energies in each case are approximately constant with d, indicating the lack of correlation between extent of hydration of the lysozyme molecule and proximity of the lysozyme molecule to the membrane. This implies the extent of hydration of lysozyme is not directly correlated with adsorption or lack thereof. Secondly, the stratification of the different conditions is obvious, indicating the significant influence of pH and ionic strength on the water-lysozyme interaction energy. As pH or ionic strength increases, the water-lysozyme interaction energy becomes less negative, indicating less extensive hydration of the lysozyme. The most and least attractive water-lysozyme interactions are for the cases of ‘Acidic’ and ‘Salt’, respectively, which correspond to lower adsorption fractions in Fig. 5-3.

Therefore, regarding water-lysozyme interaction, pH and ionic strength affect the magnitude of the energy, while adsorption of lysozyme onto the membrane causes the energy to become less negative with time. However, the energy magnitude alone is not a predictive indicator of the tendency for lysozyme to adsorb onto the membrane.

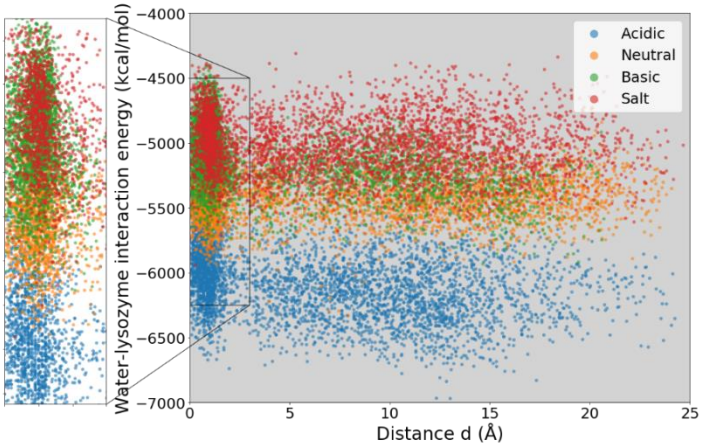

Fig. 5-8. Scatter plot of water-lysozyme interaction energy versus separation distance between the lysozyme and membrane (d), consisting of data collected from all simulation runs.

5.3.4.3 Interaction with ions

The influence of ions on local lysozyme-membrane interaction is seen in Fig. 5-5d. To further understand the effect of ions, the interaction energy between ions and the lysozyme molecule, as well as between ions and the membrane, are quantified. Earlier MD simulation studies have reported that higher ion concentrations delay the adsorption of the protein to the surface [125, 247]. Table 5-1 summarizes the means and standard deviations of the four pairs of interaction energies, for the cases of low and high ionic strengths at pH 7. Note that (i) the number of ions for the case of high ionic strength is ten times that of the low ionic strength condition; and (ii) the dominant component in the interaction energy is the longer-range electrostatics since the highly mobile ions tend to be in the bulk liquid rather than in close contact to the lysozyme or membrane.

Regarding interaction with ions, Table 5-1 reveals the following. Firstly, all the interaction energies are negative, indicating attractive interactions between all pairs. This implies that charge screening effects are at play, which in turn are expected to mitigate membrane fouling [34, 165, 242]. Although lysozyme is overall positively charged, the interaction with Na^+ is attractive, suggesting that local regions of negative charges are important, which is attributable to the high mobility of Na^+ that facilitates avoidance of repulsive local regions. Secondly, the interaction with ions is much less negative in the low ionic strength condition due to the order of magnitude lesser number of ions present in the system. Thirdly, at the higher ionic strength condition, the lysozyme molecule is more attracted to Cl^- than Na^+, while the membrane is more attracted to Na^+, which is due to affinity between opposite charges. The relative interactions with Cl^- and Na^+ are not as clear at low ionic strength because of more diffuse ions. Fourthly, the affinity between lysozyme and the ions is an order of magnitude greater than that between the membrane and the ions. Notably, the clear attractive interaction energy between lysozyme and Na^+ underscores local interactions with negative entities on lysozyme.

Table 5-1. Means and standard deviations of interaction energy terms involving ions for the cases of low and high ionic strengths at pH = 7.

Interaction energy	High ionic strength		Low ionic strength	
(kcal/mol)	Mean	Standard deviation	Mean	Standard deviation
Lysozyme - Na^+	-255	173	-61	89
Lysozyme - Cl^-	-320	112	-24	30
Membrane - Na^+	-57	35	-11	14
Membrane - Cl^-	-16	39	-5	12

5.4 Conclusions

The lack of consistent agreement regarding the influence of pH and ionic strength on membrane fouling by proteins motivated the current study. Because fouling by macromolecules appears to be tied to local interactions that are mis-represented by macroscopic characterizations, MD simulations were performed to provide molecular-level understanding of the fouling of a PVDF membrane by lysozyme under three different pH and two ionic concentrations. Our hypothesis was that local interactions are more important than the net charge in determining lysozyme adsorption to the PVDF membrane. Six repeats starting with six different initial orientations of lysozyme were performed for each feed condition. Despite the expected electrostatic attraction between the positively charged lysozyme and negatively charged membrane, results indicate stable adsorption of the positively charged lysozyme on the negatively charged membrane only in 10 out of the 24 simulation runs (i.e., 42%); with the probability of adsorption duration as low as 34%. Furthermore, in spite of the same feed condition, drastic differences are observed in the evolution of the *d* values for the six different initial orientations of the lysozyme. These results demonstrate the importance of local interactions in dictating adsorption of lysozyme made up of 164 amino acid residues.

Seven key adsorption sites on the lysozyme molecule were identified, with each site having unique mechanisms for such preferential adsorption. The following four insights on the adsorption sites are unveiled. Firstly, of the two most universal sites, one anchors due to electrostatics, while the other is not rooted in electrostatics but displays synergy with the other sites. Secondly, some sites are particularly dominant in specific feed conditions, indicating that preferential anchoring is influenced by pH and ionic strength. Thirdly, although one of the two terminals exhibits strong interaction with the membrane, it is not a common adsorption site because it is less accessible to the membrane. Fourthly, ions tend to weaken the anchoring of the adsorption sites particularly when electrostatics govern the adsorption, with Cl^- ions more responsible for the screening than Na^+ due to the more attractive lysozyme-Cl^- energy. Moreover, a wider range of adsorption angles gives higher adsorption fractions, whereas more restrictive adsorption angles are tied to lower adsorption fractions, demonstrating that freedom in adsorption angles tend to promote adsorption. With respect to membrane-lysozyme interactions, sustained negative VDW interaction energies definitively indicate adsorption, while the total interaction energies obtained from unbiased simulations are not well correlated to the probability of adsorption. The importance of the short-ranged VDW energies in correlating with adsorption further affirms that local interactions dominate, while the lack of correlation with the total energies underscores

the inadequacies of macroscopic parameters in dictating membrane fouling by lysozyme. The seven adsorption sites each exhibit different local interaction energies, providing further evidence of the importance of local membrane-protein interactions in governing adsorption. In summary, local interaction of amino acid residues at short distance is the dominant mechanism for lysozyme fouling, which is manifested by specific adsorption sites that establish strong interaction with respect to PVDF membrane by VDW interaction, with ion screening effect comes into play concurrently.

The molecular-level revelations presented here provide some explanation as to why macroscopic characterizations are deficient in explaining membrane fouling by many macromolecules and are expected to be valuable in advancing models as well as experimental designs. Future studies recommended include comparing the results here with that for a negatively charged protein, exploring biased simulations that sample the entire ensemble of molecular orientations and solvent environments, and understanding the impact of protein-protein interactions on the adsorption behavior that becomes increasingly important as surface sites become saturated.

Chapter 6 – Molecular Dynamics Study on Membrane Fouling by Oppositely Charged Proteins

Continuing from the previous chapter which investigates the local interaction occurring at different feed conditions, this chapter compares the MD simulation results of two oppositely charged proteins with respect to a negatively PVDF membrane surface. The surprising more severe fouling of negatively charged α-lactalbumin compared to positively charged lysozyme is interpreted by MD from the angle of adsorption site and local interaction.

6.1 Introduction

For the molecular-scale investigations required for unraveling such local interactions, experimental methods are limited, while MD simulations have been shown to be promising [19, 24, 39, 194]. Despite limitations of spatial and time scales, MD simulations are acknowledged to be useful in investigating membrane fouling behaviors particularly with respect to explaining fouling mechanisms and description of interfacial binding energies [19]. Tiwari et. al [118] simulated the interaction between lysozyme and layered GO, and highlighted the difference between RO and FO processes with respect to hydration repulsion, charge screening and Coulombic interactions. Shaikh et al. [34] investigated the effect of ions on the adsorption behavior of BSA onto a PVDF membrane, and showed that adsorption is avoided in the presence of excess ions due to increased hydration repulsion and changes in the diffusion coefficient of BSA. Horinek et al. [266] studied the desorption of peptide chains from a hydrophobic diamond surface, and concluded that the intimate coupling of dispersive and solvation effects are important for adsorption behavior. Our earlier study focused on the adsorption behavior of lysozyme onto the membrane under different pH and salt concentrations, and demonstrated that local interactions are important in affecting lysozyme-membrane interactions [107]. A question that remained unaddressed was the different adsorption behaviors of proteins of positive versus negative net charges, which is what motivated the current study.

To enhance the knowledge base on membrane fouling by proteins, specifically with respect to a more comprehensive understanding on the local interactions, this MD study focused on two proteins, namely, lysozyme and α-lactalbumin, which are oppositely charged (at neutral pH) and similar in size. It should be noted that, although net electrostatic considerations would predict that the positively charged lysozyme would give worse fouling on a negatively charged membrane, several experimental studies

have found that lysozyme had far less fouling potential than α-lactalbumin or other proteins with similar pI as α-lactalbumin [267, 268]. For example, the flux decline of α-lactalbumin was surprisingly found to be roughly twice as fast as that of lysozyme [268]. Although the experimental results have already indicated that the extent of membrane fouling is not directly tied to the net charge of the protein, a clear understanding on the underlying cause remained amiss. Hence, this study was targeted at closing this research gap by comparing the adsorption behaviors of these two oppositely charged proteins in terms of protein-membrane displacement, adsorption probability, anchoring points at which the protein adsorbs onto the membrane, protein-membrane and anchoring site-membrane interaction energies, and protein mobility and amino acid residue flexibility upon adsorption. MD simulations and experiments are complementary tools, because, although experimental filtration entails macroscopic effects (e.g., tangential shear, local surface roughness) that MD simulations cannot account for, experiments conversely are inadequate for unveiling angstrom-scale effects that govern membrane-filtration [39].

6.2 Simulation Methodology

Although the spatial and time scales involved in MD simulations are orders of magnitude smaller than that in experiments, the molecular-scale insights on membrane fouling by proteins revealed are not obtainable through experiments [232, 239, 242]. Since molecular motion inevitably underlies the macroscopic behavior, generating MD trajectories of the protein foulant with respect to the membrane enables description of the adsorption tendency [19].

6.2.1 Molecular structures

Structures of lysozyme and α-lactalbumin are from the Protein Data Bank (namely, 253L and 1A4V, respectively), which is a comprehensive compilation of protein structures that have been experimentally validated [252, 269]. Crystal water molecules associated with these protein structures behave similarly to the surrounding water molecules in the simulation domain. Per earlier MD simulation studies of proteins [270, 271], ligands and water molecules from the original files were deleted, both proteins were protonated at pH = 7 with CHARMM-GUI [66], then the CHARMM36m force field was assigned [255, 256]. The lysozyme and α-lactalbumin structures used in this study have overall charges of +9 e and -7 e, respectively. The degree of ionization of the amino acid constituents at pH = 7, and the corresponding makeup in lysozyme and α-lactalbumin are shown in Table 6-1.

Table 6-1. Charge natures of amino acid constituents at pH = 7, and the corresponding makeup in lysozyme and α-lactalbumin.

	Amino acid	Number of amino acid residue in lysozyme	Number of amino acid residue in α-lactalbumin
Acidic	ASP	9	12
(negatively charged)	GLU	8	8
Basic	ARG	13	1
(positively charged)	LYS	13	12
Polar (neutral)	ASN	12	4
	CYS	0	8
	GLN	5	7
	HSD	1	2
	SER	7	8
	THR	12	7
	TYR	6	4
Nonpolar (neutral)	ALA	16	5
	GLY	11	6
	ILE	10	12
	LEU	16	14
	MET	5	2
	PHE	5	4
	PRO	3	2
	TRP	3	3
	VAL	9	2
Overall charge (e)		+9	-7

The PVDF membrane structure, which is the same as that in our previous studies [36, 94], was obtained by packing and equilibrating 342 pentamer short chains into a 105 $Å^3$ space (i.e., 100 Å length by 100 Å width by 10 Å depth), resulting in a density of 1.75 g/cm^3 that agrees with experimental characterization [36]. Note that the membrane is not porous, since the typical pore size of the UF membrane is beyond the spatial scale of MD simulations, but the insights on molecular-scale protein-membrane interaction behaviors that underlie membrane fouling are nonetheless useful. The force field is the same as that in Lachet et al. [250].

6.2.2 Simulation domain setup

Fig. 6-1 displays a representative snapshot of the initial conditions for the simulation domain (dimensions of 100 Å length by 100 Å width by 90 Å height). Periodic boundary conditions were imposed in all three dimensions. In particular, the top and bottom planes of the simulation box are mirror images of the PVDF membrane, allowing the protein to interact with either. The COM of each protein was positioned such that the initial protein-membrane separation distance d is approximately 10 Å for all systems [31, 109], which is to allow for rotation of the protein in case the initial orientation is not favorable. Two proteins are added separately to compare their individual behavior. Aside from the PVDF membrane and lysozyme or α-lactalbumin, the simulation domain was filled with 30,000 TIP3P model water molecules [259] that yield a density of 1 g/cm^3 and neutralized with sodium and chloride ions to avoid charge effects from the particle mesh Ewald background [146].

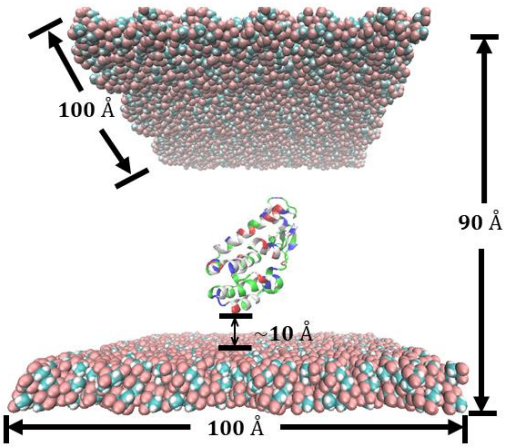

Fig. 6-1. Snapshot of initial condition for the simulation domain (dimensions of 100 Å length by 100 Å width by 90 Å height) with periodic boundary conditions. Water molecules are hidden to ease visualization. PVDF membrane is at both the bottom and top planes (the top one being the mirror image of the bottom one), with cyan representing carbon, white representing hydrogen, and pink representing fluoride. Lysozyme (initial orientation $a_x = 0°$) is colored according to the nature of the amino acid residues: white for non-polar, blue for basic, red for acidic, and green for polar.

Because of the variation of the nature of the residues throughout the protein, the interaction energies depend on which residues interact with the membrane [34, 115, 272]. Depending on the orientation of the protein, metastable states are known to be attained instead of the minimum energy state [245]. To account for such variations, the simulations for each protein were initialized using one of six orientations, which are 90° rotations about the *x*- or *y*-axis, as per earlier studies [107, 115]. Such multiple different orientations allow for different domains of the macromolecular protein to interact with the membrane initially. In particular, in view of the limited time scale of

MD simulations, statistical validity is typically based on a trade-off between more independent runs [134, 149, 153] or longer runs [169, 202, 226]. In this study, the former is adopted, specifically with respect to six independent runs with different initial orientations. These six independent runs serve as replicates, which improves the statistical validity of the MD runs within the limited time scale of 40 ns, which is a typical duration for MD simulations [24].

6.2.3 Simulation procedures

The simulations were run in LAMMPS [76]. All light bonds (i.e., covalent bonds involving hydrogen atoms) were constrained by the SHAKE algorithm, which is commonly implemented to increase stability and save computation cost [260]. Long-range electrostatic interactions were computed by the PPPM Ewald method in the reciprocal space. The Lennard-Jones (LJ) non-bonded interaction was switched off by applying inner- and outer-cutoffs of 8 Å and 10 Å, respectively, which are common thresholds [34, 260]. Energy minimization was performed first, followed by a canonical ensemble (NVT) run that increases system temperature from 30 K to 298 K. The system was subsequently relaxed at 298 K with a 500 ps NVT run, followed by an equilibration NPT (isothermal-isobaric ensemble) run for 1 ns. Nosé-Hoover thermostat and barostat were used to control temperature and pressure with coupling constants of 500 fs and 100 fs, respectively [55, 109]. The production run ensued for 40 ns under the NPT ensemble with a time step of 1 fs. VMD was used for post-processing and visualization [53].

6.3 Results and Discussion

6.3.1 Adsorption behavior

A distinctive feature of MD simulation is the direct visualization of whether and how molecules undergo adsorption onto the membrane surface, which has direct implications for fouling [39]. Accordingly, the evolutions of the lysozyme-membrane and α-lactalbumin-membrane separation distance (*d*) with time are shown in Figs. 6-2a and b, respectively, since d provides a measure of the tendency of the protein to adsorb onto the PVDF membrane [119]. Two interesting highlights are drawn. Firstly, despite the same conditions, the different initial orientations lead to significantly different trajectories of the protein, with predominantly low *d* values in some cases whereas predominantly high *d* values in other cases. The dominant influence of initial orientation agrees with earlier simulation studies of different proteins [31, 115, 118]. Secondly,

although electrostatic considerations would imply greater lysozyme-membrane affinity than that of α-lactalbumin, the *d* values for lysozyme do not appear to be distinctly smaller. This behavior is consistent with experimental results showing that the flux decline during filtration by a feed containing lysozyme was less than that by α-lactalbumin [268].

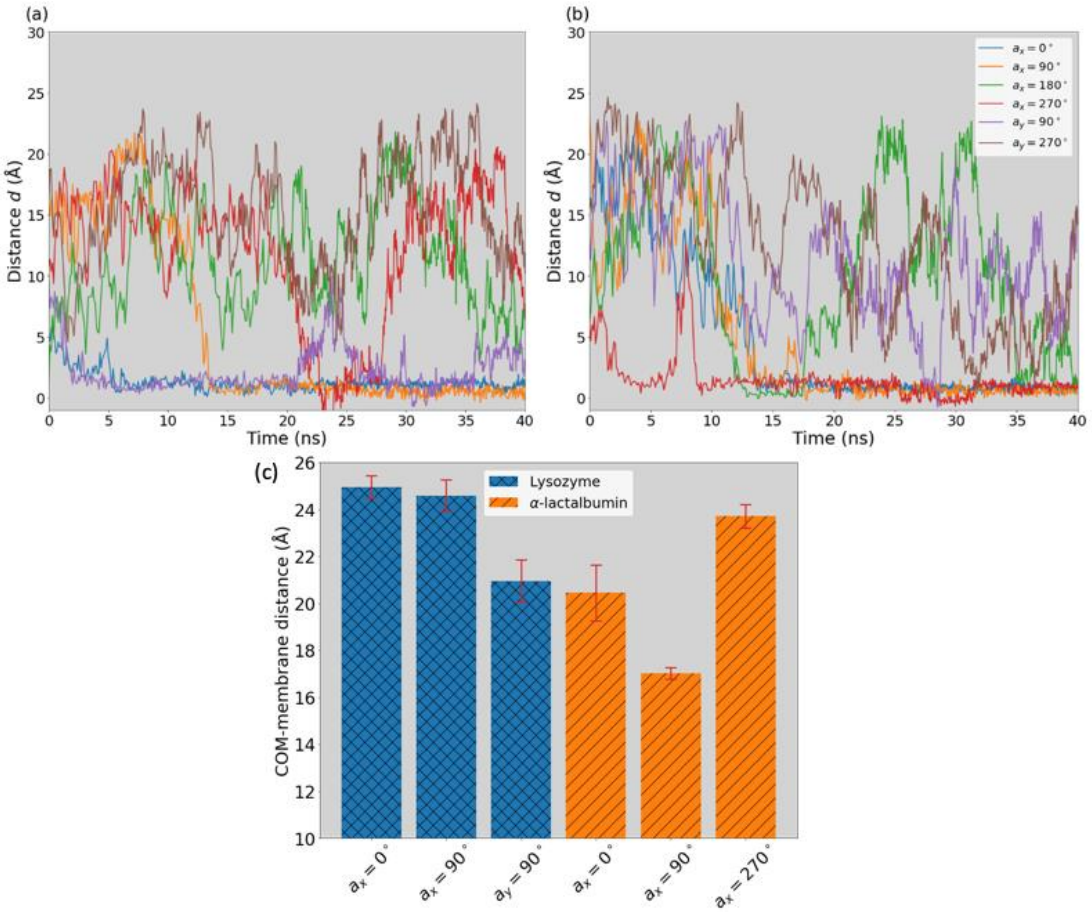

Fig. 6-2. Evolution of protein-membrane separation distance *d* for six different initial orientations of each protein: (a) lysozyme; and (b) α-lactalbumin. Variation in the *d* values at t = 0 of each subplot is the result of energy minimization, relaxation and equilibration steps conducted before the production run. (c) Average distance between the PVDF membrane surface and the center-of-mass (COM) of proteins during the last 5 ns of stable adsorption runs. Initial orientations are shown as the labels on the horizontal axis. Red error bars represent the standard deviations.

In this study, protein adsorption behavior is classified into three categories, namely, stable adsorption, transient adsorption and no adsorption, based on the values of two parameters: (i) the average protein-membrane separation distance ($\bar{d}$); and (ii) the fraction of time during which *d* is less than 4 Å (f_4), with the threshold of 4 Å chosen to reasonably capture the adsorption scenarios. Specifically, stable adsorption is when $\bar{d} <$ 4Å and $f_4 > 50\%$, whereas no adsorption is when $\bar{d} > 10$Å and $f_4 < 10\%$; the data points in between were classified as transient adsorption. Table 6-2 displays the $\bar{d}$ and f_4 values for all 12 simulation runs. Clearly, despite the opposite overall charges,

lysozyme and α-lactalbumin show the same probabilities to adsorb (i.e., three instances of stable adsorption) or not adsorb (i.e., two instances of no adsorption). Earlier experimental studies have affirmed that the overall protein charge is a poor predictor of membrane fouling [267, 268, 273, 274]. It is worth pointing out that multiple mechanisms are involved during protein fouling process, such as the formation of initial protein layer and subsequent charge screening resulted from this layer, as well as the importance of sulfhydryl groups and thiol-disulphide interactions which affects flux decline rate. Although in this study, the direct membrane-protein interaction is focused via MD, it should be kept in mind that other interactions that go beyond the current MD scale may also be critical.

Because proteins are macromolecules, local interactions by specific amino acid residues may play a more prominent role in dictating membrane fouling than the overall properties of the protein. Fig. 6-2c further displays the distance between the COM of the protein and the membrane for the six stable adsorption cases in the final 5 ns, with the small standard deviations of less than 1.2 Å further verifying the stability of the adsorption in these cases. It is evident that the COM of α-lactalbumin is somewhat closer to the PVDF surface compared to lysozyme, indicating more contacts with the membrane and stronger adsorption. Therefore, quantitative analysis was carried out to better understand the nature of the local interactions.

Table 6-2. Protein-membrane separation distance ($\bar{d}$) averaged over each 40 ns run and fraction of time when d is less than 4 Å (f_4) for six runs of each protein at different initial orientations. Values for stable adsorption runs and transient adsorption runs are in bold and underlined, respectively.

	Lysozyme		α-Lactalbumin	
	$\bar{d}$ (Å)	f_4(%)	$\bar{d}$ (Å)	f_4 (%)
$a_x = 0°$	**1.21**	**0.97**	**3.13**	**0.67**
$a_x = 90°$	**3.37**	**0.67**	**3.15**	**0.67**
$a_x = 180°$	11.57	0.02	<u>10.74</u>	<u>0.24</u>
$a_x = 270°$	<u>11.00</u>	<u>0.15</u>	**1.18**	**0.93**
$a_y = 90°$	**2.39**	**0.87**	10.36	0.06
$a_y = 270°$	15.45	0	10.84	0.09

<u>6.3.2 Adsorption site analysis</u>

Each protein is made up of many amino acid residues with their own individual characteristics (Table 6-1), which implies different parts have different affinities to the membrane. Whereas experiments are unable to probe which local site is tied to

adsorption, MD simulation enables direct identification of which residues are directly interacting with the membrane at each time point. The exact anchoring points at which the proteins adsorb onto the membrane warrants a closer inspection to understand the details of the local interactions. Earlier studies have reported that the anchoring amino acid residues can be identified via a protein-membrane distance versus residue plot [31, 118, 119]. Accordingly, Fig. 6-3 and Fig. 6-4 depict the profiles for lysozyme and α-lactalbumin in the latter 20 ns of the simulations, demonstrating that some residues are preferentially closer to the membrane while some are further apart. In addition, Table 6-3 summarizes the amino acid residues involved in the anchoring sites for each protein, defined as residues in which at least three atoms are consistently within 4 Å from the membrane surface. Two noteworthy observations are described. Firstly, five anchoring sites are available on lysozyme while only three sites are apparent on α-lactalbumin. The presence of twofold more anchoring sites of lysozyme is tied to the overall charge being opposite to that of the membrane, even though this does not give rise to greater fouling for lysozyme relative to α-lactalbumin [268]. Secondly, positively charged basic amino acid residues like ARG and LYS are common in the anchoring sites (namely, 5 out of 8 sites identified in Table 6-3), which is due to the negative charge of the membrane and in agreement with earlier studies [118, 165]. Interestingly, negatively charged acidic residues like GLU and ASP are also contained within the anchoring sites, like Site 4 of lysozyme and Site 3 of α-lactalbumin (Table 6-3), suggesting that nearby positively charged residues assist in offsetting any local electrostatic repulsion.

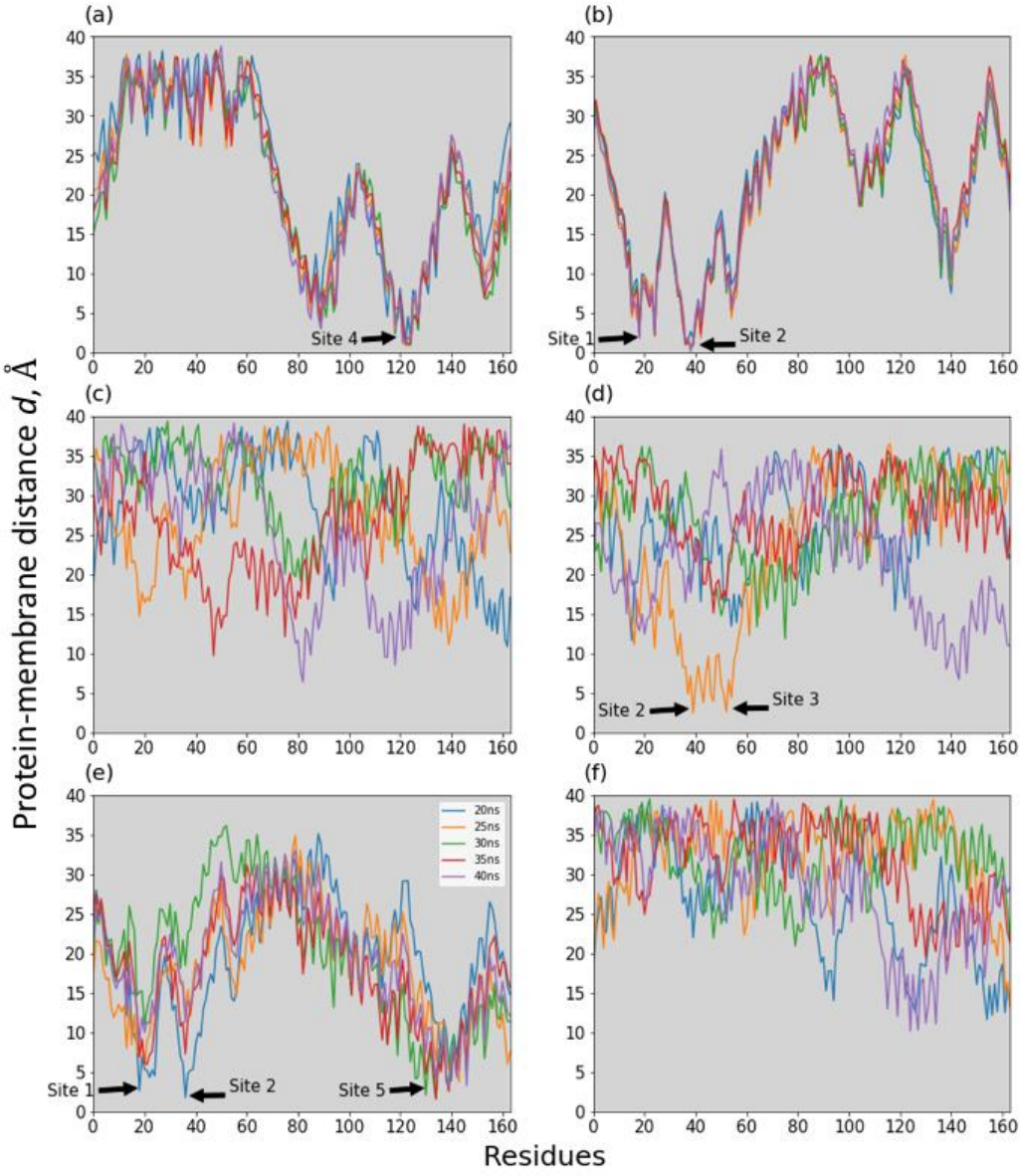

Fig. 6-3. Instantaneous distances between the PVDF membrane and all amino acid residues of lysozyme between 20 ns and 40 ns of the simulation runs. Each sub-plot represents a different initial orientation: (a) $a_x = 0°$; (b) $a_x = 90°$; (c) $a_x = 180°$; (d) $a_x = 270°$; (e) $a_y = 90°$; and (f) $a_y = 270°$. Labels indicate adsorption sites identified in stable/transient adsorption trajectories.

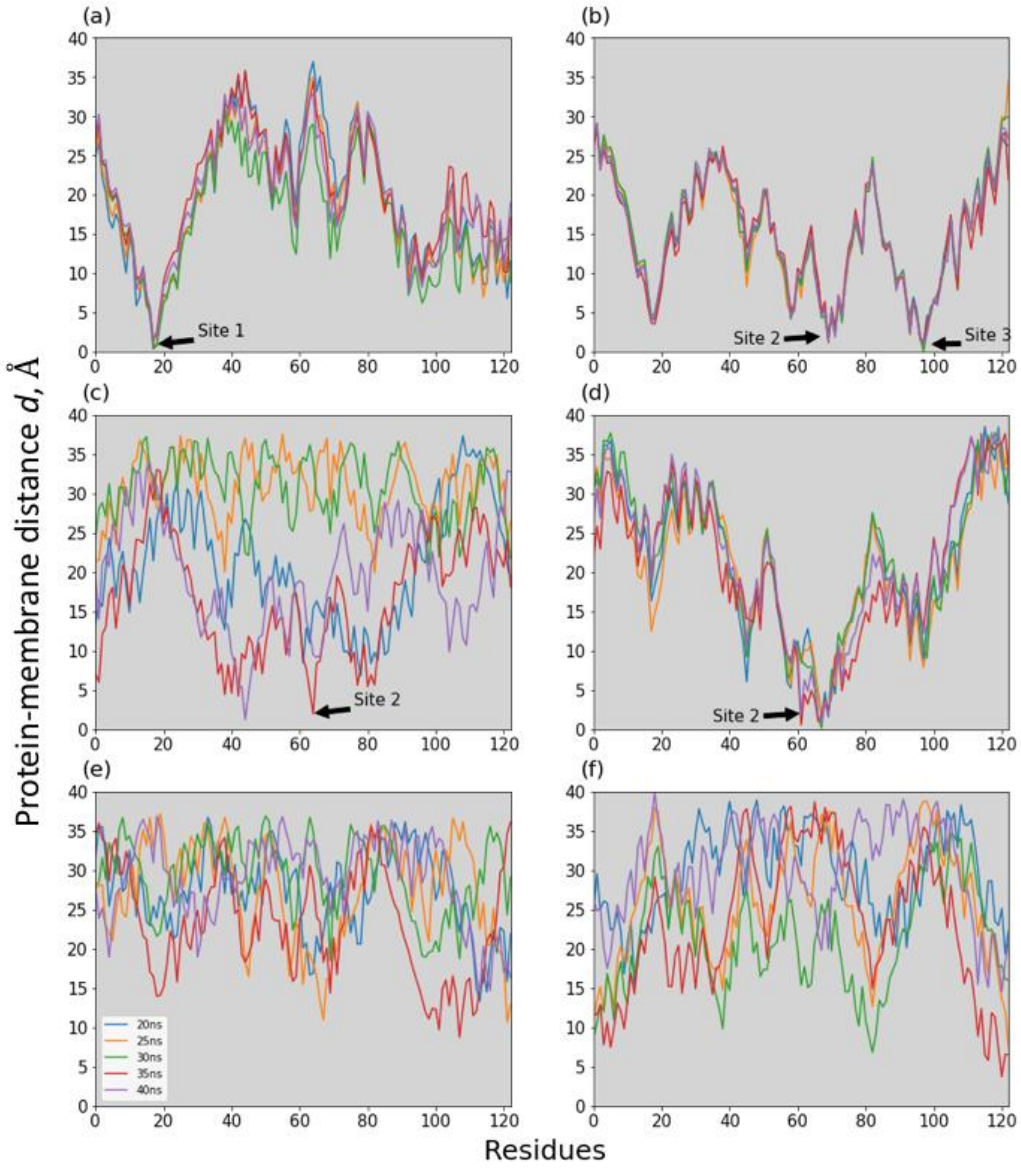

Fig. 6-4. Instantaneous distances between the PVDF membrane and all amino acid residues of α-lactalbumin between 20 ns and 40 ns of the simulation runs. Each sub-plot represents a different initial orientation: (a) $a_x = 0°$; (b) $a_x = 90°$; (c) $a_x = 180°$; (d) $a_x = 270°$; (e) $a_y = 90°$; and (f) $a_y = 270°$.

Table 6-3. Amino acid residues involved in the anchoring sites for lysozyme and α-lactalbumin, defined as residues in which at least three atoms are consistently within 4 Å from the membrane surface.

Site number	Amino acid constituents	Simulation system
Lysozyme		
1	LYS19, TYR25	$a_x = 90°; a_y = 90°$
2	PRO37, SER38, LEU39, ASN40	$a_x = 90°; a_x = 270°; a_y = 90°$
3	ASN53, ASN55	$a_x = 270°$
4	ARG119, GLN123, LYS124, ARG125, GLU128	$a_x = 0°$
5	VAL131, LYS135, ARG137, ASN140, GLN141	$a_y = 90°$
α-Lactalbumin		
1	TYR18, GLY19	$a_x = 0°$
2	LYS62, GLN65, PRO67, GLN68, ARG70, ILE72	$a_x = 90°; a_x = 180°; a_x = 270°$
3	ASP97, ILE98, LYS99	$a_x = 90°$

6.3.3 Interaction energy

Foulant-membrane and foulant-foulant interactions, commonly quantified using the extended DLVO model, are well-acknowledged to agree well with experimental fouling trends [13, 16, 275-277]. In particular, the initial deposition is tied to foulant-membrane interactions and subsequent deposition becomes tied to foulant-foulant interactions as a foulant layer forms on the membrane [46, 275]. This study harnesses the ability of MD simulations to directly compute the means and standard deviations of interaction energies [19, 39] to understand molecular-scale foulant-membrane interaction behaviors, in order to provide more insights on the incipient membrane fouling tendency by the two oppositely charged proteins. Accordingly, protein-membrane interactions were quantified in this study for time instances during which adsorption was observed (i.e., $d < 4$ Å). Fig. 6-5 displays the average protein-membrane interaction energies for different initial orientations. Three key highlights regarding protein-membrane interactions are noted as follows: (i) despite lysozyme being positively charged and thereby expected to have greater affinity to the membrane, the interaction energies in Fig. 6-5 do not indicate distinctly greater magnitudes, with negatively charged α-lactalbumin surprisingly exhibiting the most attractive energy; (ii) despite the same

protein-membrane pairing in each sub-plot in Fig. 6-5, the protein-membrane interaction energies differ by multiple folds and may even acquire an opposite sign as in the case of a_x = 90° for lysozyme, with the wide variation agreeing with an earlier simulation study [31]; and (iii) a greater magnitude of attractive interaction energy is not directly tied to stable adsorption, as evident in Fig. 6-5b, whereby the initial orientation of a_x = 180° is more attractive than two other orientations, but is the only transient adsorption case. This implies that the interaction energy is highly site-dependent. Fig. 6-6 displays the interaction energies associated with the adsorption sites identified in Table 6-3, affirming that the different adsorption sites have significantly different energies, which underlie the surprising observations in Fig. 6-5. Notably, it is not directly the interaction energy of each site that matters in the adsorption of the protein, since the synergy of multiple adsorption sites can lead to more significant attraction for the protein (Fig. 6-5), as some sites act like "hinges" for others [264]. For instance, the most attractive protein-membrane interaction in the case of α-lactalbumin occurs with an initial orientation of $a_x = 90°$, with two distinct sites (i.e., Sites 2 and 3) contributing to the adsorption simultaneously (Table 6-3). The relatively high attractive energies for Sites 2 and 3 jointly results in much stronger binding compared to the other three singular anchoring sites. As another instance, although Site 4 of lysozyme has a greater interaction energy than Site 2 of α-lactalbumin, the greatest overall interaction energy magnitude is for α-lactalbumin ($a_x = 90°$), since the latter can conjugate with another site.

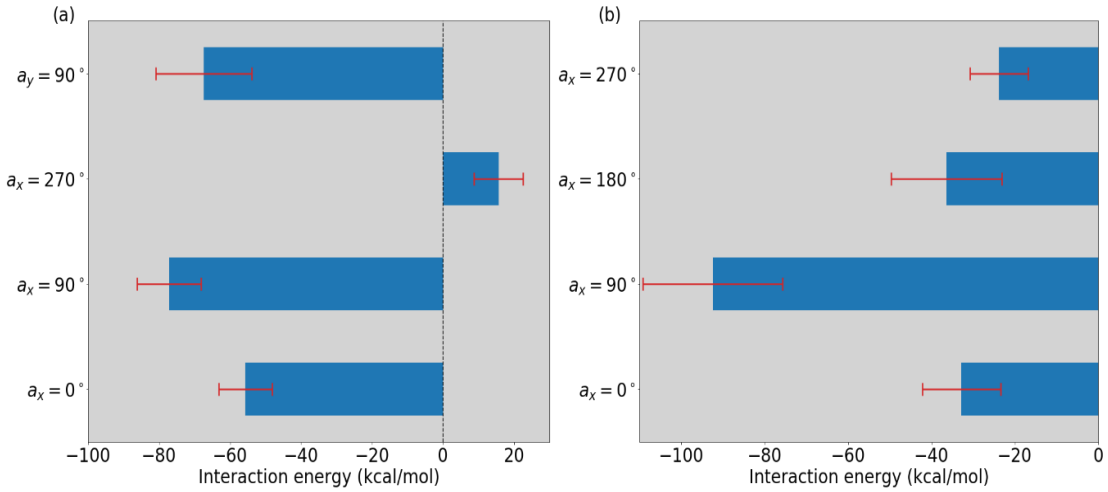

Fig. 6-5. Protein-membrane interaction energy averaged over time instances of adsorption (i.e., d < 4 Å) for the stable and transient adsorption cases of (a) lysozyme and (b) α-lactalbumin. Labels on the vertical axis indicate the initial orientation. Red error bars represent the standard deviations.

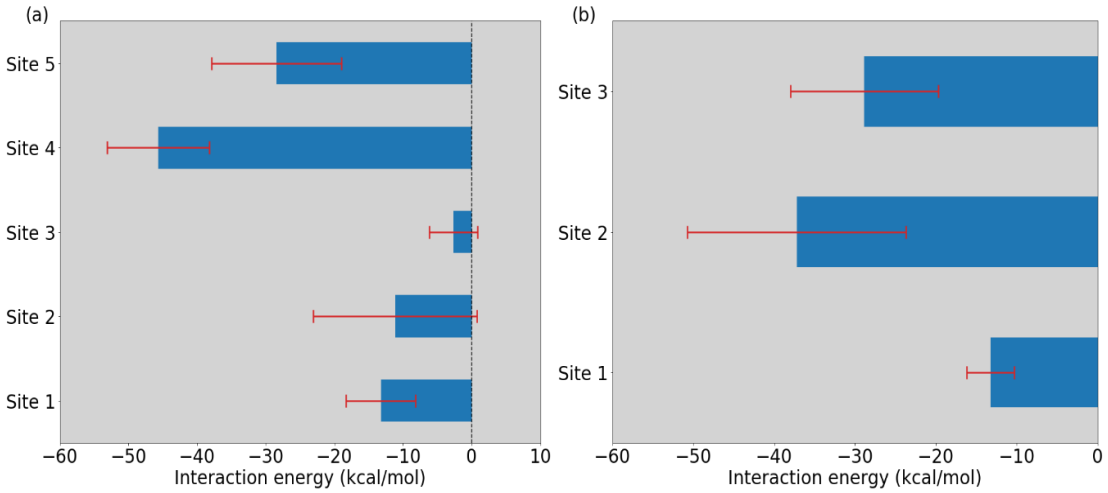

Fig. 6-6. Adsorption site-membrane interaction energy averaged over time instances of adsorption (i.e., d < 4 Å) for (a) lysozyme and (b) α-lactalbumin. Labels on the vertical axis indicate the adsorption site number in Table 6-2.

These results for the interaction energies further demonstrate the importance of local interactions that are not readily revealed by macroscopic characterizations like zeta potential. Notably, the protein with similar polarity as the membrane (i.e., α-lactalbumin) is shown to exhibit the most attractive interaction energy among the protein-membrane interaction energies revealed, which is consistent with the comparatively worse membrane fouling seen with α-lactalbumin compared to lysozyme [268].

6.3.4 Mobility and flexibility

The mobility and flexibility of the two oppositely charged protein molecules upon adsorption is examined in this section to further explore the deviation of fouling phenomena from that predicted based on the net electrostatic charge.

Post-adsorption mobility can be quantified by RMSD of the positional vector of protein's COM. Fig. 6-7 displays the evolutions for all six cases of stable adsorption for the two proteins. Interestingly, lysozyme with an initial orientation of $a_y = 90°$ exhibits the highest RMSD, although three sites contribute to the adsorption behavior (Table 6-3). Another interesting observation is the similar RMSD values for the three steady adsorption cases of α-lactalbumin, despite different interaction energies. Thus, while initial orientations of the protein and thereby the different anchoring sites result in different foulant mobility, the relationship between the number of anchoring sites and the interaction energy is unclear. Comparing the RMSD values for lysozyme and α-lactalbumin, those for the latter are lower. This general behavior is in line with earlier studies that reported that lower RMSD values of small foulants (e.g., oil, surfactants and NOMs) are well-correlated with worse fouling [36, 55, 109]. Thus, the experimental observation of relatively worse fouling by α-lactalbumin [240, 268] may be related to

the lower post-adsorption RMSD values. This indicates that the mobility of the foulant upon adsorption is likely a critical factor governing membrane fouling, with lower mobility related to worse fouling. These results indicate that the mobility of the adsorbed protein is also poorly corelated to the overall charge, again emphasizing the importance of local interactions and the drawback of trying to predict fouling from the overall zeta potential.

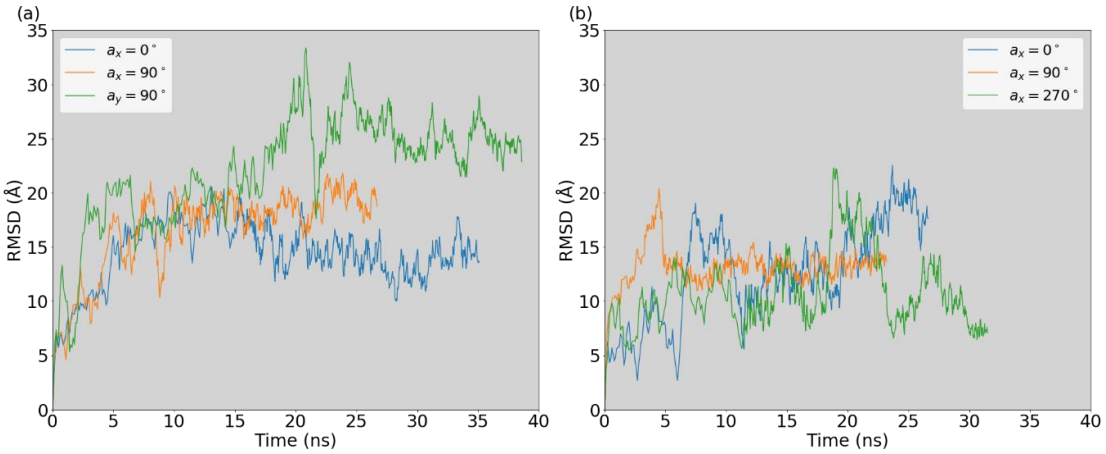

Fig. 6-7. Root-mean-squared deviation (RMSD) versus time of stable adsorption trajectories of (a) lysozyme; and (b) α-lactalbumin. The starting points of the RMSD curves are the onset instances of adsorption, resulting in different curve lengths.

In addition to RMSD, RMSF of different residues can be used to quantify the flexibility of different domains of the protein macromolecule. It should be noted that RMSD and RMSF are not directly related [272]. Fig. 6-8 presents the RMSF values within the last 5 ns of simulation of all amino acid residues for trajectories of stable adsorption. Lower RMSF indicates lower flexibility, with an earlier study classifying residues as low flexibility if the RMSF value is less than 3 Å [231]. Comparison of the RMSF values in these two figures indicates that adsorption is associated with a decrease in RMSF values. Interestingly, Fig. 6-8 shows that, (i) despite the opposite charges of the two proteins, the RMSF values for the stable adsorption cases are in the same range, indicating similar flexibility; and (ii) even for the same protein in each sub-plot, the RMSF values are again shown to be dependent on the initial orientation. The lowest RMSF values for each protein (i.e., $a_x = 90°$ for both lysozyme and α-lactalbumin) is well correlated with the most attractive protein-membrane interactions, which suggests that the low residue flexibility may be tied to worse fouling. Contrasting the RMSF values of lysozyme and α-lactalbumin, the latter has more residues with RMSF values less than 3 Å [231], indicating lower flexibility upon adsorption, which may explain the relatively worse fouling seen with the α-lactalbumin.

Combining results obtained from RMSD and RMSF, it appears that mobility and flexibility parameters of the proteins upon adsorption are not related to the overall charge of the protein, but are directly associated to the extent of fouling during membrane filtration.

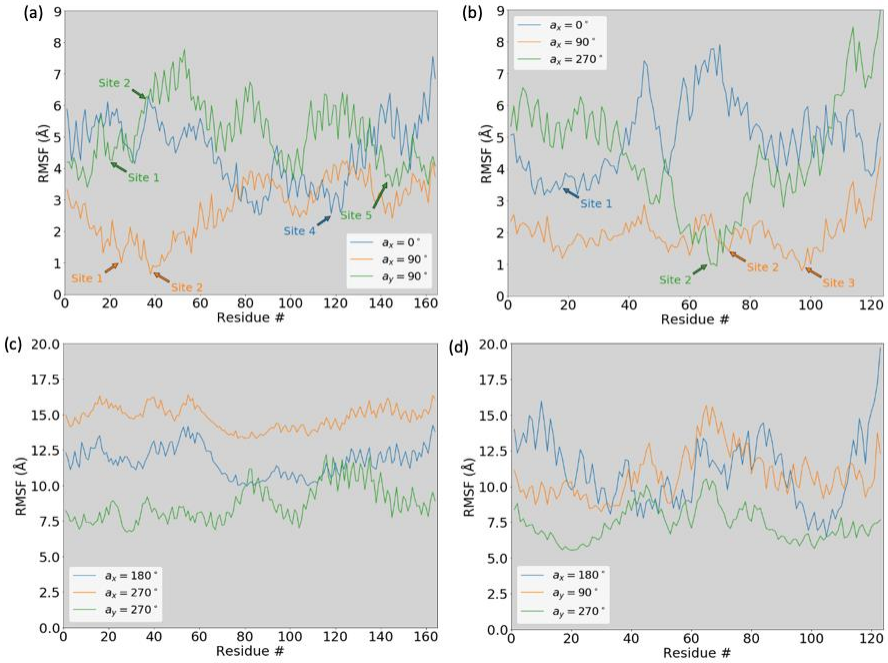

Fig. 6-8. Root-mean-squared fluctuation (RMSF) of residues in (a) lysozyme and (b) α-lactalbumin averaged over the last 5 ns of stable adsorption simulation runs; and in (c) lysozyme, and (d) α-lactalbumin averaged over the last 5 ns of transient adsorption or no adsorption simulation runs. Initial orientations are indicated by the legend.

6.4 Conclusions

Experimental results indicate that the overall protein charge is a poor predictor of membrane fouling tendency, which likely reflect the importance of local interactions by specific sites on the macromolecule in determining the fouling behavior. To understand molecular-scale interactions, MD simulations were employed here to understand and quantify the local phenomena, with each protein initialized with six different orientations. The two proteins studied in this work are positively charged lysozyme and negatively charged α-lactalbumin, while the membrane is negatively charged PVDF.

Although net electrostatic considerations would imply greater lysozyme-membrane affinity compared to that for α-lactalbumin, as evident in lysozyme having five adsorption sites while α-lactalbumin has only three, the local interactions caused the following surprising results: (1) the protein-membrane distance *d* of lysozyme do not appear to be distinctly smaller than those for α-lactalbumin; (2) both proteins exhibit similar probabilities of stable adsorption and no adsorption; (3) the protein-membrane interaction energies of lysozyme are not distinctly more attractive, with the negatively charged α-lactalbumin surprisingly exhibiting the most attractive energy due to synergy

among the adsorption sites; (4) α-lactalbumin has lower RMSD values than lysozyme; and (5) α-lactalbumin has more residues that exhibit low RMSF values than lysozyme.

The results here provide insights on the experimental observation that membrane fouling by the negatively charged α-lactalbumin is worse than that of the positively charged lysozyme when using a negatively-charged PVDF membrane, which is completely opposite to the expected behavior based on the overall charges of the proteins and membrane. For the two proteins examined here, the local interactions govern adsorption onto the membrane, rendering macroscopic characterizations like zeta potential ineffective in predicting fouling. More specifically, more severe fouling of α-lactalbumin is attributed to the dominant mechanism that several local "hot spots" are favourable to interact with PVDF membrane, which in turn decrease the overall mobility and flexibility.

It is important to note that the simulations conducted in this study ignored the effects of filtration velocity and detailed pore geometry on the protein-membrane interactions, both of which are likely to be important in determining the detailed nature of the membrane fouling that occurs during protein filtration. Nevertheless, the molecular-scale results obtained by MD trajectories are not obtainable by experiments and provide valuable insights on the membrane fouling phenomena.

Chapter 7 – Investigation of Surfactant–Membrane Interaction Using Molecular Dynamics Simulation with Umbrella Sampling

Having investigated NOMs and protein as foulant, we have switched our focus to surfactant-stabilized oil emulsion, which is critical for membrane separation processes designed for oily wastewater. Specifically, the previous dead-end filtration experimental studies have encountered an unexpected flux enhancement for CTAB stabilized oil emulsion, which was not very well explained by other theories and monitoring methods. Therefore, we have designed this simulation study, aiming at obtaining molecular-level insights near the interface when surfactant molecules are present in the feed.

7.1 Introduction

The treatment of oily wastewater, a major source of which is the produced water from oil and gas fields, has been gaining much attention [278]. Membranes are effective for the separation of oil emulsions [15, 279], wherein surfactants intrinsically present in oily wastewater serve the role of stabilizing the emulsions. Unfortunately, the knowledge on the effect of surfactant on membrane fouling remains limited. The charge effect of surfactants is a topic of interest, since surfactants can be cationic, anionic or non-ionic, giving rise to significantly different interactions with the membrane [280, 281]. Virga et al. investigated the adsorption and fouling of four types of surfactants using polyelectrolyte multilayer membranes, and found the fouling of the active layer was reversible [282]. Tian et al. [283] found via Electrical Impedance Spectroscopy (EIS) that while the increase of conductance of fouling layers with time agreed well with flux decline profile of SDS- and Tween-20 stabilized oil emulsion, extensive adsorption of the positively charged CTAB surfactant in the initial stages of filtration shielded the membrane from fouling by the oil emulsions. Trinh et al. [223] found that the relative flux trends in the presence of surfactant-stabilized oil emulsions mimicked that with only the surfactants alone, indicating the dominant influence of surfactants. In particular, the normalized flux of cetyltrimethylammonium bromide (CTAB) stabilized oil emulsion, as well as CTAB solution alone, was higher than that of deionized (DI) water, suggesting a surprising flux enhancement effect. In comparison, filtering solution containing non-ionic Tween 20 results in more or less same flux as compared to that of DI water, whereas filtering SDS solution results in noticeable flux decline. Notably, although it is generally acknowledged that the XDLVO-based interfacial interaction

energy correlates well with membrane fouling [13, 275], studies have instead indicated that DLVO works better for oil emulsions [284, 285]. Furthermore, another study suggests that the repulsive rather than attractive energy is better correlated with the extent of membrane fouling [223]. Some of these gaps in understanding the mechanisms can be bridged through MD simulations, which provide Angstrom-scale perspectives not possible via experiments.

For the investigation of such a solid/liquid interface, the evaluation of adsorption free energy is important. However, conventional MD is often inadequate due to insufficient sampling of the conformational space of the adsorbate, especially in the region close to the surface [129, 139]. Wei et al. systematically compared the performance of three computational algorithms for calculating adsorption free energies of small molecules on representative surfaces [139]. SMD was found to be computationally efficient for an interfacial system with a hydrophobic surface, whereas umbrella sampling had better performance compared to both SMD and metadynamics for a hydrophilic surface. These methods have been applied to characterize surfactant-surface interactions too. Li et al. investigated the PMF profile of anionic sodium dodecyl sulfate (SDS) surfactant with respect to the acrylate latex surface using umbrella sampling, and concluded that PMF can be decomposed into two separate terms contributed by the hydrophobic tail and charged headgroup [150]. Yan and Yuan applied SMD to simulate the effect of cationic CTAB surfactant on the detachment of residual oil from silica nanopores, and found that the energy required for fluid to displace oil droplets is smaller in the presence of CTAB [132]. These biased simulations provide meaningful physical insights into the nature and origin of interactions between surfactant, surface, and surrounding solvent molecules by quantifying the free energy [139], making it a useful complementary tool to membrane filtration experiments.

Targeting the research gap on the role of surfactants in membrane filtration, MD simulation runs with umbrella sampling were performed in the current work. Three surfactants with different charges were investigated, including positively charged CTAB, negatively charged SDS, and non-ionic Tween 20. The membrane surface was hydrophilic PVDF. Unbiased simulations were performed first to allow systems to equilibrate. Then, a series of biased simulations were carried out based on umbrella sampling for each surfactant, followed by the derivation of the PMF plots using WHAM [286, 287]. The Gibbs free energy was further decomposed into an enthalpic term and an entropic term.

7.2 Methods and Materials

7.2.1 Experiments

This study involved dead-end filtration operated at constant TMP of 20 kPa, which was regulated by two gear pumps (Cole Palmer, model No. GJ-N23.PF1S.A) in series. The upper feed chamber of the filtration cell was 35 mm width by 35 mm breadth by 15 mm height. Four feed inlets were positioned 0.5 mm below the upper wall at the mid-points of the four side walls, so as to reduce tangential flows on the membrane. As for the lower permeate chamber, it was 35 mm in diameter and 15 mm height. Flat-sheet hydrophilic PVDF membranes (Merck; Durapore; Product No. GVWP04700; nominal pore size = 0.22 μm; porosity = 70%) were used for filtration. Each piece of membrane had a circular active filtration area of 9.6 cm^2 and zeta potential of -26.4 mV (Anton Paar, SurPass 3). A circular porous stainless-steel plate, which was 35 mm in diameter and 2 mm in height, was placed under the membrane to mechanically support the membrane.

The surfactants investigated had different charges, namely, positively charged CTAB (Sigma-Aldrich, 52365-50G), negatively charged SDS (Sigma-Aldrich, 75746-250G) and nonionic Tween 20 (Sigma-Aldrich, P1379-1L). At the start of each experiment, filtration of DI water was performed for 30 min at 20 kPa to condition the membrane. During the experiment, the permeate flux was recorded every 60 s. The feed contained surfactant to DI water at a mass ratio of 1:20,000 to give a surfactant concentration of 50 ppm. The TOC concentrations (Shimadzu, TOC-VCSH) of the feed and permeate (after 200 mL of permeation) were measured for each experiment. The difference in the TOC values between the feed and permeate gave an indication of the percentage of the surfactant amount that was retained by the membrane.

7.2.2 Simulation

7.2.2.1 Membrane

The PVDF plane used (100 Å length by 100 Å width by 10 Å depth) was that from earlier studies [36, 94], with a density of 1.75 g/cm^3 [288]. Due to the limited spatial scale, no pore is included and the depth is much shorter than the experimental membrane thickness (of millimetre order), which is a common simplified value found in MD literature [98, 118, 150]. However, this surface is hydrophobic because it was used experimentally for membrane distillation [94, 289, 290], so the simulated PVDF surface was modified to make it hydrophilic to mimic those used in the experiments in this study. To add the appropriate number of functional groups, both hydrophobic (Durapore

GVHP; Merck-Millipore) and hydrophilic (Merck, product No. GVWP04700) membranes were analyzed using FTIR (IRAffinity-1S, Shimadzu) and X-ray photoelectron spectroscopy (XPS, Kratos Axis Supra, Shimadzu). Comparing the FTIR spectra, hydroxyl and carboxyl groups were identified only in the hydrophilic membrane. Furthermore, the XPS spectrum shows the atomic concentration of oxygen on the hydrophilic membrane is 11%. Therefore, since 11% corresponds to 294 oxygen atoms, 98 hydroxyl (i.e., -OH) groups and 98 carboxyl (i.e., -COOH) groups were randomly added to the PVDF surface simulated to mimic the hydrophilic membrane used experimentally.

To ensure the same charge as the experimental membrane, the zeta potential of the membrane was measured using Surpass 3 (Anton Paar) to be -26.4 mV. Based on the Grahame equation [251], the overall charge of the membrane surface was determined as -1.29 C. Therefore, the charges of the atoms on the PVDF surface simulation were adjusted to match this value. More details are provided in the next section.

7.2.2.2 Force field parameters and system packing

In the earlier studies on the hydrophobic PVDF membrane [36, 94], non-bonded force field parameters were obtained from Lachet et al. [250]. Here, the additional parameters corresponding to the added hydroxyl and carboxyl groups were extracted from OPLS-AA force field [207]. Partial charges of atoms were first tuned based on the density functional theory (DFT) so that the overall charge of the membrane is zero. Subsequently, to make the membrane negatively charged per the measured zeta potential value (i.e., -26.4 mV), 3 out of the 98 carboxyl groups on the surface were deprotonated, since the partial charge of carboxylic hydrogen is 0.45. Fig. 7-1 displays the final charge distribution of the resultant structure.

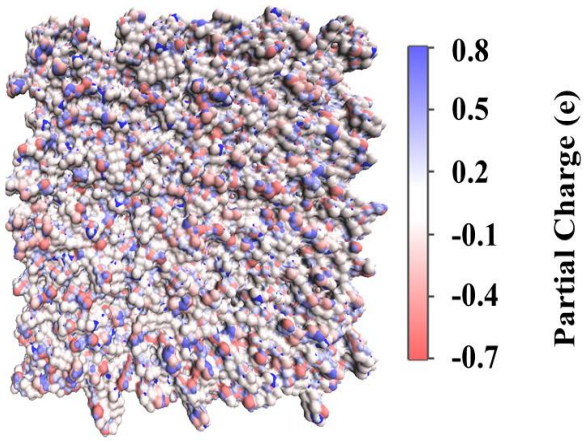

Fig. 7-1. Charge distribution of the hydrophilic PVDF membrane surface.

The structures and chemical formulas for the three surfactants used in this study are shown in Fig. 7-2. As is common for surfactant simulation studies [105, 120, 132], OPLS-AA force field was applied to all three. Packmol [65] was used to pack the three simulation systems. Specifically, the PVDF membrane was fixed at the bottom plane, and three identical surfactant molecules were added to the simulation box and solvated with 25,000 SPC/E water molecules [48]. As the PVDF membrane structure had been equilibrated during the construction process [36], all atoms of the membrane were fixed in space during the simulation to avoid bulk drifting of the surface. Since the experimental condition of 50 ppm translates to less than 0.1 surfactant molecule in the simulation domain, three surfactant molecules were added to generate statistically valid results, as per earlier simulation studies of surfactants [36, 55]. In addition, in line with the common practice for periodic boundary conditions in MD simulations [31, 118], three neutral, rigid graphene layers were stacked and placed at the top plane to prevent interaction between the surfactant and mirror image of the PVDF membrane. The simulation domain dimensions are 100 Å by length, 100 Å by width and 95 Å by height. The length and width of the simulation box (i.e., *x*- and *y*-directions, respectively) are large enough so that surfactant molecules do not interact with their periodic images, whereas the dimension normal to the surface (i.e., *z*-direction) is sufficiently large to allow sufficient space to pull surfactant until it becomes freely in the bulk liquid for the biased simulations.

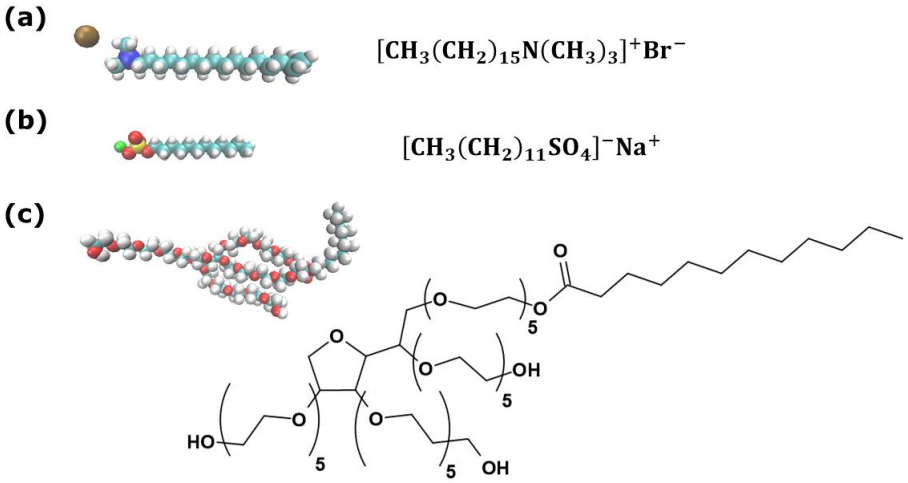

Fig. 7-2. Chemical structures and formulas for the three surfactants used in the simulation: (a) cationic CTAB; (b) anionic SDS; and (c) non-ionic Tween 20. In the structures, cyan represents carbon, white represents hydrogen, blue represents nitrogen, red represents oxygen, brown represents bromide, yellow represents sulfur, and green represents sodium.

7.2.2.3 Potential of mean force

PMF describes the free energy of a molecule with respect to the reaction coordinate, which is the distance between the COM of the surfactant and the membrane surface (χ):

$$\chi = z_{surf} - z_{mem} \quad \text{Eq. (38)}$$

To define the coordinate of the surfactant (z_{surf}), representative atoms were selected from the headgroups of the surfactants that have important influences on PMF [150, 291], namely, nitrogen for CTAB, sulfur atom for SDS, and oxygen in the five-membered sorbitan ring of Tween 20. As for the coordinate of the PVDF surface (z_{mem}), the highest *z*-coordinate was used as the reference point. It should be noted that negative χ value does not mean that the surfactant has penetrated into the polymer matrix, but rather the local *z*-coordinate variation of the surface. The range of χ investigated is -5 Å to 20 Å, with the upper limit being such that the surfactant is fully detached from the surface.

7.2.2.4 Simulation procedures

All simulations were conducted in LAMMPS [76]. Periodic boundary conditions were applied in all three directions of the simulation domain, and post-processing and visualization of trajectories performed in VMD [53]. Calculation of the long-range electrostatic interactions were done by the PPPM Ewald method in the reciprocal space. All parameter settings (e.g., thermostat and barostat constants) were kept the same, except that the cut-off for the Lennard-Jones non-bonded interaction was decreased from 18 Å to 12 Å to speed up the calculation, which is in line with other simulation studies [137, 140]. To validate this reduction, an equilibration run with a cut-off of 18 Å had been conducted. The average temperature and density of the system is different from the same runs with a cut-off of 12 Å by less than 0.2%, with a simulation CPU hour saving of 70%. Before performing umbrella sampling to obtain the PMF curve of surfactants, all three systems were equilibrated in an unbiased manner (i.e., no external force was exerted on the surfactants) per that in earlier studies on surfactants [36, 55]. The equilibration NPT runs were conducted for 1 ns, and the temperature, density, and total energy of all three surfactant systems vary within 0.4% of the respective average value, indicating that systems had been well equilibrated. The production runs of the unbiased simulations were firstly conducted for 5 ns using a time step of 1 fs under NPT ensemble. Subsequently, the time step was increased to 2 fs and another 10 ns NPT run was conducted. These short unbiased runs ensured system stability, so the final configurations after 15 ns were used as the respective initial point for umbrella sampling

[115, 132]. Similar to other surfactant simulation studies [105, 292], all the following biased simulations were run with a time step of 2 fs.

Umbrella sampling is an efficient method for PMF calculation to ensure sufficient sampling for obtaining representative energy profiles [293]. Starting with the final configuration of unbiased simulations, the surfactant was dragged to the specific reaction coordinate, and a harmonic potential applied (stiff spring constant of 25 $\frac{kcal}{mol \cdot Å^2}$ and a moving rate of 1 m/s [141, 150]) such that the surfactant fluctuates spatially about $\pm$ 0.5 Å for 3 ns as an equilibration step [137]. Then, a harmonic potential with a weaker spring constant of 6.25 $\frac{kcal}{mol \cdot Å^2}$ was applied for 5 ns [132, 151], during which the random reaction coordinates of the system were recorded every 2 ps for post-processing using WHAM to obtain the corresponding free energy values [151], with error analysis performed using Monte Carlo bootstrap method [147]. Note that harmonic potential was only applied in the *z*-direction, allowing surfactants to freely rotate around and translate in the other two directions. A total of 26 reaction coordinates in the range of -5 Å $\leq \chi \leq$ 20 Å that are 1 Å apart [150, 291] were assessed with the Colvars module in LAMMPS. Before computing the PMF, to ensure that an appropriate spring constant K was selected, the histograms of values of reaction coordinate χ recorded within each umbrella sampling window are plotted to confirm that reasonable overlap was achieved between adjacent windows, affirming the complete range of χ has been sampled properly [132, 139].

7.3 Results and Discussion

7.3.1 Experimental results

Fig. 7-3 displays the normalized flux with respect to time for the feeds containing the different surfactants, namely, positively charged CTAB, non-ionic Tween 20 and negatively charged SDS [223]. Note that the feed only contained DI water in the first 6 minutes, after which the targeted 50 ppm of surfactant was introduced. Clearly, upon the introduction of the surfactants, the flux for the feed containing CTAB increased significantly by approximately 15%, that with Tween 20 remained constant, and that with SDS declined by approximately 7%. Since flux generally declines during filtration, even for the filtering of surfactant [281, 294-298], the most surprising result is the increase in flux relative to that of DI water feed by CTAB and also the lack of flux decline for Tween 20.

Fig. 7-4 presents the percentage by mass of surfactants adsorbed on the membrane after filtering 200 mL of each feed containing 50 ppm of one of the three surfactants.

The retention was quantified by normalizing the difference between the feed and permeate TOC values with the TOC of the feed. It is shown that the retention was the greatest for CTAB (~20 - 25%), followed by Tween 20 (~13%), then SDS (~5%). Past studies have reported that the retention of the surfactant by the membrane could be due to the adsorption onto the membrane structure [299] or the formation of surfactant micelles that are retained [300]. The very low retention of SDS by the membrane indicates that the adsorption of SDS on the membrane was insignificant, presumably due to the negative charges of both SDS and the membrane. However, despite the electrostatic repulsion, the normalized flux for the feeds containing SDS (Fig. 7-3) was the only one that dropped significantly below one.

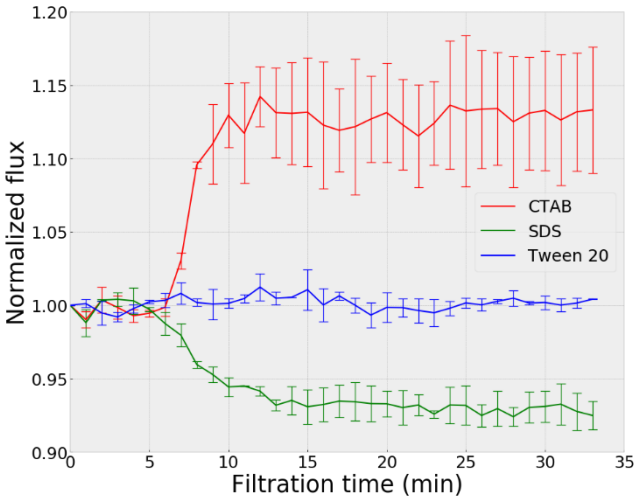

Fig. 7-3. Evolution of normalized fluxes (i.e., normalized with respect to initial fluxes for feed containing only DI water, as shown in the first 6 minutes) during dead-end filtration of feeds containing 50 ppm of surfactants. PVDF membrane (nominal pore diameter = 0.22 µm) was used and TMP of 20 kPa was implemented. The error bars represent the standard deviations of the repeated experiments.

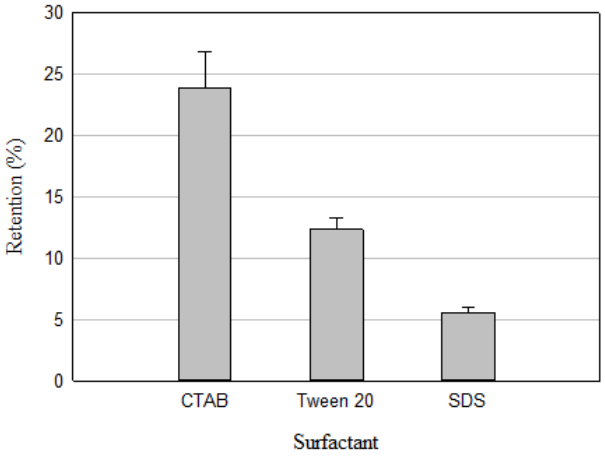

Fig. 7-4. Percentage by mass retention of CTAB, Tween 20 and SDS by the membrane after 200 mL of permeate was obtained. The feed had 50 ppm of the targeted surfactant. PVDF membrane (nominal pore diameter = 0.22 µm) was used and TMP of 20 kPa was implemented.

7.3.2 Equilibrating simulation systems

Before applying umbrella sampling, systems were allowed to equilibrate with no external force applied to the surfactants for 15 ns. System configurations at the end of 15 ns of production run are shown in Fig. 7-5. Regardless of surfactant type, only one out of three surfactant molecules is adsorbed onto the membrane surface, while the remaining two remain in the bulk liquid away from the membrane. Hence, the number of surfactants adsorbed does not correlate with retention data shown in Fig. 7-4, indicating that other factors need to be considered when comparing the behaviors of surfactant adsorption.

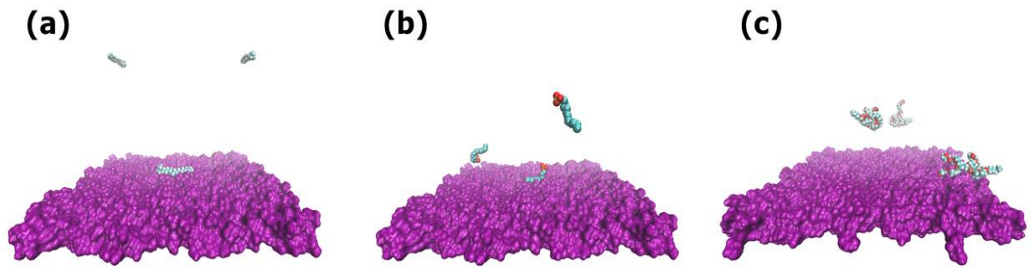

Fig. 7-5. Snapshots of system configuration after unbiased simulation runs of 15 ns for three molecules of (a) CTAB; (b) SDS; and (c) Tween 20. PVDF membranes are shown in purple at the bottom, and surfactant molecules are drawn in the same style as the schematic in Fig. 7-2. All water molecules are hidden for visualization purpose. Surfactant molecules floating around in the bulk liquid has negligible interaction with the membrane, whereas those attached to the surface (one for each type) is deemed to be adsorbed. These configurations were used as the starting point for the subsequent umbrella sampling.

RMSD of surfactant molecules over the last 10 ns of production runs are plotted in Fig. 7-6, reflecting how much the molecule has moved with respect to its initial position. Compared to the un-adsorbed surfactants, the adsorbed surfactants has (i) lower RMSD values, because of the relatively lack of mobility once anchored onto the membrane; and (ii) remain relatively constant RMSD values, reflecting equilibrium states.

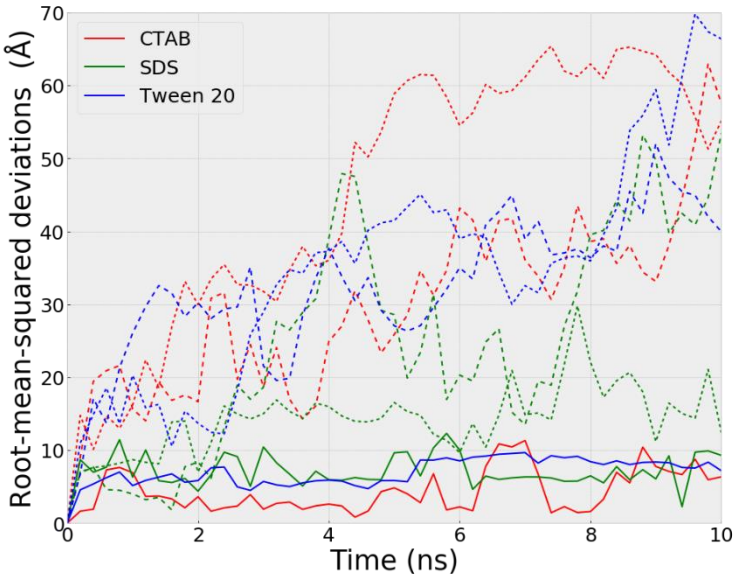

Fig. 7-6. RMSD profiles of each surfactant molecule during the last 10 ns of production runs. Different type of surfactants is distinguished by color as indicated by the legend. Solid lines represent the adsorbed surfactants shown in Fig. 7-5 with low mobility due to strong anchoring onto the membrane surface, while the dashed lines the unadsorbed ones which largely remain in bulk liquid with much higher mobility compared to adsorbed ones.

The interaction energies were assessed for the equilibrated adsorbed systems. In LAMMPS, the instantaneous interaction energy between different entities is directly computable based on force field parameters. Fig. 7-7 displays the interaction energy values between different entities (namely, surfactant-water, surfactant-membrane and water-membrane) averaged over the last 10 ns of simulation runs. Regarding surfactant-water interaction (Fig. 7-7a), Tween 20 has the strongest extent of hydration due to multiple hydroxyl groups (Fig. 7-2), while CTAB the least. The number of water-surfactant hydrogen bonds follows the same trend. The relative values by the three surfactants do not agree with the relative flux (Fig. 7-3) and retention (Fig. 7-4). With respect to surfactant-membrane interaction (Fig. 7-7b), the most attractive is for SDS, followed by Tween 20 then CTAB, which disagrees with the experimental retention trends (Fig. 7-4) and also that computed from DLVO theory in previous studies [223, 283]. As for membrane-water interaction (Fig. 7-7c), that for CTAB and SDS are similar while that for Tween 20 is slightly more attractive.

The lack of correlation to experiments may not be so surprising, considering earlier studies indicating that DLVO rather than the more well-acknowledged XDLVO predicts membrane fouling by surfactant-stabilized oil emulsions more accurately [284, 285], and another study suggesting that the repulsive rather than attractive energy is better correlated with the extent of membrane fouling [223]. The adsorption of the surfactant is in fact a transition between two states, specifically, from the initial dissolution state in which the surfactant is well surrounded by bulk water molecules, to

the adsorbed state in which the surfactant and membrane are partly dehydrated for direct surfactant-membrane contact. Thus, neither of the three interaction energies alone is adequate for correlating with the adsorption behavior. It should be noted that such inconsistency between solute-membrane interaction energy and filtration flux has been previously noted [107, 108, 301]. On one hand, for the same foulant, because of the similar extents of hydration in different environments, the flux trend can be directly correlated with foulant-membrane interaction energy [107, 108]. On the other hand, when different foulants are compared, the more significantly different extents of hydration have non-negligible influences on the overall free energy, and thereby the foulant-membrane energy is not directly correlated with the flux trends [301]. In this study, three surfactants have distinctly different hydrations (Fig. 7-7a), which necessitates the consideration of the overall free energy. This motivated the current study to further explore the contradictions through unbiased simulations. Accordingly, the umbrella sampling runs were conducted to extract the free energy values from PMF curves to better understand the different behaviors of the surfactants.

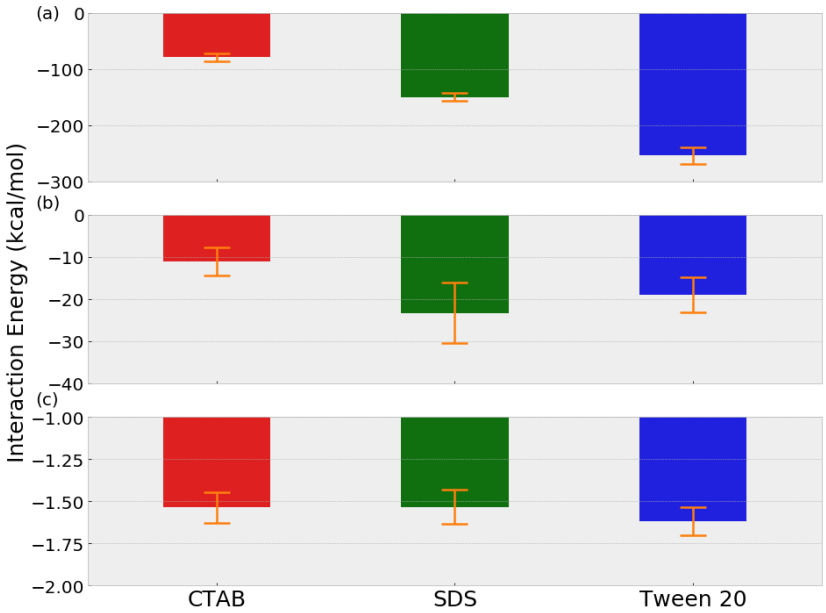

Fig. 7-7. Average interaction energy between different entities over the last 10 ns of unbiased production runs before performing umbrella sampling: (a) surfactant-water, per surfactant molecule; (b) surfactant-membrane, per surfactant molecule; (c) water-membrane, per water molecule. Error bars stand for standard deviations of the values during the 10 ns.

7.3.3 Umbrella sampling

Umbrella sampling was implemented for the adsorbed surfactants (Fig. 7-3). The PMF curves obtained via WHAM for the three surfactants are shown in Fig. 7-8. Per

earlier studies [105, 148], the PMF curves are shifted such that ΔG value at χ = 20 Å is zero (i.e., surfactant is fully detached from the membrane and freely in the bulk water).

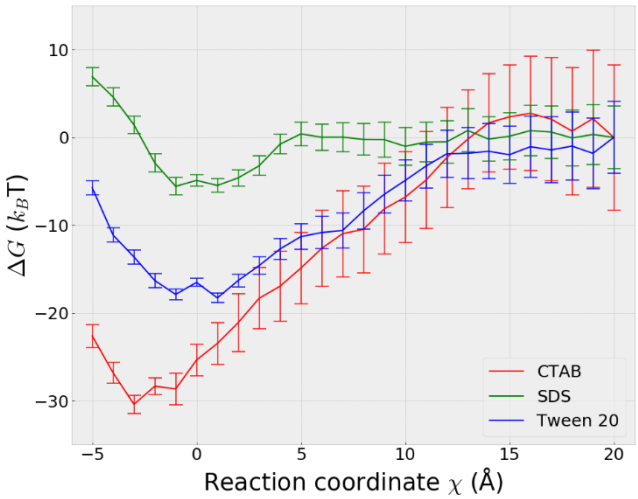

Fig. 7-8. PMF for three surfactants interacting with the PVDF membrane computed from umbrella sampling trajectories using WHAM. Curves are shifted so that free energy ΔG is zero at χ = 20 Å, as per earlier studies. Hence, ΔG values at each point represent the free energy of surfactant at specific χ with respect to when it is in bulk liquid. Error bars computed via bootstrap method.

Fig. 7-8 shows the Gibbs free energy (ΔG) versus reaction coordinate plots for the three surfactants, whose trends are expected of such energy profiles. Specifically, as the distance decreases, the ΔG magnitudes are negligible at larger distances and gradually increase (i.e., become attractive) to reach peak values, then decrease again as the steric hindrance effect dominates. The reaction coordinate corresponding to the minimum ΔG, known as equilibrium distance, is smallest for CTAB and largest for Tween 20. This is tied to the charges of the surfactants, with electrostatic attraction for CTAB leading to closer proximity [150]. In contrast to the trends in Fig. 7-7b, in which the surfactant-membrane interaction energy is the most negative for SDS, followed by Tween 20 then CTAB, Fig. 7-8 indicates that the ΔG value is the most negative for CTAB, followed by Tween 20 then SDS. Notably, the most attractive CTAB-membrane interaction displayed in Fig. 7-8 agrees with earlier reflectometry and EIS studies showing the strongest binding of CTAB onto the PVDF membrane [282, 283]. This validates the better predictive capability of ΔG, which concurrently accounts for all the three interactions in Fig. 7-7, namely, surfactant-water, surfactant-membrane and water-membrane. More specifically, the most negative ΔG for CTAB is expected to be correlate with the most significant flux enhancement (Fig. 7-3) [223] and retention (Fig. 7-4), which will be further illustrated in the following section.

7.3.4 Radial distribution function

To obtain detailed molecular level understanding of surfactant-membrane interactions, the RDF was analyzed. Specifically, the RDF, denoted by $g(r)$, depicts the concentration of a specific molecule with respect to distance r from another molecule [20], and thereby provides an indication of the affinity between the two entities. RDF is used here to reveal underlying reasons for differences in the ΔG profiles (Fig. 7-8) of the three surfactants and corresponding flux trend differences (Fig. 7-3).

Quantitative analysis via the RDF of the nitrogen atom on CTAB with respect to different atoms of the PVDF membrane is displayed in Fig. 7-9. Note that the nitrogen atom on CTAB is also used in the PMF analysis (section 7.2.2.3). The $g(r)$ values are exceptionally high for the CTAB–oxygen pair, indicating that the favorable free energy of CTAB is attributed to the hydroxyl and carboxylic groups on the PVDF surface. Interestingly, for SDS at the same distance, the hydrophilic head is consistently anchored onto the PVDF surface whereas the hydrophobic tail appears clearly repelled from the surface in some instances. Hence, between CTAB and SDS, the relative lack of affinity of the hydrophobic tail of the latter to PVDF underlies the unfavorable ΔG.

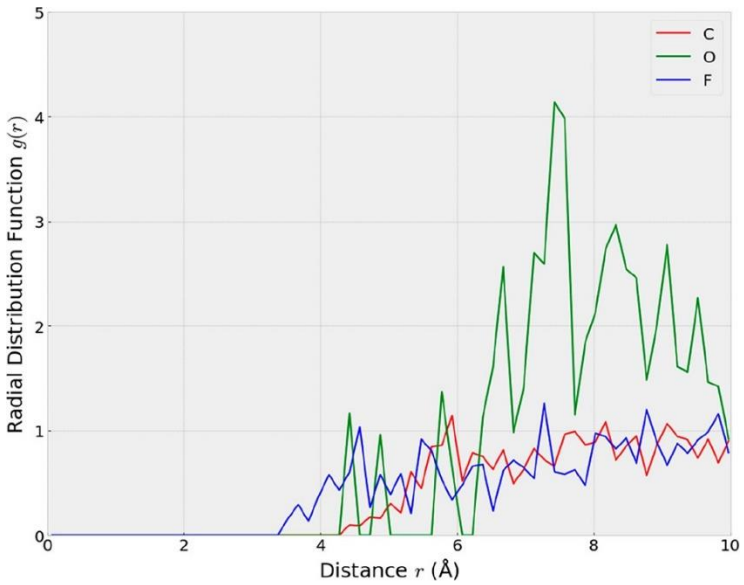

Fig. 7-9. RDF between the nitrogen atom on the adsorbed CTAB and various atoms (namely, carbon, oxygen, and fluoride) on the PVDF membrane, computed based on the umbrella sampling trajectory at the equilibrium distance of $\chi = -3$ Å.

Furthermore, Fig. 7-10 plots the RDFs between the oxygen atoms in water molecules within 10 Å of the PVDF surface for each surfactant at their respective equilibrium distances (identified in Fig. 7-8). The RDF curves of SDS and Tween 20 largely overlap, indicating similar water networks at the PVDF surface. On the other hand, the $g(r)$ values of water molecules for the CTAB system are lower than the other two surfactants, reflecting a relatively looser water network near the PVDF surface,

which has been tied to higher permeation [16] and larger diffusion coefficient of water molecules [302].

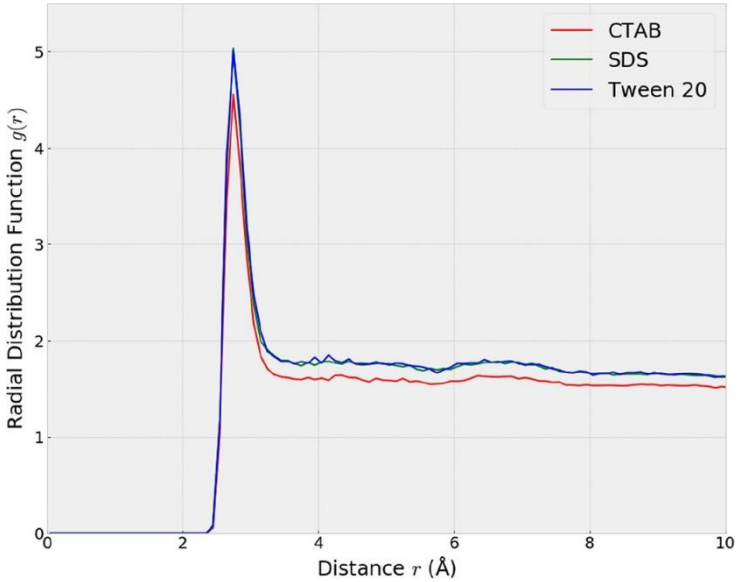

Fig. 7-10. RDF between oxygen atoms in water molecules within 10 Å from the PVDF surface. All curves are computed using the umbrella sampling trajectory at the corresponding equilibrium distances of three surfactants identified in Fig. 7-8. The SDS and Tween 20 plots almost superimpose on each other.

7.3.5 Enthalpic and entropic contribution

To further understand the adsorption behaviors of different surfactants, the Gibbs free energy (G) can be decomposed into enthalpic (H) and entropic (S) components [148, 151, 162]. In particular, adsorption onto a hydrophilic surface tends to be enthalpy-driven, whereby the favorable enthalpy term compensates for the loss of entropy upon adsorption due to steric hindrance [140]. Based on the definition of free energy (i.e., $\Delta G = \Delta H - T\Delta S$), the conventional approach evaluates enthalpic and entropic terms by running multiple simulations at different temperatures and performing a linear fitting. Recently, Gaberle et al. [162] pointed out that such a method may underestimate the entropy term since it neglects system dynamics with respect to temperature (T) by assuming ΔH and ΔS to be constant. Accordingly, a more accurate method has been reported to calculate the $-T\Delta S$ term [163] as shown by Eq. (34). Note that temperature T has been incorporated into the entropy term so that it has the same unit as that of ΔG and ΔH, allowing a direct comparison. The integration limit χ_m is the maximum reaction coordinate (20 Å), so that, similar to the free energy, entropy term also becomes zero when surfactant is fully detached from the surface. The enthalpic term is then computed by taking the difference between ΔG and $-T\Delta S$ at every reaction coordinate sampled.

The ΔG, ΔH and $-T\Delta S$ values are plotted against reaction coordinate for each surfactant in each sub-plot in Fig. 7-11. As the surfactant approaches the membrane surface, the decrease of entropy (i.e., increase of $-T\Delta S$) in Fig. 7-11 is relatively smooth, which indicates flexibility of all three surfactant structures [162]. Moreover, the adsorptions of all three surfactants are enthalpy-driven, reflected by the consistent negative ΔH values and positive $-T\Delta S$ values for most points, except for SDS when χ becomes very small. Hence, it is evident that surfactant charge only has an effect on the adsorption strength but does not determine whether the adsorption is driven by enthalpy or entropy. This is consistent with an earlier study [140], which indicates that hydrophilic surfaces (as in this case) tend to be enthalpic-driven, whereas hydrophobic surfaces (e.g., graphene) tend to be entropic-driven. In other words, the occurrence of minimum adsorption free energy shown in Fig. 8 results from the compromise between the enthalpic force towards the surface and entropic force towards the bulk liquid [148].

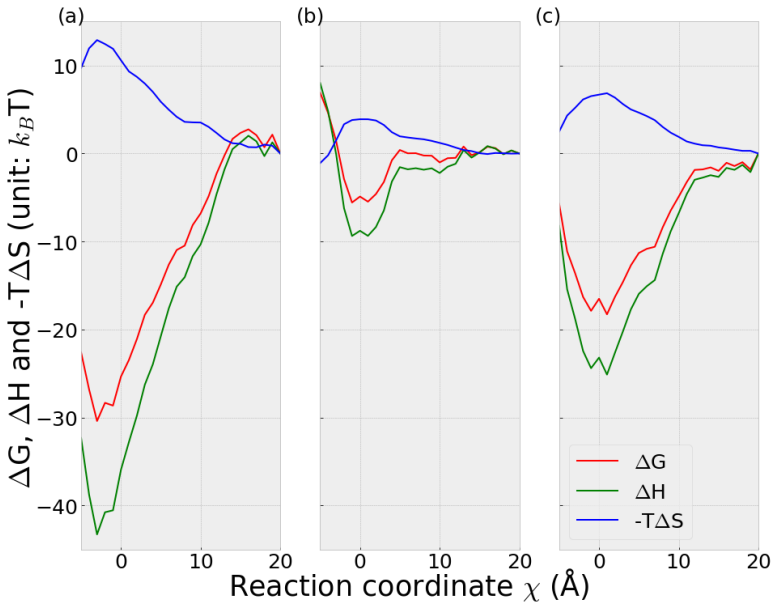

Fig. 7-11. Variation of ΔG, ΔH and $-T\Delta S$ with respect to reaction coordinate computed from umbrella sampling trajectories of (a) CTAB; (b) SDS; and (c) Tween 20. The unit on each *y*-axis is k_BT.

Regarding CTAB (Fig. 7-8a), although the entropy loss ($-T\Delta S$) is the highest upon adsorption, it is countered by the most negative enthalpy change (ΔH), resulting in the most attractive ΔG. In contrast, for SDS, both ΔG and ΔH become positive when χ is small, indicating repulsion from the membrane surface as SDS gets too close. Therefore, Fig. 7-11 sheds more light onto the flux (Fig. 7-3) and retention (Fig. 7-4) behaviors of the surfactants. Specifically, as a surfactant approaches the membrane, CTAB gets attracted and remains attracted due to the negative ΔG values at the low χ values, whereas SDS gets attracted (i.e., negative ΔG) then repelled (i.e., positive ΔG) when it

gets too close. Correspondingly, CTAB adsorption onto the membrane is most energetically favorable while SDS the least.

7.4 Conclusions

Although membrane-based separation of oil emulsions is well-studied, the role of surfactant remained incompletely understood. In particular, CTAB has been reported to give a surprising enhanced flux relative to that by DI water alone [223]. To better understand this, MD simulations were conducted. Specifically, the molecular-level interactions between surfactants with different charges, namely, cationic CTAB, anionic SDS and nonionic Tween 20, and a hydrophilic PVDF membrane surface were studied.

Unbiased MD simulations quantify the surfactant-water, surfactant-membrane and water-membrane interactions, but none appears well-correlated to the relative flux trends due to the significant interplay among all three. Specifically, because surfactant-membrane adhesion involves local dehydration as well as affinity of both entities, either of the three interaction energies alone is inadequate. To account for all interactions concurrently, umbrella sampling was performed to obtain the PMF curves. The results affirm that flux enhancement and highest retention of CTAB was caused by the most significant CTAB adsorption and the highest water density near the surface, which is underlie by the most negative enthalpic energy at small CTAB-membrane distances and corresponding highest water-membrane RDF peak. On the other hand, the flux decline and lowest retention of SDS was caused by the least SDS adsorption and lowest water-membrane RDF peak at the equilibrium distance, which is underlie by not only the least negative peak ΔH value but also repulsive enthalpic interactions at very small SDS-membrane distances. Such mechanistic understandings obtained at the Angstrom level are not possible by experiments and are useful for providing more insights into the roles of surfactants in membrane-separation applications.

This study preliminary investigated the interaction between different surfactants and membrane in atomistic resolution. Research effort should be dedicated to further include the effect of oil droplets or micellization of surfactant in future. In addition, there could be a potential trade-off regarding process performance versus degradability and reusability of surfactant, which should also be considered for environmental sustainability.

Chapter 8 – Molecular Dynamics Investigation of Membrane Fouling in Organic Solvents

All studies presented in previous chapter investigated membrane fouling phenomenon in aqueous systems. Nevertheless, membrane separation also plays an important role in pharmaceutical processes where organic solvent environment becomes very common. Earlier experimental studies had shown that fouling insights obtained in water systems may not be directly translated into organic solvent systems. Therefore, this study was designed to investigate how organic solvent network near membrane-foulant interface affected the fouling behavior.

8.1 Introduction

In recent decades, membrane technology has grown rapidly particularly in the field of water treatment [10, 303, 304]. Leveraging on well-established operations of water-based systems, there has been increasing interest in the possibility of applying membrane-filtration to organic solvent-based feeds [305, 306]. To this end, fabrication of organic solvent resistant membranes with limited membrane swelling has been investigated extensively [307]. Marchetti et al. [306] summarized the transport models used for the design and prediction of organic solvent NF processes, highlighting the significance of solute-membrane interactions and the corresponding influence on the filtration process. Regarding the scale-up of solvent-resistant NF units from laboratory to pilot-plant and production scale, Lim et al. [305] reviewed the state-of-the-art mixed matrix and thin film nanocomposite membranes used in various industries, and concluded excellent recovery, rejection and cost reduction can be achieved.

With the general acknowledgement of membrane fouling as a major hurdle for harnessing the advantages of membrane-filtration compared to conventional separation processes, a comprehensive database on mitigation of fouling induced by typical foulants present in aqueous feeds has been collated [13, 14, 308]. As for a corresponding effort on understanding the membrane fouling phenomenon during organic solvent filtration, less attention has been given so far. Zaidi and Kumar [309] studied dead-end UF of PEG and dextran in water-ethanol mixtures, and found that significant gel formation and concentration polarization occurred at a much higher bulk solute concentration compared to that in pure water. Yin et al. [310, 311] systematically compared the fouling extents of colloidal foulants in various organic solvents. Flux decline and cake resistance in dead-end operation were interpreted with the DLVO/XDLVO theory and fouling model to reveal the effect of solvent polarity on the

fouling extent. Lay and Chew [312] recently utilized the DOTM technique to quantify the critical flux of silica particles in cross-flow MF. The shear-induced diffusion model turned out to be applicable only in water and formamide, and the solvation film effect must be included in ethanol to account for additional silica-silica repulsion. Based on all these experimental results, it is clear that solvent type significantly affects membrane fouling behavior. Therefore, the current study is targeted at contributing to the knowledge base through providing molecular-level insights.

As with experiments, the continuous phase is usually water for membrane-fouling studies using MD [118], while relatively little information is known for organic solvents. Liu et al. [100] developed an efficient MD protocol to simulate the swelling of polymeric membranes in organic solvents. The swelling degree of membranes was found to be correlated with the mean pore size, and the solubility parameter difference between solvent and membrane. Xiong et al. [57] investigated the adsorption of a polyaromatic compound onto the silica surfaces in heptane and toluene with the umbrella sampling method, and identified that the solute molecules were only adsorbed onto the surface in heptane to form strip-shaped aggregates, whereas remained suspended in bulk toluene. Mohtashami et al. [313] focused on the stability of enzymes in organic solvents and concluded that the tertiary structure is the critical control factor for stability. Moreover, polar and non-polar solvents resulted in different enzyme structures, with the presence of water playing a pivotal role. Collectively, these MD studies have harnessed the benefits of MD to enhance the understanding on effect of organic solvents. To further build on this, the current study aims to assess what underlies the different membrane fouling behaviors in different solvents.

The relative lack of understanding on the effect of organic solvent on membrane fouling motivated the current study. MD simulations were performed for the dextran foulant and a PAN membrane in three solvents, namely, water, formamide and ethanol. The tendencies for dextran to adsorb onto the membrane in the different solvents were first evaluated, and the model used was validated with experimental flux decline results. Then, the dextran-membrane, solvent-dextran and solvent-membrane interaction energies, along with the number of hydrogen bonds between the three pairs, as well as the solvent-accessible surface area (SASA) of dextran were investigated, followed by plotting the solvent-membrane and solvent-dextran RDFs. Analysis of simulation results highlighted the importance of solvent effect in terms of competitive adsorption of dextran and solvent molecules onto the membrane surface. These results are expected to be valuable in substantiating the current limited understanding regarding molecular-

level fouling mechanism in non-aqueous environment and explaining the different membrane fouling extents in different solvents.

8.2 Simulation Methodology

All the molecules used in the simulation are presented in Fig. 8-1.

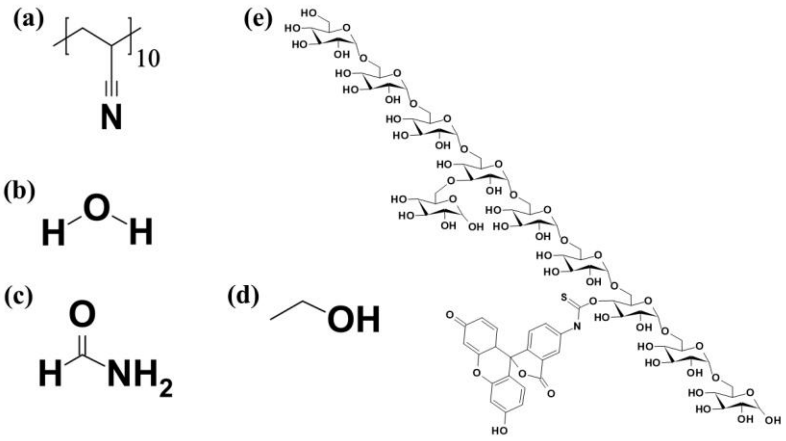

Fig. 8-1. Chemical formula of molecules simulated: (a) PAN membrane, with each chain consisting of 10 acrylonitrile monomer units; (b) – (d): solvent molecules investigated, namely, water, formamide and ethanol; and (e) fluorescein isothiocyanate dextran, with the backbone consisting of 9 α-D-1,6-glucose units, and a α-1,3 branching glucose unit attached at the 4th glucose unit and a fluorescein isothiocyanate side group attached at the 7th glucose unit.

8.2.1 Construction of PAN membrane

The PAN membrane used in this study was prepared based on the same method used in constructing the PVDF membrane in our earlier study [55]. Briefly, 80 short chains of acrylonitrile each consisting of 10 monomer units (Fig. 8-1a) were packed to form an amorphous structure in the simulation box, which was allowed to equilibrate until there was no significant change of density. A rigid graphene layer was added on top during the construction process to restrain the motion of polymer chains in *z*-direction and make the top surface smooth. The resultant flat substrate PAN membrane has dimensions of approximately 80 Å length by 80 Å width by 22 Å depth. The final density of the PAN membrane is around 1.14 g/cm^3, which is close to experimental value of 1.18 g/cm^3 [314].

8.2.2 Dextran structure

Dextran, a polysaccharide, was modeled in a similar manner as our previous study [109]. As shown in Fig. 8-1e, the backbone of dextran consists of 9 units of glucose units which are connected in α-D-1,6 manner. Moreover, natural dextran consists of approximately 5% of branched α-1,3 linkages [315], so a branched glucose unit was

added at the 4th unit of the main chain. Lastly, a fluorescent side group, whose structure is given by SigmaAldrich to be consistent with the experiments (Section 8.3), was added to the 7th glucose unit. The positions of the side groups are random in nature, and specified as such in this study to avoid chain-end effects, as an earlier study has demonstrated that the position of one side chain does not significantly affect the interaction energy and binding affinity [134]. The molecular weight of the dextran molecule used in the simulation is 2 kDa, similar to the model polysaccharide in our previous study [109].

8.2.3 System packing and simulation details

The initial system configuration was prepared by Packmol [65]. The PAN membrane was placed as a rigid, fixed surface at the bottom of the simulation box, and one dextran molecule was placed at a distance of 10 Å from the membrane surface [313, 316]. Only one dextran was included, which translates to a feed concentration of 0.2 g/L. The densities of the solvents governed the number of solvent molecules (Fig. 8-1b – d) used in the respective simulation box, namely, 12800 for water, 6000 for formamide and 4000 for ethanol. The dimension of simulation box was approximately 85 Å × 85 Å × 80 Å. Although it is possible for foulant to interact with the upper membrane surface which is the mirror image of the bottom one [107], the *z*-dimension turned out to be large enough so that such a phenomenon was not observed during all runs. OPLS-AA force field parameters, which have been widely implemented for organic solvents [57, 100, 317, 318], were assigned to the PAN membrane, solvent, and dextran molecule. The SPC/E model was applied for water molecules [48]. Since the solvation effect is the focus of this study, unbiased simulation was applied avoid any perturbation of solvent network resulted from external pulling force. Moreover, past studies tended to use one single run to simulate polysaccharide with repetitive monomer units [169, 202, 226] which are similar to dextran backbone, whereas multiple runs start from different initial orientations, or multiple molecules placed at different initial position are a common practice for polysaccharide with varying monomer units [134, 149, 153]. Considering that there are two approaches for MD simulation to enhance sampling of phase space (i.e., more independent runs, or longer simulation time) [87], it was determined that two replicate runs with different initial dextran orientations were conducted for each solvent with a relatively long production time length for statistical validity.

The simulations were performed in LAMMPS [76]. Periodic boundary conditions were applied to all boundaries of the simulation domain. The VDW interactions were calculated by the LJ non-bonded interaction with the cut-off set to be 15 Å, as per earlier studies [57, 132, 319]. Long-ranged electrostatic interactions were computed in the reciprocal space by the PPPM Ewald method. All covalent bonds involving hydrogen in solvent molecules were constrained by the SHAKE algorithm in order to enhance simulation stability [36, 313, 316]. All simulation runs follow the same sequence as per earlier studies [36, 55, 94, 109]: (i) energy minimization of the system at 30 K; (ii) canonical ensemble (NVT) run at 298 K for 200 ps; (iii) relaxation NVT run at 298 K for 500 ps; (iv) equilibration run under the isothermal-isobaric ensemble (NPT) for 1 ns; (v) production run for 30 ns, with snapshots saved every 0.1 ns for analysis. The duration of the production run is within the typical range of MD studies [24]. Temperature and pressure in the NPT runs were controlled by Nosé-Hoover thermostat and barostat with coupling constants of 500 fs and 100 fs, respectively. The time step was selected to be 1 fs. Postprocessing of simulation data and visualization of saved snapshots were performed with VMD [53]. One single run took approximately 15 days to complete with 24-core CPU and Message Passing Interface enabled.

8.3 Experimental Setup

8.3.1 Chemicals

Solvent-resistant PAN UF membranes (UF 010104) were purchased from Solsep. The mean pore size was 54.3 nm, as measured by evapoporometry [320]. DI water was generated by the Milli-Q device (Merck-Millipore; Massachusetts, USA). Formamide with a purity higher than 99% (ReagentPlus®) was purchased from Sigma-Aldrich. Neutral fluorescein isothiocyanate (FITC) dextran (60842-46-8) with molecular weight specified as 4 kDa was also purchased from Sigma-Aldrich.

8.3.2 Cross-flow filtration

A bench-scale cross-flow membrane filtration system was used for the filtration experiments. The polytetrafluoroethylene (PTFE) membrane cell had an active area of 42 cm^2. A piston-metering pump (Eldex Laboratories, USA) was used as the feed pump, generating a constant cross-flow volumetric flow rate of 80 mL/min. The feed concentration was kept constant by continuous recycling of the permeate to the feed tank. The TMP, which was monitored using a pressure gauge (Coleparmer, USA), was

controlled by two stainless steel valves and a pressure gauge stainless steel joints was applied for adjustment.

A new PAN membrane was used for each experiment. The filtration system was rinsed with pure solvents (i.e., water or formamide) before every run; it should be noted that ethanol was not tested because of significant sedimentation of dextran despite ultrasonication. In order to generate similar initial solvent fluxes, the TMP values applied were 60 kPa for water and 200 kPa for formamide. The three steps implemented for each experiment are described as follows: (1) pure solvent filtration for 1 hour; (2) the targeted dextran amount was added to attain a concentration of 0.2 g/L and the system was allowed to stabilize for 15 minutes; and (3) filtration ensued for 6 hours, with permeate samples collected every 1 hour and weighed with an electric weighing balance (ME4002, Mettler-Toledo, Switzerland) to quantify the permeate flux.

The dextran concentration in feed and permeate samples were analyzed with UV-vis measurement (Shimadzu UV 2450 Spectrometer) in quartz cuvettes. Samples collected were stored at 4 ℃ for less than 24 hours and warmed to room temperature just prior to the measurement. The wavelengths of UV absorbance in water and formamide were 490 nm and 505 nm, respectively.

8.4 Results and Discussion

8.4.1 Adsorption behavior

Fig. 8-2 displays the final system configurations of dextran in the three solvents, namely, water, formamide and ethanol, with two independent runs of different initial dextran orientations for each solvent. Because dextran is a macromolecule, it orientates differently in different adsorption scenarios even in the same solvent, which agrees with earlier studies [118, 121]. Qualitatively, it is clear that the affinity between dextran and the PAN membrane is significant in water and ethanol, but weak in formamide. This highlights the non-negligible influence of the solvent medium in the adsorption tendency, which agrees with earlier experimental studies on different membrane fouling behaviors by the same foulant in different solvents [310-312].

The adsorption behavior of dextran onto the PAN membrane can be quantified by the distance between them during the production run (Eq. (37)). Successful adsorption of dextran is evidenced by small d value since dextran needs to displace the original solvent molecules on the membrane surface. Fig. 8-3 displays the evolution of d throughout the 30 ns of production run, which reflects whether dextran can be spontaneously adsorbed to the surface. The d values at $t = 0$ are different due to the energy minimization, relaxation, and equilibration steps before the production run,

despite the same initialization of the dextran-membrane separation as 10 Å in all cases. Two observations are worth highlighting from Fig. 8-3. Firstly, repeated runs of the same solvent give similar profiles, even though the anchoring points shown in Fig. 8-2 are different between the two independent runs. This indicates the different initial and subsequent orientations of dextran have negligible influence on the adsorption tendency in all three solvents, which deviates from earlier studies reporting the dominant influence of protein orientation on adsorption [115, 118], because of the repetitive monomer units on polysaccharides as opposed to the non-uniform charge distribution on proteins induced by various constituent amino acids. Secondly and more importantly, the three solvents result in distinctly different profiles, corroborating with Fig. 8-2 in terms of the significant effect of solvent type on the adsorption behavior. Among the three solvents, as evident in the *d* values, dextran adsorbs most strongly in water, followed by ethanol then formamide. Furthermore, the least fluctuations of the *d* values in water also reflect the most stable adsorption.

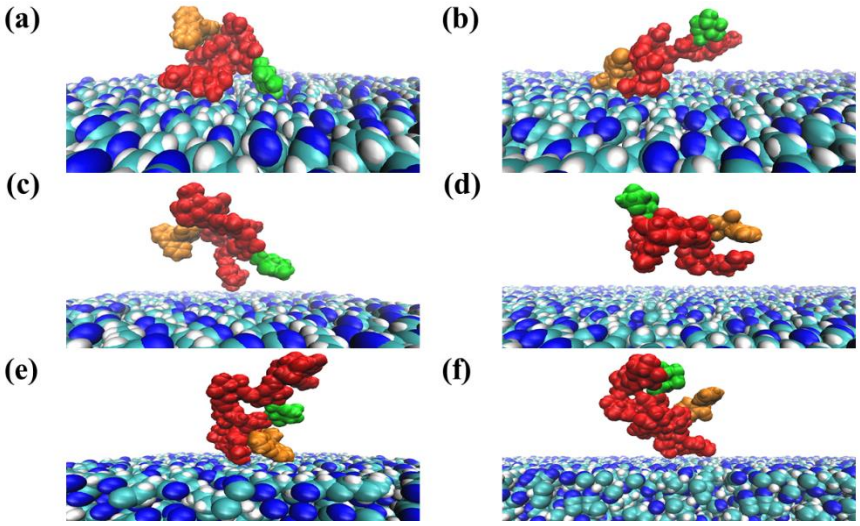

Fig. 8-2. System configurations at the end of 30 ns production runs for dextran in three different solvents: two runs each for (a and b) water, (c and d) formamide and (e and f) ethanol. PAN membrane is displayed with VDW style in VMD and atoms are colored blue for nitrogen, cyan for carbon and white for hydrogen. Dextran is displayed with SURF style in VMD: the backbone is colored red, the branched glucose unit green and the fluorescent side group orange. All solvent molecules are hidden for easier visualization of dextran adsorption onto the PAN membrane.

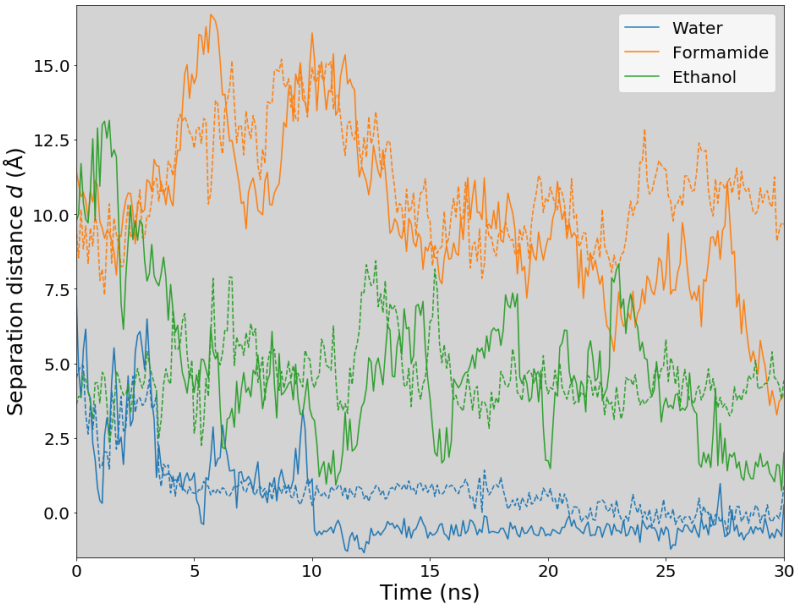

Fig. 8-3. Evolution of dextran-membrane separation distance d for two runs each in water, formamide and ethanol. The solvents are represented by different colors, and repeated runs by dashed lines.

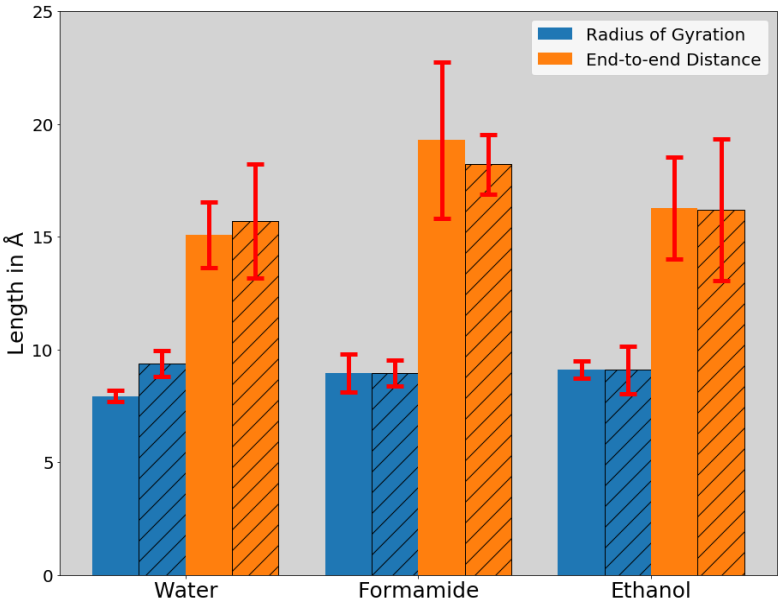

Fig. 8-4. Average radius of gyration and end-to-end distance of dextran in three solvents. Oxygen atoms in the 1st and 9th glucose ring of the backbone are selected to represent two terminals of dextran. Two replicate runs for each solvent are represented by unshaded and shaded bars. The error bars represent standard deviations.

The size of folding behavior of dextran can be further investigated based on radius of gyration and its end-to-end distance. Fig. 8-4 displays the average values obtained from six independent runs. The variation in end-to-end distance indicate that dextran went through a certain extent of unfolding and refolding during the simulation, whereas relatively stable value of radius of gyration proved that the overall structure was still intact. Moreover, these two values appear to be slightly smaller in water, indicating that dextran has a less open structure when adsorbed to the PAN surface compared to

unadsorbed cases. This also agrees with observation in Fig. 8-2a and 8-2b where multiple parts of dextran tended to attach to the surface.

8.4.2 Model validation

MD simulations regarding membrane fouling are usually linked with experimental results like permeation flux [36], surface imaging [55], spectroscopy [32, 109], solute removal measured by dissolved organic carbon or UV [226], etc. If acceptable match is found between simulation model and experiments, further analysis shall be conducted to characterize fouling process by computing various parameters that are difficult to obtain in experiments based on MD trajectories.

Validation of the model was carried out through comparison with experimental flux and rejection results. Note the solvents tested did not include ethanol due to the poor dissolution of dextran despite ultrasonication. Fig. 8-5 presents the experimental normalized flux and rejection trends over 6 hours of filtration of 0.2 g/L of dextran in water and formamide. The flux declines were limited because the hydrodynamic diameter of dextran was three orders of magnitude smaller than the membrane pores. Fouling had still occurred as proven by another complete experimental study of our group [321]. Nonetheless, the filtration behavior of dextran was clearly solvent-dependent in that the normalized flux decline was more severe in water, indicating more severe fouling as filtration proceeded. This agrees with the simulation results in Figs. 8-2 and 8-3. Specifically, the worse fouling experimentally observed in water (Fig. 8-5) agrees with the greater affinity between dextran and the membrane revealed by the simulations (Figs. 8-2 and 8-3). Moreover, higher dextran rejection was also consistently observed for water in Fig. 8-5b. Due to much smaller size of dextran compared to membrane pores, rejection values appear to be quite low throughout the filtration. Rejection values agree with simulation results as well. In water, higher retention is observed since dextran has higher tendency to be adsorbed onto membrane surface or deposit inside the pore. In contrast, dextran prefers to stay in bulk formamide and passes through to the permeate together with solvent flow, resulting in very low rejection value, sometimes even negative which is attributed to the augmented concentration polarization effect occurring when rejection is very low [322]. These results provide qualitative validation of the model.

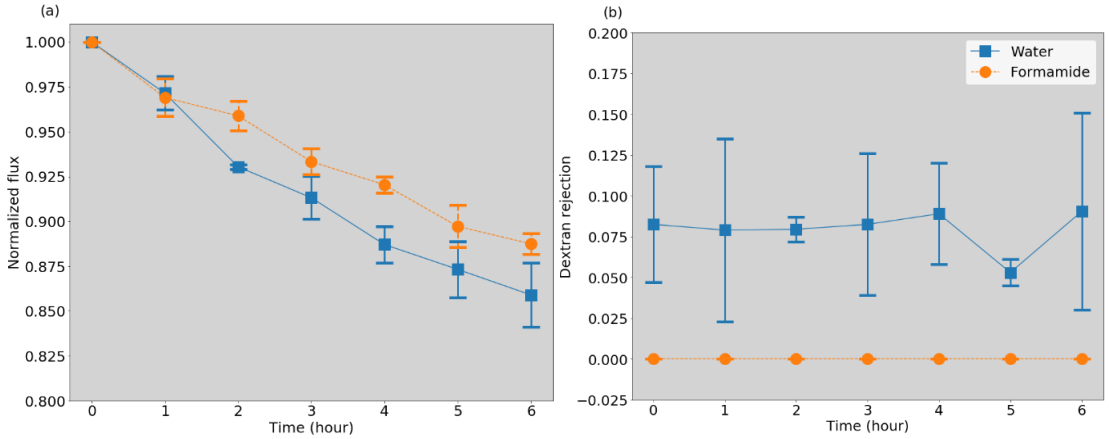

Fig. 8-5. Experimental flux (a) and rejection (b) trends of cross-flow filtration of 0.2 g/L dextran solution in water and formamide. The TMP values were 60 kPa for water and 200 kPa for formamide to ensure similar initial fluxes of around 400 LMH.

8.4.3 Interaction energy

The Gibbs free energy of foulant-membrane interaction has been shown to be a good predictor of membrane fouling [13]. On the other hand, in contrast to surface-foulant interaction which serves as the driving force for adsorption, the solvent phase tends to provide a repelling force against stable adsorption [140]. Therefore, comparison of interaction energy values in different solvent environment gives critical information regarding how solvation interaction varies with respect to solvent type and thus, how fouling is affected consequently. MD simulation enables the direct computation of the interaction energy between different entities, and with OPLS-AA force field applied, the interaction can be further decomposed into electrostatic and VDW constituents. The effectiveness of using interaction energy between different entities to characterize membrane fouling processes has been proven by earlier studies [36, 107, 118]. Fig. 8-6 plots the average interaction energies between three pairs of entities, namely, dextran-membrane, solvent-dextran, and solvent-membrane, in all three solvents.

Regarding the dextran-membrane interaction energy (Fig. 8-6a), the solvent effect is evident. Whereas the dextran-membrane interaction is clearly attractive in water, that in formamide and ethanol are not so obviously. This underlies the smallest dextran-membrane separation distance in water in Fig. 8-3 and the more severe fouling in Fig. 8-5. Indeed, the dextran-membrane interaction energy is highly dependent on *d*, demonstrated by Fig. 8-7. It is evident that VDW component is negligible when *d* is relatively large, showing its shorter range as compared to electrostatic component. In comparison with runs in two organic solvents, both electrostatic and VDW component of dextran-membrane interaction energy becomes highly attractive in water when dextran is firmly adsorbed onto the membrane (i.e., small *d* values). With respect to

solvent-dextran interaction (Fig. 8-6b), the influence of solvent is relatively less, with that in ethanol slightly less attractive than the other two. Notably, although all three solvents are polar and protic, the electrostatic interaction is predominant in water, whereas the electrostatic contribution is less for the formamide and ethanol solvents. This observation underlines intrinsic differences between aqueous and organic solvents. As for solvent-membrane interaction (Fig. 8-6c), that in water is least attractive, followed by ethanol then formamide. This indicates that the stronger the affinity between the solvent and membrane is, the weaker the dextran adsorbs onto the membrane. In particular, for all solvents, the VDW components are consistently greater than the electrostatic ones, indicating the relative dominance of these short-range forces in binding the solvent to the membrane and thereby creating a barrier to dextran adsorption. In summary, the importance of solvation effect on adsorption is highlighted by values present in Fig. 8-6. Without external force applied, solvent networks formed by formamide and ethanol were much harder to break compared to water. Thus, interaction energy analysis conducted from unbiased simulation serve as a simple and effective method to predict fouling potential in different solvent conditions.

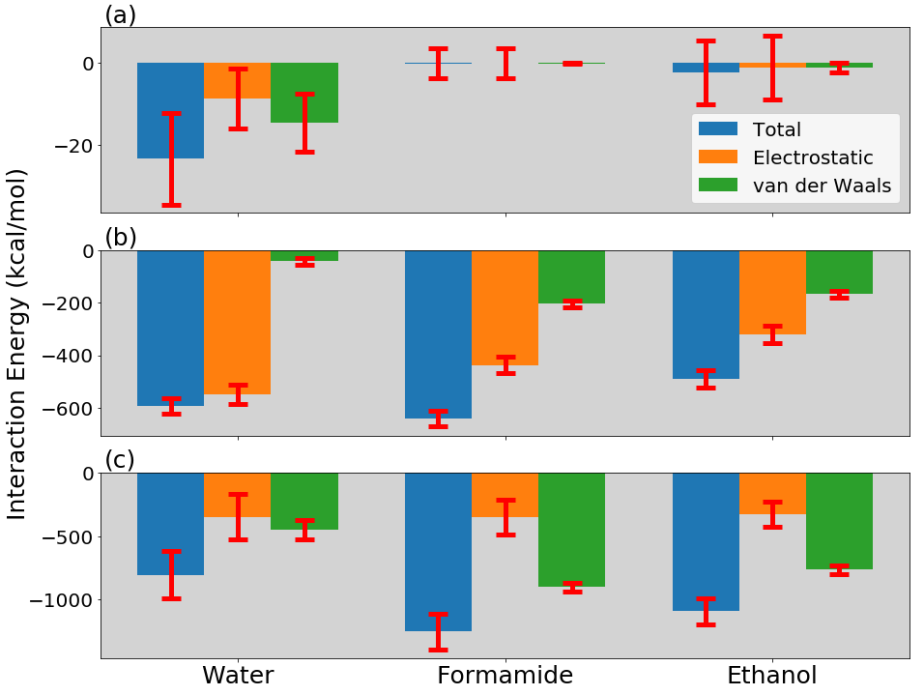

Fig. 8-6. Average interaction energy between different pairs of entities in the three solvents: (a) dextran-membrane; (b) solvent-dextran; and (c) solvent-membrane. The error bars represent standard deviations.

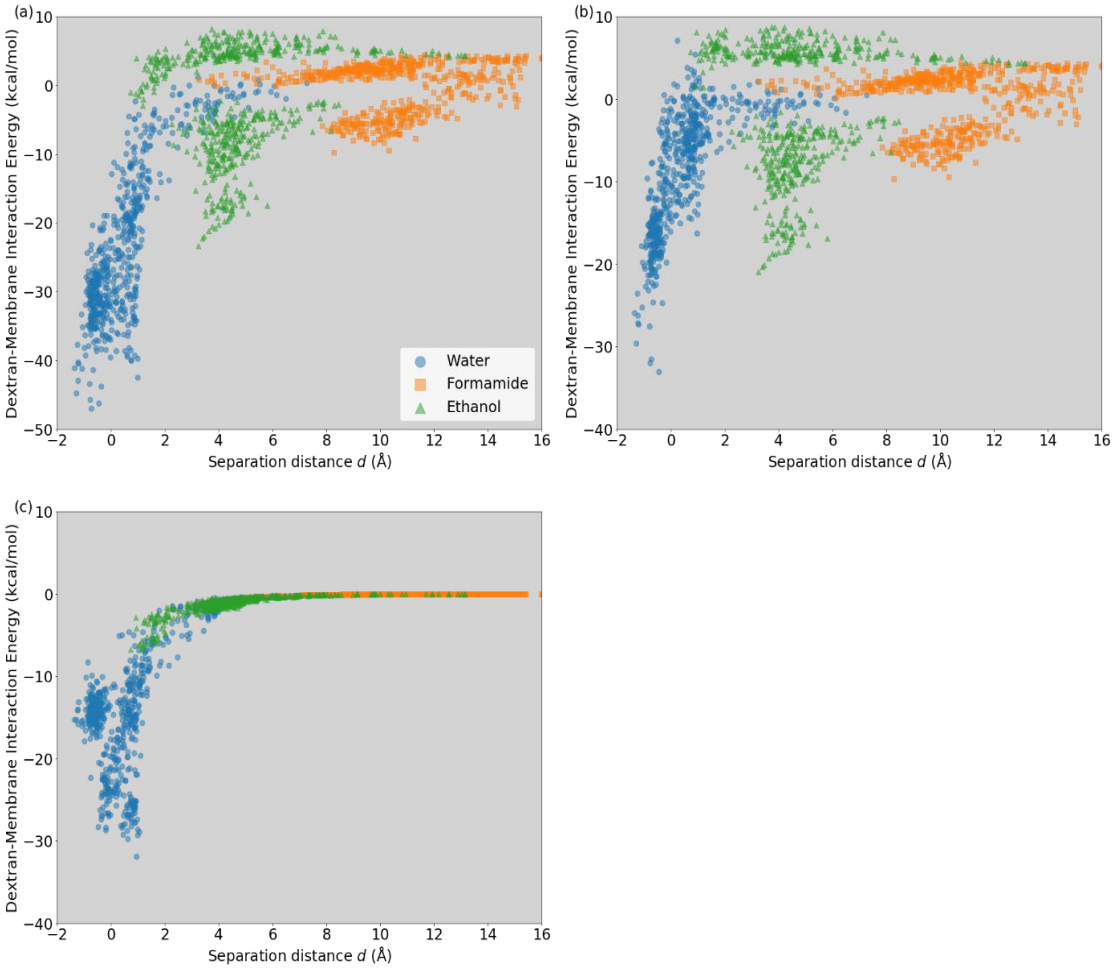

Fig. 8-7. Plots of dextran-membrane interaction energy with respect to separation distance *d* in three solvents represented by different marker colors. (a) Total interaction energy; (b) Electrostatic component; (c) VDW component.

8.4.4 SASA and hydrogen bond

Because the solvent-dextran interaction energies are similar for the three solvents (Fig. 8-6b), further investigation of the solvent effect was carried out through quantifying the SASA of dextran and number of hydrogen bonds, as detailed in Table 8-1. The SASA of dextran, which represents the surface area on dextran in contact with the solvent, was readily quantified via an embedded algorithm in VMD [316]. This deviates from the conventional VDW surface area defined by radii of atoms, since macromolecules have complex structures like internal cavities that are inaccessible to surrounding solvent molecules [323]. With respect to hydrogen bond, the donor-acceptor distance and angle cut-off for hydrogen bond were set respectively to 3.5 Å and 30° [214], as per earlier studies [55, 94, 109]. In particular, for the solvent-solvent pair, the number of hydrogen bonds was averaged over all the solvent molecules within 10 Å of the PAN membrane surface, where the solvent network is perturbed by both the membrane and dextran.

Table 8-1. Summary of solvent-accessible surface areas (SASA) for dextran and number of hydrogen bonds formed between different pairs in three solvents. Values are averaged over all snapshots saved from the production run.

	Water	Formamide	Ethanol
SASA (nm^2)	19.89 ± 1.19	21.14 ± 0.81	20.40 ± 1.05
Number of hydrogen bonds			
Solvent-solvent (per solvent molecule)	1.24 ± 0.05	0.92 ± 0.03	0.57 ± 0.03
Dextran-dextran (per dextran molecule)	1.77 ± 1.46	3.65 ± 1.23	5.19 ± 1.62
Solvent-dextran (per dextran molecule)	54.34 ± 5.04	49.89 ± 5.23	32.37 ± 5.04

Table 8-1 shows that the mean SASA is the highest for formamide, followed by ethanol then water, which agrees with the adsorption (Fig. 8-3) and fouling (Fig. 8-5) trends. This is because high SASA indicates greater solvent coverage, and thereby greater tendency to stay in the bulk liquid and lesser tendency to interact with the membrane. While the solvent-dextran interaction energy for water is in between that of formamide and ethanol (Fig. 8-6b), the SASA value of water is the least, suggesting a lack of correlation between the two parameters and the relative importance of the latter in relation to adsorption. Regarding hydrogen bonding, water is the most superior, resulting in the highest number of hydrogen bonds between the solvent-solvent and solvent-dextran pairs, which in turn leads to the least number of hydrogen bonds between dextran molecules. Since hydrogen bonds are relatively weak interactions, the greatest number of hydrogen bonds between dextran and solvent in water (Table 8-1) not only gives a solvent-dextran interaction energy in water that is less than that in formamide (Fig. 8-6b), but also does not tie in well with the highest adsorption tendency (Fig. 8-3). This indicates that the number of hydrogen bonds may not serve as a reliable predictor of membrane fouling.

8.4.5 RDF

By definition, RDF, denoted by $g(r)$, is the density that a molecule experiences as a function of radial distance r normalized with respect to the bulk density in the simulation domain [324]. RDF enables direct visualization of how solvent molecules

form solvation shells (i.e., aggregation of solvent molecules at a specific radius, as denoted by distinct peaks) around the membrane and dextran. It should be noted that representative atoms that form similar bonds need to be selected for determining RDF [109]. In this study, the oxygen atom in water and ethanol, and nitrogen atom in formamide are selected to represent the solvent, since all of them are sp^3 hybridized, able to form hydrogen bonds and yield RDF curves with similar shapes. Figs. 8-8 and 9 illustrate the RDF plots of the solvent-membrane pair and solvent-dextran, respectively.

Fig. 8-8 presents the solvent-membrane RDF plots with nitrogen in the PAN representing the membrane, revealing the geometrical arrangement of solvent molecules near the membrane surface. Since solvent molecules tend to experience rapid exchange rate at the interface which is fast enough to sample this region, the free energy difference can be directly computed based on RDF [139], which are mirror symmetry compared to RDF curves in Fig. 8-8. A few points are worth highlighting. Firstly, the RDF curves of the two runs in formamide and ethanol almost perfectly superimpose on each other, whereas the two in water are slightly different despite similar overall shape. This is tied to the strongest adsorption of dextran onto the PAN surface in water (Fig. 8-3), which causes the film structure to be influenced by the orientation of the dextran molecule. Secondly, the intensity of the RDF peak is the highest for formamide, which agrees with the highest solvent-membrane interaction energy (Fig. 8-6c). This implies that the membrane surface is most extensively surrounded by the formamide molecules, which deters adsorption by dextran and thereby causes the least adsorption tendency by dextran (Fig. 8-3). Fig. 8-8 reveals that the spatial arrangement of the solvent molecules are similar, likely due to the similar natures of polar and protic, but the densities of the solvents in the solvent shell differ, which influences the membrane fouling tendency.

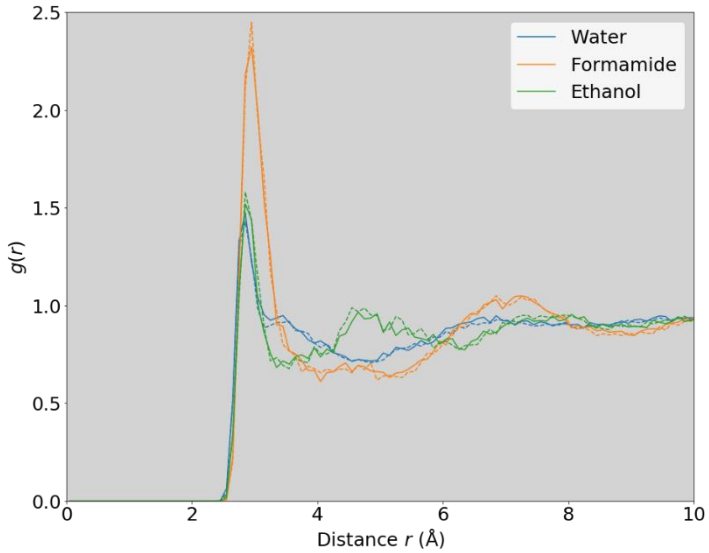

Fig. 8-8. RDF plots of solvent-membrane pair. Center atoms selected are nitrogen for PAN membrane and formamide, oxygen for water and ethanol. Two runs of each solvent are represented by solid and dash lines of the same color.

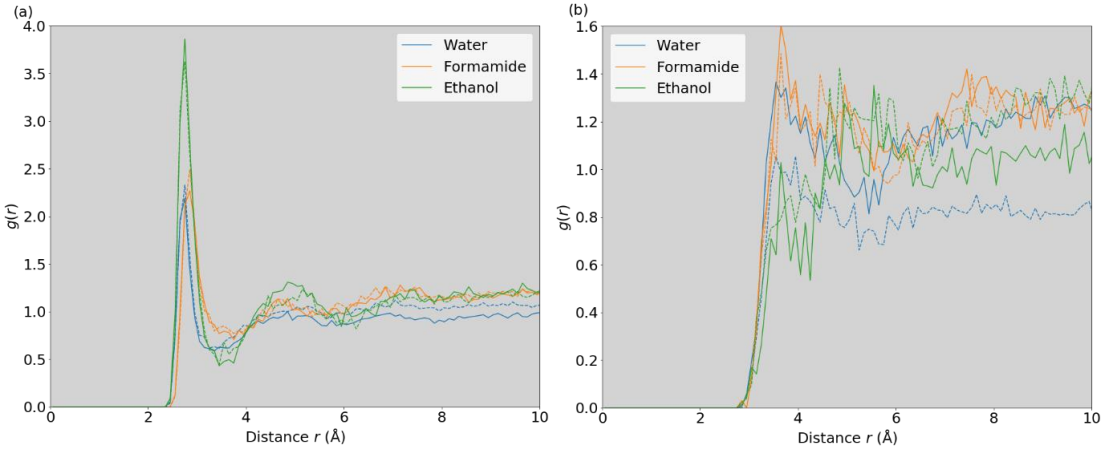

Fig. 8-9. RDF plots of solvent-dextran pair. Center atoms selected for solvent molecules are nitrogen for formamide, and oxygen for water and ethanol. Center atoms selected for dextran are: (a) hydroxyl oxygen atoms which represent the backbone and branching glucose unit; (b) aromatic carbon atoms which represent the fluorescein side group. Two repeat runs of each solvent are represented by solid and dash lines.

Furthermore, although partial inward folding may occur, solvent molecules are still able to accommodate small gaps formed in between and access to all groups of dextran. Fig. 8-9 explores the aggregation of solvent molecules around dextran through solvent-dextran RDF curves quantitatively. It should be noted that unlike solvent molecules, free energy profile of dextran can only be generated using methods like SMD and umbrella sampling [139], which go beyond the scope of this study due to different simulation techniques and much longer simulation time needed to ensure sufficient sampling of space. Since dextran is a macromolecule with different distinct parts, two sets of RDFs are generated, with Fig. 8-9a obtained using the hydroxyl oxygen to represent the backbone and the branching unit, and Fig. 8-9b obtained by using the

aromatic carbon to represent the fluorescein side group. The different shapes of the RDF curves in Figs. 8-9a and b implies that the behaviors at different local sub-regions of dextran are different. For Fig. 8-9a, solvent molecules aggregate at specific distances from dextran, forming distinct solvation shells represented by the local maxima and an overall RDF curve shape largely resembling that in Fig. 8-8. The positions of the solvation shells are similar among the solvents, with the first shell located at around 2.75 Å and the second shell at around 5 Å. However, the peak magnitude at 2.75 Å is much higher in ethanol compared to the other two solvents, indicating that more ethanol molecules are aggregated in the first solvation shell closest to dextran. This agrees with an earlier experimental study that reported the preferential formation of a solvation film around the foulant in ethanol but not water and formamide [312, 325]. This observation highlights that although both ethanol and formamide are polar and protic organic solvents, fouling mitigation mechanism is quite different: ethanol solvation film around the foulant versus strong formamide-membrane affinity. In comparison, Fig. 8-9b shows that the shape of RDF curves corresponding to the fluorescein side group in dextran do not exhibit distinct peaks, which means that the solvent molecules do not form well-defined solvation shells. This could be attributed to the more complex structure of the side group, which involves multiple fused aromatic rings as shown in Fig. 8-1e. Among the solvents, the densities of solvent molecules surrounding dextran are generally higher for formamide. Collectively, Figs. 8-9a and b indicate that relatively lower densities of water molecules around dextran, which agrees with the lowest SASA values for dextran (Table 8-1) and is tied to the highest adsorption tendency (Fig. 8-3).

8.5 Conclusions

To enhance the mechanistic understanding on membrane fouling in organic solvents, MD simulations were carried out for the dextran foulant and a PAN membrane in three solvents, namely, water, formamide and ethanol. The dextran-membrane separation distance profiles show that the adsorption tendency was the greatest for water, followed by ethanol then formamide. This agrees with the experimental data revealing worse flux decline for water relative to formamide. The results demonstrate the significant influence of solvent environment on membrane fouling.

Regarding interaction energies, the greatest adsorption tendency in water is tied to the most attractive dextran-membrane interaction, while the least adsorption tendency in formamide to the most attractive solvent-dextran and solvent-membrane interactions.

This suggests enhanced solvation of the foulant or membrane deters foulant adsorption onto the membrane and thereby mitigates membrane fouling. This is further substantiated by the higher SASA values for dextran in formamide and ethanol, and also distinctly highest densities reflected in the RDF plots of the solvent-membrane and solvent-dextran pairs for respectively formamide and ethanol.

The solvation of foulant and membrane by water deviates from that by other similarly polar and protic solvents, which has important implications in membrane fouling. Solvent properties significantly affect the compactness of the original solvent network formed on top of the membrane, and hence determine whether dextran has sufficient driving force overcome such an energy barrier and adsorb to the surface. Thus, choosing specific organic solvents that possess strong solvation capability of either membrane or foulant could be a promising fouling mitigation option. This study underscores the need for further understanding of membrane fouling behaviors in organic solvents, particularly as such applications proliferate in various industries.

Chapter 9 – Future Perspectives

In this thesis, after reviewing the existing studies of using MD simulation in membrane fouling field, representative studies conducted for foulants like NOMs, protein, surfactants are presented in detail. Molecular-level insights revealed by MD has proven that fouling is highly dependent on both foulant characteristics at atomic scale (e.g., specific adsorption sites on protein) and surrounding solution environment (e.g., the formation of solvation film around membrane or foulant by organic solvents). Macroscopic parameters obtained in experiments, like zeta potential or hydrophilicity, may not be 100% reliable when it comes to fouling tendency prediction. Although MD has already evolved into a powerful technique to characterize fouling systems beyond the scale of conventional experiments, there are still ample room for development, especially related to some of its intrinsic limitations. In this chapter, future perspective of MD for membrane fouling are proposed.

Rapid development of computational power has facilitated a tremendous increase in the number of studies using MD simulations to investigate the membrane fouling phenomenon, which is a primary challenge in membrane-filtration processes. The literature review part of this thesis started with a summary of the general workflow for constructing a MD system for studying fouling, with an overview of basic theoretical MD principles. Subsequently, key parameters generated from unbiased MD trajectories, which are widely used to describe interfacial behaviors, are discussed. Typical methods to present and interpret these parameters are presented. Then, to tackle the difficulty of inadequate sampling by unbiased simulations, representative biased simulation techniques with enhanced sampling algorithms are presented. Illustrative FEL results from literature are exhibited to reveal the dynamics of foulant/adsorbate near the surface. Finally, the commonly reported model foulants in MD studies are reviewed to summarize their respective fouling characteristics identified from corresponding papers. Based on the comprehensive review, six separate studies conducted throughout the 4-year candidature period of PhD are presented in detail. MD simulations were proven to be excellent supplement experimental studies, which are limited in the spatial scale provide by MD. Fig. 9 overviews the future outlook of MD in the membrane fouling field, highlighting a few directions that remain relatively under-developed at this moment and would benefit from the dedication of further research efforts.

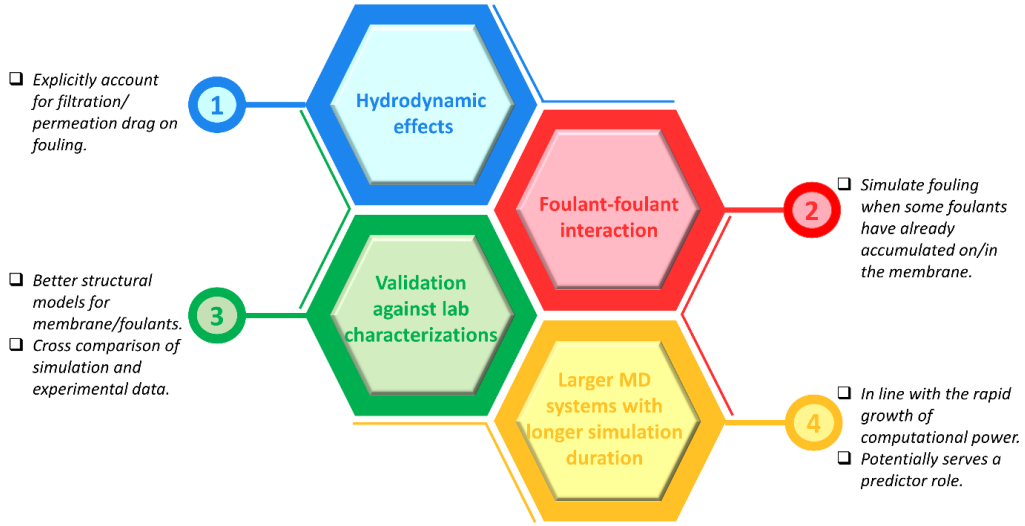

Fig. 9. Future outlook of the usage of MD for membrane fouling investigation.

Firstly, there seems to be a lack of MD studies focusing on the effect of hydrodynamics (e.g., permeation drag on the presence of filtration) on fouling. This is because the pore size of MF/UF membrane is beyond the spatial scale of MD, so the membrane is usually modeled as a non-porous plane without any explicit pores. While non-equilibrium MD studies do exist for NF/RO membrane with permeation occurring, the transmembrane pressure applied is much higher than the practical operation, ranging from 50 bar [133] to 4000 bar [56], to limit the time scale necessary while still capturing the underlying physics [100]. Future study is required to verify whether such a high pressure is representative of the actual fouling scenario. Methods to overcome such a shortcoming of MD need to be developed in the future. A potential solution to account for hydrodynamic effects on fouling would be to include an appropriate magnitude of body force on the foulant in the direction of permeation, so as to approximate the effect of filtration. The effect of crossflow and more complex flows in hollow fiber or tubular modules also need to be accounted for.

Secondly, most of the past studies have only included one foulant molecule in the system. In other words, the focus was on the initial stage of fouling, during which the governing factor is the interaction between the foulant in bulk solution and a clean membrane surface. However, foulant-foulant interaction becomes non-negligible with the progression of filtration due to the accumulation of foulants on the membrane surface or inside the membrane matrix. Although the limited spatial and time scale of MD precludes capture of the whole filtration process, it is still worth investigating how fouling is affected when the membrane surface is entirely or partially covered by foulant. For instance, the MD system can be designed in such a way that some foulant are pre-adsorbed to the membrane surface. There have been a few studies on foulant-foulant

interaction by including more than one foulant molecule in the system [93, 114, 118], but more studies are warranted to obtain a more comprehensive understanding.

Thirdly, for enhancing validation of MD models, better designed experiments can be carried out in future studies. As mentioned in section 2.1.4, experimental data are available for the preparation of MD systems (e.g., density and surface charge of membrane samples), as well as validation of simulation results (e.g., flux decline or foulant retention data). With the increasing sophistication of experimental characterization techniques, more accurate model structures for both membrane and foulant can potentially be built. Similarly, advanced fouling characterization methods like spectroscopic (e.g., secondary ion mass spectrometry [110]) and on-line monitoring (e.g., DOTM [55]) may also be more valuable for validating for MD models in the future.

Lastly, with the rapid increase in computational prowess, the length and time scales of MD are expected to be significantly augmented in the future. For example, MD simulation nowadays is a better depiction for organic fouling scenario in which foulant size is small, and only a simplified model for other types of fouling where foulant size is larger and may form a continuous form to block the flow. With the ability to simulate larger foulant molecules in a larger box, other type of fouling is expected to be accounted for more accurately. The usage of MD to explore ongoing processes is relatively well-established, but the implementation as a predictive tool like CFD remains stymied with the current computational power [20]. Hence, running MD in a faster and more efficient manner needs further revolutionary changes, which would significantly benefit the understanding and prediction of membrane fouling in practical applications. Table 9 provides a rough estimation for the requirement of computational power to simulate some fouling properties which are not possible for MD to simulate now.

Table 9. Estimation of required computational power increase to simulate some important features in a reasonable manner with MD.

Properties desired to simulate via MD	Approximate requirement of computational power increase
Porous membrane	10^5
Scaling	10^2
Mixture of foulants	10^3
Fouling history	10^9

Bibliography

[1] C.Y. Tang, T.H. Chong, A.G. Fane, Colloidal interactions and fouling of NF and RO membranes: a review, Adv. Colloid Interface Sci., 164 (2011) 126-143.
[2] S.P. Nunes, P.Z. Culfaz-Emecen, G.Z. Ramon, T. Visser, G.H. Koops, W. Jin, M. Ulbricht, Thinking the future of membranes: Perspectives for advanced and new membrane materials and manufacturing processes, J. Membr. Sci., 598 (2020) 117761.
[3] Y.J. Lim, K. Goh, M. Kurihara, R. Wang, Seawater desalination by reverse osmosis: Current development and future challenges in membrane fabrication – A review, J. Membr. Sci., 629 (2021) 119292.
[4] C.Y. Tang, Z. Yang, H. Guo, J.J. Wen, L.D. Nghiem, E. Cornelissen, Potable Water Reuse through Advanced Membrane Technology, Environ. Sci. Technol., 52 (2018) 10215-10223.
[5] K. Park, J. Kim, D.R. Yang, S. Hong, Towards a low-energy seawater reverse osmosis desalination plant: A review and theoretical analysis for future directions, J. Membr. Sci., 595 (2020) 117607.
[6] A.L. Zydney, New developments in membranes for bioprocessing – A review, J. Membr. Sci., 620 (2021) 118804.
[7] A.L. Zydney, Continuous downstream processing for high value biological products: A Review, Biotechnol. Bioeng., 113 (2016) 465-475.
[8] Y. Pouliot, Membrane processes in dairy technology—From a simple idea to worldwide panacea, Int. Dairy J., 18 (2008) 735-740.
[9] J.F. Brennecke, B. Freeman, Reimagining petroleum refining, Science, 369 (2020) 254-255.
[10] N.N. Li, A.G. Fane, W.W. Ho, T. Matsuura, Advanced membrane technology and applications, John Wiley & Sons, 2011.
[11] P. Wang, T.-S. Chung, Recent advances in membrane distillation processes: Membrane development, configuration design and application exploring, J. Membr. Sci., 474 (2015) 39-56.
[12] P. Krzeminski, L. Leverette, S. Malamis, E. Katsou, Membrane bioreactors – A review on recent developments in energy reduction, fouling control, novel configurations, LCA and market prospects, J. Membr. Sci., 527 (2017) 207-227.
[13] J.W. Chew, J. Kilduff, G. Belfort, The behavior of suspensions and macromolecular solutions in crossflow microfiltration: An update, J. Membr. Sci., 601 (2020) 117865.
[14] Q. She, R. Wang, A.G. Fane, C.Y. Tang, Membrane fouling in osmotically driven membrane processes: A review, J. Membr. Sci., 499 (2016) 201-233.
[15] E. Tummons, Q. Han, H.J. Tanudjaja, C.A. Hejase, J.W. Chew, V.V. Tarabara, Membrane fouling by emulsified oil: A review, Sep. Purif. Technol., 248 (2020) 116919.
[16] R. Zhang, Y. Liu, M. He, Y. Su, X. Zhao, M. Elimelech, Z. Jiang, Antifouling membranes for sustainable water purification: strategies and mechanisms, Chem. Soc. Rev., 45 (2016) 5888-5924.
[17] L.D. Tijing, Y.C. Woo, J.-S. Choi, S. Lee, S.-H. Kim, H.K. Shon, Fouling and its control in membrane distillation—A review, J. Membr. Sci., 475 (2015) 215-244.
[18] E.H. Lee, J. Hsin, M. Sotomayor, G. Comellas, K. Schulten, Discovery through the computational microscope, Structure, 17 (2009) 1295-1306.
[19] H. Ebro, Y.M. Kim, J.H. Kim, Molecular dynamics simulations in membrane-based water treatment processes: A systematic overview, J. Membr. Sci., 438 (2013) 112-125.
[20] A. Mollahosseini, A. Abdelrasoul, Molecular dynamics simulation for membrane separation and porous materials: A current state of art review, J. Mol. Graph. Model, 107 (2021) 107947.
[21] E. Strohmaier, J. Dongarra, H. Simon, M. Meuer, Top 500 The List, in, 2021.

[22] P.T. Cummings, C. McAbe, C.R. Iacovella, A. Ledeczi, E. Jankowski, A. Jayaraman, J.C. Palmer, E.J. Maginn, S.C. Glotzer, J.A. Anderson, J. Ilja Siepmann, J. Potoff, R.A. Matsumoto, J.B. Gilmer, R.S. DeFever, R. Singh, B. Crawford, Open‐source molecular modeling software in chemical engineering focusing on the Molecular Simulation Design Framework, AIChE J, 67 (2021) e17206.
[23] K.A. Feenstra, B. Hess, H.J.C. Berendsen, Improving efficiency of large time-scale molecular dynamics simulations of hydrogen-rich systems, J. Comput. Chem., 20 (1999) 786-798.
[24] S.A. Adcock, J.A. McCammon, Molecular dynamics: survey of methods for simulating the activity of proteins, Chem. Rev., 106 (2006) 1589-1615.
[25] W. Beckner, Y. He, J. Pfaendtner, Chain Flexibility in Self-Assembled Monolayers Affects Protein Adsorption and Surface Hydration: A Molecular Dynamics Study, J. Phys. Chem. B., 120 (2016) 10423-10432.
[26] K. Li, S. Li, L. Liu, W. Huang, Y. Wang, C. Yu, Y. Zhou, Molecular dynamics simulation studies of the structure and antifouling performance of a gradient polyamide membrane, Phys. Chem. Chem. Phys., 21 (2019) 19995-20002.
[27] Y. Takizawa, S. Inukai, T. Araki, R. Cruz-Silva, N. Uemura, A. Morelos-Gomez, J. Ortiz-Medina, S. Tejima, K. Takeuchi, T. Kawaguchi, T. Noguchi, T. Hayashi, M. Terrones, M. Endo, Antiorganic Fouling and Low-Protein Adhesion on Reverse-Osmosis Membranes Made of Carbon Nanotubes and Polyamide Nanocomposite, ACS Appl. Mater Interfaces, 9 (2017) 32192-32201.
[28] S. Tiwari, A. Gogoi, K. Anki Reddy, Effect of an ionic environment on membrane fouling: a molecular dynamics study, Phys. Chem. Chem. Phys., 23 (2021) 5001-5011.
[29] Y. Xiang, R.G. Xu, Y. Leng, Molecular Dynamics Simulations of a Poly(ethylene glycol)-Grafted Polyamide Membrane and Its Interaction with a Calcium Alginate Gel, Langmuir, 32 (2016) 4424-4433.
[30] Y. Ma, S. Velioğlu, Z. Yin, R. Wang, J.W. Chew, Molecular dynamics investigation of membrane fouling in organic solvents, J. Membr. Sci., 632 (2021) 119329.
[31] T. Wei, M.A. Carignano, I. Szleifer, Molecular dynamics simulation of lysozyme adsorption/desorption on hydrophobic surfaces, J. Phys. Chem. B., 116 (2012) 10189-10194.
[32] T. Virtanen, P. Parkkila, A. Koivuniemi, J. Lahti, T. Viitala, M. Kallioinen, M. Mänttäri, A. Bunker, Characterization of membrane–foulant interactions with novel combination of Raman spectroscopy, surface plasmon resonance and molecular dynamics simulation, Sep. Purif. Technol., 205 (2018) 263-272.
[33] Y. Ma, A.L. Zydney, R. Wang, J.W. Chew, Molecular dynamics study on membrane fouling by oppositely charged proteins, AIChE J., 67 (2021) e17335.
[34] A.R. Shaikh, H. Karkhanechi, T. Yoshioka, H. Matsuyama, H. Takaba, D.M. Wang, Adsorption of Bovine Serum Albumin on Poly(vinylidene fluoride) Surfaces in the Presence of Ions: A Molecular Dynamics Simulation, J. Phys. Chem. B., 122 (2018) 1919-1928.
[35] Y. Ma, S. Velioğlu, T.A. Trinh, R. Wang, J.W. Chew, Investigation of Surfactant–Membrane Interaction Using Molecular Dynamics Simulation with Umbrella Sampling, ACS ES&T Engineering, 1 (2021) 1470-1480.
[36] S. Velioğlu, L. Han, J.W. Chew, Understanding membrane pore-wetting in the membrane distillation of oil emulsions via molecular dynamics simulations, J. Membr. Sci., 551 (2018) 76-84.
[37] Q. Jiang, Z.-Y. Liu, W. Guo, Z. Su, W. Ma, L. Zhang, S. Zhao, Analysis of zwitterionic membrane fouling mechanism caused by HPAM in the presence of electrolytes, RSC Advances, 11 (2021) 16268-16274.

[38] A. YazdanYar, U. Aschauer, P. Bowen, Adsorption Free Energy of Single Amino Acids at the Rutile (110)/Water Interface Studied by Well-Tempered Metadynamics, J. Phys. Chem. C., 122 (2018) 11355-11363.
[39] H.F. Ridgway, J. Orbell, S. Gray, Molecular simulations of polyamide membrane materials used in desalination and water reuse applications: Recent developments and future prospects, J. Membr. Sci., 524 (2017) 436-448.
[40] M. Shen, S. Keten, R.M. Lueptow, Dynamics of water and solute transport in polymeric reverse osmosis membranes via molecular dynamics simulations, J. Membr. Sci., 506 (2016) 95-108.
[41] M. Yao, L.D. Tijing, G. Naidu, S.-H. Kim, H. Matsuyama, A.G. Fane, H.K. Shon, A review of membrane wettability for the treatment of saline water deploying membrane distillation, Desalination, 479 (2020) 114312.
[42] X. Song, B. Gan, Z. Yang, C.Y. Tang, C. Gao, Confined nanobubbles shape the surface roughness structures of thin film composite polyamide desalination membranes, J. Membr. Sci., 582 (2019) 342-349.
[43] M. Mozafari, S.F. Seyedpour, S.K. Salestan, A. Rahimpour, A.A. Shamsabadi, M.D. Firouzjaei, M.R. Esfahani, A. Tiraferri, H. Mohsenian, M. Sangermano, M. Soroush, Facile Cu-BTC surface modification of thin chitosan film coated polyethersulfone membranes with improved antifouling properties for sustainable removal of manganese, J. Membr. Sci., 588 (2019) 117200.
[44] M. Wang, J. Wang, J. Jiang, Membrane Fouling: Microscopic Insights into the Effects of Surface Chemistry and Roughness, Adv. Theory and Simul., 5 (2021) 2100395.
[45] X.Y. Liu, W. Chen, H.Q. Yu, Probing protein-induced membrane fouling with in-situ attenuated total reflectance fourier transform infrared spectroscopy and multivariate curve resolution-alternating least squares, Water Res., 183 (2020) 116052.
[46] J. Liu, T. Huang, R. Ji, Z. Wang, C.Y. Tang, J.O. Leckie, Stochastic Collision-Attachment-Based Monte Carlo Simulation of Colloidal Fouling: Transition from Foulant-Clean-Membrane Interaction to Foulant-Fouled-Membrane Interaction, Environ. Sci. Technol., 54 (2020) 12703-12712.
[47] W.L. Jorgensen, J. Chandrasekhar, J.D. Madura, R.W. Impey, M.L. Klein, Comparison of simple potential functions for simulating liquid water, J. Chem. Phys., 79 (1983) 926-935.
[48] H. Berendsen, J. Grigera, T. Straatsma, The missing term in effective pair potentials, J. Phys. Chem., 91 (1987) 6269-6271.
[49] H.M. Berman, J. Westbrook, Z. Feng, G. Gilliland, T.N. Bhat, H. Weissig, I.N. Shindyalov, P.E. Bourne, The Protein Data Bank, Nucleic Acids Res., 28 (2000) 235-242.
[50] A. Roy, A. Kucukural, Y. Zhang, I-TASSER: a unified platform for automated protein structure and function prediction, Nat. Protoc., 5 (2010) 725-738.
[51] Y. Escalona, D. Petrov, C. Oostenbrink, Vienna soil organic matter modeler 2 (VSOMM2), J. Mol. Graph. Model, 103 (2020) 107817.
[52] M.D. Hanwell, D.E. Curtis, D.C. Lonie, T. Vandermeersch, E. Zurek, G.R. Hutchison, Avogadro: an advanced semantic chemical editor, visualization, and analysis platform, J. of Cheminformatics, 4 (2012) 17.
[53] W. Humphrey, A. Dalke, K. Schulten, VMD: visual molecular dynamics, J. Mol. Graph., 14 (1996) 33-38, 27-38.
[54] C. Klein, J. Sallai, T.J. Jones, C.R. Iacovella, C. McCabe, P.T. Cummings, A Hierarchical, Component Based Approach to Screening Properties of Soft Matter, in: R.Q. Snurr, C.S. Adjiman, D.A. Kofke (Eds.) Foundations of Molecular Modeling and Simulation, Springer Singapore, Singapore, 2016, pp. 79-92.

[55] M.B. Tanis-Kanbur, S. Velioğlu, H.J. Tanudjaja, X. Hu, J.W. Chew, Understanding membrane fouling by oil-in-water emulsion via experiments and molecular dynamics simulations, J. Membr. Sci., 566 (2018) 140-150.
[56] L. Qin, J.E. Tobiason, H. Huang, Water and humic acid transport in graphene-derived membrane: Mechanisms and implications to functional membrane design, J. Membr. Sci., 613 (2020) 118441.
[57] Y. Xiong, T. Cao, Q. Chen, Z. Li, Y. Yang, S. Xu, S. Yuan, J. Sjöblom, Z. Xu, Adsorption of a Polyaromatic Compound on Silica Surfaces from Organic Solvents Studied by Molecular Dynamics Simulation and AFM Imaging, J. Phys. Chem. C, 121 (2017) 5020-5028.
[58] V.T. Bui, A. Abdelrasoul, D.W. McMartin, Investigation on the stability and antifouling properties of polyvinylidene fluoride (PVDF)-zwitterion mixed matrix membranes (MMMs) using molecular dynamics simulation (MDS), Comput. Mater. Sci., 187 (2021) 110079.
[59] Z. Zhou, S. Rajabzadeh, A.R. Shaikh, Y. Kakihana, W. Ma, H. Matsuyama, Effect of surface properties on antifouling performance of poly(vinyl chloride-co-poly(ethylene glycol)methyl ether methacrylate)/PVC blend membrane, J. Membr. Sci., 514 (2016) 537-546.
[60] Q. Shi, K. Zhang, R. Lu, J. Jiang, Water desalination and biofuel dehydration through a thin membrane of polymer of intrinsic microporosity: Atomistic simulation study, J. Membr. Sci., 545 (2018) 49-56.
[61] H. Zhu, Z. Chen, L. Qin, L. Zhang, J. Zhou, Simulated preparation and hydration property of a new-generation zwitterionic modified PVDF membrane, J. Membr. Sci., (2022) 120498.
[62] Y. Tang, Y. Lin, D.M. Ford, X. Qian, M.R. Cervellere, P.C. Millett, X. Wang, A review on models and simulations of membrane formation via phase inversion processes, J. Membr. Sci., 640 (2021) 119810.
[63] E. Harder, D.E. Walters, Y.D. Bodnar, R.S. Faibish, B. Roux, Molecular dynamics study of a polymeric reverse osmosis membrane, J. Phys. Chem. B, 113 (2009) 10177-10182.
[64] K. Li, S. Li, W. Huang, C. Yu, Y. Zhou, MembrFactory: A Force Field and composition Double Independent Universal Tool for Constructing Polyamide Reverse Osmosis Membranes, J. Comput. Chem., 40 (2019) 2432-2438.
[65] L. Martinez, R. Andrade, E.G. Birgin, J.M. Martinez, PACKMOL: a package for building initial configurations for molecular dynamics simulations, J. Comput. Chem., 30 (2009) 2157-2164.
[66] S. Jo, T. Kim, V.G. Iyer, W. Im, CHARMM-GUI: a web-based graphical user interface for CHARMM, J. Comput. Chem., 29 (2008) 1859-1865.
[67] A.K. Malde, L. Zuo, M. Breeze, M. Stroet, D. Poger, P.C. Nair, C. Oostenbrink, A.E. Mark, An Automated Force Field Topology Builder (ATB) and Repository: Version 1.0, J. Chem. Theory Comput., 7 (2011) 4026-4037.
[68] J. Wang, W. Wang, P.A. Kollman, D.A. Case, Automatic atom type and bond type perception in molecular mechanical calculations, J. Mol. Graph. Model, 25 (2006) 247-260.
[69] C. Klein, A.Z. Summers, M.W. Thompson, J.B. Gilmer, C. McCabe, P.T. Cummings, J. Sallai, C.R. Iacovella, Formalizing atom-typing and the dissemination of force fields with foyer, Comput. Mater. Sci., 167 (2019) 215-227.
[70] P.K. Weiner, P.A. Kollman, AMBER: Assisted model building with energy refinement. A general program for modeling molecules and their interactions, J. Comput. Chem, 2 (1981) 287-303.
[71] K. Vanommeslaeghe, E. Hatcher, C. Acharya, S. Kundu, S. Zhong, J. Shim, E. Darian, O. Guvench, P. Lopes, I. Vorobyov, A.D. Mackerell, Jr., CHARMM general

force field: A force field for drug-like molecules compatible with the CHARMM all-atom additive biological force fields, J. Comput. Chem., 31 (2010) 671-690.
[72] P. Dauber-Osguthorpe, V.A. Roberts, D.J. Osguthorpe, J. Wolff, M. Genest, A.T. Hagler, Structure and energetics of ligand binding to proteins: Escherichia coli dihydrofolate reductase-trimethoprim, a drug-receptor system, Proteins, 4 (1988) 31-47.
[73] N. Schmid, A.P. Eichenberger, A. Choutko, S. Riniker, M. Winger, A.E. Mark, W.F. van Gunsteren, Definition and testing of the GROMOS force-field versions 54A7 and 54B7, Eur. Biophys. J., 40 (2011) 843-856.
[74] W.L. Jorgensen, D.S. Maxwell, J. Tirado-Rives, Development and Testing of the OPLS All-Atom Force Field on Conformational Energetics and Properties of Organic Liquids, J. Am. Chem. Soc., 118 (1996) 11225-11236.
[75] A.D. MacKerell, Jr., M. Feig, C.L. Brooks, 3rd, Improved treatment of the protein backbone in empirical force fields, J. Am. Chem. Soc., 126 (2004) 698-699.
[76] S. Plimpton, Fast parallel algorithms for short-range molecular dynamics, J. Comput. Phys., 117 (1995) 1-19.
[77] H.J.C. Berendsen, D. van der Spoel, R. van Drunen, GROMACS: A message-passing parallel molecular dynamics implementation, Comput. Phys. Commun., 91 (1995) 43-56.
[78] J.C. Phillips, D.J. Hardy, J.D.C. Maia, J.E. Stone, J.V. Ribeiro, R.C. Bernardi, R. Buch, G. Fiorin, J. Henin, W. Jiang, R. McGreevy, M.C.R. Melo, B.K. Radak, R.D. Skeel, A. Singharoy, Y. Wang, B. Roux, A. Aksimentiev, Z. Luthey-Schulten, L.V. Kale, K. Schulten, C. Chipot, E. Tajkhorshid, Scalable molecular dynamics on CPU and GPU architectures with NAMD, J. Chem. Phys., 153 (2020) 044130.
[79] L. Verlet, Computer "Experiments" on Classical Fluids. I. Thermodynamical Properties of Lennard-Jones Molecules, Phys. Rev., 159 (1967) 98-103.
[80] S. Toxvaerd, O.J. Heilmann, J.C. Dyre, Energy conservation in molecular dynamics simulations of classical systems, J. Chem. Phys., 136 (2012) 224106.
[81] A. Fijany, T. Çağın, A. Jaramillo-Botero, W. Goddard, A Fast Algorithm for Massively Parallel, Long-Term, Simulation of Complex Molecular Dynamics Systems, in: E.H. D'Hollander, F.J. Peters, G.R. Joubert, U. Trottenberg, R. Völpel (Eds.) Parallel Computing - Fundamentals, Applications and New Directions, North-Holland, 1998, pp. 505-515.
[82] A. Arnold, F. Fahrenberger, C. Holm, O. Lenz, M. Bolten, H. Dachsel, R. Halver, I. Kabadshow, F. Gahler, F. Heber, J. Iseringhausen, M. Hofmann, M. Pippig, D. Potts, G. Sutmann, Comparison of scalable fast methods for long-range interactions, Phys. Rev. E Stat. Nonlin. Soft Matter Phys., 88 (2013) 063308.
[83] J.-P. Ryckaert, G. Ciccotti, H.J.C. Berendsen, Numerical integration of the cartesian equations of motion of a system with constraints: molecular dynamics of n-alkanes, J. Comput. Phys., 23 (1977) 327-341.
[84] B. Hess, H. Bekker, H.J.C. Berendsen, J.G.E.M. Fraaije, LINCS: A linear constraint solver for molecular simulations, J. Comput. Chem, 18 (1997) 1463-1472.
[85] S. Miyamoto, P.A. Kollman, Settle: An analytical version of the SHAKE and RATTLE algorithm for rigid water models, J. Comput. Chem, 13 (1992) 952-962.
[86] P.H. Hünenberger, Thermostat Algorithms for Molecular Dynamics Simulations, in: C. Dr. Holm, K. Prof. Dr. Kremer (Eds.) Advanced Computer Simulation, Springer Berlin Heidelberg, Berlin, Heidelberg, 2005, pp. 105-149.
[87] H.C. Andersen, Molecular dynamics simulations at constant pressure and/or temperature, J. Chem. Phys., 72 (1980) 2384-2393.
[88] H.J.C. Berendsen, J.P.M. Postma, W.F. van Gunsteren, A. DiNola, J.R. Haak, Molecular dynamics with coupling to an external bath, J. Chem. Phys., 81 (1984) 3684-3690.
[89] D.J. Evans, B.L. Holian, The Nose–Hoover thermostat, J. Chem. Phys., 83 (1985) 4069-4074.

[90] G.J. Martyna, D.J. Tobias, M.L. Klein, Constant pressure molecular dynamics algorithms, J. Chem. Phys., 101 (1994) 4177-4189.
[91] M.E. Tuckerman, J. Alejandre, R. López-Rendón, A.L. Jochim, G.J. Martyna, A Liouville-operator derived measure-preserving integrator for molecular dynamics simulations in the isothermal–isobaric ensemble, J. Phys. A Math. Gen., 39 (2006) 5629-5651.
[92] Y.-l. Liu, K. Xiao, A.-q. Zhang, X.-m. Wang, H.-w. Yang, X. Huang, Y.F. Xie, Exploring the interactions of organic micropollutants with polyamide nanofiltration membranes: A molecular docking study, J. Membr. Sci., 577 (2019) 285-293.
[93] Y. Ma, T. Hua, T.A. Trinh, R. Wang, J.W. Chew, Molecular dynamics simulation of the competitive adsorption behavior of effluent organic matters by heated aluminum oxide particles (HAOPs), Sep. Purif. Technol., 292 (2022) 120961.
[94] Y.Z. Tan, S. Velioglu, L. Han, B.D. Joseph, L.G. Unnithan, J.W. Chew, Effect of surfactant hydrophobicity and charge type on membrane distillation performance, J. Membr. Sci., 587 (2019) 117168.
[95] Y. Kawabata, R.R. Gonzales, K. Nakagawa, T. Shintani, H. Matsuyama, Y. Fujimura, T. Kawakatsu, T. Yoshioka, Molecular dynamics study on the elucidation of polyamide membrane fouling by nonionic surfactants and disaccharides, Phys. Chem. Chem. Phys., 23 (2021) 20313-20322.
[96] Y. Xiang, R.-G. Xu, Y. Leng, How alginate monomers contribute to organic fouling on polyamide membrane surfaces?, J. Membr. Sci., 643 (2022) 120078.
[97] Z.-K. Li, Y. Liu, L. Li, Y. Wei, J. Caro, H. Wang, Ultra-thin titanium carbide (MXene) sheet membranes for high-efficient oil/water emulsions separation, J. Membr. Sci., 592 (2019) 117361.
[98] K. Kubiak-Ossowska, K. Tokarczyk, B. Jachimska, P.A. Mulheran, Bovine Serum Albumin Adsorption at a Silica Surface Explored by Simulation and Experiment, J. Phys. Chem. B, 121 (2017) 3975-3986.
[99] Z.E. Hughes, J.D. Gale, Molecular dynamics simulations of the interactions of potential foulant molecules and a reverse osmosis membrane, J. Mater. Chem., 22 (2012) 175-184.
[100] J. Liu, Q. Xu, J. Jiang, A molecular simulation protocol for swelling and organic solvent nanofiltration of polymer membranes, J. Membr. Sci., 573 (2019) 639-646.
[101] W.-Y. Ahn, A.G. Kalinichev, M.M. Clark, Effects of background cations on the fouling of polyethersulfone membranes by natural organic matter: Experimental and molecular modeling study, J. Membr. Sci., 309 (2008) 128-140.
[102] Y. He, L. Qin, H. Huang, Calcium-enhanced retention of humic substances by carbon nanotube membranes: Mechanisms and implication, J. Membr. Sci., 629 (2021) 119273.
[103] T. Lan, J. Liao, Y. Yang, Z. Chai, N. Liu, D. Wang, Competition/Cooperation between Humic Acid and Graphene Oxide in Uranyl Adsorption Implicated by Molecular Dynamics Simulations, Environ. Sci. Technol., 53 (2019) 5102-5110.
[104] R. Zhang, W. Yan, C. Jing, Experimental and molecular dynamic simulation study of perfluorooctane sulfonate adsorption on soil and sediment components, J. Environ. Sci. (China), 29 (2015) 131-138.
[105] G.M. Meconi, N. Ballard, J.M. Asua, R. Zangi, Adsorption and desorption behavior of ionic and nonionic surfactants on polymer surfaces, Soft Matter, 12 (2016) 9692-9704.
[106] B. Yan, G. Munoz, S. Sauve, J. Liu, Molecular mechanisms of per- and polyfluoroalkyl substances on a modified clay: a combined experimental and molecular simulation study, Water Res., 184 (2020) 116166.
[107] Y. Ma, A.L. Zydney, J.W. Chew, Membrane fouling by lysozyme: Effect of local interaction, AIChE J., 67 (2021) e17212.

[108] Z.Y. Liu, Q. Jiang, Z. Jin, Z. Sun, W. Ma, Y. Wang, Understanding the Antifouling Mechanism of Zwitterionic Monomer-Grafted Polyvinylidene Difluoride Membranes: A Comparative Experimental and Molecular Dynamics Simulation Study, ACS Appl. Mater Interfaces, 11 (2019) 14408-14417.
[109] Y. Ma, S. Velioğlu, M.B. Tanis-Kanbur, R. Wang, J.W. Chew, Mechanistic understanding of the adsorption of natural organic matter by heated aluminum oxide particles (HAOPs) via molecular dynamics simulation, J. Membr. Sci., 598 (2020) 117651.
[110] S. Wu, X. Hua, B. Ma, H. Fan, R. Miao, M. Ulbricht, C. Hu, J. Qu, Three-Dimensional Analysis of the Natural-Organic-Matter Distribution in the Cake Layer to Precisely Reveal Ultrafiltration Fouling Mechanisms, Environ. Sci. Technol., 55 (2021) 5442-5452.
[111] C. Bartels, Analyzing biased Monte Carlo and molecular dynamics simulations, Chem. Phys. Lett., 331 (2000) 446-454.
[112] L. Sutto, M. D'Abramo, F.L. Gervasio, Comparing the Efficiency of Biased and Unbiased Molecular Dynamics in Reconstructing the Free Energy Landscape of Met-Enkephalin, J. Chem. Theory Comput., 6 (2010) 3640-3646.
[113] G. Fiorin, M.L. Klein, J. Hénin, Using collective variables to drive molecular dynamics simulations, Mol. Phys., 111 (2013) 3345-3362.
[114] M. Tournois, S. Mathe, I. Andre, J. Esque, M.A. Fernandez, Surface charge distribution: a key parameter for understanding protein behavior in chromatographic processes, J. Chromatogr. A, 1648 (2021) 462151.
[115] S. Lecot, Y. Chevolot, M. Phaner-Goutorbe, C. Yeromonahos, Impact of Silane Monolayers on the Adsorption of Streptavidin on Silica and Its Subsequent Interactions with Biotin: Molecular Dynamics and Steered Molecular Dynamics Simulations, J. Phys. Chem. B, 124 (2020) 6786-6796.
[116] I. Marquetti, S. Desai, Molecular modeling the adsorption behavior of bone morphogenetic protein-2 on hydrophobic and hydrophilic substrates, Chem. Phys. Lett., 706 (2018) 285-294.
[117] D. Zare, J.R. Allison, K.M. McGrath, Molecular Dynamics Simulation of beta-Lactoglobulin at Different Oil/Water Interfaces, Biomacromolecules, 17 (2016) 1572-1581.
[118] S. Tiwari, A. Gogoi, K.A. Reddy, What governs the nature of fouling in forward osmosis (FO) and reverse osmosis (RO)? A molecular dynamics study, Phys. Chem. Chem. Phys., 21 (2019) 24165-24176.
[119] T. Wei, M.A. Carignano, I. Szleifer, Lysozyme adsorption on polyethylene surfaces: why are long simulations needed?, Langmuir, 27 (2011) 12074-12081.
[120] P. De Angelis, A. Cardellini, P. Asinari, Exploring the Free Energy Landscape To Predict the Surfactant Adsorption Isotherm at the Nanoparticle-Water Interface, ACS Cent. Sci., 5 (2019) 1804-1812.
[121] K. Mazeau, L. Charlier, The molecular basis of the adsorption of xylans on cellulose surface, Cellulose, 19 (2012) 337-349.
[122] S. O'Mahony, C. O'Dwyer, C.A. Nijhuis, J.C. Greer, A.J. Quinn, D. Thompson, Nanoscale dynamics and protein adhesivity of alkylamine self-assembled monolayers on graphene, Langmuir, 29 (2013) 7271-7282.
[123] C. Mucksch, H.M. Urbassek, Accelerated Molecular Dynamics Study of the Effects of Surface Hydrophilicity on Protein Adsorption, Langmuir, 32 (2016) 9156-9162.
[124] J. Liang, G. Fieg, S. Jakobtorweihen, Molecular Dynamics Simulations of Competitive Protein Adsorption onto Chromatographic Media, in: J.J. Klemeš, P.S. Varbanov, P.Y. Liew (Eds.) 24th European Symposium on Computer Aided Process Engineering, Elsevier, 2014, pp. 937-942.

[125] K. Kubiak-Ossowska, G. Burley, S.V. Patwardhan, P.A. Mulheran, Spontaneous membrane-translocating peptide adsorption at silica surfaces: a molecular dynamics study, J. Phys. Chem. B, 117 (2013) 14666-14675.
[126] Y. Xia, R. Zhang, Y. Xing, X. Gui, Improving the adsorption of oily collector on the surface of low-rank coal during flotation using a cationic surfactant: An experimental and molecular dynamics simulation study, Fuel, 235 (2019) 687-695.
[127] Q. Shi, Y. Su, W. Chen, J. Peng, L. Nie, L. Zhang, Z. Jiang, Grafting short-chain amino acids onto membrane surfaces to resist protein fouling, J. Membr. Sci., 366 (2011) 398-404.
[128] M. Darvishi, M. Foroutan, Molecular investigation of oil–water separation using PVDF polymer by molecular dynamic simulation, RSC Advances, 6 (2016) 74124-74134.
[129] C.M. Mao, J. Sampath, K.G. Sprenger, G. Drobny, J. Pfaendtner, Molecular Driving Forces in Peptide Adsorption to Metal Oxide Surfaces, Langmuir, 35 (2019) 5911-5920.
[130] G. He, M. Zhang, Q. Zhou, G. Pan, Molecular dynamics simulations of structural transformation of perfluorooctane sulfonate (PFOS) at water/rutile interfaces, Chemosphere, 134 (2015) 272-278.
[131] I.-C. Yeh, J.L. Lenhart, B.C. Rinderspacher, Molecular Dynamics Simulations of Adsorption of Catechol and Related Phenolic Compounds to Alumina Surfaces, J. Phys. Chem. C, 119 (2015) 7721-7731.
[132] H. Yan, S. Yuan, Molecular Dynamics Simulation of the Oil Detachment Process within Silica Nanopores, J. Phys. Chem. C, 120 (2016) 2667-2674.
[133] M.S. Jahan Sajib, Y. Wei, A. Mishra, L. Zhang, K.I. Nomura, R.K. Kalia, P. Vashishta, A. Nakano, S. Murad, T. Wei, Atomistic Simulations of Biofouling and Molecular Transfer of a Cross-linked Aromatic Polyamide Membrane for Desalination, Langmuir, 36 (2020) 7658-7668.
[134] Q. Zhang, H. Brumer, H. Agren, Y. Tu, The adsorption of xyloglucan on cellulose: effects of explicit water and side chain variation, Carbohydr. Res., 346 (2011) 2595-2602.
[135] E.G. Brandt, A.P. Lyubartsev, Molecular Dynamics Simulations of Adsorption of Amino Acid Side Chain Analogues and a Titanium Binding Peptide on the TiO2 (100) Surface, J. Phys. Chem. C, 119 (2015) 18126-18139.
[136] T. Lan, H. Wang, J. Liao, Y. Yang, Z. Chai, N. Liu, D. Wang, Dynamics of Humic Acid and Its Interaction with Uranyl in the Presence of Hydrophobic Surface Implicated by Molecular Dynamics Simulations, Environ. Sci. Technol., 50 (2016) 11121-11128.
[137] M. Poorsargol, M. Alimohammadian, B. Sohrabi, M. Dehestani, Dispersion of graphene using surfactant mixtures: Experimental and molecular dynamics simulation studies, Appl. Surf. Sci., 464 (2019) 440-450.
[138] D.A. McQuarrie, J.D. Simon, Molecular thermodynamics, Sterling Publishing Company, 1999.
[139] Q. Wei, W. Zhao, Y. Yang, B. Cui, Z. Xu, X. Yang, Method Evaluations for Adsorption Free Energy Calculations at the Solid/Water Interface through Metadynamics, Umbrella Sampling, and Jarzynski's Equality, Chemphyschem, 19 (2018) 690-702.
[140] X. Wang, X. Yang, H. Chen, X. Yang, Z. Xu, Entropy-Enthalpy Compensation in Peptide Adsorption on Solid Surfaces: Dependence on Surface Hydration, Langmuir, 36 (2020) 10822-10829.
[141] M. Paloncyova, K. Berka, M. Otyepka, Convergence of Free Energy Profile of Coumarin in Lipid Bilayer, J. Chem. Theory Comput., 8 (2012) 1200-1211.
[142] S. Park, F. Khalili-Araghi, E. Tajkhorshid, K. Schulten, Free energy calculation from steered molecular dynamics simulations using Jarzynski’s equality, J. Chem. Phys., 119 (2003) 3559-3566.

[143] J.A.R. Willemsen, S.C.B. Myneni, I.C. Bourg, Molecular Dynamics Simulations of the Adsorption of Phthalate Esters on Smectite Clay Surfaces, J. Phys. Chem. C, 123 (2019) 13624-13636.
[144] M. Deighan, J. Pfaendtner, Exhaustively sampling peptide adsorption with metadynamics, Langmuir, 29 (2013) 7999-8009.
[145] C.D. Christ, A.E. Mark, W.F. van Gunsteren, Basic ingredients of free energy calculations: a review, J. Comput. Chem., 31 (2010) 1569-1582.
[146] M. Hoefling, F. Iori, S. Corni, K.E. Gottschalk, Interaction of amino acids with the Au(111) surface: adsorption free energies from molecular dynamics simulations, Langmuir, 26 (2010) 8347-8351.
[147] J.S. Hub, B.L. de Groot, D. van der Spoel, g_wham—A Free Weighted Histogram Analysis Implementation Including Robust Error and Autocorrelation Estimates, J. Chem. Theory Comput., 6 (2010) 3713-3720.
[148] E.R. Azhagiya Singam, Y. Zhang, G. Magnin, I. Miranda-Carvajal, L. Coates, R. Thakkar, H. Poblete, J. Comer, Thermodynamics of Adsorption on Graphenic Surfaces from Aqueous Solution, J. Chem. Theory Comput., 15 (2019) 1302-1316.
[149] Y. Wang, J. Wohlert, L.A. Berglund, Y. Tu, H. Ågren, Molecular dynamics simulation of strong interaction mechanisms at wet interfaces in clay–polysaccharide nanocomposites, J. Mater. Chem. A, 2 (2014) 9541-9547.
[150] Z. Li, K.A. Fichthorn, S.T. Milner, Surfactant Binding to Polymer-Water Interfaces in Atomistic Simulations, Langmuir, 32 (2016) 7519-7529.
[151] F. Brunel, O. Boyron, A. Clement, C. Boisson, Molecular Dynamics Simulation of Ethylene/Hexene Copolymer Adsorption onto Graphene: New Insight into Thermal Gradient Interaction Chromatography, Macromol. Chem. Phys., 220 (2019) 1800496.
[152] A. Grossfield, WHAM: the weighted histogram analysis method, in: version 2.0.11.
[153] Z. Zhao, V.H. Crespi, J.D. Kubicki, D.J. Cosgrove, L. Zhong, Molecular dynamics simulation study of xyloglucan adsorption on cellulose surfaces: effects of surface hydrophobicity and side-chain variation, Cellulose, 21 (2014) 1025-1039.
[154] Z. Kuang, K.M. Singh, D.J. Oliver, P.B. Dennis, C.C. Perry, R.R. Naik, Gamma estimator of Jarzynski equality for recovering binding energies from noisy dynamic data sets, Nat. Commun., 11 (2020) 5517.
[155] S.W. Hung, P.Y. Hsiao, C.C. Chieng, Dynamic information for cardiotoxin protein desorption from a methyl-terminated self-assembled monolayer using steered molecular dynamics simulation, J. Chem. Phys., 134 (2011) 194705.
[156] M. Mijajlovic, M.J. Penna, M.J. Biggs, Free energy of adsorption for a peptide at a liquid/solid interface via nonequilibrium molecular dynamics, Langmuir, 29 (2013) 2919-2926.
[157] Z. Zhang, T. Wu, Q. Wang, H. Pan, R. Tang, Impact of interfacial high-density water layer on accurate estimation of adsorption free energy by Jarzynski's equality, J. Chem. Phys., 140 (2014) 034706.
[158] C. Jarzynski, Nonequilibrium Equality for Free Energy Differences, Phys. Rev. Lett., 78 (1997) 2690-2693.
[159] R.H. Meissner, G. Wei, L.C. Ciacchi, Estimation of the free energy of adsorption of a polypeptide on amorphous SiO2 from molecular dynamics simulations and force spectroscopy experiments, Soft Matter, 11 (2015) 6254-6265.
[160] A. Barducci, G. Bussi, M. Parrinello, Well-tempered metadynamics: a smoothly converging and tunable free-energy method, Phys. Rev. Lett., 100 (2008) 020603.
[161] D.A. McQuarrie, J.D. Simon, Physical chemistry: a molecular approach, University science books Sausalito, CA, 1997.
[162] J. Gaberle, D.Z. Gao, M.B. Watkins, A.L. Shluger, Calculating the Entropy Loss on Adsorption of Organic Molecules at Insulating Surfaces, J. Phys. Chem. C, 120 (2016) 3913-3921.

[163] D.E. Smith, L. Zhang, A.D.J. Haymet, Entropy of association of methane in water: a new molecular dynamics computer simulation, J. Am. Chem. Soc., 114 (2002) 5875-5876.
[164] I. Andricioaei, M. Karplus, On the calculation of entropy from covariance matrices of the atomic fluctuations, J. Chem. Phys., 115 (2001) 6289-6292.
[165] K. Kubiak-Ossowska, B. Jachimska, P.A. Mulheran, How Negatively Charged Proteins Adsorb to Negatively Charged Surfaces: A Molecular Dynamics Study of BSA Adsorption on Silica, J. Phys. Chem. B, 120 (2016) 10463-10468.
[166] A. Steudle, J. Pleiss, Modelling of Lysozyme Binding to a Cation Exchange Surface at Atomic Detail: The Role of Flexibility, Biophys. J., 100 (2011) 3016-3024.
[167] J. Zhong, P. Wang, Y. Zhang, Y. Yan, S. Hu, J. Zhang, Adsorption mechanism of oil components on water-wet mineral surface: A molecular dynamics simulation study, Energy, 59 (2013) 295-300.
[168] L.O. Villacorte, Liquid Chromatography – Organic Carbon Detection (LC-OCD), in: E. Drioli, L. Giorno (Eds.) Encyclopedia of Membranes, Springer Berlin Heidelberg, Berlin, Heidelberg, 2014, pp. 1-3.
[169] Y. Xiang, Y. Liu, B. Mi, Y. Leng, Hydrated polyamide membrane and its interaction with alginate: a molecular dynamics study, Langmuir, 29 (2013) 11600-11608.
[170] M.B. Stewart, D.T. Myat, M. Kuiper, R.J. Manning, S.R. Gray, J.D. Orbell, A structural basis for the amphiphilic character of alginates - Implications for membrane fouling, Carbohydr. Polym., 164 (2017) 162-169.
[171] J.I. Monroe, S. Jiao, R.J. Davis, D. Robinson Brown, L.E. Katz, M.S. Shell, Affinity of small-molecule solutes to hydrophobic, hydrophilic, and chemically patterned interfaces in aqueous solution, Proc. Natl. Acad. Sci. USA, 118 (2021) e2020205118.
[172] N.H. Lee, G. Amy, J.P. Croue, H. Buisson, Identification and understanding of fouling in low-pressure membrane (MF/UF) filtration by natural organic matter (NOM), Water Res., 38 (2004) 4511-4523.
[173] X. Cui, K.-H. Choo, Natural organic matter removal and fouling control in low-pressure membrane filtration for water treatment, Environ. Eng. Res., 19 (2014) 1-8.
[174] B. Malczewska, J. Liu, M.M. Benjamin, Virtual elimination of MF and UF fouling by adsorptive pre-coat filtration, J. Membr. Sci., 479 (2015) 159-164.
[175] F. Chen, S. Peldszus, A.M. Elhadidy, R.L. Legge, M.I. Van Dyke, P.M. Huck, Kinetics of natural organic matter (NOM) removal during drinking water biofiltration using different NOM characterization approaches, Water Res., 104 (2016) 361-370.
[176] A. Cipollina, G. Micale, L. Rizzuti, Seawater desalination: conventional and renewable energy processes, Springer Science & Business Media, 2009.
[177] B. Malczewska, M.M. Benjamin, Efficacy of hybrid adsorption/membrane pretreatment for low pressure membrane, Water Res., 99 (2016) 263-271.
[178] A. Bhatnagar, M. Sillanpaa, Removal of natural organic matter (NOM) and its constituents from water by adsorption - A review, Chemosphere, 166 (2017) 497-510.
[179] L.F. Wang, M.M. Benjamin, A multi-spectral approach to differentiate the effects of adsorbent pretreatments on the characteristics of NOM and membrane fouling, Water Res., 98 (2016) 56-63.
[180] K.J. Howe, A. Marwah, K.P. Chiu, S.S. Adham, Effect of coagulation on the size of MF and UF membrane foulants, Environ. Sci. Technol., 40 (2006) 7908-7913.
[181] M. Yan, D. Wang, J. Ni, J. Qu, C.W. Chow, H. Liu, Mechanism of natural organic matter removal by polyaluminum chloride: effect of coagulant particle size and hydrolysis kinetics, Water Res., 42 (2008) 3361-3370.
[182] C. Stoquart, P. Servais, P.R. Bérubé, B. Barbeau, Hybrid membrane processes using activated carbon treatment for drinking water: a review, J. Membr. Sci., 411 (2012) 1-12.

[183] B. Ma, C. Hu, X. Wang, Y. Xie, W.A. Jefferson, H. Liu, J. Qu, Effect of aluminum speciation on ultrafiltration membrane fouling by low dose aluminum coagulation with bovine serum albumin (BSA), J. Membr. Sci., 492 (2015) 88-94.
[184] J. Kim, Z. Cai, M.M. Benjamin, Effects of adsorbents on membrane fouling by natural organic matter, J. Membr. Sci., 310 (2008) 356-364.
[185] K.J. Howe, M.M. Clark, Effect of coagulation pretreatment on membrane filtration performance, J. Am. Water Works Assoc., 98 (2006) 133-146.
[186] E. Barbot, S. Moustier, J. Bottero, P. Moulin, Coagulation and ultrafiltration: Understanding of the key parameters of the hybrid process, J. Membr. Sci., 325 (2008) 520-527.
[187] A. Maartens, P. Swart, E. Jacobs, Feed-water pretreatment: methods to reduce membrane fouling by natural organic matter, J. Membr. Sci., 163 (1999) 51-62.
[188] Z. Cai, C. Wee, M.M. Benjamin, Fouling mechanisms in low-pressure membrane filtration in the presence of an adsorbent cake layer, J. Membr. Sci., 433 (2013) 32-38.
[189] Z. Cai, M.M. Benjamin, NOM fractionation and fouling of low-pressure membranes in microgranular adsorptive filtration, Environ. Sci. Technol., 45 (2011) 8935-8940.
[190] J. Kim, Z. Cai, M.M. Benjamin, NOM fouling mechanisms in a hybrid adsorption/membrane system, J. Membr. Sci., 349 (2010) 35-43.
[191] Z. Cai, J. Kim, M.M. Benjamin, NOM removal by adsorption and membrane filtration using heated aluminum oxide particles, Environ. Sci. Technol., 42 (2008) 619-623.
[192] J. Kim, W. Shi, Y. Yuan, M.M. Benjamin, A serial filtration investigation of membrane fouling by natural organic matter, J. Membr. Sci., 294 (2007) 115-126.
[193] L.F. Wang, M.M. Benjamin, HAOPs pretreatment to reduce membrane fouling: Foulant identification, removal, and interactions, J. Membr. Sci., 515 (2016) 219-229.
[194] E. Braun, J. Gilmer, H.B. Mayes, D.L. Mobley, J.I. Monroe, S. Prasad, D.M. Zuckerman, Best Practices for Foundations in Molecular Simulations [Article v1.0], Living J. Comput. Mol. Sci., (2018) 5957.
[195] K. Boussu, B. Van der Bruggen, A. Volodin, J. Snauwaert, C. Van Haesendonck, C. Vandecasteele, Roughness and hydrophobicity studies of nanofiltration membranes using different modes of AFM, J. Colloid. Interface Sci., 286 (2005) 632-638.
[196] J.M. McHale, A. Navrotsky, A.J. Perrotta, Effects of Increased Surface Area and Chemisorbed H2O on the Relative Stability of Nanocrystalline γ-Al2O3and α-Al2O3, J. Phys. Chem. B, 101 (1997) 603-613.
[197] A. Phan, D.R. Cole, A. Striolo, Liquid ethanol simulated on crystalline alpha alumina, J. Phys. Chem. B, 117 (2013) 3829-3840.
[198] J.C. Liu, Effect of Operational Parameters on Microgranular Adsorptive Filtration (μGAF), in: University of Washington, 2015.
[199] A.G. Piotr, P.T. Artur, F. Sylwester, W. Jerzy, K. Piotr, Z. Wojciech, MD simulation of organics adsorption from aqueous solution in carbon slit-like pores. Foundations of the pore blocking effect, J. Phys. Condens. Matter, 26 (2014) 055008.
[200] M. Jorge, C. Schumacher, N.A. Seaton, Simulation Study of the Effect of the Chemical Heterogeneity of Activated Carbon on Water Adsorption, Langmuir, 18 (2002) 9296-9306.
[201] C.L. McCallum, T.J. Bandosz, S.C. McGrother, E.A. Müller, K.E. Gubbins, A Molecular Model for Adsorption of Water on Activated Carbon: Comparison of Simulation and Experiment, Langmuir, 15 (1999) 533-544.
[202] N. Shaari, S.K. Kamarudin, S. Basri, Molecular dynamics simulations of sodium alginate/sulfonated graphene oxide membranes properties, Heliyon, 4 (2018) e00808.
[203] L.T. Sein, J.M. Varnum, S.A. Jansen, Conformational modeling of a new building block of humic acid: approaches to the lowest energy conformer, Environ. Sci. Technol., 33 (1999) 546-552.

[204] P. Saparpakorn, J. Kim, S. Hannongbua, Investigation on the binding of polycyclic aromatichydrocarbons with soil organic matter: A theoretical approach, Molecules, 12 (2007) 703-715.
[205] S. Meylan, F. Hammes, J. Traber, E. Salhi, U. von Gunten, W. Pronk, Permeability of low molecular weight organics through nanofiltration membranes, Water Res., 41 (2007) 3968-3976.
[206] E.R. Dickenson, R.S. Summers, J.P. Croue, H. Gallard, Haloacetic acid and trihalomethane formation from the chlorination and bromination of aliphatic beta-dicarbonyl acid model compounds, Environ. Sci. Technol., 42 (2008) 3226-3233.
[207] G.A. Kaminski, R.A. Friesner, J. Tirado-Rives, W.L. Jorgensen, Evaluation and Reparametrization of the OPLS-AA Force Field for Proteins via Comparison with Accurate Quantum Chemical Calculations on Peptides, J. Phys. Chem. B, 105 (2001) 6474-6487.
[208] K. Kahn, T.C. Bruice, Parameterization of OPLS–AA force field for the conformational analysis of macrocyclic polyketides, J. Comput. Chem., 23 (2002) 977-996.
[209] S. Velioglu, S. Keskin, Simulation of H2/CH4 mixture permeation through MOF membranes using non-equilibrium molecular dynamics, J. Mater. Chem. A Mater., 7 (2019) 2301-2314.
[210] W.M. Deen, Analysis of Transport Phenomena, Topics in Chemical Engineering, Oxford University Press, New York, 1998.
[211] D.C. Rapaport, Equilibrium properties of simple fluids, in: The Art of Molecular Dynamics Simulation, Cambridge University Press, Cambridge, 2004, pp. 83-119.
[212] D. Eisenberg, W. Kauzmann, W. Kauzmann, The structure and properties of water, Oxford University Press on Demand, 2005.
[213] A. Luzar, D. Chandler, Structure and hydrogen bond dynamics of water–dimethyl sulfoxide mixtures by computer simulations, J. Chem. Phys., 98 (1993) 8160-8173.
[214] M. Ferrario, M. Haughney, I.R. McDonald, M.L. Klein, Molecular ‐ dynamics simulation of aqueous mixtures: Methanol, acetone, and ammonia, J. Chem. Phys., 93 (1990) 5156-5166.
[215] D. Frenkel, B. Smit, Dissipative Particle Dynamics, in: D. Frenkel, B. Smit (Eds.) Understanding Molecular Simulation, Academic Press, San Diego, 2002, pp. 465-478.
[216] C.G. Gray, K.E. Gubbins, C.G. Joslin, Chapter 8 - Surface Properties, in: Theory of Molecular Fluids: Volume 2: Applications, Oxford University Press, 2011.
[217] M. Gonçalves, M. Molina-Sabio, F. Rodriguez-Reinoso, Modification of activated carbon hydrophobicity by pyrolysis of propene, J. Anal. Appl. Pyrolysis, 89 (2010) 17-21.
[218] M. Holz, S.R. Heil, A. Sacco, Temperature-dependent self-diffusion coefficients of water and six selected molecular liquids for calibration in accurate 1H NMR PFG measurements, Phys. Chem. Chem. Phys., 2 (2000) 4740-4742.
[219] I.M. Svishchev, P.G. Kusalik, Structure in liquid water: A study of spatial distribution functions, J. Chem. Phys., 99 (1993) 3049-3058.
[220] S. Modarresi, M.M. Benjamin, Insights and Model for Understanding Natural Organic Matter Adsorption onto Mixed Adsorbents, Environ. Sci. Technol., 52 (2018) 6343-6349.
[221] S. Velten, D.R. Knappe, J. Traber, H.P. Kaiser, U. von Gunten, M. Boller, S. Meylan, Characterization of natural organic matter adsorption in granular activated carbon adsorbers, Water Res., 45 (2011) 3951-3959.
[222] F. Zamani, A. Ullah, E. Akhondi, H.J. Tanudjaja, E.R. Cornelissen, A. Honciuc, A.G. Fane, J.W. Chew, Impact of the surface energy of particulate foulants on membrane fouling, J. Membr. Sci., 510 (2016) 101-111.
[223] T.A. Trinh, Q. Han, Y. Ma, J.W. Chew, Microfiltration of oil emulsions stabilized by different surfactants, J. Membr. Sci., 579 (2019) 199-209.

[224] H.J. Tanudjaja, J.W. Chew, Assessment of oil fouling by oil-membrane interaction energy analysis, J. Membr. Sci., 560 (2018) 21-29.
[225] Y. Chun, T. Hua, A. Anantharaman, J.W. Chew, N. Cai, M. Benjamin, R. Wang, Organic matter removal from a membrane bioreactor effluent for reverse osmosis fouling mitigation by microgranular adsorptive filtration system, Desalination, 506 (2021) 115016.
[226] D.T. Myat, M.B. Stewart, M. Mergen, O. Zhao, J.D. Orbell, S. Gray, Experimental and computational investigations of the interactions between model organic compounds and subsequent membrane fouling, Water Res., 48 (2014) 108-118.
[227] A. Sundermann, R. Solc, D. Tunega, G. Haberhauer, M.H. Gerzabek, C. Oostenbrink, Vienna Soil-Organic-Matter Modeler--Generating condensed-phase models of humic substances, J. Mol. Graph. Model, 62 (2015) 253-261.
[228] Q. Sun, H.B. Xie, J. Chen, X. Li, Z. Wang, L. Sheng, Molecular dynamics simulations on the interactions of low molecular weight natural organic acids with C60, Chemosphere, 92 (2013) 429-434.
[229] L.N. Breitner, K.J. Howe, D. Minakata, Effect of Functional Chemistry on the Rejection of Low-Molecular Weight Neutral Organics through Reverse Osmosis Membranes for Potable Reuse, Environ. Sci. Technol., 53 (2019) 11401-11409.
[230] J. Cao, Y. Liang, Y. Masuda, H. Koga, H. Tanaka, K. Tamura, S. Takagi, T. Matsuoka, Molecular simulation of CH4 adsorption behavior in slit nanopores: Verification of simulation methods and models, AIChE J., 65 (2019) e16733.
[231] L.M. Espinoza-Fonseca, J.G. Trujillo-Ferrara, Conformational changes of the p53-binding cleft of MDM2 revealed by molecular dynamics simulations, Biopolymers, 83 (2006) 365-373.
[232] J. Lee, S. Jeong, Y. Ye, V. Chen, S. Vigneswaran, T. Leiknes, Z. Liu, Protein fouling in carbon nanotubes enhanced ultrafiltration membrane: Fouling mechanism as a function of pH and ionic strength, Sep. Purif. Technol., 176 (2017) 323-334.
[233] S. Shao, W. Fu, X. Li, D. Shi, Y. Jiang, J. Li, T. Gong, X. Li, Membrane fouling by the aggregations formed from oppositely charged organic foulants, Water Res., 159 (2019) 95-101.
[234] R. Miao, L. Wang, N. Mi, Z. Gao, T. Liu, Y. Lv, X. Wang, X. Meng, Y. Yang, Enhancement and Mitigation Mechanisms of Protein Fouling of Ultrafiltration Membranes under Different Ionic Strengths, Environ. Sci. Technol., 49 (2015) 6574-6580.
[235] Y.N. Wang, C.Y. Tang, Fouling of nanofiltration, reverse osmosis, and ultrafiltration membranes by protein mixtures: the role of inter-foulant-species interaction, Environ. Sci. Technol., 45 (2011) 6373-6379.
[236] A. Sethuraman, G. Vedantham, T. Imoto, T. Przybycien, G. Belfort, Protein unfolding at interfaces: slow dynamics of alpha-helix to beta-sheet transition, Proteins, 56 (2004) 669-678.
[237] J. Tian, M. Pan, Y. Ma, J.W. Chew, Effect of membrane fouling on chiral separation, J. Membr. Sci., 593 (2020) 117352.
[238] M.M. Rohani, A.L. Zydney, Role of electrostatic interactions during protein ultrafiltration, Adv. Colloid. Interface Sci., 160 (2010) 40-48.
[239] D. Breite, M. Went, I. Thomas, A. Prager, A. Schulze, Particle adsorption on a polyether sulfone membrane: how electrostatic interactions dominate membrane fouling, RSC Advances, 6 (2016) 65383-65391.
[240] M. Hadidi, A.L. Zydney, Fouling behavior of zwitterionic membranes: Impact of electrostatic and hydrophobic interactions, J. Membr. Sci., 452 (2014) 97-103.
[241] Y. Li, S.C. Soh, T.-S. Chung, S.Y. Chan, Exploration of ionic modification in dual-layer hollow fiber membranes for long-term high-performance protein separation, AIChE J., 55 (2009) 321-330.

[242] R. Miao, L. Wang, M. Zhu, D. Deng, S. Li, J. Wang, T. Liu, Y. Lv, Effect of Hydration Forces on Protein Fouling of Ultrafiltration Membranes: The Role of Protein Charge, Hydrated Ion Species, and Membrane Hydrophilicity, Environ. Sci. Technol., 51 (2017) 167-174.
[243] D.J. Hughes, Z. Cui, R.W. Field, U.K. Tirlapur, In situ three-dimensional characterization of membrane fouling by protein suspensions using multiphoton microscopy, Langmuir, 22 (2006) 6266-6272.
[244] C. Liu, L. Chen, L. Zhu, Fouling behavior of lysozyme on different membrane surfaces during the MD operation: An especial interest in the interaction energy evaluation, Water Res., 119 (2017) 33-46.
[245] L.M. Szott, T.A. Horbett, Protein interactions with surfaces: Computational approaches and repellency, Curr. Opin. Chem. Biol., 15 (2011) 683-689.
[246] C. Mucksch, H.M. Urbassek, Molecular dynamics simulation of free and forced BSA adsorption on a hydrophobic graphite surface, Langmuir, 27 (2011) 12938-12943.
[247] K. Kubiak-Ossowska, M. Cwieka, A. Kaczynska, B. Jachimska, P.A. Mulheran, Lysozyme adsorption at a silica surface using simulation and experiment: effects of pH on protein layer structure, Phys. Chem. Chem. Phys., 17 (2015) 24070-24077.
[248] S.Y. Park, S.H. Choi, J.W. Chung, S.-Y. Kwak, Anti-scaling ultrafiltration/microfiltration (UF/MF) polyvinylidene fluoride (PVDF) membranes with positive surface charges for Ca2+/silica-rich wastewater treatment, J. Membr. Sci., 480 (2015) 122-128.
[249] H. Na, Y. Zhao, C. Zhao, C. Zhao, X. Yuan, Effect of hot-press on electrospun poly(vinylidene fluoride) membranes, Polym. Eng. Sci., 48 (2008) 934-940.
[250] V. Lachet, J.M. Teuler, B. Rousseau, Classical force field for hydrofluorocarbon molecular simulations. Application to the study of gas solubility in poly(vinylidene fluoride), J. Phys. Chem. A, 119 (2015) 140-151.
[251] H.J. Butt, K. Graf, M. Kappl, The Electric Double Layer, in: Physics and Chemistry of Interfaces, 2003, pp. 42-56.
[252] B.K. Shoichet, W.A. Baase, R. Kuroki, B.W. Matthews, A relationship between protein stability and protein function, Proc. Natl. Acad. Sci. USA, 92 (1995) 452-456.
[253] M.A. Grant, A new membrane filtration medium for simultaneous detection and enumeration of Escherichia coli and total coliforms, Appl. Environ. Microbiol., 63 (1997) 3526-3530.
[254] C. Stauber, C. Miller, B. Cantrell, K. Kroell, Evaluation of the compartment bag test for the detection of Escherichia coli in water, J. Microbiol. Methods, 99 (2014) 66-70.
[255] J. Huang, S. Rauscher, G. Nawrocki, T. Ran, M. Feig, B.L. de Groot, H. Grubmuller, A.D. MacKerell, Jr., CHARMM36m: an improved force field for folded and intrinsically disordered proteins, Nat. Methods, 14 (2017) 71-73.
[256] R.B. Best, X. Zhu, J. Shim, P.E. Lopes, J. Mittal, M. Feig, A.D. Mackerell, Jr., Optimization of the additive CHARMM all-atom protein force field targeting improved sampling of the backbone phi, psi and side-chain chi(1) and chi(2) dihedral angles, J. Chem. Theory Comput., 8 (2012) 3257-3273.
[257] W.M. Haynes, CRC handbook of chemistry and physics, CRC press, 2014.
[258] E.D. Abeyrathne, H.Y. Lee, D.U. Ahn, Sequential separation of lysozyme, ovomucin, ovotransferrin, and ovalbumin from egg white, Poult. Sci., 93 (2014) 1001-1009.
[259] A.D. MacKerell, D. Bashford, M. Bellott, R.L. Dunbrack, J.D. Evanseck, M.J. Field, S. Fischer, J. Gao, H. Guo, S. Ha, D. Joseph-McCarthy, L. Kuchnir, K. Kuczera, F.T. Lau, C. Mattos, S. Michnick, T. Ngo, D.T. Nguyen, B. Prodhom, W.E. Reiher, B. Roux, M. Schlenkrich, J.C. Smith, R. Stote, J. Straub, M. Watanabe, J. Wiorkiewicz-Kuczera, D. Yin, M. Karplus, All-atom empirical potential for molecular modeling and dynamics studies of proteins, J. Phys. Chem. B, 102 (1998) 3586-3616.

[260] Y. Baek, P. Emami, N. Singh, A. Ilott, E. Sahin, A. Zydney, Stereospecific interactions between histidine and monoclonal antibodies, Biotechnol. Bioeng., 116 (2019) 2632-2639.
[261] Q. She, C.Y. Tang, Y.-N. Wang, Z. Zhang, The role of hydrodynamic conditions and solution chemistry on protein fouling during ultrafiltration, Desalination, 249 (2009) 1079-1087.
[262] K.L. Jones, C.R. O'Melia, Protein and humic acid adsorption onto hydrophilic membrane surfaces: effects of pH and ionic strength, J. Membr. Sci., 165 (2000) 31-46.
[263] X. He, F. Meng, A. Lin, J. Li, C.Y. Tang, Characteristics and fouling propensity of polysaccharides in the presence of different monovalent ions, AIChE J., 62 (2016) 2501-2507.
[264] A.S. Freed, S.M. Cramer, Protein-surface interaction maps for ion-exchange chromatography, Langmuir, 27 (2011) 3561-3568.
[265] C.M. Roth, J.E. Sader, A.M. Lenhoff, Electrostatic Contribution to the Energy and Entropy of Protein Adsorption, J. Colloid Interface Sci., 203 (1998) 218-221.
[266] D. Horinek, A. Serr, M. Geisler, T. Pirzer, U. Slotta, S.Q. Lud, J.A. Garrido, T. Scheibel, T. Hugel, R.R. Netz, Peptide adsorption on a hydrophobic surface results from an interplay of solvation, surface, and intrapeptide forces, Proc. Natl. Acad. Sci. USA, 105 (2008) 2842-2847.
[267] L. Palacio, C.C. Ho, P. Prádanos, A. Hernández, A.L. Zydney, Fouling with protein mixtures in microfiltration: BSA–lysozyme and BSA–pepsin, J. Membr. Sci., 222 (2003) 41-51.
[268] S.T. Kelly, A.L. Zydney, Protein fouling during microfiltration: comparative behavior of different model proteins, Biotechnol. Bioeng., 55 (1997) 91-100.
[269] N. Chandra, K. Brew, K.R. Acharya, Structural evidence for the presence of a secondary calcium binding site in human alpha-lactalbumin, Biochemistry, 37 (1998) 4767-4772.
[270] A. Rudling, A. Orro, J. Carlsson, Prediction of Ordered Water Molecules in Protein Binding Sites from Molecular Dynamics Simulations: The Impact of Ligand Binding on Hydration Networks, J. Chem. Inf. Model, 58 (2018) 350-361.
[271] Y. Tao, Z.H. Rao, S.Q. Liu, Insight derived from molecular dynamics simulation into substrate-induced changes in protein motions of proteinase K, J. Biomol. Struct. Dyn., 28 (2010) 143-158.
[272] M. Persico, G. Daigle, S. Kadel, V. Perreault, G. Pellerin, J. Thibodeau, L. Bazinet, Predictive models for determination of peptide fouling based on the physicochemical characteristics of filtration membranes, Sep. Purif. Technol., 240 (2020) 116602.
[273] L. Palacio, C.C. Ho, A.L. Zydney, Application of a pore-blockage--cake-filtration model to protein fouling during microfiltration, Biotechnol. Bioeng., 79 (2002) 260-270.
[274] C. Güell, R.H. Davis, Membrane fouling during microfiltration of protein mixtures, J. Membr. Sci., 119 (1996) 269-284.
[275] J. Brant, A.E. Childress, Assessing short-range membrane–colloid interactions using surface energetics, J. Membr. Sci., 203 (2002) 257-273.
[276] J. Liu, Y. Fan, Y. Sun, Z. Wang, D. Zhao, T. Li, B. Dong, C.Y. Tang, Modelling the critical roles of zeta potential and contact angle on colloidal fouling with a coupled XDLVO - collision attachment approach, J. Membr. Sci., 623 (2021) 119048.
[277] C. Boo, S. Hong, M. Elimelech, Relating Organic Fouling in Membrane Distillation to Intermolecular Adhesion Forces and Interfacial Surface Energies, Environ. Sci. Technol., 52 (2018) 14198-14207.
[278] J.A. Veil, M.G. Puder, D. Elcock, R.J. Redweik Jr, A white paper describing produced water from production of crude oil, natural gas, and coal bed methane, in, Argonne National Lab., IL (US), 2004.

[279] H.J. Tanudjaja, C.A. Hejase, V.V. Tarabara, A.G. Fane, J.W. Chew, Membrane-based separation for oily wastewater: A practical perspective, Water Res., 156 (2019) 347-365.
[280] D. Lu, T. Zhang, J. Ma, Ceramic membrane fouling during ultrafiltration of oil/water emulsions: roles played by stabilization surfactants of oil droplets, Environ. Sci. Technol., 49 (2015) 4235-4244.
[281] K. Boussu, C. Kindts, C. Vandecasteele, B. Van der Bruggen, Surfactant fouling of nanofiltration membranes: measurements and mechanisms, Chemphyschem, 8 (2007) 1836-1845.
[282] E. Virga, M.A. Parra, W.M. de Vos, Fouling of polyelectrolyte multilayer based nanofiltration membranes during produced water treatment: The role of surfactant size and chemistry, J. Colloid. Interface Sci., 594 (2021) 9-19.
[283] J. Tian, T.A. Trinh, M.N. Kalyan, J.S. Ho, J.W. Chew, In-situ monitoring of oil emulsion fouling in ultrafiltration via electrical impedance spectroscopy (EIS): Influence of surfactant, J. Membr. Sci., 616 (2020) 118527.
[284] H.J. Tanudjaja, V.V. Tarabara, A.G. Fane, J.W. Chew, Effect of cross-flow velocity, oil concentration and salinity on the critical flux of an oil-in-water emulsion in microfiltration, J. Membr. Sci., 530 (2017) 11-19.
[285] Z. He, S. Kasemset, A.Y. Kirschner, Y.H. Cheng, D.R. Paul, B.D. Freeman, The effects of salt concentration and foulant surface charge on hydrocarbon fouling of a poly(vinylidene fluoride) microfiltration membrane, Water Res., 117 (2017) 230-241.
[286] S. Kumar, J.M. Rosenberg, D. Bouzida, R.H. Swendsen, P.A. Kollman, THE weighted histogram analysis method for free-energy calculations on biomolecules. I. The method, J. Comput. Chem., 13 (1992) 1011-1021.
[287] S. Kumar, J.M. Rosenberg, D. Bouzida, R.H. Swendsen, P.A. Kollman, Multidimensional free-energy calculations using the weighted histogram analysis method, J. Comput. Chem., 16 (1995) 1339-1350.
[288] A. Qin, X. Li, X. Zhao, D. Liu, C. He, Preparation and characterization of nano-chitin whisker reinforced PVDF membrane with excellent antifouling property, J. Membr. Sci., 480 (2015) 1-10.
[289] Y.Z. Tan, L. Han, W.H. Chow, A.G. Fane, J.W. Chew, Influence of module orientation and geometry in the membrane distillation of oily seawater, Desalination, 423 (2017) 111-123.
[290] L. Han, Y.Z. Tan, T. Netke, A.G. Fane, J.W. Chew, Understanding oily wastewater treatment via membrane distillation, J. Membr. Sci., 539 (2017) 284-294.
[291] F. Jiménez-Ángeles, A. Khoshnood, A. Firoozabadi, Molecular Dynamics Simulation of the Adsorption and Aggregation of Ionic Surfactants at Liquid–Solid Interfaces, J. Phys. Chem. C, 121 (2017) 25908-25920.
[292] T.E. de Oliveira, F. Leonforte, L. Nicolas-Morgantini, A.-L. Fameau, B. Querleux, F. Thalmann, C.M. Marques, Fluid bilayer phase in aqueous mixtures of fatty alcohol and cationic surfactant, Phys. Rev. Res., 2 (2020) 013075.
[293] G.M. Torrie, J.P. Valleau, Nonphysical sampling distributions in Monte Carlo free-energy estimation: Umbrella sampling, J. Comput. Phys., 23 (1977) 187-199.
[294] K. Majewska-Nowak, I. Kowalska, M. Kabsch-Korbutowicz, Ultrafiltration of SDS solutions using polymeric membranes, Desalination, 184 (2005) 415-422.
[295] R. Field, S. Hang, T. Arnot, The influence of surfactant on water flux through microfiltration membranes, J. Membr. Sci., 86 (1994) 291-304.
[296] A.-S. Jönsson, B. Jönsson, The influence of nonionic and ionic surfactants on hydrophobic and hydrophilic ultrafiltration membranes, J. Membr. Sci., 56 (1991) 49-76.
[297] E. Fernández, J.M. Benito, C. Pazos, J. Coca, Ceramic membrane ultrafiltration of anionic and nonionic surfactant solutions, J. Membr. Sci., 246 (2005) 1-6.

[298] I. Kowalska, M. Kabsch-Korbutowicz, K. Majewska-Nowak, T. Winnicki, Separation of anionic surfactants on ultrafiltration membranes, Desalination, 162 (2004) 33-40.
[299] G. Akay, R.J. Wakeman, Mechanisms of permeate flux decay, solute rejection and concentration polarisation in crossflow filtration of a double chain ionic surfactant dispersion, J. Membr. Sci., 88 (1994) 177-195.
[300] G. Akay, R.J. Wakeman, Crossflow microfiltration behaviour of a double-chain cationic surfactant dispersion in water—I. The effect of process and membrane characteristics on permeate flux and surfactant rejection, Chem. Eng. Sci., 49 (1994) 271-283.
[301] L. Yao, Z. Qin, Q. Chen, M. Zhao, H. Zhao, W. Ahmad, L. Fan, L. Zhao, Insights into the nanofiltration separation mechanism of monosaccharides by molecular dynamics simulation, Sep. Purif. Technol., 205 (2018) 48-57.
[302] M. Dahanayaka, R. Babicheva, Z. Chen, A.W.-K. Law, M.S. Wu, K. Zhou, Atomistic simulation study of GO/HKUST-1 MOF membranes for seawater desalination via pervaporation, Appl. Surf. Sci., 503 (2020) 144198.
[303] A.G. Fane, R. Wang, M.X. Hu, Synthetic membranes for water purification: status and future, Angew. Chem. Int. Ed. Engl., 54 (2015) 3368-3386.
[304] M.A. Shannon, P.W. Bohn, M. Elimelech, J.G. Georgiadis, B.J. Mariñas, A.M. Mayes, Science and technology for water purification in the coming decades, in: Nanoscience and Technology, Co-Published with Macmillan Publishers Ltd, UK, 2009, pp. 337-346.
[305] S.K. Lim, K. Goh, T.-H. Bae, R. Wang, Polymer-based membranes for solvent-resistant nanofiltration: A review, Chin. J. Chem. Eng., 25 (2017) 1653-1675.
[306] P. Marchetti, M.F. Jimenez Solomon, G. Szekely, A.G. Livingston, Molecular separation with organic solvent nanofiltration: a critical review, Chem. Rev., 114 (2014) 10735-10806.
[307] G. Szekely, M.F. Jimenez-Solomon, P. Marchetti, J.F. Kim, A.G. Livingston, Sustainability assessment of organic solvent nanofiltration: from fabrication to application, Green Chem., 16 (2014) 4440-4473.
[308] S. Jiang, Y. Li, B.P. Ladewig, A review of reverse osmosis membrane fouling and control strategies, Sci. Total Environ., 595 (2017) 567-583.
[309] S. Zaidi, A. Kumar, Effects of ethanol concentration on flux and gel formation in dead end ultrafiltration of PEG and dextran, J. Membr. Sci., 237 (2004) 189-197.
[310] Z. Yin, Y. Ma, B. Tanis-Kanbur, J.W. Chew, Fouling behavior of colloidal particles in organic solvent ultrafiltration, J. Membr. Sci., 599 (2020) 117836.
[311] Z. Yin, R.J.E. Yeow, Y. Ma, J.W. Chew, Link between interfacial interaction and membrane fouling during organic solvent ultrafiltration of colloidal foulants, J. Membr. Sci., 611 (2020) 118369.
[312] H.T. Lay, J.W. Chew, Critical flux of colloidal foulant in microfiltration: Effect of organic solvent, J. Membr. Sci., 616 (2020) 118531.
[313] M. Mohtashami, J. Fooladi, A. Haddad-Mashadrizeh, M.R. Housaindokht, H. Monhemi, Molecular mechanism of enzyme tolerance against organic solvents: Insights from molecular dynamics simulation, Int. J. Biol. Macromol., 122 (2019) 914-923.
[314] B. Fryczkowska, A. Machnicka, D. Binias, C. Slusarczyk, J. Fabia, The Influence of Graphene Addition on the Properties of Composite rGO/PAN Membranes and Their Potential Application for Water Disinfection, Membranes (Basel), 10 (2020) 58.
[315] J.W. Van Cleve, W.C. Schaefer, C.E. Rist, The Structure of NRRL B-512 Dextran. Methylation Studies2, J. Am. Chem. Soc., 78 (1956) 4435-4438.
[316] L. Zhu, W. Yang, Y.Y. Meng, X. Xiao, Y. Guo, X. Pu, M. Li, Effects of organic solvent and crystal water on gamma-chymotrypsin in acetonitrile media: observations from molecular dynamics simulation and DFT calculation, J. Phys. Chem. B, 116 (2012) 3292-3304.

[317] Q. Lin, S. Liao, L. Li, W. Li, F. Yue, F. Peng, J. Ren, Solvent effect on xylose conversion under catalyst-free conditions: insights from molecular dynamics simulation and experiments, Green Chem., 22 (2020) 532-539.
[318] K. Karki, D. Roccatano, Molecular Dynamics Simulation Study of Chlorophyll a in Different Organic Solvents, J. Chem. Theory Comput., 7 (2011) 1131-1140.
[319] S. Hezaveh, S. Samanta, G. Milano, D. Roccatano, Molecular dynamics simulation study of solvent effects on conformation and dynamics of polyethylene oxide and polypropylene oxide chains in water and in common organic solvents, J. Chem. Phys., 136 (2012) 124901.
[320] E. Akhondi, F. Zamani, J.W. Chew, W.B. Krantz, A.G. Fane, Improved design and protocol for evapoporometry determination of the pore-size distribution, J. Membr. Sci., 496 (2015) 334-343.
[321] Z. Yin, S. Aggarwal, R.J.E. Yeow, L. Kong, J.W. Chew, Membrane filtration of dextran solutions with water and formamide as solvent, Separ. Sci. Technol., 57 (2021) 637-655.
[322] S. Zeidler, U. Kätzel, P. Kreis, Systematic investigation on the influence of solutes on the separation behavior of a PDMS membrane in organic solvent nanofiltration, J. Membr. Sci., 429 (2013) 295-303.
[323] B. Lee, F.M. Richards, The interpretation of protein structures: estimation of static accessibility, J. Mol. Biol., 55 (1971) 379-400.
[324] J.W. Daily, Chapter 9 - Liquids, in: Statistical Thermodynamics: An Engineering Approach, Cambridge University Press, Cambridge, 2018.
[325] J. Ren, S. Song, A. Lopez-Valdivieso, J. Shen, S. Lu, Dispersion of Silica Fines in Water-Ethanol Suspensions, J. Colloid. Interface Sci., 238 (2001) 279-284.